

Collisionless ion collection by non-emitting spherical bodies in $E \times B$ fields

by

Leonardo Patacchini

S.M., Massachusetts Institute of Technology (2007)
Ingénieur diplômé de l'Ecole Polytechnique (X2002)

Submitted to the Department of Nuclear Science and Engineering
in partial fulfillment of the requirements for the degree of

Doctor of Philosophy in Applied Plasma Physics

at the

MASSACHUSETTS INSTITUTE OF TECHNOLOGY

February 2010

© Massachusetts Institute of Technology 2010. All rights reserved.

Author
.....

Department of Nuclear Science and Engineering
October 6, 2009

Certified by
.....

Ian H. Hutchinson
Professor
Thesis Supervisor

Certified by
.....

Brian LaBombard
Principal Research Scientist
Thesis Reader

Accepted by
.....

Jacquelyn C. Yanch
Chair, Department Committee on Graduate Students

Collisionless ion collection by non-emitting spherical bodies in $\mathbf{E} \times \mathbf{B}$ fields

by

Leonardo Patacchini

Submitted to the Department of Nuclear Science and Engineering
on October 6, 2009, in partial fulfillment of the
requirements for the degree of
Doctor of Philosophy in Applied Plasma Physics

Abstract

The three-dimensional interaction of a magnetized, collisionless flowing plasma with a non-emitting conducting sphere is solved in the entire range of physically allowed parameters, in the ion-collecting regime. This can be considered as the “spherical Mach probe” problem, establishing how the ion flux to the surface varies with orientation and external velocity; the study is however of broader interest, as the sphere can also be seen as a dust particle or any ionospheric body. The core tool developed for this study is the fully parallelized (particle + field solver) Particle-In-Cell code SCEPTIC3D, three-dimensional evolution of SCEPTIC, accounting for the full ion distribution function and Boltzmann electrons.

Investigations are first carried out in the quasineutral limit. Results include a report of ion current dependence on the external plasma parameters, as well as a theoretical calibration for transverse Mach probes with four electrodes oriented at 45° to the magnetic field in a plane of flow and magnetic field, valid for arbitrary temperature and ion magnetization. The analysis is preceded by an independent semi-analytic treatment of strongly magnetized ion collection by oblique surfaces, successfully validating SCEPTIC3D’s behaviour.

The finite shielding length regime is more complex, and an important transition in plasma structure occurs when the Debye length goes over the average ion Larmor radius. Studies of ion collection show that the ion current can exceed the (unmagnetized) OML limit at weak magnetization, and the Mach probe calibration method proposed in the context of quasineutral plasmas holds up to Debye lengths equal to about 10% of the probe radius.

A further analysis consists in calculating the force exerted by the flow on spherical dust. In short Debye length plasmas a strong drag component antiparallel to the convective electric field forms, causing the dust to spin faster than what predicted by its Larmor frequency. At intermediate and large Debye length the ion-drag in the direction of transverse flow is found to reverse in subsonic conditions, but the internal Laplace force appears to be positive, and larger in magnitude than the negative ion-drag.

Thesis Supervisor: Ian H. Hutchinson
Title: Professor

Thesis Reader: Brian LaBombard
Title: Principal Research Scientist

Acknowledgments

As the end of my journey as a doctoral student approaches, it is with the deepest gratitude that I acknowledge those who contributed to its success.

First and foremost I would like to thank my advisor Pr. Ian Hutchinson for his trust and support. I measure the great liberty that I benefited from, be it in setting my own research directions or in undertaking abundant and often unrelated coursework. I shall also not forget his uninterrupted time-commitment, as well as prompt proofreading of countless papers and thesis drafts. Closely working with a scientist having such a deep physical insight has been a pleasure, and after four years I can corroborate what the French consul in Boston told me after meeting Pr. Hutchinson at a cocktail: “Your advisor looks pretty smart !”.

I am deeply indebted to the MIT Nuclear Science and Engineering Department and the Plasma Science and Fusion Center faculty, scientists and support staff. In particular Pr. Sidney Yip, Pr. Ronald Parker, Pr. Jeffrey Freidberg, Pr. Miklos Porkolab, Pr. Ian Hutchinson and Dr. Peter Catto, with whom I had close contact through classes; my reader Dr. Brian Labombard for his valuable advices and comments; Dr. John Wright and Dr. Paul Bonoli for helping me use the cluster Loki; and last but not least Valerie Censabella for her administrative support.

I acknowledge financial support from the MIT Nuclear Science and Engineering Department and the US Department of Energy, as well as the kind hospitality of the Alcator group for letting me use and abuse the control-room workstations.

I must express my sincere gratitude to Pr. Giovanni Lapenta for hosting me in his research group at Los Alamos National Laboratory during the summer 2006; this period resulted in a fruitful collaboration, and helped me mature the knowledge gathered in my first year at MIT. I am also indebted to the late Pr. Hiroshima Noguchi, who hosted me in his research group at Keio University during the summer 2008 despite very unfavorable circumstances; I will not forget you.

My time here wouldn’t have been such a wonderful experience without the joy of taking Japanese language classes at MIT and Harvard. Special thanks to Shingu,

Nagaya, Nagatomi, Matsumura, Shiomi, Yamanaka and Fujisaki Sensei; as well as to Daniela Reichert for helping me organize my stay in Japan during the summer 2008.

I am deeply indebted to my parents for their love and support throughout my entire life, and for their encouragement to undertake my Doctoral research in the United States. I know how happy they are to see me returning home.

Contents

Abstract	3
Acknowledgments	5
Contents	7
List of Figures	11
List of Tables	14
I Thesis outline	15
I.1 Background	15
I.2 Nomenclature	17
I.3 Structure	19
II Probes in zero Debye length, strongly magnetized plasmas	23
II.1 Foreword on Langmuir probes	23
II.1.1 Unmagnetized probes	23
II.1.2 Magnetized probes	28
II.2 Foreword on magnetized, transverse Mach probes	32
II.2.1 The Mach probe concept	32
II.2.2 General isothermal formulation	34
II.2.3 Relative weight of the different transport mechanisms	38
II.2.4 The question of ion recycling	41
II.3 The quasi-collisionless convective model	42
II.3.1 Presheath equations	42
II.3.2 Discussion of the diffusive limit	43
II.3.3 Convective limit	44
II.4 Convective solution	45

II.4.1	Solution method	45
II.4.2	Isothermal fluid solution	48
II.4.3	Analogy with the plasma expansion into a vacuum	49
II.4.4	Free-flight solution	49
II.5	Results and physical discussion	50
II.5.1	Plasma profiles	50
II.5.2	Ion flux-density to a flat probe	52
II.5.3	Extension to transverse Mach probes	54
II.5.4	Mach probe calibration	57
II.6	2D analytic free-flight density contours	59
II.6.1	Strongly magnetized limit	59
II.6.2	Comparison with the magnetic-free regime	61
III	SCEPTIC3D	63
III.1	Model and computational method	63
III.1.1	Problem formulation	63
III.1.2	Code mesh	66
III.1.3	Orbit integration	72
III.2	Quasineutral operation	73
III.2.1	Boundary conditions	73
III.2.2	Accuracy	74
III.2.3	Axisymmetry resolution	76
III.3	Finite Debye length operation	78
III.3.1	Parallelized Poisson solver	78
III.3.2	Electrostatic Maxwell stress tensor	83
III.3.3	Magnetostatic Maxwell stress tensor	89
IV	Spheres in zero Debye length, arbitrarily magnetized plasmas	91
IV.1	Plasma profiles	91
IV.1.1	Infinite ion magnetization	91
IV.1.2	Intermediate ion magnetization	96

IV.2	Ion saturation current	97
IV.2.1	Free-flight current	97
IV.2.2	Self-consistent ion current	99
IV.3	Transverse Mach probe calibration	101
V	Spheres in infinite Debye length, arbitrarily magnetized plasmas	109
V.1	Foreword on dust charging in the unmagnetized regime	110
V.1.1	Dusty plasmas	110
V.1.2	Orbit Motion Limited shielding	113
V.1.3	Orbit Motion Limited charging	117
V.2	Ion collection in the drift approximation	118
V.2.1	1D-kinetic/2D-drift model	119
V.2.2	Results and physical discussion	124
V.2.3	The question of stationary magnetoplasmas	126
V.3	Review of collection in stationary, large Debye length magnetoplasmas	128
V.3.1	Parker-Murphy upper bound current	128
V.3.2	Free-flight magnetized current	130
V.3.3	Helical upper bound current	133
V.3.4	Ion current calculations	134
V.4	Ion collection in arbitrarily magnetized flowing plasmas	136
V.4.1	Total ion current	136
V.4.2	Angular ion flux-density distribution	138
V.4.3	Plasma profiles	139
VI	Spheres in finite Debye length, arbitrarily magnetized plasmas	141
VI.1	Foreword on electron-collecting space tethers	142
VI.1.1	Electrodynamic tethers	142
VI.1.2	Electron collection by the TSS subsatellite	143
VI.2	Plasma profiles	146
VI.2.1	Strong ion magnetization	146
VI.2.2	Intermediate ion magnetization	149

VI.3	Self-consistent ion current	155
VI.3.1	Current dependence on ion magnetization	155
VI.3.2	Current-Voltage characteristics at low Debye length	157
VI.3.3	Transverse Mach probe calibration	161
VII	Dust grain dynamics	165
VII.1	Foreword on unmagnetized dust dynamics	165
VII.1.1	Dielectric response approach to the ion-drag force	166
VII.1.2	Binary collision approach to the ion-drag force	168
VII.1.3	Force Evaluation with SCEPTIC	171
VII.2	2D calculations in parallel-drifting magnetoplasmas	172
VII.2.1	Free-flight calculations	172
VII.2.2	Self-consistent calculations	174
VII.3	Capacitance calculations in $\mathbf{E} \times \mathbf{B}$ fields	178
VII.4	Force calculations in $\mathbf{E} \times \mathbf{B}$ fields	179
VII.4.1	Free-flight calculations at infinite magnetization	179
VII.4.2	Calculation of the non ion-drag forces	183
VII.4.3	Momentum conservation in SCEPTIC3D	186
VII.4.4	Ion-drag solutions at low Debye length	187
VII.4.5	Ion-drag solutions at intermediate and large Debye length .	191
VIII	Conclusions	199
VIII.1	Position of the problem and computational approach	199
VIII.2	Summary of physical results	200
VIII.3	Directions for future work	203
A	Boltzmann electron response	207
A.1	Electron density distribution	207
A.2	Electron current	208

List of Figures

I-1	Thesis Map	20
II-1	Magnetized Langmuir probe characteristics	29
II-2	Diffusive presheath model	31
II-3	Magnetic presheath	31
II-4	Example of Gundestrup probes	33
II-5	Planar probe geometry	37
II-6	Ion orbits in $\mu - v$ space	47
II-7	Evolution of the ion distribution function along the presheath	50
II-8	Evolution of density and temperature along the presheath	51
II-9	Evolution of the parallel ion flux-density along the presheath	53
II-10	Mach probe calibration factor	55
II-11	Ion flux-ratios	55
II-12	2D convex probe with circular cross-section	56
II-13	Angular distribution of ion saturation flux	57
II-14	Magnetized free-flight density contours	60
II-15	Comparison of magnetized and unmagnetized free-flight contours	62
III-1	Problem geometry	67
III-2	3D and 2D views of SCEPTIC3D's computational domain	67
III-3	1D representation of the computational grid	69
III-4	Computational noise in the quasineutral regime	76
III-5	2D benchmarking of SCEPTIC3D in the quasineutral regime	77
III-6	Solver accuracy 1	88
III-7	Solver accuracy 2	88

IV-1	Problem reduction to two dimensions in the $\Lambda_{De} \ll R_L \ll R_p$ scaling	92
IV-2	Density contour-plots at strong magnetization	94
IV-3	Comparison between the 1D-kinetic treatment and SCEPTIC3D	95
IV-4	Parallel ion temperature contour-plots	96
IV-5	Density contour-plots at intermediate magnetization	98
IV-6	Free-flight ion current as a function of magnetization	100
IV-7	Self-consistent ion current as a function of magnetization	102
IV-8	Angular ion flux-density distribution	103
IV-9	3D color-plot of ion flux-density to the probe	104
IV-10	Upstream to downstream flux ratios at $\eta = 3\pi/4$ and $\eta = \pi/4$	106
IV-11	Calibration factor as function of magnetization and temperature	106
V-1	Example of dust particles	111
V-2	Dust created by the Alcator C-Mod lower hybrid launcher	112
V-3	OML ion current to a spherical probe	119
V-4	3D ion orbits in physical space	123
V-5	Ion current in the drift approximation at infinite Debye length	125
V-6	Ion flux-ratios in the drift approximation at infinite Debye length	127
V-7	Total ion current in the quasineutral regime	127
V-8	Critical magnetic bottles in a Coulomb potential	130
V-9	Helical orbits parametrization	131
V-10	Magnetized ion current to a stationary Coulomb sphere	136
V-11	Total ion current as a function of β_i at infinite Debye length	137
V-12	Angular ion flux-density distribution	138
V-13	Critical streamlines as a function of probe potential	140
V-14	Critical streamlines at low magnetization	140
VI-1	Artist view of a space tether	143
VI-2	C-V characteristic from the TSS-1R experiment	144
VI-3	Ion charge-density contour-plots on the $\{0, \mathbf{e}_y, \mathbf{e}_z\}$ -plane	147
VI-4	Ion charge-density contour-plots on the $\{0, \mathbf{e}_x, \mathbf{e}_y\}$ -plane	148

VI-5	Potential contour-lines at strong magnetization	150
VI-6	Parallel temperature contour-lines	151
VI-7	Perpendicular temperature contour-lines	152
VI-8	Charge-density contour-plots on the $\{0, \mathbf{e}_y, \mathbf{e}_z\}$ -plane	153
VI-9	Charge-density contour plots on the $\{0, \mathbf{e}_x, \mathbf{e}_y\}$ -plane	153
VI-10	Cyclotron wakes in the presence of cross-field drifts	154
VI-11	Ion current as a function of magnetization	156
VI-12	C-V characteristics at finite Debye length	158
VI-13	Ion current versus the Parker-Murphy upper bound	160
VI-14	Critical magnetic bottles in a D-H potential	162
VI-15	Upstream to downstream flux-ratios at $\eta = 3\pi/4$ and $\eta = \pi/4$. . .	163
VI-16	Calibration factor as function of magnetization and temperature . .	164
VII-1	Unmagnetized ion-drag force as a function of drift velocity	172
VII-2	Free-flight ion-drag as a function of magnetization in parallel flows .	174
VII-3	Self-consistent drag as a function of magnetization in parallel flows .	177
VII-4	Effective shielding length in $\mathbf{E} \times \mathbf{B}$ fields	180
VII-5	Free-flight drag as a function of magnetization in cross-field flows .	182
VII-6	Momentum conservation in SCEPTIC3D	188
VII-7	Ion-drag at $\lambda_{De} = 0.03$ in pure cross-field flows	190
VII-8	Non ion-drag forces at $\lambda_{De} = 0.03$ in pure cross-field flows	191
VII-9	Ion-drag at $\lambda_{De} = 0.03$	192
VII-10	Ion-drag at moderate and large Debye length in the \mathbf{e}_y -direction .	194
VII-11	Ion-drag at moderate and large Debye length in the \mathbf{e}_x -direction . .	195
VII-12	Non ion-drag forces at moderate and large Debye length	197
A-1	Two orbit types in the presence of a magnetic field	209

List of Tables

I.1	Examples of magnetized plasma-collector interaction	17
I.2	Thesis nomenclature	19
II.1	Sample plasma parameters for typical Alcator C-Mod SOL conditions	40
V.1	Sample parameters relevant to dust studies in tokamak-edge conditions	113

Chapter I

Thesis outline

I.1 Background

Interest in the physics of plasma interaction with ion-absorbing bodies has not faded since the almost century-old work of Mott-Smith and Langmuir [1, 2], to whom the technique of flux-sensing (or electric) probes is due. The concept of electric probes is simple: from the insertion of one or more small electrodes in a discharge and the measure of collected currents, one seeks to infer local plasma properties such as the electron temperature (*Langmuir probes*) or the plasma drift velocity (*Mach probes*). Because biased (usually negatively), probes modify the neighbouring electrostatic potential and particle distribution functions. The challenge is therefore not so much the experimental operation itself, rather the development of reliable theories relating the collected fluxes to the unperturbed plasma properties [3, 4].

To develop such theories, it is customary to consider bodies with spherical geometry. Of course this simplification greatly eases the analysis, but perhaps more important broadens the applicability of the developed results to the more recent field of dusty plasmas [5]. Because electron mobility is much higher than the ions', dust particles usually tend to charge until they acquire a potential negative enough to repel the excess electrons and collect a zero net current. Calculating the charging rate, as well as quantities such as the drag force exerted on the particles by drifting plasmas, involves the same physics as the interpretation of probe measurements, albeit dust

grains are usually two to three orders of magnitude smaller than probes.

The motivation for this thesis is to improve our understanding of ion collection by negatively charged electrodes in flowing magnetized plasmas, in the entire range of ion magnetization β_i and electron Debye length over electrode radius λ_{De} . In order to concentrate on basic plasma phenomena, the complexity of non-plasma physics is reduced as follows. It is first assumed that the probe is ideal (we refer to “probe”, “electrode” or “dust” regardless of the physical nature of the collector), that is to say it absorbs every particle striking it and releases neutral atoms or molecules at a rate that balances the incoming flux of ions. Deviations from ideality come from different solid state physics reactions resulting in electron emission at the surface; those phenomena will be disregarded bearing in mind that they might not be negligible in situations involving for instance ionospheric plasmas, where UV radiation can cause strong enough photoemission to positively charge orbiting bodies. It is further assumed that the probe bias is negative enough for a Debye sheath to form; in this regime, the electron density and the electrostatic potential around the probe are simply related by a Boltzmann exponential.

Despite the unfortunate insufficiency of communication between laboratory-plasma and space-physics communities, the interaction of spacecraft with their environment shares many properties with the above mentioned probes or dust particulates. However because the quantity of interest is usually the attracted electron rather than ion current, no Boltzmann electron treatment is possible and more specific calculations are required. Examples of plasmas where the average ion Larmor radius R_L compares to the size of relevant perturbing objects are proposed in table (I.1).

A convenient way to treat the problem is to follow the Particle-In-Cell (PIC) approach [8]: instead of directly solving the continuity equation for the ion distribution function coupled to Poisson equation for the potential, a large set of computational particles are advanced according to the equations of motion. Using the 2D/3v (two-dimensional physical space, three-dimensional velocity space) PIC code SCEP-TIC [9, 10, 11, 12], the problem has been comprehensively solved in unmagnetized plasmas. The main challenge in the presence of a background magnetic field is the

	$T_{e\infty}$ (eV)	$T_{i\infty}$ (eV)	B (T)	N_∞ (m $^{-3}$)	R_{Le} (μm)	R_L (μm)	Λ_{De} (μm)	R_L compares to
Mid-plane SOL	10	30	5	10^{18}	1.9	200	23	dust
Divertor region	5	5	5	10^{20}	1.3	81	1.7	dust
Magnetron	3	0.025	$2.4 \cdot 10^{-2}$	$2.5 \cdot 10^{16}$	210	$5.3 \cdot 10^3$	81	probe
F-layer	0.1	0.1	$5 \cdot 10^{-5}$	10^{11}	$1.9 \cdot 10^4$	$3.2 \cdot 10^6$	$7.4 \cdot 10^3$	satellite

Table I.1: Examples of plasmas where the average ion Larmor radius R_L compares to the size of dust particles ($R_p \sim 1 - 200 \mu\text{m}$), flux-sensing probes ($R_p \sim 1\text{-}5\text{mm}$), or man-made satellites ($R_p \sim 1\text{m}$). The first two examples are typical DD (D^+ plasma) Tokamak plasmas. Experimental parameters for the Magnetron (Ar^+ discharge) are taken from Ref. [6], and atmospheric data for the F-layer (O^+ plasma) is from Ref. [7].

requirement for cross-field transport in the collector's magnetic shadow in order for the presheath to merge with the plasma at infinity. When no such effect is accounted for, only the Large Debye length plasmas when the potential distribution around the collector adopts a Coulomb form [13], or weakly magnetized plasmas where the ratio of sphere radius over mean ion Larmor radius $\beta_i \lesssim 1$ [14] can be treated.

I.2 Nomenclature

In this thesis, special care has been taken to ensure notation consistency. The key parameters and variables are referenced in table (I.2).

Dimensional plasma parameters

$T_{i,e}$	Ion (electron) temperature	
$T_{i\infty}$	Ion temperature at infinity	
N_∞	External electron density	
$N_{i,e}$	Ion (electron) charge-density	
Λ_{De}	Electron Debye length	Eq. (II.1)
Z	Ion charge-number	
e	Elementary charge	

m	Ion mass	
\mathbf{v}_d	(Total) external drift velocity	
v_∞, v_\perp	Parallel and perpendicular external drift velocities	
\mathbf{B}	Magnetic field	
ω_c	Ion Larmor angular frequency	
δ	Angle of \mathbf{v}_d to \mathbf{B}	
c_{sI}	Isothermal ion sound speed	Eq. (II.20)
$v_{ti,e}$	Ion (electron) thermal speed	Eq. (II.31)
$\Gamma_{i,e}^0$	Ion (electron) thermal charge flux-density	Eq. (II.3)
c_s	Bohm ion sound speed	Eq. (II.9)
γ_i	Ion adiabatic index	Eq. (II.10)
c_{s0}	Cold ion sound speed	Eq. (II.13)
R_L	Mean ion Larmor radius	Eq. (II.19)
\mathbf{E}_{cnv}	Convective electric field	
Φ	Probe-induced electrostatic potential distribution	
$\bar{\nu}_{ei}$	Averaged e-i momentum transfer Coulomb collision frequency	Eq. (II.34)

Dimensional probe parameters

R_p	Spherical probe radius
Φ_p	Probe mean potential (external bias)
Φ_f	Probe mean floating potential
$\Gamma_{i,e}$	Ion (electron) charge flux-density to the probe
$I_{i,e}$	Ion (electron) <i>total</i> current to the probe
I	Net current to the probe e ($I_i - I_e$)
$\Gamma_{i,es}$	Ion (electron) saturation charge flux-density to the probe
$I_{i,es}$	Ion (electron) saturation current to the probe
\mathbf{j}	Net current-density circulating in the probe

Dimensionless parameters

τ	External ion to electron temperature ratio	Eq. (II.5)
$n_{i,e}$	Ion (electron) <i>charge</i> density normalized to N_∞	
n	<i>Charge</i> density normalized to N_∞ in quasineutral plasmas	
ϕ	Electrostatic potential normalized to T_e/e	
χ	Electrostatic potential normalized to $-T_{i\infty}/Ze$	
λ_{De}	Electron Debye length normalized to R_p	
β_i	Probe radius over mean ion Larmor radius	Eq. (IV.1)
M_∞, M_\perp	Parallel and perpendicular external isothermal Mach numbers	
\mathbf{w}_d	(Total) external drift velocity normalized to v_{ti}	
w_∞, w_\perp	Parallel and perpendicular external drift velocities normalized to v_{ti}	

Table I.2: Key parameters and definitions used throughout this thesis.

I.3 Structure

Including the present outline, this thesis is structured in 7 chapters placed in logical order such as to progressively cover the $\beta_i - \lambda_{De}$ parameter map in figure I-1.

Chapter 2

The kinetic equation governing a strongly magnetized quasineutral transverse plasma flow past a convex ion-collecting object is solved numerically for arbitrary ion to electron temperature ratio τ . The approximation of isothermal ions adopted in a recent fluid treatment of the same plasma model [15] is shown to have no more than a small quantitative effect on the solution. In particular, the ion flux-density to an elementary portion of the object still only depends on the local surface orientation. We rigorously show that the solution can be condensed in a single “calibration factor” M_c ,

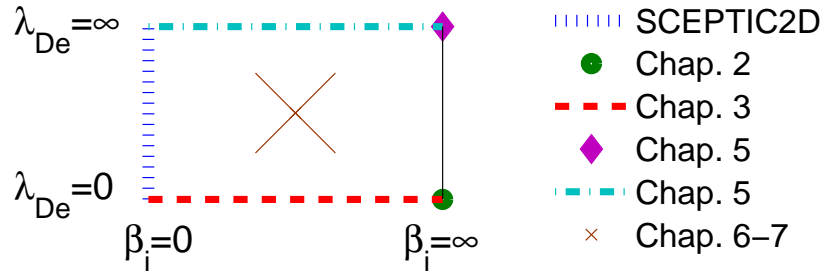


Figure I-1: $\beta_i - \lambda_{De}$ (ion magnetization - electron Debye length) parameter-space that we propose to explore in this thesis. “SCEPTIC2D” refers to previous two-dimensional investigations by Hutchinson [9, 10, 11, 12].

function of τ only, enabling Mach probe measurements of parallel and perpendicular flows by probing flux ratios at two different angles in the plane of flow and magnetic field.

Chapter 3

The two-dimensional parallel Particle-In-Cell (PIC) code SCEPTIC [9, 10, 11, 12], designed to solve the axi-symmetric interaction of a collisionless flowing plasma with a negatively charged ion-collecting sphere, is extensively modified to resolve the third, azimuthal dimension. The new code version SCEPTIC3D can therefore operate in the inherently three-dimensional configuration where background orthogonal magnetic and electric fields drive a cross-field flow. While the particle advance is distributed as in the 2D version, a new parallelized 3D Poisson solver based on the linear minimum residual algorithm has been developed.

Chapter 4

The ion saturation current (i.e. at zero Debye length) to a spherical probe in the entire range of ion magnetization is computed with SCEPTIC3D. Results are compared

with prior SCEPTIC calculations valid in the magnetic-free regime, and with the semi-analytic solutions of chapter 2. At intermediate magnetization (ion Larmor radius close to the probe radius) the plasma density profiles show a complex three-dimensional structure that SCEPTIC3D can fully resolve, and contrary to intuition the ion current can exceed the unmagnetized limit provided the ion temperature is low enough. Our results are conveniently condensed in a single factor M_c , function of ion temperature and magnetic field only, providing the theoretical calibration for a transverse Mach probe with four electrodes placed at 45° to the magnetic field in a plane of flow and magnetic field.

Chapter 5

First, the kinetic equation governing a strongly magnetized transverse plasma flow past a sphere in the vacuum limit (large Debye length) is solved numerically for a selection of plasma parameters. It is observed that contrary to the quasineutral strongly magnetized regime discussed in chapter 2, the ion current continuously tends towards the no-drift limit as the cross-field flow is reduced, with a sensitivity much higher than in vacuum unmagnetized conditions (OML [10]). Because the convective electric field is shielded by the conductor however, the ions only have a parallel velocity when collected and no “Mach probe”-like calibration is possible. The same problem is then solved with SCEPTIC3D accounting for finite ion magnetization, showing that the ion current to dust particles in tokamak-edge relevant conditions can exceed the litterature-assumed OML value by a significant amount.

Chapter 6

We here take advantage of SCEPTIC3D’s full capabilities, by bridging the gap between the quasineutral (chapter 4) and vacuum (chapter 5) regimes through the accountancy of finite Debye length. An important transition in plasma structure is found to occur when the Debye length goes over the average ion Larmor radius, hence the Debye sheath and magnetic presheath merge, in particular opening the possibility for weakly damped cyclotron wakefields. Studies of ion collection show

that exceeding of the OML current limit at weak magnetization also occurs in intermediate Debye length conditions, and the Mach probe calibration method proposed in the context of quasineutral plasmas holds up to Debye lengths equal to about 10% of the probe radius.

Chapter 7

A further analysis of interest in the finite Debye length regime is to compute the ion-drag force exerted by the plasma on the sphere, typically a dust particle. In short Debye length plasmas a strong drag component antiparallel to the convective electric field forms, causing the dust to spin much faster than what predicted by its Larmor frequency. At intermediate and large Debye length the ion-drag component in the direction of transverse flow is found to reverse in subsonic conditions, but estimates of currents circulating inside the dust suggest that the resulting Laplace force is in the positive direction, and larger in magnitude than the ion-drag.

Chapter II

Probes in zero Debye length, strongly magnetized plasmas

II.1 Foreword on Langmuir probes

II.1.1 Unmagnetized probes

The Langmuir probe

The development of models describing the contact between plasmas and solid surfaces, initiated by Langmuir and Mott-Smith in the 1920s [1, 2], is amongst the oldest ongoing endeavours of plasma physics. Original investigations were mainly motivated by the prospect of diagnosing discharge properties with a small electrode, the *Langmuir probe*. The method is essentially based upon interpreting the net current collected by the probe from the plasma, as a function of the applied bias voltage.

Let us consider a probe plunged in a uniform, Maxwellian plasma consisting of a single species of monoionized ions, with charge-number Z . Because the ion to electron mass ratio m/m_e is large and thermalization is driven by Coulomb collisions, ions and electrons equilibrate among themselves much faster than with each other. We therefore describe the ion and electron unperturbed distribution functions by Maxwellians with different temperatures $T_{i\infty}$ and T_e , but equal *charge density* N_∞ and drift velocity \mathbf{v}_d .

When the probe bias Φ_p is lower than space potential, $\Phi_0 = 0$ by convention, ions are attracted and collected at a rate in general dependent on Φ_p . If however the electron Debye length

$$\Lambda_{De} = \sqrt{\frac{\epsilon_0 T_e}{N_\infty e^2}} \quad (\text{II.1})$$

is much shorter than the probe size, the electrons neutralize the ions down to a thin layer at its surface called Debye sheath, and the probe is strongly shielded. In this regime it is observed that in the limit $\Phi_p \ll -T_e/e$, the ion current I_i saturates to a value I_{is} independent of Φ_p . Most electrons are on the contrary repelled, hence their current is governed by a Boltzmann factor; for collisionless unmagnetized electrons [4]:

$$I_e = A \Gamma_e^0 \exp\left(\frac{e \Phi_p}{T_e}\right), \quad (\text{II.2})$$

where

$$\Gamma_e^0 = N_\infty \left(\frac{T_e}{2\pi m_e}\right)^{1/2} \quad (\text{II.3})$$

is the electron thermal flux density, and A the probe area.

If we exclude surface electron emission effects, important in so-called “emissive probe” measurements, the total current $I = e(I_i - I_e)$ as a function of Φ_p can be cast in the form [4, 3]

$$I = I_{is} \left\{ 1 - \exp\left[\frac{e(\Phi_p - \Phi_f)}{T_e}\right] \right\}, \quad (\text{II.4})$$

where Φ_f is the *a priori* unknown floating potential, bias at which the probe current vanishes. The discharge electron temperature T_e can then be measured by fitting I_{is} , Φ_f and T_e in Eq. (II.4) to experimental Current-Voltage (C-V) characteristics $I(\Phi_p)$.

The Bohm Condition

Because the probe acts as a particle sink and is furthermore biased, it collects ions from a perturbed plasma. Relating the ion saturation current to physical plasma properties “at infinity”, such as N_∞ or the ion to electron temperature ratio

$$\tau = \frac{T_{i\infty}}{Z T_e}, \quad (\text{II.5})$$

therefore requires an understanding of the self-consistent interaction between the probe and the plasma. The exact solution depends on the probe shape, and is in general obtained through a numerical treatment. This is usually done by assuming that (a) outside the Debye sheath the plasma is quasineutral, i.e. the ion and electron *charge* densities are quasi-equal : $N_i \simeq N_e$ and (b) the repelled electrons are Boltzmann distributed in the entire perturbed plasma:

$$N_e(\Phi) = N_\infty \exp\left(\frac{e\Phi}{T_e}\right). \quad (\text{II.6})$$

The perturbed plasma region outside the Debye sheath, where quasineutrality holds, is usually called presheath. More details on the Boltzmann electron distribution and current are given in appendix A.

Because the Debye sheath is assumed to be thin compared to the probe size, hence its local curvature radius, one can describe the presupposed collisionless ion dynamics at the sheath edge by the following one-dimensional continuity

$$\langle v \rangle \frac{\partial N}{\partial \xi} + N \frac{\partial \langle v \rangle}{\partial \xi} = 0 \quad (\text{II.7})$$

and momentum

$$mN\langle v \rangle \frac{\partial \langle v \rangle}{\partial \xi} = -\frac{\partial(NT_i)}{\partial \xi} - Ze \frac{\partial \Phi}{\partial \xi} \quad (\text{II.8})$$

equations, where in ξ is distance from the Debye sheath edge, $\langle v \rangle$ is the ion fluid velocity towards the probe, and $N = N_i = N_e$. Defining the Bohm sound speed by

$$c_s = \left(\frac{ZT_e + \gamma_i T_i}{m} \right)^{1/2}, \quad (\text{II.9})$$

where γ_i is the effective adiabatic index

$$\gamma_i = \frac{1}{T_i} \frac{d(N_i T_i)}{dN_i}, \quad (\text{II.10})$$

and taking advantage of quasineutrality, we can rewrite Eq. (II.8) as

$$c_s^2 \frac{\partial N}{\partial \xi} + N \langle v \rangle \frac{\partial \langle v \rangle}{\partial \xi} = 0. \quad (\text{II.11})$$

It immediately appears that the system composed by Eqs (II.7,II.11) has a non constant solution if and only if

$$\begin{vmatrix} \langle v \rangle & N \\ c_s^2 & N \langle v \rangle \end{vmatrix} = 0. \quad (\text{II.12})$$

This is the Bohm condition, stating that the ion fluid velocity at the sheath edge equals the Bohm sound speed ($\langle v \rangle = v_{is} = c_s$). Eqs (II.7,II.11) only apply at the exact sheath edge; if $\xi < 0$ (sheath) quasineutrality does not apply, and if $\xi > 0$ (presheath) the physics is either multi-dimensional, or requires additional ingredients such as collisions, ionization/recombination, ...

Spherical probe in a cold plasma

Dimensionally, in a collisionless plasma the ion saturation current is of the order $AN_\infty c_{s0}$, where

$$c_{s0} = \left(\frac{ZT_e}{m} \right)^{1/2} \quad (\text{II.13})$$

is the cold ion sound speed. In the specific case of stationary cold ions ($\mathbf{v}_d = 0$ and $\tau \ll 1$), analytic solutions can be found for highly symmetric probe geometries, such as spherical or cylindrical with circular cross-section.

Indeed in a cold ion plasma the Bohm condition states that at the sheath edge $v_{is} = c_{s0}$. Furthermore the problem for a spherical probe in a stationary plasma is spherically symmetric, and ion energy conservation implies that the sheath edge potential Φ_s satisfies $v_{is} = (-2Ze\Phi_s/m)^{1/2}$, i.e.

$$\Phi_s = -\frac{1}{2} \frac{T_e}{e}. \quad (\text{II.14})$$

Since at the sheath edge quasineutrality still holds, the ion density there is $N_{is} = N_\infty \exp(e\Phi_s/T_e) = \exp(-1/2)$, yielding the ion flux-density upon multiplication by

v_{is} .

The probe ion current is therefore [4]

$$I_{is} = A \exp\left(-\frac{1}{2}\right) N_\infty c_{s0}, \quad (\text{II.15})$$

where $A = 4\pi R_p^2$ and R_p is the spherical probe radius. By definition, I_{is} is equal to the electron current (Eq. (II.2)) at floating potential

$$\Phi_f = \frac{1}{2} \frac{T_e}{e} \left[\ln\left(2\pi \frac{Zm_e}{m}\right) - 1 \right]. \quad (\text{II.16})$$

Eq. (II.4) is typically fitted for T_e in the range $\Phi_p \in [\ll \Phi_f : \sim \Phi_f]$. For example, in a fully ionized helium plasma ($Z = 2$ and $m \simeq 7350m_e$): $\Phi_f \simeq -3.7T_e/e$.

Finite sheath thickness

Once the above results for the sheath entrance potential (Eq. (II.14)) and the ion current (Eq. (II.15)) are obtained in the infinitesimal Debye length regime, it is possible to *a posteriori* estimate the sheath thickness Δ . One simple idea is to treat the electron density in the sheath as negligible, and solve Poisson equation between Φ_p and Φ_s .

The calculation is discussed in Ref. [4], and the result approximately given by:

$$\Delta \simeq 1.02 \Lambda_{De} \left[(-\phi_p)^{1/2} - \frac{1}{\sqrt{2}} \right]^{1/2} \left[(-\phi_p)^{1/2} + \sqrt{2} \right], \quad (\text{II.17})$$

where

$$\phi_p = \frac{e\Phi_p}{T_e} \quad (\text{II.18})$$

is the normalized probe potential. The important points to notice in Eq. (II.17) is that $\Delta \propto \Lambda_{De}$ and Δ increases with $|\phi_p|$. For example if the probe is at floating potential (Eq. (II.16)) in a pure helium plasma: $\Delta \simeq 4\Lambda_{De}$.

A first correction to the ion current when $\Lambda_{De} \lesssim R_p$ can then be obtained by replacing A by $A(1 + \Delta/R_p)^2$ in Eq. (II.15). In the opposite limit $\Lambda_{De} \gg R_p$, so-

called Orbit Motion Limited (OML) calculations presented in section V.1.3 apply. In this thesis chapter, we concentrate on situations where $\Delta \ll R_p$.

II.1.2 Magnetized probes

Magnetic field effects on C-V characteristics

The presence of a background magnetic field \mathbf{B} introduces considerable complexity to the previous picture. In particular, the ion saturation current also depends on the magnetic field strength, as well as the probe surface orientation with respect to the field lines.

Figure (II-1a) shows a schematic diagram of the tilting Langmuir probe array experiment of Matthews and coauthors [16], designed to investigate the influence of magnetic field angle on the C-V characteristics. Experiments were performed at the boundary of the DITE (Divertor Injection Tokamak Experiment) tokamak, operating with toroidal magnetic field $B = 1.55T$ and helium plasma. The results, compiled in Fig. (II-1b), show that the ion saturation current decreases as the angle of probe normal to magnetic field θ approaches 90° .

This can be interpreted as follows. Except for $\theta = 90^\circ$, fitting Eq. (II.4) to the ion saturation portion of the C-V characteristics yields an electron temperature $T_e \sim 25eV$, that we here assume equal to $T_{i\infty}$. The average ion Larmor radius at infinity for a Maxwellian plasma ($R_L = (2v_{ti} \int_0^\infty w^2 dw)/\omega_c$ with $\omega_c = ZeB/m$ and v_{ti} later defined by Eq. (II.31))

$$R_L = \frac{1}{ZeB} \left(\frac{\pi T_{i\infty} m}{2} \right)^{1/2} \quad (\text{II.19})$$

is therefore $R_L \simeq 0.4mm$, much smaller than the probe ($40mm \times 60mm$). As a consequence the ions are tied to the field lines, and only see the projection of the probe on the plane perpendicular to \mathbf{B} .

The tokamak line-integrated electron density is $3 \cdot 10^{19}m^{-3}$. Arbitrarily assuming, as a magnitude estimate, that the boundary density where measurements are per-

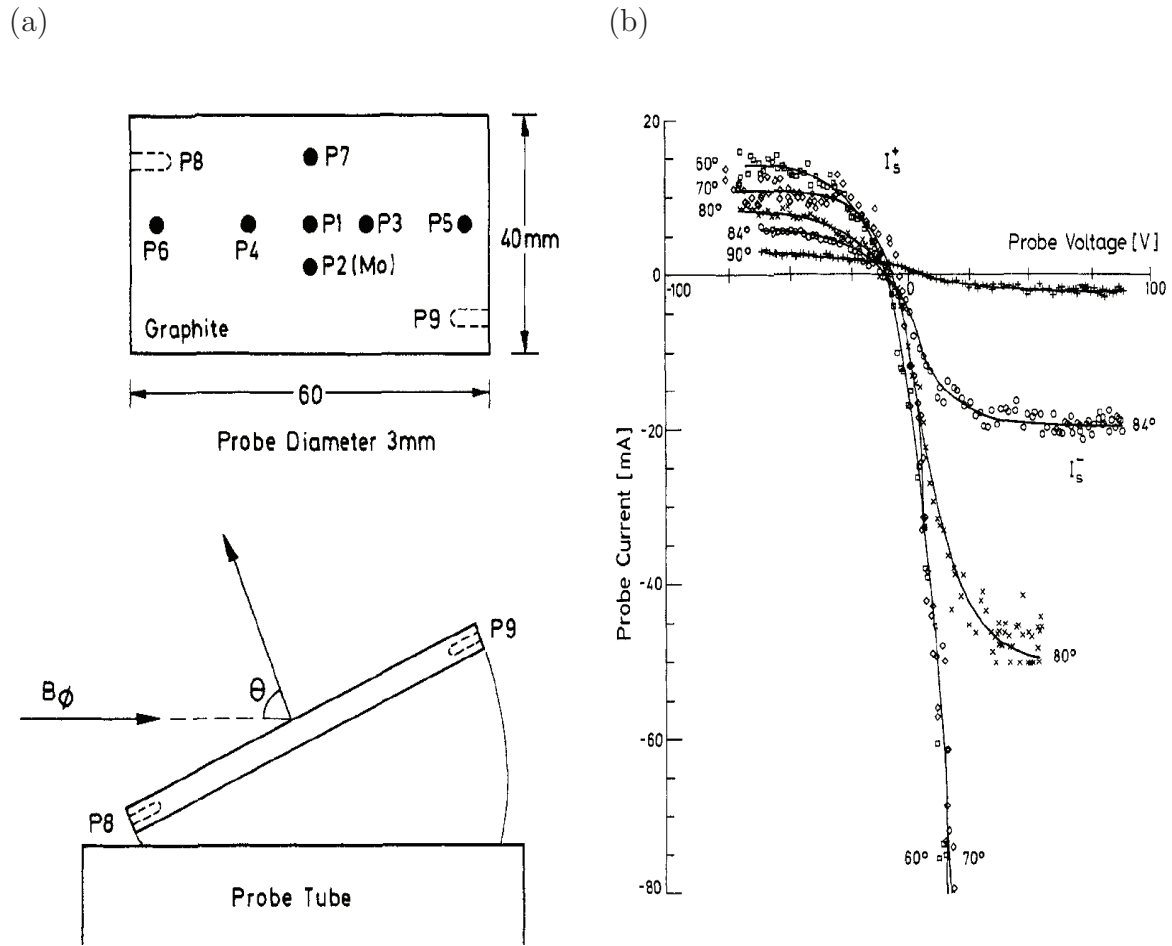


Figure II-1: (a) Tilting Langmuir probe array described in Ref. [16]. (b) Compilation of Langmuir probe characteristics from the P1 electrodes for angles in the range $\theta \in [60^\circ : 90^\circ]$.

formed is 30 times smaller, the Langmuir probe operates with $N_\infty = 10^{18} m^{-3}$ and $\Lambda_{De} = 37 \mu m$. This justifies the thin sheath assumptions, confirmed by the ion current in Fig. (II-1b) indeed saturating in the limit of strongly negative bias.

When $\theta = 90^\circ$, the probe surface is at grazing angle with the magnetic field, yet the ion saturation current does not vanish. It is unclear what the reason is in this particular experiment, and several hypothesis are advanced in Ref. [16]. What is sure is that there must be cross-field ion transport in the vicinity of the electrodes, which in general occurs through one of the following mechanisms:

- Convective cross-field transport due to a transverse convective electric field \mathbf{E}_{cnv} ;
- Classical transport, due to ion-electron Coulomb collisions or charge-exchange with background neutrals for instance;
- Anomalous transport due to plasma fluctuations on a scale $\gtrsim R_L$;
- Ionization and recombination.

In fact cross-field transport must occur along the entire probe presheath, regardless of the surface tilt angle. If this were not the case, the plasma perturbation would extend indefinitely along the field lines up to the discharge walls, and no current would be collected. Figure (II-2) illustrates how the probe presheath elongates along the magnetic shadow in the strong magnetization limit, when cross-field flux is modeled as diffusive [4].

The magnetized Bohm condition

In addition to the sheath and presheath sketched in Fig. (II-2), an intermediate clearly distinct quasineutral region called “magnetic presheath” forms in the regime $\Lambda_{De} \ll R_L \ll R_p$ ¹. As shown by the 1D expansion of Fig. (II-3), the magnetic presheath sets the transition between the presheath where the ions are tied to the magnetic field lines, and the sheath where the ions flow towards the probe.

¹Note that the space physics community tends to use the term “magnetic presheath” for “presheath”

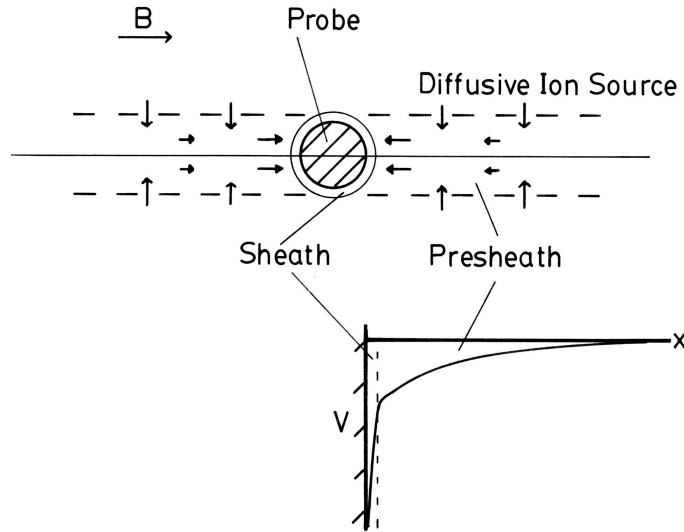


Figure II-2: Probe sheath and presheath when the ions are strongly magnetized, and cross-field transport modeled as diffusive. In this case no cross-field convective drift exists, hence the plasma at infinity is either stationary, or drifting along the magnetic field lines (from Ref. [4]).

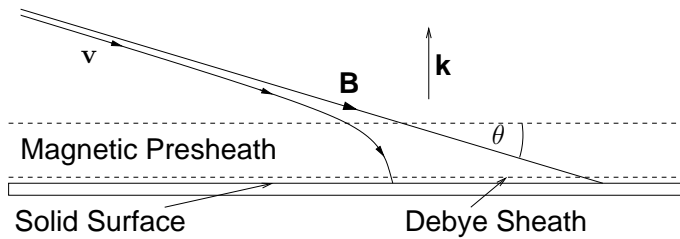


Figure II-3: Magnetized ion collection by a solid surface in the regime $\Lambda_{De} \ll R_L \ll R_p$. The ion Larmor motion is broken in the so-called “magnetic presheath”, whose thickness is $\sim R_L$. In the absence of convective electric field, the ions enter the magnetic presheath with a parallel fluid velocity $\langle v_{\parallel} \rangle = c_s$, and the Debye sheath with a normal fluid velocity $|\langle \mathbf{v} \rangle \cdot \mathbf{k}| = c_s$. Note a difference $\pi/2$ in the definition of θ with respect to Fig. (II-1a) (from Ref. [4]).

The Bohm condition at the Debye sheath edge ($|\langle \mathbf{v} \rangle \cdot \mathbf{k}| = c_s$) still holds here. Upon considering the variable ξ in Eqs (II.7,II.11) as the position along the field lines in the presheath taken from the magnetic presheath edge, it is straightforward to see that the ions enter the magnetic presheath with $\langle v_{\parallel} \rangle = c_s$. This is the magnetized Bohm condition in the absence of convective electric field. As for the unmagnetized case, most of the challenge is to solve the presheath equations. The next section discusses the well established isothermal fluid approach to do so, in the context of transverse Mach probe calibration, before proceeding with new kinetic results.

II.2 Foreword on magnetized, transverse Mach probes

II.2.1 The Mach probe concept

Transverse Mach probes [4] are an essential tool to measure plasma fluid velocities close to tokamak separatrix and Scrape-Off Layers (SOL) [17, 18], where ions drift towards the diverter plates at a substantial fraction of the sound speed. The effort is in particular motivated by the need to understand edge sheared flows, thought to reduce turbulence in tokamaks and facilitate the transition from L to H confinement mode [19, 20].

Magnetized Mach probe operation is simple in concept: by comparing the ion saturation current at different angles in the plane of flow and magnetic field, one seeks to measure the external, or unperturbed (intended as in the absence of probe) plasma Mach number \mathbf{M} , decomposed into a cross-field component M_{\perp} and a free parallel component M_{∞} : $\mathbf{M} = M_{\perp} \mathbf{e}_{\perp} + M_{\infty} \mathbf{e}_{\parallel}$. In this thesis, Mach numbers are defined as the drift velocity divided by the isothermal ion sound speed: $\mathbf{M} = \mathbf{v}_d / c_{sI}$, where

$$c_{sI} = \left(\frac{ZT_e + T_{i\infty}}{m} \right)^{1/2}. \quad (\text{II.20})$$

The most promising probe design is perhaps the so-called Gundestrup [21], characterized by a set of (at least 3) different electrodes spanning the tip of a single insulating head (see Fig. (II-4)).

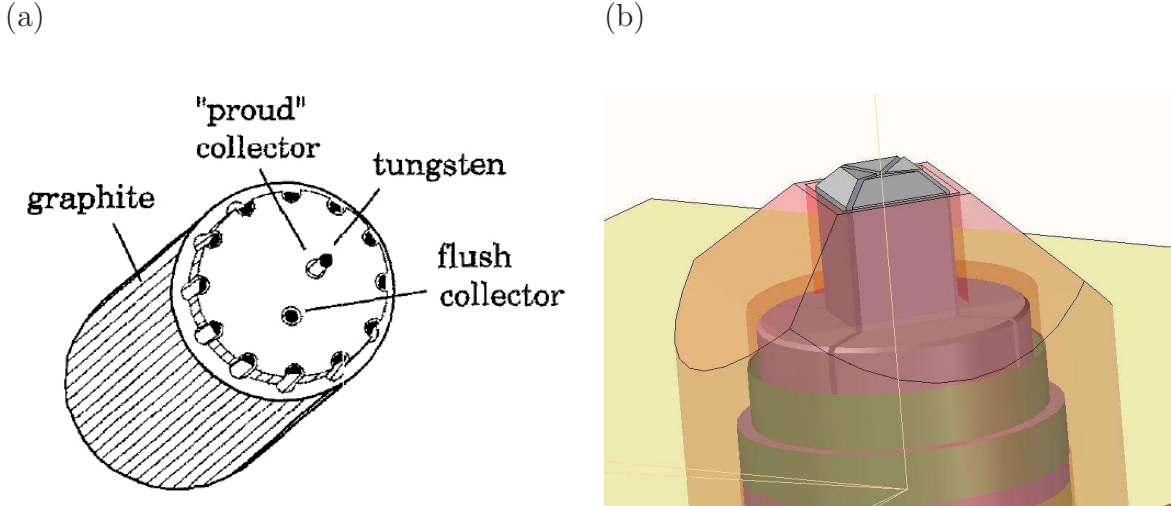


Figure II-4: (a) Drawing of the probe on which the term Gundestrup has been coined [21]; twelve tungsten pins span the tip of a cylindrical head. (b) CAD view of the WASP (Wall Actuated Scanning Probe), a four-electrode Gundestrup probe installed in the inner wall of the Alcator C-Mod tokamak [22].

Mach Probe heads perturb the magnetized plasma in a similar way as the flat Langmuir probe shown in Fig. (II-1a), and in order to find a theoretical calibration relating the ion saturation flux to the different electrodes to the external Mach number, we need to solve the plasma equations in the probe presheath. This requires taking into account one of the cross-field transport effects introduced in paragraph II.1.1.

Upon describing the anomalous cross-field flux as diffusive and in the absence of convective transport, an isothermal fluid formulation of the presheath equations can be solved in the limit of infinite magnetization [23, 24], when the ion motion is one-dimensional because it is constrained by the magnetic field. This provides the theoretical calibration for a Mach probe with electrodes facing parallel and antiparallel to the field, when the flow is field-aligned. This approach, heuristically based on an unknown diffusion rate, proved fruitful because the ion current solution only depends on the ratio of particle to momentum diffusion rates, which was argued to be close to one [25]; the absolute value of the diffusivity only affecting the presheath length. The result is usually expressed by a calibration factor M_c , such that the ratio of upstream to downstream ion flux density to the probe for a plasma flowing at isothermal parallel

Mach number M_∞ , is

$$R \simeq \exp\left(\frac{M_\infty}{M_c}\right). \quad (\text{II.21})$$

For equal particle and momentum diffusivities the model yields $M_c \simeq 0.41$, in agreement with Laser Induced Fluorescence (LIF) measurements [26] to within experimental uncertainty. The kinetic formulation of the same model [27], accounting for the ion thermal dynamics, yields similar calibration factors with slight dependence on the ion to electron temperature ratio at infinity.

In situations where the plasma has a transverse flow component M_\perp , due to strong radial electric fields in tokamaks' edge for instance, diffusion is not required and purely convective equations are more appropriate. The recently solved isothermal fluid formulation of this model [15] predicts for subsonic flows a flux ratio

$$R = \exp\left(\frac{M_\infty - M_\perp \cot \eta_p}{M_c}\right), \quad (\text{II.22})$$

where $\eta_p \in [0 : \pi]$ is the angle of downfield probe surface to magnetic field in the plane of flow and magnetic field (see Fig. (II-5)). $M_c = 1/2$ exactly as anticipated in Ref. [25] for the particular case of a semi-infinite probe, but the treatment in Ref. [15] has the remarkable property of being applicable to finite-sized probes of arbitrary convex shape.

Because it can also operate as an array of Langmuir probes and measure basic quantities such as temperature, density and potential, the transverse Mach probe is becoming a quasi-routine diagnostic, now starting to be installed in difficult-to-access regions such as the high-field side of the Alcator C-Mod tokamak [22].

II.2.2 General isothermal formulation

It is instructive to discuss the isothermal formulation of the 1D magnetized presheath model, by first including several transport terms, and discussing their relative weight afterwards.

Let us consider a planar probe, tilted by an angle η_p in the plane of magnetic field

$\mathbf{B} \parallel \mathbf{e}_z$ and ion cross-field velocity $\mathbf{v}_\perp \parallel \mathbf{e}_y$. In the limit of infinite magnetization considered here, \mathbf{v}_\perp is constant and constrained by its external driver, taken to be a uniform convective electric field in the $-\mathbf{e}_x$ direction:

$$\mathbf{v}_\perp = \mathbf{E}_{\text{cnv}} \times \frac{\mathbf{B}}{B^2}. \quad (\text{II.23})$$

We further impose the probe to be negatively biased enough for the electrons to be isothermal and Boltzmann distributed (Eq. (II.6)); in dimensionless form;

$$N_e = N_\infty \exp \phi. \quad (\text{II.24})$$

We only model the quasineutral presheath region where $N_i = N_e = N$ (recall that N_i is the ion charge-density, equal to Z times the ion density), assuming that it extends down to a thin magnetic presheath at the probe surface [4].

We account for cross-field transport through random ion exchange between the perturbed region (or presheath) and the outer plasma, taking place exclusively in the \mathbf{e}_x direction at a volumetric rate Ω [24]. We set $\Omega = \Omega_c + \Omega_a$, where Ω_c and Ω_a are respectively the classical and anomalous contributions. This is admittedly an over-simplified picture, but models particles and momentum diffusing into and out of the presheath at equal rate, which is consistent with reasonable physical arguments [25] as well as experiments [26]. For consistency, we also account for a classical effective parallel momentum collision frequency ν_c , arising from the same physics as Ω_c .

Ionization and recombination processes are of complex nature, and as a first approximation we model them by uniform volumetric frequencies ν_I and $\nu_R N_\infty$, such that the (electron impact) ionization rate is $\nu_I N$, and the (direct) recombination rate is $\nu_R N^2$; recall that in our quasineutral treatment ion and electron charge-densities are equal. Self-consistency of this simple model requires $\nu_I = \nu_R N_\infty$ in order for the ion fluid to tend towards its unperturbed state at infinity, which is of course incorrect in SOLs where ionization is balanced by transport rather than recombination. A second self-consistency prerequisite is that background neutrals and ions flow at the same speed.

The ion continuity equation in steady state is therefore

$$\frac{\partial}{\partial z} (N\langle v \rangle) + v_{\perp} \frac{\partial N}{\partial y} = \left(\Omega + \nu_I \frac{N}{N_{\infty}} \right) (N_{\infty} - N), \quad (\text{II.25})$$

and, upon approximating the ions as isothermal, the parallel ion momentum equation becomes

$$\begin{aligned} & Nm\langle v \rangle \frac{\partial \langle v \rangle}{\partial z} + Nmv_{\perp} \frac{\partial \langle v \rangle}{\partial y} + m\langle v \rangle \left(\Omega + \nu_I \frac{N}{N_{\infty}} \right) (N_{\infty} - N) \\ &= -NZT_e \frac{\partial \phi}{\partial z} - T_{i\infty} \frac{\partial N}{\partial z} + m\Omega (N_{\infty}v_{\infty} - N\langle v \rangle) + m\nu_I N \left(v_{\infty} - \frac{N}{N_{\infty}} \langle v \rangle \right) + mN\nu_c (v_{\infty} - \langle v \rangle). \end{aligned} \quad (\text{II.26})$$

The left-hand side “ Ω ”-term in Eq. (II.26) originates from particle diffusion into and out of the presheath, while the right-hand side “ Ω ”-term accounts for viscosity. Taking advantage of the Boltzmann distribution of the electrons and substituting the isothermal ion sound speed $c_{sI} = [(ZT_e + T_{i\infty}) / m]^{1/2}$ (Eq. (II.20)) in Eq. (II.26), the momentum equation simplifies to

$$N\langle v \rangle \frac{\partial \langle v \rangle}{\partial z} + Nv_{\perp} \frac{\partial \langle v \rangle}{\partial y} = -c_{sI}^2 \frac{\partial N}{\partial z} + [\Omega N_{\infty} + (\nu_I + \nu_c) N] (v_{\infty} - \langle v \rangle). \quad (\text{II.27})$$

Equations (II.25, II.27) are slightly different from what derived in Ref. [28], where neutrals were assumed stationary, ionization and recombination not in balance, and classical collisionality omitted.

The problem geometry, *a priori* two-dimensional, is shown in Fig. (II-5). The perturbed plasma can be divided into three distinct regions: upfield and downfield presheaths independent of each other, and a shock which we do not need to analyze. In order to go further in the analysis, it is convenient to perform the following change in variables:

$$\begin{cases} z \\ y \end{cases} \mapsto \begin{cases} u &= \frac{z}{y} \\ w &= \frac{\Omega}{v_{\perp}} [z - yu_p] \end{cases}, \quad (\text{II.28})$$

where u is the cotangent of the angle between the magnetic field and the position vector (fan angle), and w is a normalized distance to the probe along the parallel

direction. The probe coordinates are singular, at $u = u_p = \cot \eta_p$ and $w = w_p = 0$. Further normalizing velocities to the isothermal sound speed ($M = \langle v \rangle / c_{sI}$ and $M_\perp = v_\perp / c_{sI}$), Eqs (II.25,II.27) become

$$(M - M_\perp u) \frac{\partial N}{\partial u} + N \frac{\partial M}{\partial u} = - \frac{w}{u - u_p} \left[(M - M_\perp u_p) \frac{\partial N}{\partial w} + N \frac{\partial M}{\partial w} \right] + \frac{w}{u - u_p} M_\perp \left(1 + \frac{\nu_I}{\Omega} \frac{N}{N_\infty} \right) (N_\infty - N), \quad (\text{II.29})$$

$$\frac{\partial N}{\partial u} + N (M - M_\perp u) \frac{\partial M}{\partial u} = - \frac{w}{u - u_p} \left[\frac{\partial N}{\partial w} + N (M - M_\perp u_p) \frac{\partial M}{\partial w} \right] + \frac{w}{u - u_p} M_\perp N_\infty \left(1 + \frac{\nu_I + \nu_c}{\Omega} \frac{M}{N_\infty} \right) (M_\infty - M). \quad (\text{II.30})$$

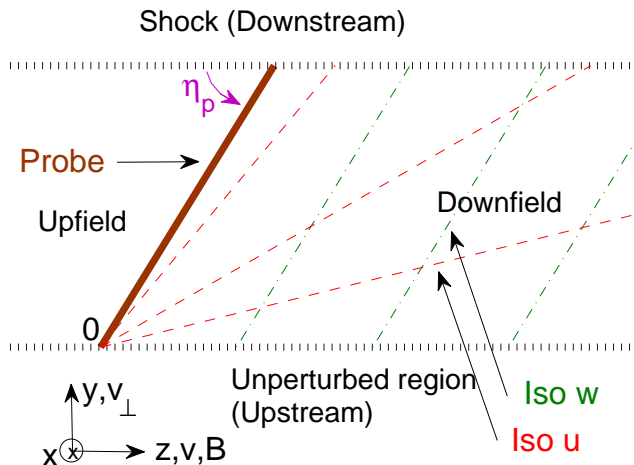


Figure II-5: Illustration of the “planar probe” geometry. \mathbf{B} and the parallel velocity \mathbf{v} are in the \mathbf{e}_z direction, while the cross field drift \mathbf{v}_\perp is along \mathbf{e}_y . \mathbf{e}_x is the ignorable axis, but supports the convective electric field. The downfield region can be parametrized by (z, y) or (u, w) , where u measures the fan angle cotangent at the origin, and w the parallel distance to the probe.

System (II.29,II.30) is the general formulation of the isothermal strongly magnetized Mach-probe model, including cross-field transport by classical and anomalous diffusion, convective motion, and accounting for ionization and recombination. Those

last effects involving the ion parent neutral can be considered as cross-field transport mechanisms, since neutrals do not feel the magnetic field hence literally transport charge and momentum in and out of the presheath.

II.2.3 Relative weight of the different transport mechanisms

Let us now estimate the magnitude of the different transport mechanisms in the following sample SOL conditions: pure hydrogen plasma with $N = 10^{19} m^{-3}$, $T_{i\infty} = T_e = 30 eV$, $B = 5 T$, and probe with transverse size $\Delta x = 2 mm$.

The “ $e^- + H \rightarrow 2e^- + H^+$ ” ionization cross section at $30 eV$ is $\sigma_I = 6.2 \cdot 10^{-17} cm^2$ [29], hence $\langle \sigma_I v_e \rangle \sim \sigma_I v_{te} = 2.0 \cdot 10^{-14} m^3 s^{-1}$. Similarly the “ $H + H^+ \rightarrow H^+ + H$ ” charge exchange cross-section at $30 eV$ is $\sigma_{cx} = 260 \cdot 10^{-17} cm^2$ [29], yielding $\langle \sigma_{cx} v_i \rangle \sim \sigma_{cx} v_{ti} = 2.0 \cdot 10^{-14} m^3 s^{-1}$. The property $\langle \sigma_I v_e \rangle \sim \langle \sigma_{cx} v_i \rangle$ is typical of hydrogen-like species in the $10 - 200 eV$ range. It is unclear what to choose as ionization level, since the neutral dynamics in tokamak edges is not fully understood yet. For instance, taking the neutral density to be 10^4 smaller than the electron density yields $\nu_I = N \langle \sigma_I v_e \rangle / 10^4 \sim \nu_{cx} \simeq 20 s^{-1}$.

In the above discussion we introduced the ion thermal speed

$$v_{ti} = \left(\frac{2T_{i\infty}}{m} \right)^{1/2}, \quad (\text{II.31})$$

defined as the most probable ion velocity in the plasma rest frame. The electron-ion momentum transfer Coulomb collision frequency for an electron with velocity v_e and stationary ion target is

$$\nu_{ei} = N \left(\frac{Ze^2}{4\pi\epsilon_0} \right)^2 \frac{4\pi}{m_e^2 v_e^3} \ln \Lambda, \quad (\text{II.32})$$

where $\ln \Lambda \sim 15$ is the Coulomb logarithm², yielding an approximate Maxwellian averaged collision frequency upon replacing v_e by v_{te} :

$$\bar{\nu}_{ei} \sim N \frac{\sqrt{2}}{16\pi\epsilon_0^2} \frac{Z^2 e^4}{m_e^{1/2} T_e^{3/2}} \ln \Lambda, \quad (\text{II.33})$$

² $\ln \Lambda$ is the usual notation for the Coulomb logarithm ($\sim \ln(\lambda_D/p_{90})$), not to be confused with the Debye length Λ_D .

or upon proper averaging over the Maxwellian electron distribution [29]:

$$\bar{\nu}_{ei} = N \frac{\sqrt{2}}{12\pi^{3/2}\epsilon_0^2} \frac{Z^2 e^4}{m_e^{1/2} T_e^{3/2}} \ln \Lambda. \quad (\text{II.34})$$

Momentum conservation then readily yields the ion-electron average momentum transfer collision frequency $\bar{\nu}_{ie} = \bar{\nu}_{ei} m_e / m \simeq 1500 s^{-1}$ for our specific parameters.

The classical ion diffusion tensor in a coordinate system where \mathbf{B} is oriented along the \mathbf{e}_z axis is

$$\bar{D} = \begin{pmatrix} D_{\perp} & D_{\times} & 0 \\ -D_{\times} & D_{\perp} & 0 \\ 0 & 0 & D_{\parallel} \end{pmatrix}, \quad (\text{II.35})$$

where

$$D_{\parallel} = \frac{T_i}{m\nu_c}, \quad (\text{II.36})$$

and upon defining the Hall term

$$\beta = \frac{\omega_c}{\nu_c} = \frac{ZeB}{m\nu_c} \quad (\text{II.37})$$

the transverse terms can be written

$$D_{\perp} = D_{\parallel} \frac{1}{1 + \beta^2}, \quad D_{\times} = D_{\parallel} \frac{\beta}{1 + \beta^2}. \quad (\text{II.38})$$

Here ν_c is the sum of the different classical momentum exchange collision frequency contributions. In our specific example $\nu_c = \nu_{cx} + \bar{\nu}_{ie} \simeq \bar{\nu}_{ie}$, yielding $D_{\perp c} \simeq 2.4 \cdot 10^{-5} m^2 s^{-1}$. The classical cross-field volumetric exchange rate is therefore $\Omega_c \sim D_{\perp c} / \Delta x^2 \simeq 6 s^{-1}$. Estimating the anomalous cross-field diffusivity as given by the Bohm value $D_{\perp a} = T_e / (16eB) \simeq 0.375 m^2 s^{-1}$, the anomalous volumetric exchange rate is $\Omega_a \simeq 6.3 \cdot 10^4 s^{-1}$.

We therefore have the following scaling:

$$\nu_{cx} \sim \nu_I \sim \Omega_c \ll \bar{\nu}_{ie} \ll \Omega_a, \quad (\text{II.39})$$

and the appropriate general set of fluid presheath equations to consider reduces to

$$(M - M_{\perp}u) \frac{\partial N}{\partial u} + N \frac{\partial M}{\partial u} = -\frac{w}{u - u_p} \left[(M - M_{\perp}u_p) \frac{\partial N}{\partial w} + N \frac{\partial M}{\partial w} \right] + \frac{w}{u - u_p} M_{\perp} (N_{\infty} - N), \quad (\text{II.40})$$

$$\frac{\partial N}{\partial u} + N (M - M_{\perp}u) \frac{\partial M}{\partial u} = -\frac{w}{u - u_p} \left[\frac{\partial N}{\partial w} + N (M - M_{\perp}u_p) \frac{\partial M}{\partial w} \right] + \frac{w}{u - u_p} M_{\perp} N_{\infty} (M_{\infty} - M). \quad (\text{II.41})$$

The term

$$\frac{u - u_p}{w} = \frac{v_{\perp}}{\Omega y} \quad (\text{II.42})$$

measures the relative weight of convection to cross-field diffusion, and suggests defining the Reynolds number

$$\text{Re} = \frac{v_{\perp}}{\Omega \Delta y}, \quad (\text{II.43})$$

where Δy is the probe extent in the transverse flow direction. Solving Eqs (II.40,II.41) in the limit $\text{Re} \rightarrow 0$ yields the flux ratio (II.21), and in the limit $\text{Re} \rightarrow \infty$ the flux ratio (II.22).

A summary of the numeric parameters considered here is given in table (II.1)

External ion/electron temperatures	$T_{i\infty,e}$	30eV
External charge-density	N	10^{19}m^{-3}
Magnetic field	B	5T
Probe transverse dimension	Δx	2mm
Ion c.x. frequency	ν_{cx}	20s^{-1}
Ionization frequency	ν_I	20s^{-1}
Ion-electron Coulomb mom. ex. frequency	$\bar{\nu}_{ie}$	1500s^{-1}
Electron-ion Coulomb mom. ex. frequency	$\bar{\nu}_{ei}$	$2.6 \cdot 10^6\text{s}^{-1}$
Classical cross-field volumetric exchange rate	Ω_c	6s^{-1}
Anomalous cross-field volumetric exchange rate	Ω_a	$6.3 \cdot 10^4\text{s}^{-1}$

Table II.1: Sample plasma parameters for typical Alcator C-Mod SOL conditions, for which the 1D strongly magnetized Mach probe presheath equations (II.40,II.41) apply.

II.2.4 The question of ion recycling

In deriving Sys (II.40,II.41), we assumed the probe surface to behave as an ideal ion and electron sink, i.e. we neglected surface electron emission effects. The probe however releases neutral atoms and/or molecules at a rate that balances the incoming flux of ions, which for strongly negative biases has been neutralized by electrons supplied by the external circuit. As a consequence the neutral density near the surface can be of the order the ion density, opening the possibility for ionization-induced ion recycling, the importance of which depends on the ionization mean-free-path l_{ion} and the probe geometry.

Let us consider an oversimplified picture where neutrals leave the surface with pure radial velocity and ionize at a distance l_{ion} . Presumably the neutrals most likely to be recycled are those ionizing in the probe magnetic shadow, hence the fraction of collected ion current due to recycling can be expressed in the form $\eta = \epsilon/(1-\epsilon)$, where ϵ is the ratio of neutral-front surface over probe magnetic shadow perpendicular (to **B**) cross-section. For spherical or cylindrical probes with radius R_p , $\epsilon \sim (R_p/l_{ion})^2$ and $\epsilon \sim R_p/l_{ion}$, respectively. For pyramidal probes, neutral are mostly emitted out of the collection tube, hence ϵ might be negligible as suggested by Gangadhara and LaBombard (see for instance Fig. (11) in Ref. [30]).

For Deuterium, D_2 molecules form on the probe surface and enter the plasma where they immediately dissociate, resulting in D atoms with energy $E_d \sim 3\text{eV}$ from molecular dissociation. Using the sample parameters of table II.1, we obtain $l_{ion} \sim \sqrt{2E_d/m}/(N\langle\sigma_I v_e\rangle) \sim 85\text{mm}$, indicating that recycling should not significantly alter the presheath equations for millimeter-sized probes. It is however important to recognize that as we approach the separatrix where plasma densities reach $N \sim 10^{20}\text{m}^{-3}$, l_{ion} becomes comparable to typical probe dimensions and measurements could indeed be corrupted by recycling. We will not address this possibility in this thesis.

II.3 The quasi-collisionless convective model

System (II.40,II.41) is the set of isothermal fluid equations describing the presheath of strongly magnetized mach probes at ion saturation. Although all the physical ingredients are included, it is *a priori* difficult to estimate the error arising from the isothermal approximation. The purpose of this thesis chapter is to solve the kinetic formulation of the same convective, strongly magnetized Mach probe model. This approach naturally provides information about the ion distribution function in the presheath, and is not based on approximate fluid closures. After deriving the appropriate ion kinetic equation and discussing our solution method, we show that the findings of Ref. [15] are not a consequence of the isothermal approximation, and apply for arbitrary ion to electron temperature ratios. In particular, (a) flux ratios for subsonic flows are still given by $R = \exp [(M_\infty - M_\perp \cot \eta_p) / M_c]$, where M_c varies with temperature between $1/2$ and $1/\sqrt{2\pi}$, and (b) the solution applies to arbitrary-shaped convex probes. This straightforwardly allows simple calibration of four-electrode Gundestrup-like Mach probes.

II.3.1 Presheath equations

We still account for anomalous cross-field transport through random ion exchange between the perturbed region (or presheath) and the outer plasma, taking place exclusively in the \mathbf{e}_x direction at a volumetric rate Ω [24]. The key requirement of the so-called “quasi-collisionless” model is that Ω be much larger than the ion-electron momentum transfer Coulomb collision frequency $\bar{\nu}_{ie}$, in order for the parallel ion dynamics to be collisionless.

The problem geometry is still well described by Fig. (II-5). In each region (upfield, downfield, and the non analyzed shock), we write the ion kinetic equation in steady state as

$$v \frac{\partial f}{\partial z} + v_\perp \frac{\partial f}{\partial y} - \frac{ZT_e}{m} \frac{\partial \phi}{\partial z} \frac{\partial f}{\partial v} = \Omega (f_\infty - f), \quad (\text{II.44})$$

where $f(y, z, v)$ is the normalized ion distribution function in the parallel direction, m the ion mass, and v refers to the parallel velocity variable. In the unperturbed region,

the ions are Maxwellian with parallel drift velocity v_∞ and temperature $T_{i\infty}$. Drift velocities will usually be given in terms of isothermal Mach numbers $M_\perp = v_\perp/c_{sI}$ and $M_\infty = v_\infty/c_{sI}$, with the isothermal ion sound speed defined by Eq. (II.20).

We here discuss the downfield equations, the upfield physics being recovered upon replacing (η_p, v) by $(\pi - \eta_p, -v)$. It is therefore convenient to make the change of variables proposed in Eq. (II.28), repeated here for convenience.

$$\begin{cases} z \\ y \end{cases} \mapsto \begin{cases} u &= \frac{z}{y} \\ w &= \frac{\Omega}{v_\perp} [z - yu_p] \end{cases}, \quad (\text{II.45})$$

where $u = \cot \eta$ is the cotangent of the angle between the magnetic field and the position vector (fan angle), and w is a normalized distance to the probe along the parallel direction. The probe coordinates are singular, at $u_p = \cot \eta_p$ and $w_p = 0$. Recalling the cold ion sound speed definition $c_{s0} = (ZT_e/m)^{1/2}$ (Eq. (II.13)), Eq. (II.44) can be rewritten as follows:

$$(v - v_\perp u) \frac{\partial f}{\partial u} - c_{s0}^2 \frac{\partial \phi}{\partial u} \frac{\partial f}{\partial v} = -\frac{w}{u - u_p} \left[(v - v_\perp u_p) \frac{\partial f}{\partial w} - c_{s0}^2 \frac{\partial \phi}{\partial w} \frac{\partial f}{\partial v} \right] + \frac{w}{u - u_p} v_\perp (f_\infty - f). \quad (\text{II.46})$$

Eq. (II.46) is the general formulation of the strongly magnetized Mach-probe model, including cross-field transport by both diffusion and convective motion. It is the kinetic analog of the fluid equations (II.40, II.41), hence not surprisingly the relative weight of the two transport effects is still measured by the Reynolds number

$$\text{Re}(y) = \frac{v_\perp}{\Omega y} = \frac{u - u_p}{w}. \quad (\text{II.47})$$

II.3.2 Discussion of the diffusive limit

Initial investigations of the present model by Hutchinson [23, 24] in its isothermal fluid formulation, and later by Chung and Hutchinson [27] in the kinetic formalism, considered parallel flows ($v_\perp = 0$) only, hence $\text{Re} = 0$ and the cross-field transport required to repopulate the probe magnetic shadow was purely diffusive. In the case

$\text{Re} \ll 1$, Eq. (II.46) reduces to

$$(v - v_{\perp} u_p) \frac{\partial f}{\partial w} - c_{s0}^2 \frac{\partial \phi}{\partial w} \frac{\partial f}{\partial v} = v_{\perp} (f_{\infty} - f). \quad (\text{II.48})$$

Van Goubergen and coauthors [31] considered non zero convective velocity, but still solved the diffusive limit implicitly assuming $\text{Re} \ll 1$ as well.

The ion distribution function at the magnetic presheath entrance (hence the collected ion current), solution of Eq. (II.48) at $w = 0$, is clearly independent of Ω : our model is therefore not based on any estimate of this heuristic parameter. In fact Ω does not even need to be spatially uniform, rather could be function of $z - y u_p$ (parallel distance from the probe surface) provided the definition of w in Eq. (II.28) is replaced by $w = \Omega/v_{\perp} \int (dz - u_p dy)$. The numeric value of Ω nevertheless affects the diffusive presheath length, scaling as $\Delta w \sim c_{sI}/v_{\perp}$ i.e. $L_d \sim c_{sI}/\Omega$ in physical units.

II.3.3 Convective limit

The question is, can we really use the diffusive equation when the cross-field velocity is not negligible ? Let us consider again an equithermal plasma ($ZT_e = T_{i\infty}$), and anomalous cross-field transport described by the Bohm diffusivity $D_{\perp} = T_e/16eB \simeq \Omega \Delta x^2$. Substituting the ion isothermal sound Larmor radius $\rho_{sI} = \sqrt{(ZT_e + T_{i\infty}) m}/eB$, the characteristic Reynolds number $\text{Re}(\Delta y)$ is:

$$\text{Re}(\Delta y) = \frac{v_{\perp}}{\Omega \Delta y} \simeq 32 M_{\perp} \frac{\Delta x}{\Delta y} \frac{\Delta x}{\rho_{sI}}. \quad (\text{II.49})$$

The strong ion magnetization condition requires $\Delta x \gg \rho_{sI}$, let us say $\Delta x \gtrsim 20 \rho_{sI}$ (10 Larmor diameters in Δx). If we are interested in measuring non negligible perpendicular velocities, such as $M_{\perp} \gtrsim 0.1$, $\text{Re}(\Delta y) \ll 1$ implies $\Delta y/\Delta x \gg 64$. Mach probes are of course not built with such an high aspect ratio, therefore Eq. (II.48) is only suitable to situations with $M_{\perp} \ll 1$.

For finite values of M_{\perp} , we should rather consider the opposite limit $\text{Re}(\Delta y) \gg 1$,

when the second term in the right-hand side of Eq. (II.46) can be eliminated and the physics becomes purely convective (Ω cancels in $w\partial/\partial w$). The problem boundary conditions are that the plasma be unperturbed when $u \rightarrow \infty$ and $w \leq w^*(u)$, where w^* is defined by $w^*(u) = (u - u_p)/\text{Re}(\Delta y)$. $w > w^*(u)$ corresponds to the shock region ($y > \Delta y$), hence not to a boundary in physical space. Provided $w \leq w^*(u)$, the above boundary conditions only depend on u ; the equation being furthermore hyperbolic in u , $\partial/\partial w = 0$ and the solutions only depend on u . This argument self-consistently holds with ϕ being a function of u only, since in the quasineutral regime the potential is unambiguously determined by the local density. Of course if we were to consider a finite Debye length plasma, whose potential is governed by the three-dimensional elliptic Poisson equation, ϕ (hence f) would *a priori* depend on u , w , and presumably also the transverse position in the \mathbf{e}_x direction.

The appropriate kinetic equation that we need to solve is therefore

$$(v - v_{\perp}u) \frac{\partial f}{\partial u} - c_{s0}^2 \frac{\partial \phi}{\partial u} \frac{\partial f}{\partial v} = 0, \quad (\text{II.50})$$

coupled with quasineutrality $\phi = \ln [\int f(v)dv]$. The corresponding convective presheath length scales as $L_c \sim \Delta y c_{sI}/v_{\perp}$.

II.4 Convective solution

II.4.1 Solution method

Equation (II.50) shows that f is conserved along (u, v) orbits that satisfy

$$\frac{dv}{du|_{\text{Orbit}}} = -c_{s0}^2 \frac{\partial \phi / \partial u}{v - v_{\perp}u}. \quad (\text{II.51})$$

These orbits are not energy-conserving, but consistent with the ions only feeling the parallel gradient of the electrostatic potential while moving across the field lines. The work originating from the \mathbf{e}_y part of the potential gradient is exactly canceled by the work of the convective field $\mathbf{E}_{\text{cnv}} = -\mathbf{v}_{\perp} \times \mathbf{B}$, as the ions slowly drift in the \mathbf{e}_x

direction with velocity $v_x = -mc_{s0}^2/(Ze)\nabla\phi \times \mathbf{B}/B^2$.

Equation (II.51) is invariant upon making the changes $v \mapsto v - v_\infty$ and $v_\perp u \mapsto v_\perp u - v_\infty$. We can therefore solve Eq. (II.50) as illustrated in Fig. (II-6), using the notation

$$\mu = v_\perp u - v_\infty \quad (\text{II.52})$$

for compactness. We start at infinity ($\mu \gg 1$), where the normalized parallel ion distribution function is Maxwellian with drift velocity v_∞ and thermal speed $v_{ti} = (2T_{i\infty}/m)^{1/2}$, $f_\infty(v) = f_M(v - v_\infty)$:

$$f_\infty(v) = \frac{1}{v_{ti}\sqrt{\pi}} \exp\left[-\frac{(v - v_\infty)^2}{v_{ti}^2}\right]. \quad (\text{II.53})$$

There a set of orbits, typically originating in the range $v_0 \in [v_\infty - 4v_{ti}, v_\infty + 4v_{ti}]$, is integrated according to Eq. (II.51) using an explicit fourth order Runge Kutta scheme. The ion distribution function at position μ and velocity v is then obtained by tracing the orbit back to its starting velocity v_0 :

$$f(\mu, v) = f_M[v_0(\mu, v - v_\infty)]. \quad (\text{II.54})$$

As we do not know the potential gradient a priori, we start with the initial guess $\partial\phi/\partial u = M_\perp$ and iterate the orbit integration with the self-consistent potential $\phi = \ln(n)$ up to convergence, where the ion (electron) charge-density is given by

$$n(\mu) = \int f(\mu, v) dv = \int f_M[v_0(\mu, \xi)] d\xi, \quad (\text{II.55})$$

where $\xi = v - v_\infty$. Similarly, the parallel charge flux-density in the frame moving with velocity v_∞ and ion temperature are

$$n(\mu)(\langle v \rangle - v_\infty) = \int \xi f_M[v_0(\mu, \xi)] d\xi, \quad (\text{II.56})$$

$$T_i(\mu) = \frac{n_\infty}{n(\mu)} \int [\xi - (\langle v \rangle - v_\infty)]^2 f_M[v_0(\mu, \xi)] d\xi. \quad (\text{II.57})$$

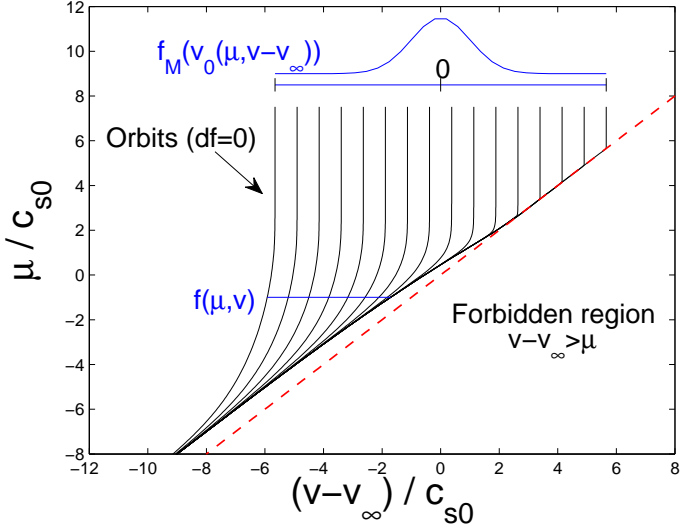


Figure II-6: Ion orbits in $\mu - v$ space for an ion to electron temperature ratio $\tau = 1$, at convergence of the numerical iteration. Phase space density at position μ (Eq. (II.52)) is obtained by tracing the orbit back to infinity, where the parallel ion distribution function is known to be Maxwellian with drift velocity v_∞ .

The main quantity of interest, the (positively defined) ion saturation flux-density to the probe expressed in charge per unit time per unit surface perpendicular to the magnetic field, is then given by $\Gamma_{i\parallel} = [-n_p v(u_p) \sin \eta_p + n_p M_\perp c_{sI} \cos \eta_p] / \sin \eta_p$:

$$\Gamma_{i\parallel} = n_p [M_\perp u_p - M_p] c_{sI}, \quad (\text{II.58})$$

where $n_p = n(u_p)$ and $M_p = \langle v \rangle(u_p) / c_{sI}$. If the probe normal is in the $\{\mathbf{e}_y, \mathbf{e}_z\}$ -plane (for example on a purely two-dimensional probe, or on the major cross-section of a sphere), the ion saturation flux-density per unit probe surface is

$$\Gamma_i = \Gamma_{i\parallel} |\sin \eta_p|. \quad (\text{II.59})$$

II.4.2 Isothermal fluid solution

The fluid equations (continuity and momentum) equivalent to Eq. (II.50) are

$$\begin{aligned} \frac{1}{c_s} (\langle v \rangle - v_{\perp} u) \frac{\partial n}{\partial u} + \frac{n}{c_s} \frac{\partial \langle v \rangle}{\partial u} &= 0 \\ \frac{\partial n}{\partial u} + \frac{n}{c_s^2} (\langle v \rangle - v_{\perp} u) \frac{\partial \langle v \rangle}{\partial u} &= 0 \end{aligned}, \quad (\text{II.60})$$

where c_s is the Bohm ion sound speed (Eq. (II.9)), and γ_i the ion adiabatic index (Eq. (II.10)). c_s is not the speed at which sound waves would propagate in the presheath, as it arises from steady-state equations, rather the speed at which information travels in the parallel direction.

System (II.60) cannot be solved because it lacks closure (c_s is unknown), thus motivating our kinetic treatment. It is however clear that for the density and fluid velocity to be non uniform, the determinant must vanish. In other words either $n = n_{\infty}$ and $\langle v \rangle = v_{\infty}$, or $v_{\perp} u - \langle v \rangle = c_s$. This can be considered as the magnetized Bohm condition, valid at the probe edge regardless of the presheath model if the probe is infinite in the \mathbf{e}_y direction [32], but here derived in the convective regime for the entire plasma, without the \mathbf{e}_y -invariance requirement.

System (II.60) can be solved analytically when considering isothermal ions [15]:

$$n = n_{\infty} \exp(M - M_{\infty}), \quad (\text{II.61})$$

$$M - M_{\infty} = \min(0, M_{\perp} u - M_{\infty} - 1), \quad (\text{II.62})$$

where $M = \langle v \rangle / c_{sI}$. The isothermal approximation is exact in the limit of small ion to electron temperature ratio at infinity

$$\tau = \frac{T_{i\infty}}{ZT_e}, \quad (\text{II.63})$$

since the ion pressure becomes negligible compared to the electrostatic force.

II.4.3 Analogy with the plasma expansion into a vacuum

Equation (II.44) with $\Omega = 0$ is mathematically equivalent to the one-dimensional, quasineutral plasma expansion into a vacuum considered by Gurevich and Pitaevskii (Eq. (7) in Ref. [33])

$$v \frac{\partial f}{\partial z} + \frac{\partial f}{\partial t} - \frac{ZT_e}{m} \frac{\partial \phi}{\partial z} \frac{\partial f}{\partial v} = 0, \quad (\text{II.64})$$

upon replacing time t by the transverse flight time y/v_\perp . Not surprisingly therefore, the solution method described in the paragraph II.4.1 essentially follows their approach. By analogy, we refer to the region $\mu \rightarrow -\infty$ as the vacuum.

An interesting point demonstrated in Ref. [33] is that in the limit $\tau \ll 1$, the ion temperature evolution is given from the isothermal solution by $T_i/T_{i\infty} = (N/N_\infty)^2$. This property has a clear physical explanation: if we assume thermal conductivity in a cold ion plasma to be negligible, f is Maxwellian at each point in space, and phase-space conservation imposes invariance to $\max(f) = n/(\sqrt{2\pi T_i})$.

II.4.4 Free-flight solution

The kinetic equation (II.50) can be solved analytically in the free-flight regime, when the potential gradient effects on the ion motion are neglected. The orbits in $\mu-v$ space are then vertical lines ending at $\mu = v - v_\infty$, and the ion distribution moments given by Eqs (II.55,II.56,II.57) have closed form expressions. Using the notation $\mu_I = \mu/c_{sI}$ and $\omega = -c_{sI}/v_{ti} = -[(1+1/\tau)/2]^{1/2}$:

$$n = \frac{n_\infty}{2} \operatorname{erfc}(\omega\mu_I) \quad (\text{II.65})$$

$$n(\langle v \rangle - v_\infty) = n_\infty \frac{c_{sI}/\omega}{2\sqrt{\pi}} \exp(-\omega^2\mu_I^2) \quad (\text{II.66})$$

$$\frac{T_i}{T_{i\infty}} = 1 + \frac{2\omega\mu_I\sqrt{\pi} \exp(-\omega^2\mu_I^2) \operatorname{erfc}(\omega\mu_I) - 2 \exp(-2\omega^2\mu_I^2)}{\pi \operatorname{erfc}(\omega\mu_I)^2}. \quad (\text{II.67})$$

After tedious but straightforward algebra, the Bohm sound speed given by Eq. (II.9) can be calculated analytically and reduces to $c_s = v_\perp u - \langle v \rangle$. In other words, the

magnetized Bohm condition discussed in paragraph II.4.2 is marginally satisfied in the entire presheath.

Free-flight calculations are justified in the limit $\tau \gg 1$ (i.e. $\omega = -1/\sqrt{2}$), since the electrostatic force becomes negligible compared to the ion pressure. We refer to this limit as the extended free-flight solution.

II.5 Results and physical discussion

II.5.1 Plasma profiles

We start the discussion of our numerical results with the plasma profiles. Figure (II-7) shows the evolution of the normalized ion distribution function f with position in the presheath, for originally equithermal ions and electrons ($\tau = 1$). The ions cool down as they are accelerated, and f has a sharp cutoff corresponding to the probe shadowing ions streaming away from it. The sheath edge, degenerate with the probe surface in our quasineutral model, is located at $\mu = \mu_p$.

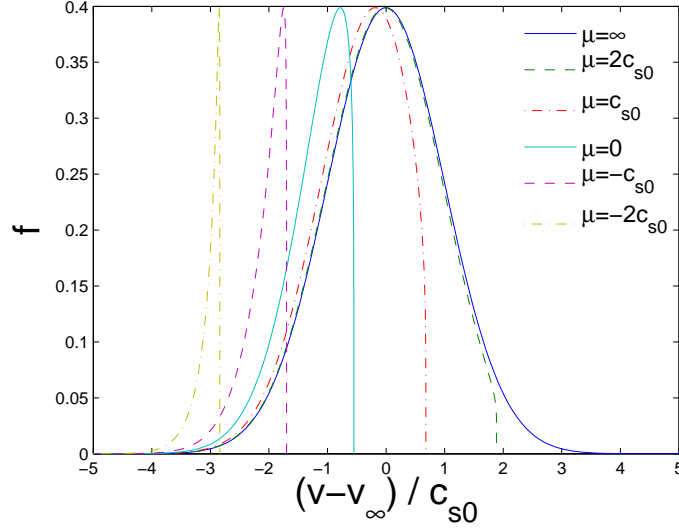


Figure II-7: Normalized ion distribution function at different positions μ (Eq. (II.52)) along the presheath, for originally equithermal ions and electrons ($\tau = 1$).

After computing the evolution of f for different temperature ratios τ , it is straight-

forward to take the moments (II.55,II.56,II.57). Density and temperature are shown in Fig. (II-8), with the fluid (Eq. (II.61) with $T_i/T_{i\infty} = (N/N_\infty)^2$) and the extended free-flight curves (Eqs (II.65,II.67)).

A first noticeable result is that those analytic solutions, valid respectively at $\tau \ll 1$ and $\tau \gg 1$, are envelopes for the profiles at arbitrary τ ; in other words the plasma properties vary monotonically with temperature ratio, which is not obvious a priori.

(a) Electron density

(b) Temperature

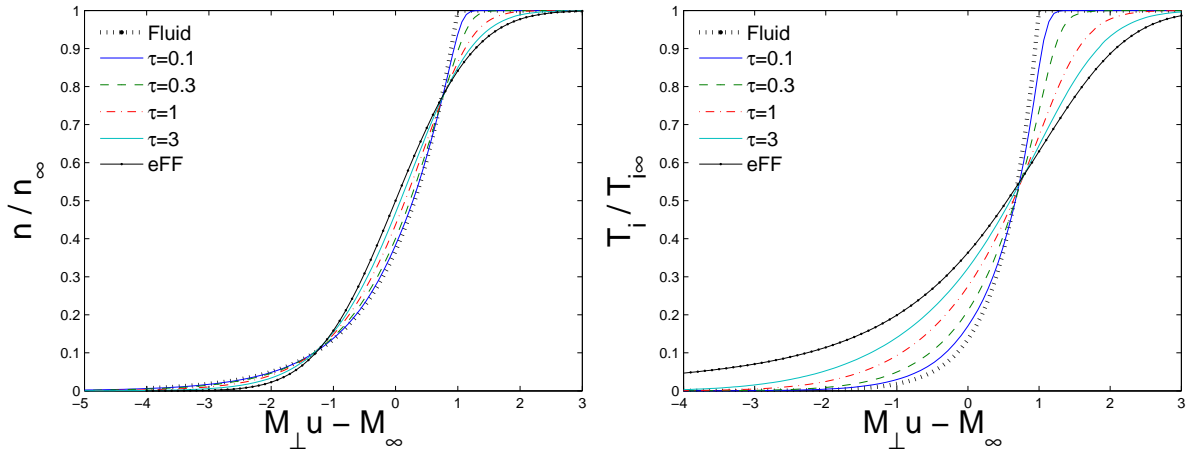


Figure II-8: Evolution of the electron density and ion temperature along the presheath parametrized by $\mu_I = M_{\perp} u - M_{\infty}$, for different temperature ratios. “Fluid” refers to Hutchinson’s fluid solution, and “eFF” to the extended free-flight solution described in Paragraph II.4.4.

Figure (II-8) shows that except when $\tau = 0$ and the fluid solution has a slope discontinuity at $M_{\perp} u - M_{\infty} = 1$, the temperature perturbation extends much farther than the density perturbation. High order moments are indeed more sensitive to the cutoff experienced by the ion distribution function on its positive velocity tail. Except for the singular case $\tau = 0$, the ion adiabatic index (II.10) therefore goes to infinity as we approach the unperturbed plasma; this is required in order for the magnetic Bohm condition to be marginally satisfied in the entire presheath.

A further point of interest in Fig. (II-8a) is that the density (hence potential) profiles are monotonic. In particular there is no localized region where the electrons are attracted, strengthening *a posteriori* our Boltzmann-electron assumption. This is a

consequence of the parallel ion motion being collisionless, and the probe being at ion saturation. The situation would be fundamentally different if the probe were biased close to space potential, i.e. operating in the collisional electron collection regime yet far from electron saturation. Indeed the potential would then overshoot at approximately one electron mean-free-path from the probe sheath edge, in order for the collected electrons to overcome Coulomb friction with the ions. Such effect, reported in kinetic [34] and fluid [35] treatments, as well as experimentally observed [36], is absent for our purposes.

II.5.2 Ion flux-density to a flat probe

The ion flux-density to the probe (Eq. (II.58)) can be rewritten

$$\Gamma_{i\parallel} = [-n_p(M_p - M_\infty) + n_p(M_\perp u_p - M_\infty)] c_{sI}, \quad (\text{II.68})$$

where $n(M - M_\infty)c_{sI}$ corresponds to the parallel ion flux-density in the frame moving with velocity v_∞ . This term can be computed from our kinetic simulations using Eq. (II.56), and is plotted for different values of τ in Fig. (II-9).

Provided the flow Mach number is moderate and the probe surface is not grazing the magnetic field, the interesting physics lies around $\mu_I = 0$, recalling the definition $\mu_I = M_\perp u - M_\infty$. It can be derived directly from the ion kinetic equation that

$$n(M - M_\infty) = -\frac{\Gamma_0}{c_{sI}} + O(\mu_I)^2, \quad (\text{II.69})$$

$$n = n_0 + O(\mu_I), \quad (\text{II.70})$$

where we defined $n_0 = n(\mu_I = 0)$ and $\Gamma_0 = n_0(v_\infty - v(\mu_I = 0))$; recall that our calculations are performed in the downfield region of the probe, hence $n(\langle v \rangle - v_\infty) \leq 0$. We can therefore define α and β such that Eq. (II.68) expanded to third order in $\mu_{Ip} = M_\perp u_p - M_\infty$ is

$$\Gamma_{i\parallel} = [\Gamma_0(1 + \alpha\mu_{Ip}^2) + n_0\mu_{Ip}(1 + \beta\mu_{Ip}^2)c_{sI}] + O(\mu_{Ip})^4. \quad (\text{II.71})$$

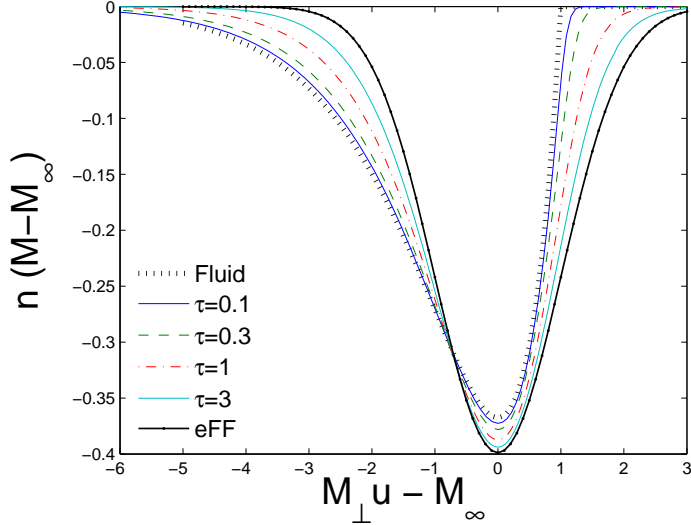


Figure II-9: Evolution of the parallel ion flux-density in the frame moving with velocity v_∞ (Eq. (II.56)), normalized to the isothermal sound speed c_{sI} . ‘‘Fluid’’ refers to Hutchinson’s fluid solution (Eqs (II.61,II.62)), and ‘‘eFF’’ to the extended free-flight solution (Eq. (II.66)).

The upfield physics is recovered upon replacing (η_p, v) by $(\pi - \eta_p, -v)$, enabling evaluation of the upstream to downstream ion current ratio $R = \Gamma_{i\parallel}^{\text{Up}} / \Gamma_{i\parallel}^{\text{Do}}$

$$R = \frac{\Gamma_0(1 + \alpha\mu_{Ip}^2) - n_0\mu_{Ip}(1 + \beta\mu_{Ip}^2)c_{sI}}{\Gamma_0(1 + \alpha\mu_{Ip}^2) + n_0\mu_{Ip}(1 + \beta\mu_{Ip}^2)c_{sI}} + O(\mu_{Ip})^4. \quad (\text{II.72})$$

With the notation

$$M_c = \frac{1}{2} \frac{\Gamma_0}{n_0 c_{sI}} \quad (\text{II.73})$$

and $\epsilon = 1/2 + 6(\beta - \alpha)M_c^2$, Eq. (II.72) simplifies to

$$R = 1 - \frac{\mu_{Ip}}{M_c} + \frac{1}{2} \frac{\mu_{Ip}^2}{M_c^2} - \frac{1 + \epsilon}{6} \frac{\mu_{Ip}^3}{M_c^3} + O\left(\frac{\mu_{Ip}}{M_c}\right)^4. \quad (\text{II.74})$$

ϵ can be calculated numerically from our kinetic code, but this will not prove necessary as ϵ is extremely small, of the percent order. The analytic limits are $\epsilon = 0$ at $\tau \ll 1$ and $\epsilon = (1 - 3/\pi)/2 \simeq 0.02$ at $\tau \gg 1$.

In other words,

$$R = \frac{\Gamma_{i\parallel}^{\text{Up}}}{\Gamma_{i\parallel}^{\text{Do}}} = \exp\left(\frac{M_\infty - M_\perp u_p}{M_c}\right) \quad (\text{II.75})$$

to second order in μ_{Ip} exactly, and almost to third order, with all the physics included in M_c .

Calculation of M_c requires the temperature dependence of Γ_0 and n_0 corresponding to the slice $\mu_I = M_\perp u - M_\infty = 0$ in Figs (II-8a,II-9). Figure (II-10) shows our numerical solution, interpolated between the fluid and extended free-flight limits as follows:

$$M_c(\tau) = \kappa M_{c|\tau=0} + (1 - \kappa) M_{c|\tau=\infty}, \quad (\text{II.76})$$

where analytic limits are

$$M_{c|\tau=0} = 1/2, \text{ and } M_{c|\tau=\infty} = 1/\sqrt{2\pi}. \quad (\text{II.77})$$

The interpolating coefficient is fitted to the numerical solution by

$$\kappa(\tau) = \frac{1}{2} \operatorname{erfc}(0.12 + 0.40 \ln \tau). \quad (\text{II.78})$$

Figure (II-11) shows the upstream to downstream ion flux ratio against $M_\infty - M_\perp u_p \in [0, 3]$. For supersonic flows Eq. (II.75) is in theory not valid, the error on $\ln R$ at $M_\infty - M_\perp u_p = 2$ is however only $\sim 10\%$.

II.5.3 Extension to transverse Mach probes

The purpose of a transverse Mach probe is to measure M_\perp and M_∞ . The two main competing designs are rotating probes, where a planar electrode such as schematized in Fig. (II-5) is rotated to measure fluxes at different tilt angles η_p , and Gundersen-like probes, where simultaneous measurements at different angles are made by a set of electrodes spanning a single probe head [26].

Although we derived and solved our governing equations with the assumption that the probe is flat, the solution is applicable to any convex probe, upon considering η

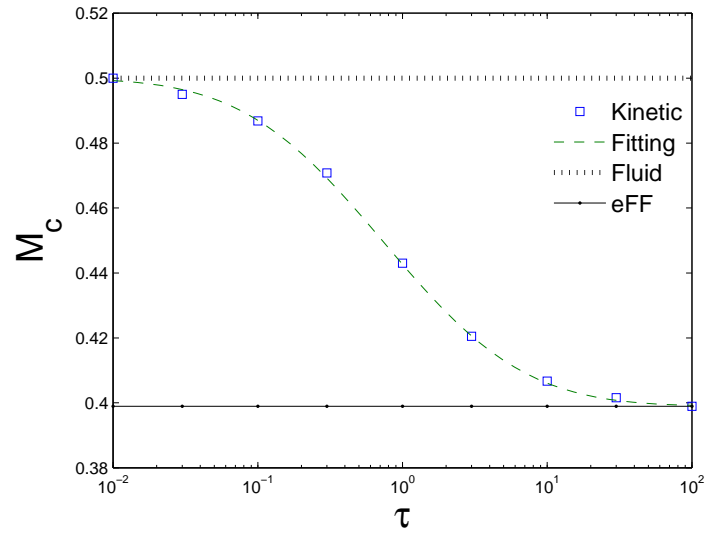


Figure II-10: Mach probe calibration factor M_c as a function of temperature ratio τ . M_c varies from $M_c = 1/2$ in cold ion plasmas (“Fluid”) to $M_c = 1/\sqrt{2\pi}$ in hot ion plasmas (“eFF”). “Fitting” refers to the analytic expression (II.76).

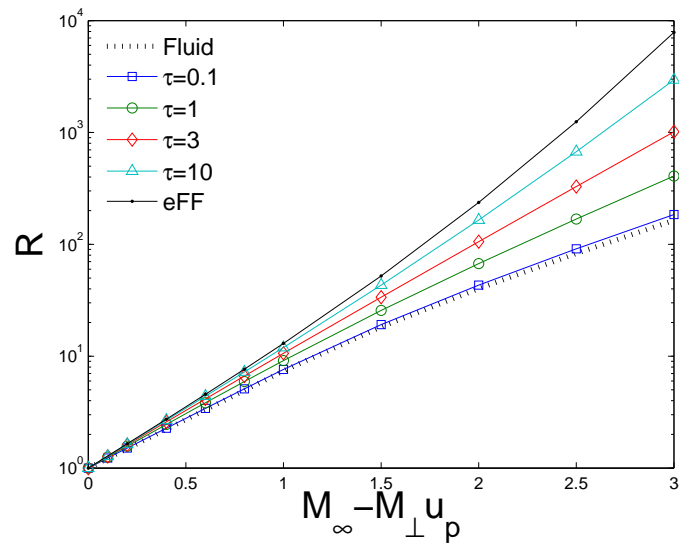


Figure II-11: Upstream to Downstream flux ratio against $M_\infty - M_\perp u_p \in [0, 3]$, for different temperature ratios. The tangents of the flux ratio logarithms at the origin have a slope given by $1/M_c(\tau)$.

as the angle between the magnetic field and the line passing by the considered point and tangent to the probe. This configuration is illustrated in Fig. (II-12) for the case where the probe cross-section is circular. It is here easier to think in terms of $\theta = \eta - \pi/2$, angle between the magnetic field and the normal to the probe surface, because for circular cross-sections it can be interpreted as the polar angle.

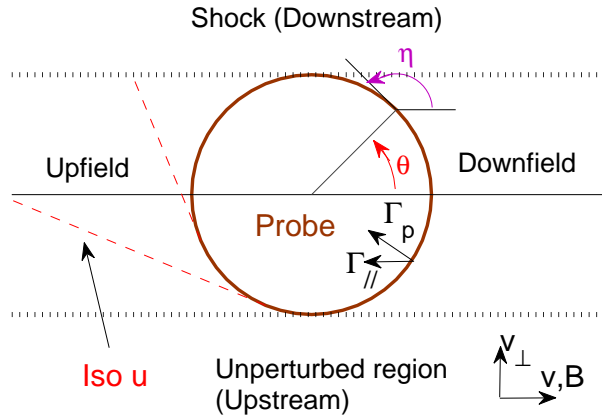


Figure II-12: Schematic view of a convex probe with circular cross-section. Each point at the probe surface is parametrized by the angle between the magnetic field and the local probe tangent (η in the downfield region), or by $\theta = \eta - \pi/2$. The plasma solutions are invariant along the lines of constant u , the probe tangents.

This was proved in the isothermal fluid formulation [15], by analyzing the characteristics of the coupled continuity and momentum equations. In the same publication, a second proof was given by considering the convex envelope of an arbitrarily shaped two-dimensional probe as the limiting case of a multifaceted polygonal surface. For this second argument to be valid here, one needs to show that information can not propagate in the direction of decreasing u . Mathematically, this simply derives from the kinetic equation (II.50) being hyperbolic in u in the quasineutral regime considered here. The physical interpretation is that (a) the orbits shown in Fig. (II-6) are never reflected, in other words the ion trajectories curve towards the probe, and (b) the magnetic Bohm condition is always marginally satisfied, hence information trav-

eling at the Bohm sound speed (in the frame locally moving with the fluid at velocity $\langle v \rangle \mathbf{e}_z + v_\perp \mathbf{e}_y$) is confined to the lines of constant u .

Figure (II-13) shows the angular distribution of ion saturation flux-density for a drift $M_\infty = 0.5$ and $M_\perp = 0.5$, calculated from the kinetic equation with $\tau = 1$. Comparison with the isothermal fluid and extended free-flight solutions shows that the ion temperature has little quantitative impact on the flux distribution, when normalized to the isothermal sound speed. The difference is maximal at $\cos \theta = \pm 1$, and vanishes at $\cos \theta = 0$ where the probe either collects the unperturbed flow ($\theta = -\pi/2$), or zero flux ($\theta = \pi/2$).

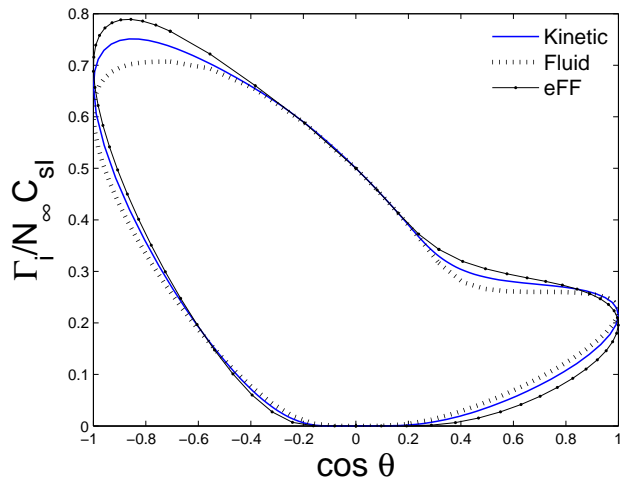


Figure II-13: Angular distribution of ion saturation flux-density (Γ_i , defined in Eq. (II.59)) for a drift $M_\infty = 0.5$ and $M_\perp = 0.5$ from our numerical kinetic solutions with $\tau = 1$, compared with the isothermal fluid and extended free-flight solutions. θ is the angle between the magnetic field and the normal to the probe surface, in the plane of flow and magnetic field.

II.5.4 Mach probe calibration

The simplest experimental procedure to find M_\perp and M_∞ is to measure the upstream to downstream flux ratio at two different angles, with either a flat or a convex Gundersen probe: $R_1 = \Gamma_{i\parallel}(\eta_1 + \pi)/\Gamma_{i\parallel}(\eta_1)$ and $R_2 = \Gamma_{i\parallel}(\eta_2 + \pi)/\Gamma_{i\parallel}(\eta_2)$. It is desirable to avoid grazing angles with the magnetic field in order for the exponential calibration

introduced in paragraph II.5.2 to be applicable, while maximizing the tilt spacings to limit experimental noise. The optimal choice is therefore $\eta_1 = 3\pi/4$ and $\eta_2 = \pi/4$, yielding

$$M_{\perp} = \frac{M_c}{2} (\ln R_1 - \ln R_2), \quad (\text{II.79})$$

$$M_{\infty} = \frac{M_c}{2} (\ln R_1 + \ln R_2). \quad (\text{II.80})$$

Equations (II.79,II.80) require four measurements, while physically only three single measurements should be needed to find the problem's three unknowns (N_{∞} , M_{\perp} and M_{∞}). The temperature ratio τ is indeed treated as an input, supposed to be known from other diagnostics. Unfortunately M_c would only provide a three-point calibration valid to first order in the flow Mach number, each additional order requiring an additional calibration factor. Only probing flux ratios at angles $\eta + \pi$ over η as in Eq. (II.72) takes full advantage of the symmetries in the kinetic equation solutions, yielding the compact, quasi-third order formula (II.75).

If one is interested in M_{∞} only, it is in theory possible to measure R on the magnetic axis (parallel Mach probe configuration), and the calibration is then $M_{\infty} = M_c \ln R$. We however expect the double measurement (II.79,II.80) to be less sensitive to finite ion Larmor radius effects. Indeed the choice $\eta_1 = 3\pi/4$ and $\eta_2 = \pi/4$ has the elegant property of being meaningful to non magnetized Mach probes as well. Particle In Cell simulations [9] show that the unmagnetized ion flux-density distribution on a spherical probe's major cross-section is approximately given by $\Gamma_i \propto \exp(-K \cos(\theta - \theta_d)v_d/2)$, where v_d is the total flow velocity, θ_d the angle of flow with respect to the \mathbf{e}_z axis, and $K \simeq 1.34/c_{s0}$ for $\tau \lesssim 3$; the flux ratio at angle θ is therefore $R = \Gamma_i(\theta + \pi)/\Gamma_i(\theta) = \exp(K \cos(\theta - \theta_d)v_d)$. The only possible values of η such that there exists a scalar M_c such that this flux ratio can be expressed as in Eq. (II.75) are $\eta = \pm\pi/4$ or $\eta = \pm 3\pi/4$ (yielding $M_c = \pm\sqrt{2}/(Kc_{sI})$ on the sphere major cross-section in unmagnetized plasmas).

II.6 2D analytic free-flight density contours

II.6.1 Strongly magnetized limit

While Eq. (II.50) is valid in the entire plasma, we only discussed it in the upfield and downfield presheaths where the problem is effectively one-dimensional (in u). The downstream shock region is two-dimensional, and does not seem to be easily solvable by the method of orbits except in the free-flight regime.

Indeed in the limit of negligible electron pressure ion orbits are straight lines, hence the ion density in the shock is simply the sum of the densities from the two merging counterstreams (equation (II.65) for the downfield side). Defining the downfield μ_I and the upfield $\bar{\mu}_I$ as follows

$$\mu_I = M_\perp u - M_\infty \quad \text{and} \quad \bar{\mu}_I = M_\perp \bar{u} + M_\infty, \quad (\text{II.81})$$

where u and \bar{u} are the cotangents of the slopes of the two probe tangents passing from the considered point in the shock region, the density in the entire plasma region can be written:

$$\frac{N}{N_\infty} = \begin{cases} 1 & , y < -1 \\ \frac{1}{2} \operatorname{erfc}(\omega \mu_I) & , y \in [-1 : 1] \text{ and } z > 0 \\ \frac{1}{2} \operatorname{erfc}(\omega \bar{\mu}_I) & , y \in [-1 : 1] \text{ and } z < 0 \\ \frac{1}{2} [\operatorname{erfc}(\omega \mu_I) + \operatorname{erfc}(\omega \bar{\mu}_I)] & , y > 1. \end{cases} \quad (\text{II.82})$$

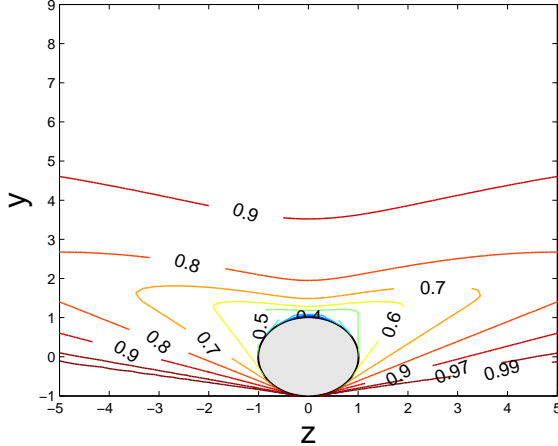
The shock solution clearly depends on the probe shape. For the specific case of a probe with circular cross-section (normalized radius $r_p = 1$), and thinking in terms of polar angle θ , we can rewrite u and \bar{u} as:

$$u = \frac{r^2 \sin \theta \cos \theta - \sqrt{r^2 - 1}}{(r \sin \theta)^2 - 1}, \quad (\text{II.83})$$

$$\bar{u} = -\frac{r^2 \sin \theta \cos \theta + \sqrt{r^2 - 1}}{(r \sin \theta)^2 - 1}, \quad (\text{II.84})$$

enabling easy plotting of the full density contours. Two examples with purely transverse plasma drift are shown in Fig. (II-14), where $w_{\perp} = v_{\perp}/v_{ti}$ and $w_{\infty} = v_{\infty}/v_{ti}$.

(a) $w_{\perp} = 0.3, w_{\infty} = 0$



(b) $w_{\perp} = 1.5, w_{\infty} = 0$

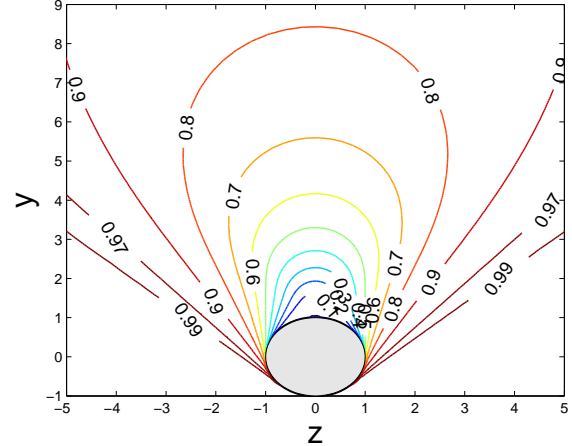


Figure II-14: 2D charge-density contours in a strongly magnetized plasma, in the free-flight limit. (a) wing-shaped wake: $w_{\perp} = 0.3, w_{\infty} = 0$ and (b) bug-shaped wake $w_{\perp} = 1.5, w_{\infty} = 0$.

In the regime of pure transverse flow ($w_{\infty} = 0$), we can use $z = r \cos \theta$ and $y = r \sin \theta$ to show that $\partial n / \partial z|_{z=0} = 0$, which is obvious by symmetry. More interesting is the second derivative

$$\frac{\partial^2 n}{\partial z^2}|_{z=0} = -\exp\left(-\frac{w_{\perp}^2}{y^2-1}\right) \frac{2w_{\perp}}{\sqrt{\pi}(y^2-1)^{3/2}} \left(1 - 2\frac{w_{\perp}^2 y^2}{y^2-1}\right). \quad (\text{II.85})$$

If $w_{\perp} \geq 1/\sqrt{2}$, i.e. $v_{\perp} \geq \sqrt{T_{i\infty}/m}$, $\partial^2 n / \partial z^2|_{z=0} > 0$ and the contours are “bug-shaped” as in Fig. (II-14b). If $w_{\perp} < 1/\sqrt{2}$, $\partial^2 n / \partial z^2|_{z=0} > 0$ for $y < (1 - 2w_{\perp}^2)^{-1/2}$ and $\partial^2 n / \partial z^2|_{z=0} < 0$ for $y > (1 - 2w_{\perp}^2)^{-1/2}$. In other words, density contours look “wing-shaped” as in Fig. (II-14a).

Although we can not prove it analytically, it is reasonable to expect the transition between the two wake shapes for arbitrary temperature ratio τ to occur at $M_{\perp} \simeq 1$ (at $\tau = \infty$, $M_{\perp} = 1$ is equivalent to $w_{\perp} = 1/\sqrt{2}$).

II.6.2 Comparison with the magnetic-free regime

It is interesting to compare the just-discussed free-flight profiles valid in the strongly magnetized limit with their magnetic-free analog.

In the absence of magnetic field, the solution is rotationally symmetric about the drift axis. If we define \mathbf{v}_r as the radial (towards the probe) velocity, \mathbf{v}_r^\perp its normal component, and φ the orientation of \mathbf{v}_r^\perp in the plane normal to \mathbf{e}_r , the ion density distribution is given by

$$\frac{N}{N_\infty} = 1 - \frac{1}{(v_{ti}\sqrt{\pi})^3} \int_0^\infty \int_0^\infty \int_0^{2\pi} \exp \left[-\frac{(\mathbf{v} - \mathbf{v}_d)^2}{v_{ti}^2} \right] H(\mathbf{v}) d\varphi dv_r v_r^\perp dv_r^\perp, \quad (\text{II.86})$$

where the impact factor H is unity if the ion orbit intersects the probe, and zero otherwise:

$$H(\mathbf{v}) = \begin{cases} 1 & , \mathbf{v}^2 - v_r^{\perp 2} r^2 \geq 0 \\ 0 & , \mathbf{v}^2 - v_r^{\perp 2} r^2 < 0. \end{cases} \quad (\text{II.87})$$

If $\chi = \theta - \theta_d$ is the angle between \mathbf{v}_d and \mathbf{e}_r , Eq. (II.86) can be integrated with the transform $\mathbf{v} \cdot \mathbf{v}_d = v_d (-v_r \cos \chi + v_r^\perp \sin \chi \cos \varphi)$, yielding

$$\frac{N}{N_\infty} = 1 - \exp [-(w_d \sin \chi)^2] \int_0^\infty \exp(-\xi^2) I_0(2w_d \xi \sin \chi) \operatorname{erfc} \left(\xi \sqrt{r^2 - 1} - w_d \cos \chi \right) \xi d\xi, \quad (\text{II.88})$$

where $w_d = v_d/v_{ti}$ and I_n is the modified Bessel function defined by Eq. (A.7).

Figure (II-15) compares the free-flight charge-density distribution on the probe major cross-section ($x = 0$) given by Eq. (II.82) and Eq. (II.88) for the case $w_d = w_\perp = 0.5$ and $w_\infty = 0$. An important point to notice is that information can propagate upstream in the absence of magnetic field, hence the density perturbation extends in the negative- y region. Also because the downstream region can be replenished three-dimensionally, the unmagnetized wake is more localized than its magnetized counterpart.

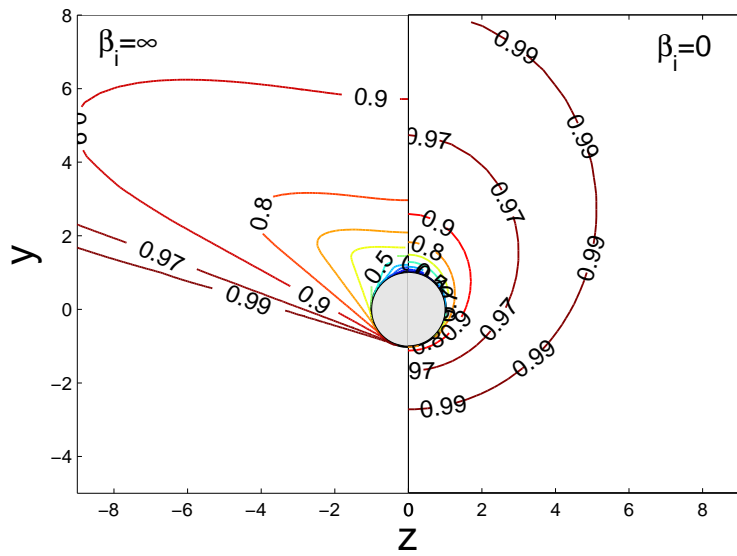


Figure II-15: Analytic free-flight charge-density contours at infinite (Eq. (II.82)) and zero (Eq. (II.88)) ion magnetization, for the case $w_d = w_\perp = 0.5$ and $w_\infty = 0$.

Chapter III

SCEPTIC3D

The previous chapter developed a semi-analytic kinetic solution to the problem of ion collection by arbitrarily-shaped bodies, in the limit of zero Debye length and infinite magnetic field. In the rest of this thesis, we wish to relax those assumptions in order to investigate finite Larmor radius and finite shielding effects.

To do so is a body-shape dependent problem of considerable complexity, for which the three dimensional hybrid Particle-In-Cell (PIC) code SCEPTIC3D has been developed. The code, specifically designed to solve the problem of ion flow past a negatively biased sphere in the presence of a uniform background magnetic field, is derived from the 2D/3v code SCEPTIC originally written by Hutchinson [9, 10, 11, 12]. The purpose of this thesis chapter is to detail the physical model, solution method, and operational regimes offered by SCEPTIC3D.

III.1 Model and computational method

III.1.1 Problem formulation

The plasma

A spherical collector of radius R_p , referred to as “probe”, “electrode”, “dust” or “sphere” regardless of its physical nature, is placed at the origin of the infinite, collisionless Maxwellian plasma described in paragraph II.1.1. We recall that the ion

charge-number is Z , the unperturbed ion and electron temperatures are $T_{i\infty}$ and T_e , and the charge density is N_∞ . A uniform background magnetic field \mathbf{B} and an orthogonal convective electric field \mathbf{E}_{cnv} induce an external “ $\mathbf{E} \times \mathbf{B}$ ” drift

$$\mathbf{v}_\perp = \mathbf{E}_{\text{cnv}} \times \frac{\mathbf{B}}{B^2}, \quad (\text{III.1})$$

adding to the free parallel drift $\mathbf{v}_\infty = v_\infty \mathbf{B}/B$. The total plasma drift velocity is therefore

$$\mathbf{v}_d = \mathbf{v}_\perp + \mathbf{v}_\infty, \quad (\text{III.2})$$

and the unperturbed ion-charge distribution function

$$f_i^\infty(\mathbf{v}) = \frac{N_\infty}{(v_{ti}\sqrt{\pi})^3} \exp\left[-\frac{(\mathbf{v} - \mathbf{v}_d)^2}{v_{ti}^2}\right], \quad (\text{III.3})$$

where we recall the ion thermal speed definition $v_{ti} = (2T_{i\infty}/m)^{1/2}$ (Eq. (II.31)).

The probe attracts ions and repels electrons, therefore perturbing their respective charge densities $N_{i,e}$ and charge flux densities $\mathbf{\Gamma}_{i,e}$, that need to be self-consistently resolved with Maxwell’s equations. In the static approximation, those reduce to Gauss and Ampere laws:

$$\nabla \cdot \mathbf{E} = e \frac{N_i - N_e}{\epsilon_0}, \quad (\text{III.4})$$

$$\nabla \times \mathbf{B} = e\mu_0(\mathbf{\Gamma}_i - \mathbf{\Gamma}_e). \quad (\text{III.5})$$

The perturbed part of the electric field originates from a scalar electrostatic potential Φ , such that

$$\mathbf{E} = \mathbf{E}_{\text{cnv}} - \nabla\Phi. \quad (\text{III.6})$$

By normalizing the potential to the electron temperature

$$\phi = \frac{e\Phi}{T_e}, \quad (\text{III.7})$$

the charge densities to N_∞

$$n_e = \frac{N_e}{N_\infty} \quad \text{and} \quad n_i = \frac{N_i}{N_\infty}, \quad (\text{III.8})$$

and recalling the definition of the unperturbed electron Debye length $\Lambda_{De} = \sqrt{\epsilon_0 T_e / N_\infty e^2}$ (Eq. (II.1)), Eq. (III.4) can conveniently be rewritten as a dimensionless electrostatic Poisson equation:

$$\nabla^2 \phi = \frac{n_e - n_i}{\Lambda_{De}^2}. \quad (\text{III.9})$$

The magnetic field originates from a vector potential \mathbf{A} such that $\mathbf{B} = \nabla \times \mathbf{A}$ and $\nabla \cdot \mathbf{A} = 0$ (Coulomb gauge). The dimensionless magnetostatic Poisson equation corresponding to Eq. (III.5) is then

$$\nabla^2 \alpha = \frac{c_{s0}^2}{c^2} \frac{\langle v_q \rangle}{c_{s0}} \frac{n_e - n_i}{\Lambda_{De}^2}, \quad (\text{III.10})$$

where c is the speed of light, $\langle v_q \rangle = (n_i \langle v_i \rangle - n_e \langle v_e \rangle) / (n_i - n_e)$ is of order c_{s0} , and α is the vector potential normalized to the ratio of magnetic field to cold-ion sound Larmor radius $\alpha = e\mathbf{A}/\sqrt{T_e m}$.

The scale length of self-consistent potential and vector potential variations are therefore $L_\Phi \sim \Lambda_{De}$ and $L_A \sim \Lambda_{De} c / c_{s0}$, respectively.

Ideal, negatively biased conducting sphere

The sphere radius R_p can take any value with respect to L_Φ , but is much smaller than L_A so that the magnetic field distribution in the plasma is of vacuum-type. Further assuming that the probe conductivity σ is small enough for the magnetic diffusion time

$$t_B = \pi \mu_0 \sigma R_p^2 \quad (\text{III.11})$$

to be negligible, the magnetic field is not affected by the probe and remains equal to its uniform, unperturbed value \mathbf{B} . We therefore do not need to solve Eq. (III.10).

The probe surface behaves as an ideal ion and electron sink. It releases neutral atoms and/or molecules at a rate that balances the incoming flux of ions, which has

been neutralized by the incoming electrons and possibly by electrons supplied by an external bias circuit. Global charge conservation in the system “plasma+probe” therefore imposes internal current densities of the order $eN_\infty c_{s0}$. Neglecting the Hall term, Ohm’s law gives the electric field magnitude in the probe as $E_{\text{int}} \sim eN_\infty c_{s0}/\sigma$, which we assume is negligible by taking σ large enough. The probe is therefore an equipotential, and its surface perturbed potential satisfies $\mathbf{E}_{\text{cav}} - \nabla\Phi(R_p, \theta, \psi) = 0$:

$$\Phi(R_p, \theta, \psi) = \Phi_p + [E_{\text{cav}} R_p] \sin \theta \cos \psi. \quad (\text{III.12})$$

E_{cav} is the (negative, since \mathbf{E}_{cav} is oriented along $-\mathbf{e}_x$) convective field, and Φ_p the probe bias, assumed negative enough for $|\mathbf{E}_{\text{cav}} R_p| + \Phi_p$ to be more negative than a few T_e s, typically $|\mathbf{E}_{\text{cav}} R_p| + \Phi_p \lesssim -2T_e/e$. The entire probe surface is then strongly electron-repelling.

In Eq. (III.12), the position is parametrized in spherical coordinates, where R is the radial distance measured from the probe center, $\theta \in [0 : \pi]$ the polar angle measured from the probe magnetic axis, and $\psi \in [0 : 2\pi]$ the azimuthal angle measured from the plane of convective and magnetic fields. We also define the Cartesian coordinate system (x, y, z) such that $\mathbf{B} = B\mathbf{e}_z$, $\mathbf{v}_\infty = v_\infty \mathbf{e}_z$, $\mathbf{v}_\perp = v_\perp \mathbf{e}_y$, and $\mathbf{E}_{\text{cav}} = -|\mathbf{E}_{\text{cav}}| \mathbf{e}_x$. A first illustration of the problem geometry is proposed in Fig. (III-1).

III.1.2 Code mesh

The probe is embedded in a spherical computational domain of radius r_b , subdivided in cells parametrized by spherical coordinates (r, θ, ψ) , and uniformly spaced in r , $\cos \theta$ and ψ . The first and last radial centers are located at $r = 1$ and $r = r_b$, and the first and last polar centers at $\cos \theta = \pm 1$; the corresponding cells are hence “half cells”. The domain is sketched in Fig. (III-2).

At each time-step, the ion charge-density and subsequent moments (velocities and cross square velocities) are linearly extrapolated to the cell centers from a set of computational ions spanning the domain (Cloud-In-Cell (CIC) approach [8]), and

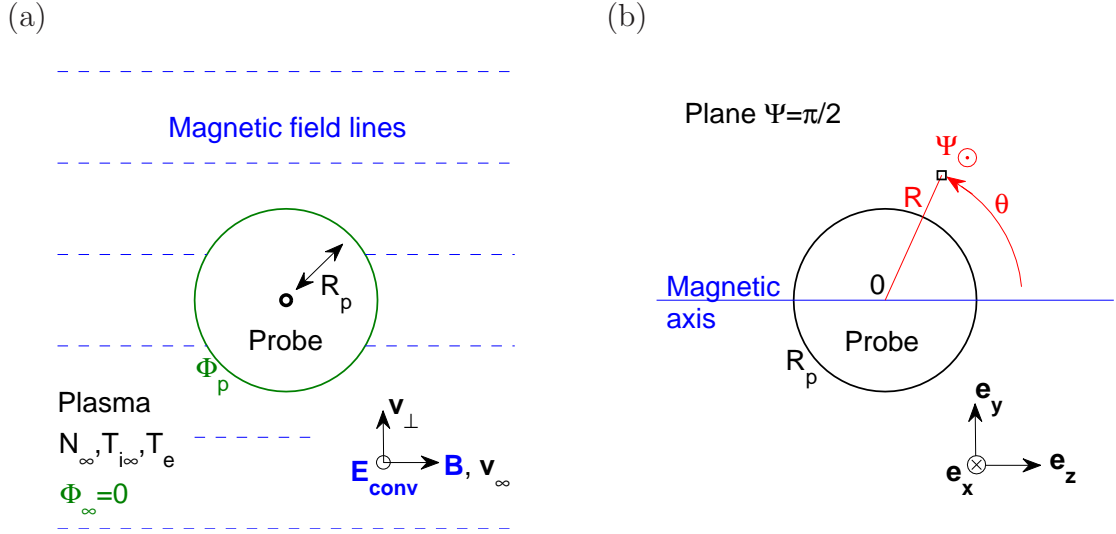


Figure III-1: (a) Problem parameters in their geometry, in the $\{0, \mathbf{e}_y, \mathbf{e}_z\}$ -plane. (b) Spherical and Cartesian coordinate systems, projected on the plane of flow and magnetic field ($\psi = \pi/2$).

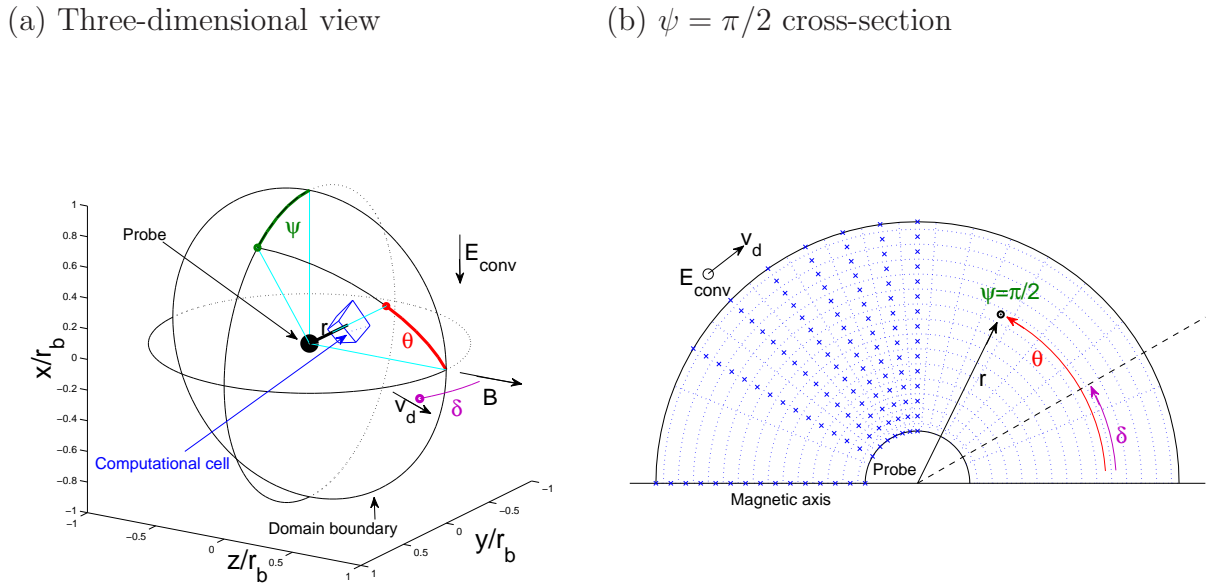


Figure III-2: (a) Three-dimensional view of the computational domain. (b) Cross-section at $\psi = \pi/2$, half plane containing the drift velocity \mathbf{v}_d . Computational cell centers for $\cos \theta \leq 0$ are indicated by “x”-symbols.

advanced according to Newton's equation

$$\frac{m}{Ze} \frac{d\mathbf{v}}{dt} = \mathbf{E}_{\text{cav}} - \nabla\Phi + \mathbf{v} \times \mathbf{B}, \quad (\text{III.13})$$

completed by $d\mathbf{x}/dt = \mathbf{v}$. The particle mover uses $\nabla\Phi$ calculated by differentiating the potential at the previous time-step on the grid and interpolating it back to each ion. The updated potential Φ at the cell centers is then obtained from the discretized ion density either by quasineutrality (quasineutral operation described in section III.2), or by solving Poisson's equation (finite Debye length operation described in section III.3), effectively completing the time-step.

Density extrapolation

Let us now examine in more detail the extrapolation and interpolation processes in order to estimate their formal accuracy. The analysis is presented on the one-dimensional grid schematized in Fig. (III-3), where ξ can represent r , $\cos\theta$ or ψ . According to the CIC approach, to each ion is associated a triangular shape-function enabling linear extrapolation of density and higher order moments to the grid centers, located at ξ_i with $i \in [1 : n]$.

The extrapolated value of a smooth moment $h(\xi)$ at an inner node i is

$$h_i = \frac{1}{\Delta\xi} \int_{\xi_{i-1}}^{\xi_{i+1}} h(\xi) \left[1 - \frac{|\xi - \xi_i|}{\Delta\xi} \right] d\xi, \quad (\text{III.14})$$

where $\Delta\xi = \xi_{i+1} - \xi_i$ is the uniform cell volume. If we take h to be a quadratic test function $h(\xi) = \alpha + \beta(\xi - \xi_i) + \gamma(\xi - \xi_i)^2$ around ξ_i , Eq. (III.14) yields $h_i = \alpha + \gamma\Delta\xi^2/6$ while $h(\xi_i) = \alpha$. The extrapolation error is therefore second order in $\Delta\xi$.

On the right (equivalently on the left) boundary, the extrapolated value of $h(\xi)$ is

$$h_n = \frac{1}{\Delta\xi/2} \int_{\xi_{n-1}}^{\xi_n} h(\xi) \left[1 - \frac{|\xi - \xi_n|}{\Delta\xi} \right] d\xi, \quad (\text{III.15})$$

where the cell volume is only $\Delta\xi/2$. Because we are on a boundary there is no differentiability requirement, hence we consider the more general test function $h(\xi) =$

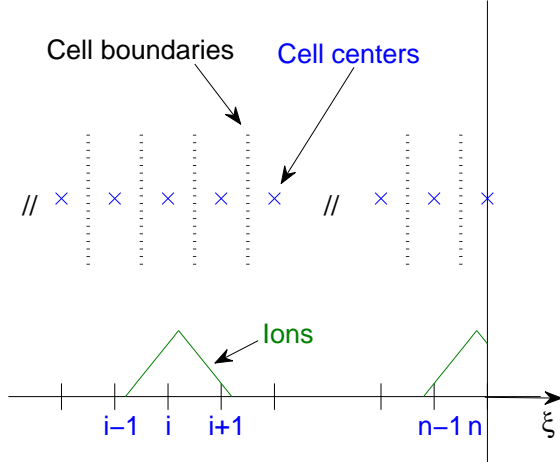


Figure III-3: One-dimensional representation of a computational grid uniformly spaced in ξ . Ion positions are extrapolated to the cell centers using a triangular shape function (CIC approach).

$\alpha + \sigma\sqrt{-\xi + \xi_n} + \beta(\xi - \xi_n) + \gamma(\xi - \xi_n)^2$ yielding $h_n = \alpha + 8(\Delta\xi)^{1/2}/15 - \beta\Delta\xi/3 + \gamma\Delta\xi^2/6$. The extrapolation error is therefore only half order in $\Delta\xi$. The three-dimensional grid has an inner boundary ($r = 1$), an outer boundary ($r = r_b$), and the axis boundaries ($\cos\theta = \pm 1$). The outer boundary is not a concern, because the plasma tends to its unperturbed condition hence the profile derivatives are small and finite ($\sigma = 0$).

The inner boundary requires more attention, in particular in the quasineutral regime where the ion density has a *physical* square root dependence [9] that needs to be resolved to more than order one half. Our solution is to average the radial velocity $\langle v_r \rangle$ at which the ions cross the boundary during a given number of previous steps (typically 40), which dividing the flux density $\Gamma_i = N\langle v_r \rangle$ known from simple particle count yields the boundary density without spacial approximation or extrapolation.

In the two-dimensional version of SCEPTIC, the axis boundary was a physical axis of symmetry, hence any moment of the distribution function could be expanded in powers of $\cos\theta$; the axis extrapolation was therefore first order accurate in $\Delta\xi$ ($\sigma = 0$). In SCEPTIC3D however, expanding a smooth function of θ about the axis

requires odd terms in $\sin \theta = \pm \sqrt{1 - (\cos \theta)^2}$ as well, implying that $\sigma \neq 0$ hence the extrapolation (III.15) is only half order accurate in $\Delta\xi$. Our solution is to average the axis density over the azimuthal angle ψ , effectively canceling the odd terms, which allows to recover first order accuracy in $\Delta\xi = \Delta \cos \theta$. Operating the extrapolation linearly in θ rather than $\cos \theta$ would give an order $\Delta\theta^2$, but because the grid is evenly spaced in $\cos \theta$ the effective accuracy would still be first order (halving $\Delta\theta$ on axis requires quadrupling the number of θ -cells).

In summary, the extrapolation is second order accurate to the inner nodes, first order accurate on axis and at the outer boundary, and non necessary on the inner boundary.

Potential gradient interpolation

When using a uniform Cartesian mesh, it is well established that in order to avoid self-forces (i.e ensure momentum conservation), the potential gradient should be pre-calculated on each cell center, and interpolated back to the ions using the same interpolation scheme as was used to perform the charge extrapolation [8]. Using the same interpolation and extrapolation schemes on a spherical mesh is however ambiguous, in particular because gradients involve position as well as derivatives:

$$\nabla_r \phi = \frac{\partial \phi}{\partial r}, \quad (\text{III.16})$$

$$\nabla_\theta \phi = \frac{1}{r} \frac{\partial \phi}{\partial \theta}, \quad (\text{III.17})$$

$$\nabla_\psi \phi = \frac{1}{r \sin \theta} \frac{\partial \phi}{\partial \psi}. \quad (\text{III.18})$$

Fortunately this thesis does not investigate plasma waves, and most ions do not undergo more than a few fly-bys around the probe. Momentum conservation is therefore easily ensured regardless of the interpolation choice, as will be confirmed in chapter VI when discussing the ion drag-force.

$\nabla_\psi \phi$ is the most straightforward term to calculate. We first linearly interpolate the potential in θ (not $\cos \theta$) and r , in order to consider the one dimensional grid of

Fig. (III-3) with $\xi = \psi$. The process for an ion located in cell i (neighborhood of ξ_i) is to calculate the potential gradient at ξ_i and on the closest cell boundary, say $\xi_{i+1/2}$:

$$\frac{\partial\phi}{\partial\xi}_{|i} = \frac{\phi_{i+1} - \phi_{i-1}}{2\Delta\xi}, \quad (\text{III.19})$$

$$\frac{\partial\phi}{\partial\xi}_{|i+1/2} = \frac{\phi_{i+1} - \phi_i}{\Delta\xi}, \quad (\text{III.20})$$

and proceed by linear interpolation of $\partial\phi/\partial\xi$ to the ion. $\nabla_\psi\phi$ is then obtained from Eq. (III.18) upon dividing by $r \sin \theta$ at the exact ion location. The calculation is second order accurate in $\Delta\xi$.

Calculation of the term $\nabla_\theta\phi$ starts similarly, by linearly interpolating the potential in ψ and r . However because the cells are equally spaced in $\cos\theta$, the finite-difference potential gradient (III.20) with $\xi = \theta$ does not correspond to the cell boundary gradient. To calculate the gradient on the axis boundary, we create shadow cells at ξ_{n+1} and ξ_0 to which we associate the potential $\phi(\xi_{n-1}, \psi + \pi)$ and $\phi(\xi_2, \psi + \pi)$. The calculation is second order accurate in $\Delta\xi$, except on axis where it is first order.

The radial term $\nabla_r\phi$ is obtained differently, in order to capture the square root potential dependence at the sheath edge appearing in the quasineutral regime. The idea is, after linearly interpolating the potential in θ and ψ , to set $\xi = \sqrt{2(r-1)}$. The potential gradient is then calculated on the left and right cell boundaries, and linearly (in ξ) interpolated back to the ion. As for the $\nabla_\theta\phi$ calculation, the cell boundary in Fig. (III-3) does therefore not correspond to the real cell boundary. In the quasineutral regime, the radial potential derivatives are calculated using

$$\frac{\partial\phi}{\partial r}_{|i-1/2} = \frac{1}{\xi} \frac{\phi_i - \phi_{i-1}}{\Delta\xi}, \quad (\text{III.21})$$

$$\frac{\partial\phi}{\partial\xi}_{|i+1/2} = \frac{1}{\xi} \frac{\phi_{i+1} - \phi_i}{\Delta\xi}, \quad (\text{III.22})$$

after creating the shadow cell at ξ_0 to which we associate the potential $2\phi(\xi_1) - \phi(\xi_2)$. The potential gradient in the quasineutral regime tends to infinity at the sheath edge (“ $r = 1$ ”) because $\partial\phi/\partial\xi$ is finite. In the finite Debye length regime however, $\partial\phi/\partial\xi$

tends to zero at the probe surface (the physical potential dependence is linear, not square-root), creating a “0/0” singularity that needs to be resolved. Therefore the potential derivatives are simply calculated by

$$\frac{\partial \phi}{\partial r}_{|i-1/2} = \frac{\phi_i - \phi_{i-1}}{\Delta r} \quad (\text{III.23})$$

$$\frac{\partial \phi}{\partial r}_{|i+1/2} = \frac{\phi_{i+1} - \phi_i}{\Delta r}, \quad (\text{III.24})$$

although the interpolation is still done linearly in ξ for consistency. The procedure is then first order accurate at the sheath edge in both the quasineutral and finite Debye length regime, and second order accurate in the rest of the domain.

The three spherical components of the acceleration are eventually transformed to Cartesian coordinates, to be used by the particle mover.

III.1.3 Orbit integration

The n_{part} particles representing ions are advanced in Cartesian coordinates using either the newly developed Cyclotronic integration scheme [37] (by default), or the standard Boris integrator [8], in the frame moving with velocity \mathbf{v}_\perp where \mathbf{E}_{cnv} vanishes. This enables us to use longer time-steps far from the probe, as the strong convective acceleration need not be resolved.

Of course, because the conducting probe shields the convective electric field out, in a frame where \mathbf{E}_{cnv} vanishes the ions see a strong electric field of the order $-\mathbf{E}_{\text{cnv}}$ within about a Debye length from the probe surface, killing the purpose of the frame change. In order to avoid this problem, as well as to increase the accuracy with which orbit-probe intersections are computed, integration is subcycled in the probe vicinity. This procedure breaks the time-reversibility of the Boris and the Cyclotronic schemes, but because no orbit is periodic or quasi-periodic we shall not be concerned about this minor effect.

III.2 Quasineutral operation

III.2.1 Boundary conditions

The total number of computational ions n_{part} in the domain is fixed, so when an ion leaves the domain (by colliding with the probe or by crossing the outer boundary) it is randomly reinjected at the outer boundary. The probability distribution of position and velocity is chosen consistent with the ions being Maxwellian with temperature $T_{i\infty}$ and drift velocity \mathbf{v}_d .

Of course the downstream region is perturbed by the probe, and the ion distribution function there is far from Maxwellian. Unless we run the code with an excessively large computational domain, plasma profiles close to the downstream outer boundary are therefore biased by our reinjection scheme. Because information can not propagate against the cross-field drift (at least on a scale longer than the average ion Larmor radius), a moderate uncertainty on the downstream potential distribution will however not affect the upstream dynamics. The saturation current will therefore be correct provided each ion collected by the probe entered the computational domain from an unperturbed plasma region. This condition is met for large enough computational domains, qualitatively:

$$r_b \gtrsim \frac{2}{M_\perp}. \quad (\text{III.25})$$

A key part of the PIC methodology is to attribute a weight to each *computational* ion, which can be seen as a measure of the inverse of the number of *physical* ions it represents. Several options are possible, in particular each weight can be fixed for the entire life-time of the particle it is attached to, or be dynamically updated at each time-step. SCEPTIC and SCEPTIC3D simulations follow the second paradigm, and at each time step each computational ion is given equal weight such that the *upstream* normalized charge density is unity.

The inner boundary in our quasineutral formulation is really the Debye sheath entrance rather than the probe surface, although geometrically the two are degenerate.

The potential at $r = 1$ is therefore still given by quasineutrality and the probe bias voltage is irrelevant. Because the potential gradient at the sheath edge has a square root singularity, it is not possible to correctly extrapolate the density there from the grid, and in Ref. [9] the sheath entrance potential was self-consistently adjusted so as to enforce the Bohm condition. In SCEPTIC3D we adopt a different approach, where the sheath entrance density (hence potential) is calculated by dividing the dimensional probe flux-density by the average radial velocity of the ions crossing the inner boundary, as discussed in paragraph III.1.2.

III.2.2 Accuracy

The code is “embarrassingly” parallelized by assigning a subset of n_{part} to each of n_{proc} processors, typically $n_{\text{proc}} = 128$ and $n_{\text{part}}/n_{\text{proc}} = 400k$. The simulation starts with uniform ion density, and runs past convergence. Code outputs such as charge-density or current densities are then averaged over the last 25% of the steps, yielding smooth solutions suitable for further postprocessing and analysis. Regardless of the number of time-steps over which the averaging is performed, we must ensure that the “raw” outputs are unaffected by the discretization of phase-space.

Due to the usage of a finite number of computational particles, the ion charge in each cell will fluctuate around its equilibrium value. Upon defining $n_{i/\text{cell}}$ as the number of particles in the considered cell, the error scales as $\delta n_{i/\text{cell}} \sim \sqrt{n_{\text{cell}}}$. This corresponds, in the quasineutral regime, to a fluctuation in cell-center potential $\delta\Phi \sim 1/\sqrt{n_{i/\text{cell}}}$ responsible for spurious scattering, hence noise in the simulation. We now propose to treat this scattering similarly to Coulomb collisions in the weak-deflection limit.

For simplicity, let us assume the background (i.e. without noise) potential distribution to be flat. Because SCEPTIC follows the Cloud In Cell approach, the electric field created by the potential fluctuation has a uniform magnitude $E \sim \delta\Phi/\Omega^{1/3}$ throughout the volume defined by the six neighboring cell centers, and zero outside; we call this volume Ω .

The flight-time of an ion passing the perturbed volume (one “collision”) with ve-

locity v is $t \sim \Omega^{1/3}/v$, which upon multiplication by the force eE yields a perpendicular deflection $\Delta v_\perp \sim eEt/m \sim e\delta\Phi/(mv)$. Provided $\Delta v_\perp \ll v$, energy conservation for the ion yields $\Delta v/v \sim e^2\delta\Phi^2/m^2v^4$. Defining the cell density n_{cell} (number of computational cells per unit volume), the ion momentum loss mean free path l due to multiple collisions with the computational cells is then easily obtained by usual integration over the collision impact parameter p : $1/l \sim n_{\text{cell}} \int (\Delta v/v) pdp$. Contrary to Coulomb collisions however, $\Delta v/v$ is not proportional to $1/p^2$, but approximately constant in the perturbed volume and zero outside.

Inner cells being the smallest, noise will first affect the region close to the probe where ions mostly have a radial motion, hence $\int pdp \sim r^2/(n_\theta n_\psi)$. Further substituting the *local* cell density $n_{\text{cell}} = n_r n_\theta n_\psi / (4\pi r^2 r_b)$ and the *local* number of computational particles per cell $n_{i/\text{cell}} \sim n_{\text{part}} r^2 / (r_b^2 n_r n_\theta n_\psi)$, the effective dimensionless computational mean-free-path at $r = r_p = 1$ scales as

$$l = \frac{n_{\text{part}} r_p^2}{n_\theta n_\psi n_r^2 r_b}. \quad (\text{III.26})$$

Figure (III-4) shows the total ion saturation current I_i to the probe as a function of $1/l$ (varied by changing the number of particles and modifying the grid), for the plasma parameters $\tau = 0.1$, $v_d = 0.5c_{s0}$, $\delta = \pi/4$, and $\beta_i = 1$. It can be seen that if we aim at noise levels of the order 1%, we need to operate with $l \gtrsim 1$; this is a rather general observation, holding not only for the selected case but for most plasma parameters. In fact the higher the ion temperature, the lower the effect of potential fluctuations.

The impression that the output does not depend on the grid coarseness when $l \gtrsim 1$ is however misleading. First we are looking at I_i , an integral quantity, hence not requiring an accurate radial resolution of the potential. Obtaining the correct angular current distribution typically requires $r_b/n_r \lesssim 0.1$. Second the chosen example is at moderate magnetization; when $\beta_i \gtrsim 2$ the presheath tends to elongate along the magnetic axis, hence accurate angular resolution is essential. Usually $n_\theta = n_\psi = 30$ proves satisfactory.

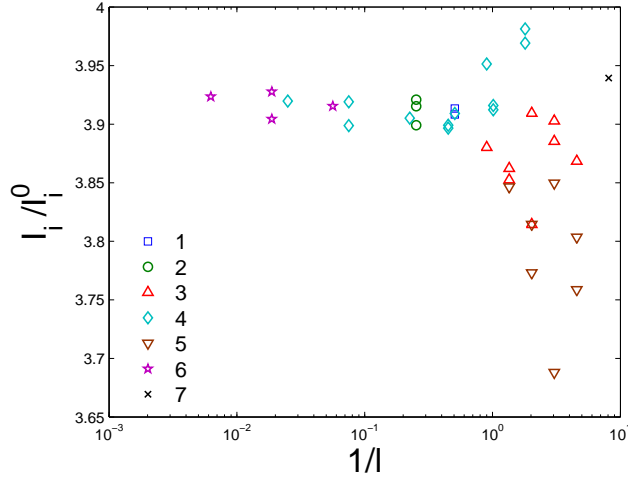


Figure III-4: Ion saturation current as a function of $1/l$. Each point corresponds to a different SCEPTIC3D run, where l is varied by changing the number of operating processors n_{proc} (400k particles per processor) and the grid. (1 \square): $n_{\text{proc}} = 512$, $r_b = 8$, $n_r = 120$, $n_{\theta,\psi} = 30$. (2 \circ): $n_{\text{proc}} = 512$, $r_b = 8$, $n_r = 120$, $n_{\theta,\psi} \leq 30$. (3 \triangle): $n_{\text{proc}} = 128$, $r_b = 8$, $n_r \geq 80$, $n_{\theta,\psi} \geq 30$. (4 \diamond): $n_{\text{proc}} = 128$, $r_b = 8$, $n_r \geq 80$, $n_{\theta,\psi} \leq 30$. (5 ∇): $n_{\text{proc}} = 128$, $r_b = 12$, $n_r \geq 80$, $n_{\theta,\psi} \geq 30$. (6 \star): $n_{\text{proc}} = 128$, $r_b = 8$, $n_r = 40$, $n_{\theta,\psi} \leq 15$. (7 \times): $n_{\text{proc}} = 32$, $r_b = 8$, $n_r = 80$, $n_{\theta,\psi} = 30$.

For production runs, we therefore set $n_\theta = n_\psi = 30$ and $n_r \simeq 10r_b$, the domain radius r_b being chosen according to the plasma drift velocity to oversatisfy Eq. (III.25). The minimal number of particles such that noise levels be of no concern is then $n_{\text{part}} \sim n_\theta n_\psi n_r^2 r_b$ at $\tau = 0.1$ ($l \sim 1$), and we allow without further optimization $n_{\text{part}} \sim 0.5 n_\theta n_\psi n_r^2 r_b$ at higher ion temperature.

In our quasineutral simulations, the Debye length is much smaller than any computational cell.

III.2.3 Axisymmetry resolution

SCEPTIC3D has the particularity of being built on a non isotropic grid with uniform $\cos \theta$ spacing. This choice was motivated by the convenience to have, at a given radial position, a computational cell volume independent of θ . The drawback of course is that extrapolating the particle positions to the grid, as well as interpolating the potential gradient back to the particles, requires special care to ensure second

order accuracy. In fact only first order accuracy is reached on axis because when n_θ is doubled, $\Delta\theta$ is only divided by $\sqrt{2}$.

A stringent test of the grid implementation consists in checking that an axisymmetric case yields the same solution regardless of the physical axis orientation. Figure (III-5) shows the average ion saturation flux-density Γ_{is} , as well as the average sheath entrance potential Φ_s , for the case $\tau = 0.1$, $v_d = c_{s0}$, $\beta_i = 0$ (magnetic-free). The solution is plotted as a function of the position projected on the drift axis ($\cos \chi$), which is here the physical symmetry axis. It can be seen that the solutions at different drift angles are almost indistinguishable, except perhaps around $\cos \chi \gtrsim 0.7$ on the Φ_s plot, which gives us strong confidence that the code performs properly.

(a) Ion charge-flux

(b) Sheath entrance potential

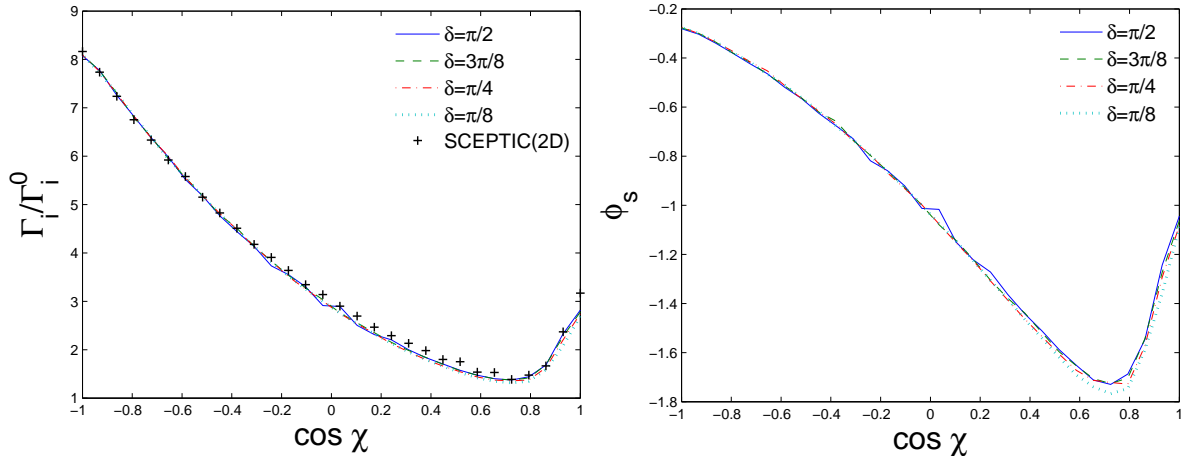


Figure III-5: (a) Ion saturation flux and (b) sheath entrance potential as a function of the position projected on the drift axis ($\cos \chi$), for the case $\tau = 0.1$, $v_d = c_{s0}$, $\beta_i = 0$ and a selection of δ s. The points labeled “SCEPTIC(2D)” correspond to the solution from the appendix in Ref. [9]. SCEPTIC3D runs have been performed with $r_b = 8$, $n_r = 120$, $n_\theta = n_\psi = 30$, and $n_{\text{part}} = 51.2M$.

Figure (III-5a) also shows the ion flux calculated by the two-dimensional code SCEPTIC(2D), from the appendix in Ref. [9]. The excellent agreement between the 2D and 3D calculations, despite drastic evolutions between the two code versions, is a further benchmark of SCEPTIC3D. More important, it suggests that there is no spontaneous breaking of symmetry in axisymmetric cases, which could jeopardize the

validity of prior 2D treatments.

The example shown here has been selected as one of the most computationally challenging, due to the collection “bump” in the downstream region arising from ion focussing. More details on this feature will be given in paragraph IV.2.2.

III.3 Finite Debye length operation

III.3.1 Parallelized Poisson solver

Inner boundary condition

Upon normalizing ∇ to $1/R_p$, Poisson equation (III.9) accounting for the Boltzmann electron distribution can be rewritten as

$$\nabla^2 \phi = \frac{\exp(\phi) - n}{\lambda_{De}^2}, \quad (\text{III.27})$$

where we refer to the ion charge density as “ n ” rather than “ n_i ”, to avoid possible confusions with the soon to be defined radial index i . In the absence of ion response Eq. (III.27) reduces to the well-known Poisson-Boltzmann equation, but we here need to include both the ion and electron charge distributions. Solution of Eq. (III.27) requires two boundary conditions.

The inner condition is straightforwardly imposed by the probe potential distribution, that we recall can be decomposed in a monopole term Φ_p and a dipole term $|\mathbf{E}_{\text{cnv}}R_p|$ oriented in the \mathbf{e}_x direction¹ (Eq. (III.12)).

Outer boundary condition

In the unmagnetized regime, Hutchinson [10] obtained the outer boundary condition on the potential from an approximate analytic solution of the shielding equations for the region beyond the computational boundary. The method is based upon assum-

¹The mathematical definition of the potential dipole moment would be $\mathbf{p}_{\text{cnv}} = - \int_{-R_p}^{R_p} E_{\text{cnv}} x^2 dx \mathbf{e}_x / R_p = (2/3) |E_{\text{cnv}} R_p| R_p \mathbf{e}_x$. In this thesis we simply refer to the “dipole term” as the potential $[E_{\text{cnv}} R_p]$.

ing that the computational domain is large enough for (a) the outer potential to be spherically symmetric regardless of the plasma drift velocity, (b) the outer dimensionless ion charge-density to be given by $n = 1 - \phi/\tau - a\lambda_{De}^2/r^2$, where the term “ $1 - \phi/\tau$ ” corresponds to the untrapped density in a 3D potential well and “ $-a/r^2$ ” to the *a priori unknown* ion depletion due to probe collection, and (c) the outer potential to be small enough to warrant linearization of the Boltzmann electron density. Equation (III.27) then becomes in the outer region:

$$\nabla^2 \phi - \frac{\phi}{\lambda_D^2} = \frac{a}{r^2}, \quad (\text{III.28})$$

where $\lambda_D = (\lambda_{De}^{-2} + \lambda_{Di}^{-2})^{-1/2}$ is the linearized Debye length. The solution of Eq. (III.28) can be cast in the form [10]

$$\frac{\partial \phi}{\partial r} = - \left(\frac{1}{\lambda_D} + \frac{1}{r} \right) \phi - \frac{a}{r} \exp \left(\frac{r}{\lambda_D} \right) E_1 \left(\frac{r}{\lambda_D} \right), \quad (\text{III.29})$$

which is adopted as Robin (“Dirichlet+Newmann”) boundary condition on the potential at the outer boundary r_b . Here, E_1 is the exponential integral function defined by $E_1(x) = \int_x^\infty \exp(-s^2)/s ds$. Because the outer potential distribution is not exactly spherically symmetric, Eq. (III.29) is imposed to each outer computational cell-center with a *local* value of “ a ” self-consistently calculated by SCEPTIC as

$$a(\theta, \psi) = \frac{r_b^2}{\lambda_{De}^2} \left[1 - \frac{\phi(r_b, \theta, \psi)}{\tau} - n(r_b, \theta, \psi) \right]. \quad (\text{III.30})$$

In magnetized plasmas, Eq. (III.28) is incorrect because (a) the potential distribution cannot be approximated as spherically symmetric, except at infinity where $\phi = 0$, and (b) the ion density cannot be cast in the form “ $n = 1 - \phi/\tau - a\lambda_{De}^2/r^2$ ”. Unless otherwise specified, we nevertheless adopt the same outer boundary condition (III.29) in SCEPTIC3D regardless of the magnetic field. This choice is of course subject to discussion, but can be motivated as follows. As explained in paragraph III.2.1, the ions are reinjected from an unperturbed drifting Maxwellian distribution, therefore the computational domain needs to be large enough for the plasma to be unperturbed

in the *upstream* region. This requirement involves $r_b \gg \lambda_D$, hence Eq. (III.28) becomes $\phi \simeq -a\lambda_D^2/r^2$, which upon substituting a from Eq. (III.30) yields $1+\phi = n$. In other words, for typical SCEPTIC3D magnetized runs, using the *unmagnetized* outer boundary condition amounts to imposing quasineutrality ($n = 1 + \phi \sim \exp \phi = n_e$), which is physically sound.

Discretization

Solving a discretized formulation of the non linear equation (III.27) would require an iterative process such as a Newton inversion, each Newton step itself involving a (presumably iterative) matrix inversion.

To avoid this complication, we assume that the potential changes only slightly between two PIC time-steps. If ϕ^* is the known potential distribution at time-step t and ϕ the unknown distribution at time-step $t+1$, it is then appropriate to linearize Eq. (III.27) about ϕ^* :

$$\nabla^2 \phi = \frac{\exp(\phi^*) [1 + (\phi - \phi^*)] - n}{\lambda_{De}^2}. \quad (\text{III.31})$$

Our goal is now to find a linear operator A (differential operator and Newmann part of the outer boundary condition), a Dirichlet boundary condition vector ω , and an effective source vector σ such that

$$A\phi + \omega = \sigma. \quad (\text{III.32})$$

Equation (III.31) can be seen as a conservation equation, where “ $-\nabla\phi$ ” is the flux and “ $\{\exp(\phi^*) [1 + (\phi - \phi^*)] - n\} / \lambda_{De}^2$ ” the source. We therefore discretize it by the method of finite volumes, according to which we look for a potential distribution ϕ such that the integral equality

$$\int_{Cell \ boundary} \nabla\phi \cdot d\mathbf{S} = \frac{1}{\lambda_{De}^2} \int_{Cell} \{\exp(\phi^*) [1 + (\phi - \phi^*)] - n\} d\Omega \quad (\text{III.33})$$

is verified in each computational cell.

To grid accuracy, i.e. second order except on axis where only first order is achieved, the charge density at each cell center is equal to the average cell density. To be precise, only first order accuracy would be achieved on the first and last radial cells as well, but this is not a concern because potential boundary conditions will be applied there. Labeling the cell center positions by r_i , $\cos \theta_j$ and ψ_k , the cell-integrated linearized charge density for $i \in [2 : n_r - 1]$, $j \in [2 : n_\theta - 1]$ and $k \in [1 : n_\psi]$ is

$$Q_{i,j,k} = \left\{ \exp(\phi_{i,j,k}^*) [1 + (\phi_{i,j,k} - \phi_{i,j,k}^*)] - n_{i,j,k} \right\} r_{i,j,k}^2 \Delta r \Delta \cos \theta \Delta \psi. \quad (\text{III.34})$$

We then discretize the left hand side of Eq. (III.33) with the assumption that $\nabla \phi$ is constant on each of the 6 cell boundaries:

$$\begin{aligned} \int_{i,j,k} \nabla \phi \cdot d\mathbf{S} &= \left(\frac{\partial \phi}{\partial r}_{|i+1/2,j,k} r_{i+1/2}^2 - \frac{\partial \phi}{\partial r}_{|i-1/2,j,k} r_{i-1/2}^2 \right) \Delta \cos \theta \Delta \psi \\ &+ \frac{1}{r_i} \left(\frac{\partial \phi}{\partial \theta}_{|i,j+1/2,k} \sin \theta_{j+1/2} - \frac{\partial \phi}{\partial \theta}_{|i,j-1/2,k} \sin \theta_{j-1/2} \right) r_i \Delta r \Delta \psi \\ &+ \frac{1}{r_i \sin \theta_j} \left(\frac{\partial \phi}{\partial \psi}_{|i,j,k+1/2} - \frac{\partial \phi}{\partial \psi}_{|i,j,k-1/2} \right) r_i \Delta r \Delta \theta_j. \end{aligned} \quad (\text{III.35})$$

The potential derivatives are straightforwardly obtained by finite differences, yielding a centered method with 7-point stencil. Using the second order approximation $\Delta \cos \theta = -\sin \theta \Delta \theta$, the previous expression can be rewritten in the more convenient form:

$$\begin{aligned} \int_{i,j,k} \nabla \phi \cdot d\mathbf{S} &= \left(\frac{\partial \phi}{\partial r}_{|i+1/2,j,k} r_{i+1/2}^2 - \frac{\partial \phi}{\partial r}_{|i-1/2,j,k} r_{i-1/2}^2 \right) \Delta \cos \theta \Delta \psi \\ &- \left(\frac{\partial \phi}{\partial \cos \theta}_{|i,j+1/2,k} \sin \theta_{j+1/2}^2 - \frac{\partial \phi}{\partial \cos \theta}_{|i,j-1/2,k} \sin \theta_{j-1/2}^2 \right) \Delta r \Delta \psi \\ &- \frac{1}{\sin \theta_j^2} \left(\frac{\partial \phi}{\partial \psi}_{|i,j,k+1/2} - \frac{\partial \phi}{\partial \psi}_{|i,j,k-1/2} \right) \Delta r \Delta \cos \theta. \end{aligned} \quad (\text{III.36})$$

We therefore define the linear operator A in Eq. (III.32) such that it operates on

ϕ as follows for $i \in [2 : n_r - 1]$, $j \in [2 : n_\theta - 1]$ and $k \in [1 : n_\psi]$:

$$(A\phi)_{i,j,k} = a_i \phi_{i+1,j,k} - b_i \phi_{i-1,j,k} + c_{i,j} \phi_{i,j+1,k} - d_{i,j} \phi_{i,j-1,k} + e_{i,j} (\phi_{i,j,k+1} - \phi_{i,j,k-1}) - [f_{i,j} + \exp(\phi_{i,j,k}^*)] \phi_{i,j,k}, \quad (\text{III.37})$$

with

$$\begin{aligned} a_i &= \lambda_{De}^2 \frac{r_{i+1/2}^2}{r_i^2 \Delta r^2}, & b_i &= \lambda_{De}^2 \frac{r_{i-1/2}^2}{r_i^2 \Delta r^2}, \\ c_{i,j} &= \lambda_{De}^2 \frac{\sin \theta_{j+1/2}^2}{r_i^2 (\Delta \cos \theta)^2}, & d_{i,j} &= \lambda_{De}^2 \frac{\sin \theta_{j-1/2}^2}{r_i^2 (\Delta \cos \theta)^2}, \\ e_{i,j} &= \lambda_{De}^2 \frac{1}{r_i^2 \sin \theta_j^2 \Delta \psi^2}, & f_{i,j} &= a_i + b_i + c_{i,j} + d_{i,j} + 2e_{i,j}. \end{aligned} \quad (\text{III.38})$$

The effective source vector is

$$\sigma_{i,j,k} = \exp(\phi_{i,j,k}^*) [1 - \phi_{i,j,k}^*] - n_{i,j,k}, \quad (\text{III.39})$$

and the Dirichlet boundary condition vector is

$$\omega_{2,j,k} = b_2 \phi_{1,j,k}, \quad \text{Inner BC,} \quad (\text{III.40})$$

$$\omega_{n_r,j,k} = a_{n_r} g_{j,k}, \quad \text{Outer BD,} \quad (\text{III.41})$$

$$\omega_{i,j,k} = 0, \quad \text{Otherwise,} \quad (\text{III.42})$$

where the inner boundary condition is Dirichlet (imposed probe potential), and the outer boundary condition is Robin (i.e. a combination of potential and potential gradient is specified) with arbitrary coefficient g .

On axis, i.e. when $j = 1$ or $j = n_\theta$, computational cells are prism-shaped rather than cubic, and their volume is (to 2^d order) $1/2r_i^2 \Delta r \Delta \cos \theta \Delta \psi$. a_i and b_i are unaf-

fected, but the coefficients $c_{i,j}$, $d_{i,j}$, and $e_{i,j}$ become

$$\begin{aligned} c_{i,1} &= 2\lambda_{De}^2 \frac{\sin \theta_{1+1/2}^2}{r_i^2 (\Delta \cos \theta)^2}, & c_{i,n_\theta} &= 0, \\ d_{i,1} &= 0, & d_{i,n_\theta} &= 2\lambda_{De}^2 \frac{\sin \theta_{n_\theta-1/2}^2}{r_i^2 (\Delta \cos \theta)^2}, \\ e_{i,1} &= \lambda_{De}^2 \frac{1}{r_i^2 \sin \theta_{1+1/4}^2 \Delta \psi^2}, & e_{i,n_\theta} &= \lambda_{De}^2 \frac{1}{r_i^2 \sin \theta_{n_\theta-1/4}^2 \Delta \psi^2}. \end{aligned} \quad (\text{III.43})$$

Minimum residual algorithm implementation

Our purpose is now to solve the linear equation (III.32) for ϕ , that we rewrite

$$A\phi = y \quad (\text{III.44})$$

with $y = \sigma - \omega$ for compactness. Writing A in matrix form involves $(n_r n_\theta n_\psi)^2$ terms, it is therefore not reasonable to directly invert it. Instead we take advantage of A being sparse, and look for an iterative method where only the action of A is required. A being symmetric but not definite positive, we opt for a variant of the well known *conjugate gradient* algorithm called the *minimum residual* method.

The algorithm implementation, completed by Jacobi preconditioning, is mostly adapted from chapter 2.7 in Ref. [38]. The idea is to start with an initial guess for the potential, typically $\phi^0 = \phi^*$ (potential at the previous PIC time-step), and iteratively update ϕ^l along search directions p^l with minimizer β^l : $\phi^{l+1} = \phi^l + \beta^l p^l$.

Finding the search directions and minimizers only requires matrix multiplications by A , which is an easily parallelizable step.

III.3.2 Electrostatic Maxwell stress tensor

Code implementation

The potential distribution around the probe in the presence of plasma flow or external fields is anisotropic, causing a non-zero electrostatic stress on the probe. Writing the

electrostatic Maxwell stress tensor as

$$\bar{\sigma}_E = \epsilon_0 \left(\mathbf{E} \mathbf{E} - \frac{1}{2} E^2 \bar{\delta} \right), \quad (\text{III.45})$$

the differential force on a portion of probe surface $d\mathbf{S}$ with normal \mathbf{e}_r is given by

$$d\mathbf{F} = \bar{\sigma}_E \cdot \mathbf{e}_r = \epsilon_0 \left[\frac{1}{2} (+E_r^2 - E_\theta^2 - E_\psi^2) \mathbf{e}_r + E_r E_\theta \mathbf{e}_\theta + E_r E_\psi \mathbf{e}_\psi \right] d\mathbf{S}, \quad (\text{III.46})$$

where E_r , E_θ and E_ψ are the radial, polar and azimuthal electric field components at the considered position. Cartesian elementary forces at (θ, ψ) are therefore

$$dF_z = \epsilon_0 \left[\frac{1}{2} (+E_r^2 - E_\theta^2 - E_\psi^2) \cos \theta - E_r E_\theta \sin \theta \right] dS, \quad (\text{III.47})$$

$$dF_x = \epsilon_0 \left[\frac{1}{2} (+E_r^2 - E_\theta^2 - E_\psi^2) \sin \theta \cos \psi + E_r E_\theta \cos \theta \cos \psi - E_r E_\psi \sin \psi \right] dS, \quad (\text{III.48})$$

$$dF_y = \epsilon_0 \left[\frac{1}{2} (+E_r^2 - E_\theta^2 - E_\psi^2) \sin \theta \sin \psi + E_r E_\theta \cos \theta \cos \psi + E_r E_\psi \cos \psi \right] dS. \quad (\text{III.49})$$

Equations (III.47, III.48, III.49) are calculated at each PIC time-step by differentiating the potential distribution calculated by SCEPTIC3D at $r = 1$ on each computational cell center, yielding the total stress

$$\mathbf{F}_E = \int_S d\mathbf{F}. \quad (\text{III.50})$$

SCEPTIC3D only considers the self-consistent electric field $-\nabla\Phi$ to compute the Maxwell stress, since the force directly arising from the external convective field \mathbf{E}_{cnv} can be obtained independently from the relation

$$\mathbf{F}_Q = Q \mathbf{E}_{\text{cnv}}, \quad (\text{III.51})$$

the total probe charge being $Q = C\Phi_p$ where C is the probe capacitance

$$C = \epsilon_0 \frac{1}{\Phi_p} \int_S E_r d\mathbf{S}. \quad (\text{III.52})$$

Linearized Poisson-Boltzmann shielding

In order to benchmark both the Poisson solver and the Maxwell stress tensor integration, we need a regime where the potential distribution can be calculated in a reasonably simple way.

Predicting the ion density distribution analytically is not as simple as obtaining the electron Boltzmann factor, hence we solve Poisson equation (III.9) by neglecting the ion response. Furthermore we limit ourselves to situations where $\Lambda_{De} \gg R_p$, implying that the potential variation close to the probe is governed by the electron density at a distance where it is almost unperturbed. Equation (A.2) can therefore be linearized about space potential $\Phi_0 = 0$.

Equation (III.9) expressed in spherical coordinates

$$\nabla^2 \phi = \frac{1}{R^2} \frac{\partial}{\partial R} \left(R^2 \frac{\partial \phi}{\partial R} \right) + \frac{1}{R^2 \sin \theta} \frac{\partial}{\partial \theta} \left(\sin \theta \frac{\partial \phi}{\partial \theta} \right) + \frac{1}{R^2 \sin^2 \theta} \frac{\partial^2 \phi}{\partial \psi^2} = \frac{\phi}{\Lambda_{De}^2} \quad (\text{III.53})$$

can be solved by separation of variables, upon defining $\phi(R, \theta, \psi) = \Xi(R)Y_\theta(\theta)Y_\psi(\psi)$.

The angular potential dependence is then given by the Legendre polynomials $Y_\theta(\theta)Y_\psi(\psi) = P_l^m(\theta, \psi)$, with l positive integer and $m \in [-l : l]$, and the radial dependence by the solution of

$$\frac{1}{\Xi} \frac{\partial}{\partial R} \left(R^2 \frac{\partial \Xi}{\partial R} \right) - \frac{R}{\Lambda_{De}^2} = l(l+1), \quad (\text{III.54})$$

which can be expanded in modified Bessel functions:

$$\Xi_l(R) = \frac{1}{\sqrt{R}} \left[A_l I_{l+1/2} \left(\frac{R}{\Lambda_{De}} \right) + B_l K_{l+1/2} \left(\frac{R}{\Lambda_{De}} \right) \right]. \quad (\text{III.55})$$

The solution of Eq. (III.53) satisfying the inner boundary condition Eq. (III.12)

and decaying at infinity is

$$\Phi = \left[\Phi_p \frac{R_p}{R} + [E_{\text{cnv}} R_p] \left(\frac{R_p}{R} \right)^2 \frac{R + \Lambda_{De}}{R_p + \Lambda_{De}} \sin \theta \cos \psi \right] \exp \left(-\frac{R - R_p}{\Lambda_{De}} \right), \quad (\text{III.56})$$

showing that the perturbed electrostatic potential distribution has a dipole term in addition to the well-known Debye-Hückel potential

$$\Phi(R) = \Phi_p \frac{R_p}{R} \exp \left(-\frac{R - R_p}{\Lambda_{De}} \right). \quad (\text{III.57})$$

The probe monopole and dipole are equally shielded by the Boltzmann electrons (exponential factor $\propto \exp(-R/\Lambda_{De})$), we must therefore account for both. In particular, treatments where the potential distribution is approximated as spherically symmetric will not be possible in the presence of “ $\mathbf{E} \times \mathbf{B}$ ” drifts.

Linearization of the electron density is not justified when $\Lambda_{De} \lesssim R_p$, in which case the right-hand-side of Eq. (III.53) should account for the full exponential term $(\exp \phi - 1)/\Lambda_{De}$ and no analytic solution exists. More development on this question is pointless since the ion response has been neglected in the first place.

The sphere-integrated electrostatic force (Eq. (III.50)) on the probe is then

$$\mathbf{F}_E = \frac{4}{3} \pi \epsilon_0 \frac{R_p^2}{\Lambda_{De}^2} R_p \Phi_p \mathbf{E}_{\text{cnv}}, \quad (\text{III.58})$$

The probe capacitance (Eq. (III.52)) is

$$C = 4\pi \epsilon_0 \left(1 + \frac{R_p}{\Lambda_{De}} \right) R_p, \quad (\text{III.59})$$

yielding the external force (Eq. (III.51))

$$\mathbf{F}_Q = 4\pi \epsilon_0 \left(1 + \frac{R_p}{\Lambda_{De}} \right) R_p \Phi_p \mathbf{E}_{\text{cnv}}. \quad (\text{III.60})$$

Daugherty and coauthors [39] performed very similar calculations, when considering the electrostatic force on an isolated particulate in a magnetic-free low-pressure

(i.e. collisional) discharge, in the presence of an ion drift induced by a parallel electric field whose role is to compensate ion-neutral friction. Although the physical conditions are different, the final formal expression for the forces is the same (Eq. (13) in Ref. [39] corresponds to $\mathbf{F}_E + \mathbf{F}_Q$ in our treatment).

Code Benchmark

The Poisson solver accounts for the full exponential term in the electron density, while the analytic solution (III.56) has been derived with a linearized electron density. This analytic potential distribution should therefore be reproduced by SCEPTIC3D provided we bypass the charge assign subroutine, and artificially impose an ion distribution $n_i = \exp \phi - \phi$. Of course the Poisson solver is not implicit in n_i , while this proposed benchmark takes n_i to be function of ϕ . It is therefore necessary, just for this benchmark, to iterate the Poisson solver step a few times up to convergence.

Figure (III-6) shows, in log-space, how the relative difference between the probe charge calculated by SCEPTIC3D and the analytic solution $C\Phi_p$ (where C is given by Eq. (III.52)) evolves upon refining the mesh. It can be seen that the fractional error ($Err = 0.5 |(Q_{th} - Q_{SC3D}) / (Q_{th} + Q_{SC3D})|$) is second order in the number of radial cells, which confirms the second-order accuracy of both the Poisson solver and the probe surface integration of the radial electric field. The error is almost independent of the number of angular cells, since the charge does not require calculations of E_θ or E_ψ .

Figure (III-7) shows the relative error on the probe-integrated Maxwell stress tensor, for which calculations of E_θ or E_ψ at the probe surface are necessary. Figure (III-7a) shows that provided the number of angular cells is large enough (here $n_\theta = n_\psi = 35$), the accuracy in n_r is second order as expected. Figure (III-7b) shows the rather surprising result that for high enough a radial resolution, the accuracy in $n_{\theta,\psi}$ appears to be third order. We do not really know how to explain this fact.

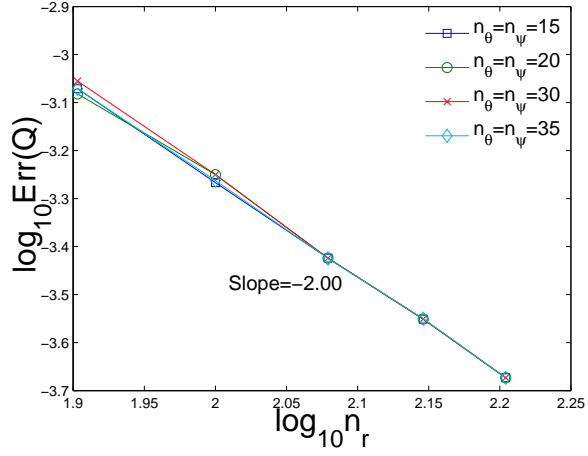


Figure III-6: Relative error on the probe charge computed by SCEPTIC3D in the “artificial” linear Poisson-Boltzmann regime, with $r_b = 6$, $\lambda_{De} = 0.5$, $|\mathbf{E}_{cnv}R_p| = T_e/e$.

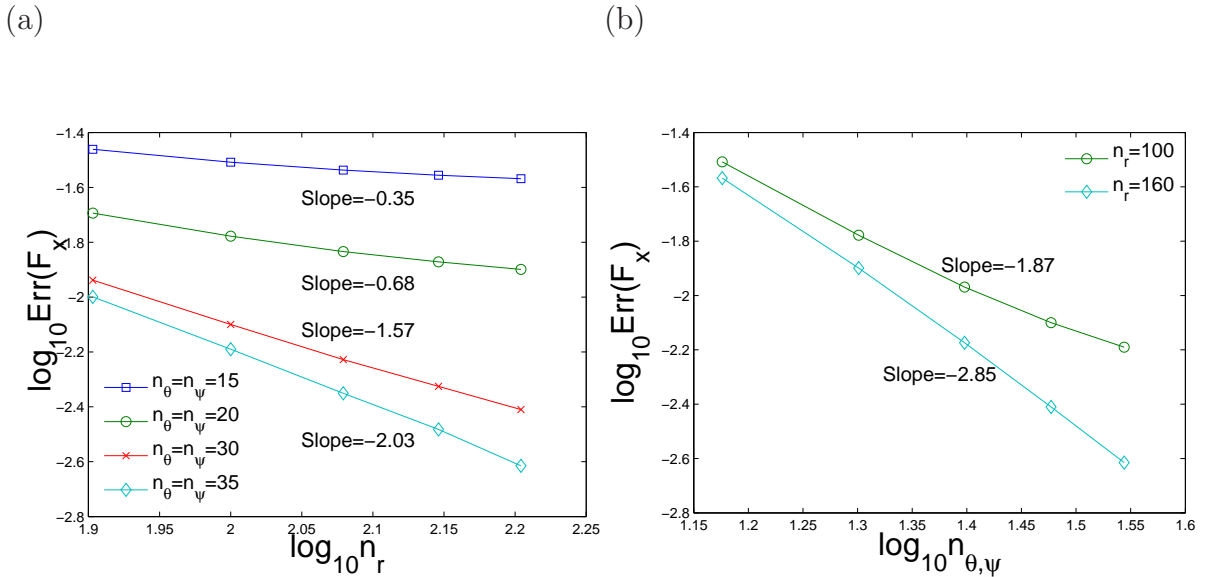


Figure III-7: Relative error on the probe-integrated Maxwell stress tensor computed by SCEPTIC3D in the “artificial” linear Poisson-Boltzmann regime, with $r_b = 6$, $\lambda_{De} = 0.5$, $|\mathbf{E}_{cnv}R_p| = T_e/e$. (a) Fixed angular resolutions, and (b) Fixed radial resolution.

III.3.3 Magnetostatic Maxwell stress tensor

Our treatment is purely electrostatic, i.e. we only consider the background magnetic field when advancing the ions. Those ions, the plasma electrons as well as the electrons moving in the conducting sphere, nevertheless carry currents inducing a first order correction to the background magnetic field.

Fortunately we do not need to solve Ampere's equation to obtain the resulting stress. Using the notation $\mathbf{B} = B_0 \mathbf{e}_z + \delta\mathbf{B}$, where $\delta B \ll B_0$, the magnetostatic Maxwell stress tensor

$$\bar{\sigma}_B = \frac{1}{\mu_0} \left(\mathbf{B}\mathbf{B} - \frac{1}{2} B^2 \bar{\delta} \right) \quad (\text{III.61})$$

writes to first order in δB :

$$\bar{\sigma}_B = \frac{1}{2\mu_0} \begin{pmatrix} -B_0^2 & 0 & 0 \\ 0 & -B_0^2 & 0 \\ 0 & 0 & +B_0^2 \end{pmatrix} + \frac{B_0}{\mu_0} \begin{pmatrix} -\delta B_z & 0 & \delta B_x \\ 0 & -\delta B_z & \delta B_y \\ \delta B_x & \delta B_y & \delta B_z \end{pmatrix}. \quad (\text{III.62})$$

Using Gauss law $\mathbf{F}_M = \int \bar{\sigma}_B d\mathbf{S} = \int \nabla \cdot \bar{\sigma}_B d\Omega$ and taking advantage of $\nabla \cdot \delta\mathbf{B} = 0$, we can write

$$\mathbf{F}_M = \frac{B_0}{\mu_0} \int \begin{pmatrix} -\frac{\partial \delta B_z}{\partial x} + \frac{\partial \delta B_x}{\partial z} \\ -\frac{\partial \delta B_z}{\partial y} + \frac{\partial \delta B_y}{\partial z} \\ 0 \end{pmatrix} d\Omega = \int \frac{\nabla \times \delta\mathbf{B}}{\mu_0} \times \mathbf{B}_0 d\Omega. \quad (\text{III.63})$$

If we define the net current density in the probe by $\mathbf{j} = \nabla \times \delta\mathbf{B}/\mu_0$, we see from Eq. (III.63) that the magnetic stress on the probe surface is merely the usual Lorentz force integrated over its volume, that we rewrite to the only relevant order as

$$\mathbf{F}_j = \left(\int_{Sphere} \mathbf{j} d\Omega \right) \times \mathbf{B}. \quad (\text{III.64})$$

Chapter IV

Spheres in zero Debye length, arbitrarily magnetized plasmas

IV.1 Plasma profiles

IV.1.1 Infinite ion magnetization

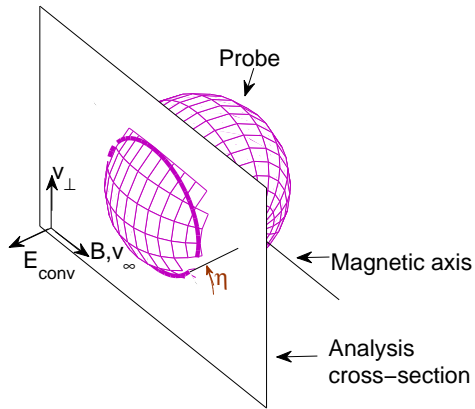
Because flow and magnetic field are not aligned, plasma profiles are inherently three-dimensional unless β_i is large enough for the flow to be constrained in planes perpendicular to the convective electric field, as illustrated in Fig. (IV-1). Here and in the rest of this thesis, the ion magnetization is defined as the ratio of the probe radius to the mean ion Larmor radius at infinity $\beta_i = R_p/R_L$:

$$\beta_i = ZeBR_p \left(\frac{2}{\pi m T_{i\infty}} \right)^{1/2}. \quad (\text{IV.1})$$

Density

Figure (IV-2) shows a selection of density contour-plots computed by SCEPTIC3D in the $\{0, \mathbf{e}_y, \mathbf{e}_z\}$ -plane for $\beta_i = 20$, in other words an average ion Larmor radius equal to a twentieth of probe radius. In each case the upstream region is clearly unperturbed, and the fluid stream-lines indicate that the collection flow tube originates from the

(a) Three-dimensional view



(b) Two-dimensional cross-section

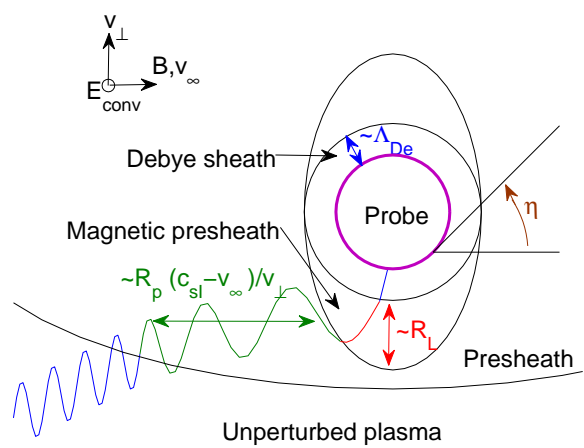


Figure IV-1: (a) Geometry of the spherical Mach probe problem in the $\Lambda_{De} \ll R_L \ll R_p$ scaling, considering a purely convective drift. (b) A “typical” collected ion starts in the upstream unperturbed plasma, drifting with cross-field velocity v_\perp . It first sees the probe when entering the presheath, where it is accelerated along \mathbf{B} over a length $\sim R_p (c_{sI} - v_\infty) / v_\perp$ (for subsonic flows) while still drifting in the cross-field direction. This one-dimensional dynamics breaks in the magnetic presheath as the ion accelerates radially towards the non neutral Debye sheath.

unperturbed region. Of course kinetic effects cause individual ions to move across the stream-lines, but intuitively the computational domain is large enough for the saturation current to be accurately computed. The simulation with $\delta = \pi/2$ shown in Fig. (IV-2b) allows easy comparison with the magnetic-free case, which has rotational symmetry about the drift axis. Because magnetized ion motion is constrained along the field lines, the downstream depleted region can only be replenished one-dimensionally and therefore extends much further than in the magnetic-free regime. The same observation was made in the free-flight regime in paragraph II.6.2.

The density contours can be compared directly with the independent one-dimensional calculations of chapter II, valid in the probe magnetic shadow defined by $x^2 + y^2 \leq 1$ when $\beta_i \gg 1$. It was shown that the plasma density only depends on the angle η , defined in Fig. (IV-1) as the angle between magnetic field and probe tangent in the plane of field and drift.

When $\tau \lesssim 0.1$, the isothermal fluid treatment of Ref. [15] according to which

$$n = \min \{1, \exp [-1 - (M_\infty - M_\perp \cot \eta)]\} \quad (\text{IV.2})$$

rigorously applies. A semi-analytic kinetic treatment such as in chapter II is required when the ion temperature is higher, although Eq. (IV.2) remains a good approximation; recall that Mach numbers are normalized to c_{sI} (Eq. (II.20)). Figure (IV-3) compares SCEPTIC3D profiles with those one-dimensional calculations when $\beta_i = 20$ and $\delta = \pi/2$, for (a) $\tau = 0.1$, $v_d = 0.5c_{s0}$ and (b) $\tau = 1$, $v_d = c_{s0}$. It can be seen that the profiles agree extremely well (less than 1% error on the isodensity lines angles), thus providing a second successful benchmark of SCEPTIC3D. Contour-lines close behind the probe, but this effect is not captured by the 1D treatments.

Careful examination of Fig. (IV-3) shows that there is a residual region on the probe leading edge where the one-dimensional calculations overestimate the density. This is due to an essential difference between the two approaches. SCEPTIC3D assumes the Debye sheath to be infinitesimally thin, but fully resolves the magnetic presheath where the ion Larmor motion is broken. Ref. [15] and chapter II on the

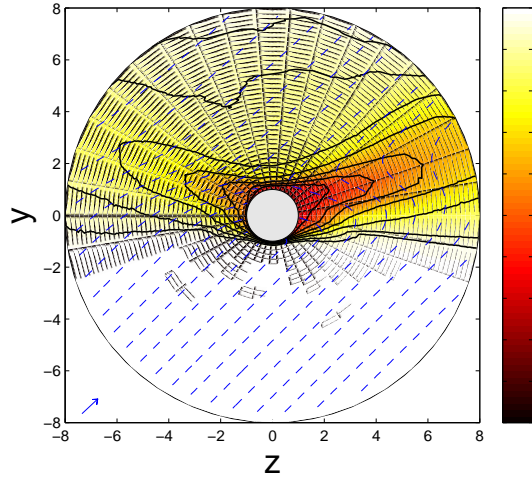
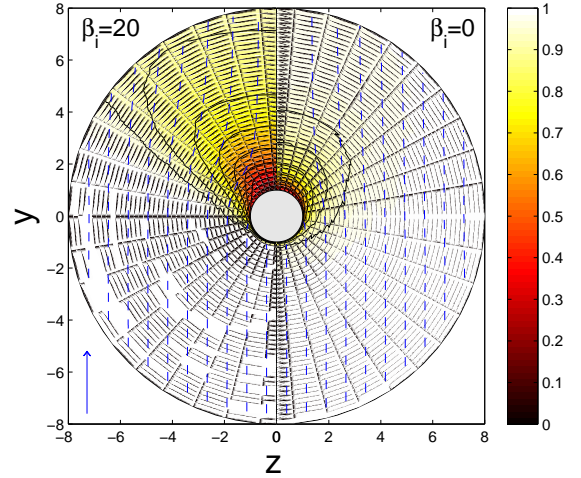
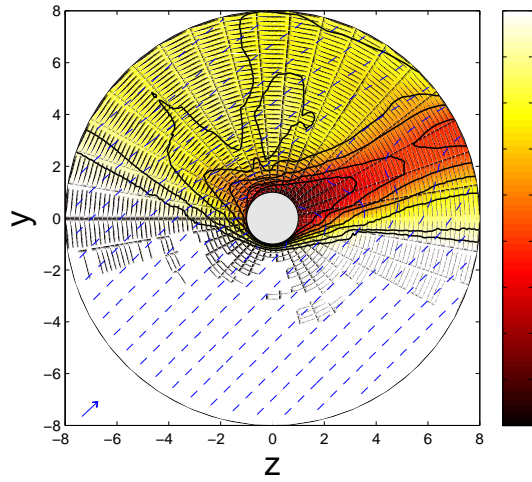
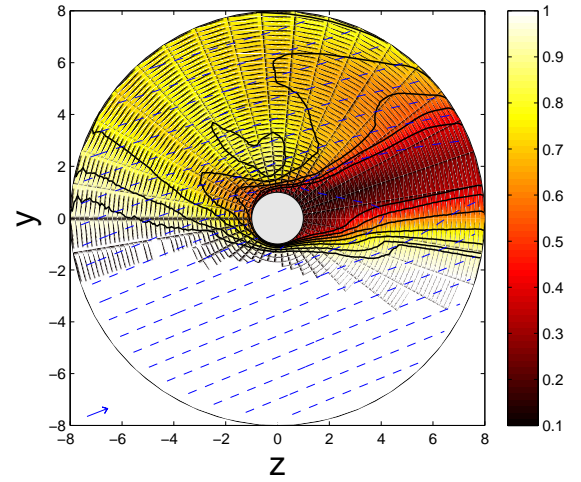
(a) $\tau = 1$, $v_d = 0.5c_{s0}$, $\delta = \pi/4$ (b) $\tau = 1$, $v_d = 1.5c_{s0}$, $\delta = \pi/2$ (c) $\tau = 0.1$, $v_d = 0.5c_{s0}$, $\delta = \pi/4$ (d) $\tau = 0.1$, $v_d = 0.5c_{s0}$, $\delta = \pi/8$ 

Figure IV-2: Selection of charge-density contour-plots in the $\{0, \mathbf{e}_y, \mathbf{e}_z\}$ -plane, with strongly magnetized ions $\beta_i = 20$ (except in (b) where a comparison with the magnetic-free regime is provided). Iso-density contours for $n = 0.4, 0.5, 0.6, 0.7, 0.8, 0.9, 0.95$ are full black, while fluid stream lines are dashed blue. The external velocity is indicated by a blue arrow on the figures' lower left corners.

(a) $\tau = 0.1, v_d = 0.5c_{s0}$

(b) $\tau = 1, v_d = c_{s0}$

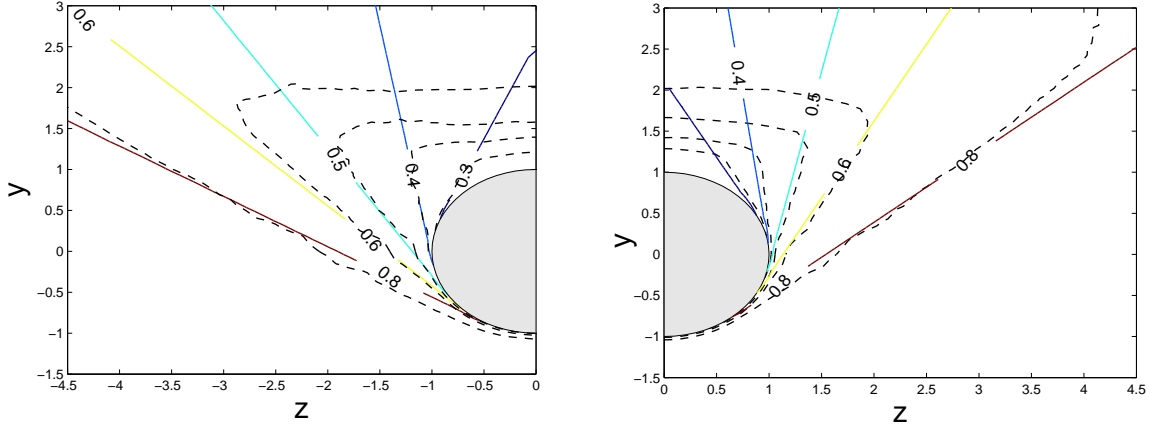


Figure IV-3: Comparison of charge-density contour-lines computed by SCEPTIC3D in the $\{0, \mathbf{e}_y, \mathbf{e}_z\}$ -plane (dashed black) with independent one-dimensional calculations (solid coloured) valid in the probe magnetic shadow when $\beta_i \gg 1$. Contours are for $n = 0.8, 0.6, 0.5, 0.4, 0.3$. SCEPTIC3D runs are performed with $\beta_i = 20$, $\delta = \pi/2$, and (a) $\tau = 0.1, v_d = 0.5c_{s0}$ and (b) $\tau = 1, v_d = c_{s0}$. One-dimensional calculations refer to (a) the isothermal formulation [15] and (b) the kinetic formulation (chapter II).

contrary assume the magnetic presheath to be infinitesimal as well, hence the density difference between SCEPTIC3D and those analytic theories is effectively the change across the magnetic presheath.

Ion temperature

SCEPTIC3D calculates the ion temperature symmetric tensor \bar{T}_i in spherical coordinates, which upon rotation yields the Cartesian components $T_{i,ab} = m (\langle v_a v_b \rangle - \langle v_a \rangle \langle v_b \rangle)$. The magnetic moment of gyrating particles is an adiabatic invariant in the strong magnetization limit, at least outside the magnetic presheath. In the bulk plasma therefore, \bar{T}_i expressed in the coordinates (x, y, z) is diagonal, and only $T_{i,zz}$ can depart from the external temperature $T_{i\infty}$.

Figure (IV-4) shows contour-plots of $T_{i,zz}$ normalized to $T_{i\infty}$ for the physical parameters of Fig. (IV-2a,b), in the $\{0, \mathbf{e}_y, \mathbf{e}_z\}$ -plane. $T_{i,zz}$ drops in the magnetic shadow as the ions are accelerated along the field, with straight isolines tangent to the probe surface. The temperature drop exactly follows the law $T_{i,zz}/T_{i\infty} = (N/N_\infty)^2$ in the

limit $\tau \ll 1$, and approximately otherwise (chapter II). In other words, the temperature perturbation extends along the magnetic shadow much further than the density perturbation, as can be seen in Fig. (IV-4a) where the tube $T_{i,zz} \leq 0.9T_{i\infty}$ is almost parallel to the magnetic axis.

$T_{i,zz}$ sharply increases where the two counterstreaming ion populations present in the right and left magnetic shadows merge (in theory $T_{i,zz} \rightarrow \infty$ at $y = 1^+$ and $z = 0$). Figure (IV-4b) shows, as in Fig. (IV-2b), that the perturbation is much more localized in the absence of magnetic field.

(a) $\tau = 1, v_d = 0.5c_{s0}, \delta = \pi/4$

(b) $\tau = 1, v_d = 1.5c_{s0}, \delta = \pi/2$

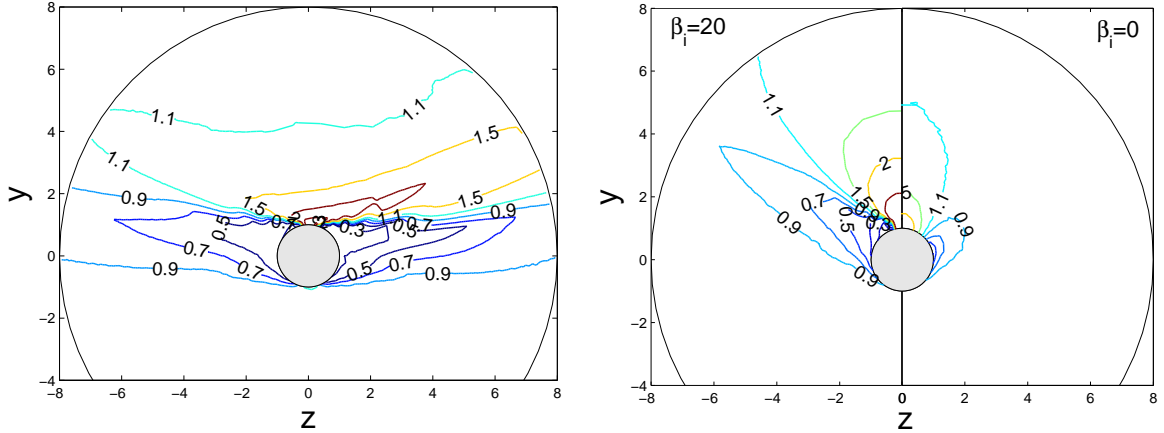


Figure IV-4: Contour-plots of $T_{i,zz}/T_{i\infty}$ in the $\{0, \mathbf{e}_y, \mathbf{e}_z\}$ -plane, with strongly magnetized ions $\beta_i = 20$ (except in (b) where a comparison with the magnetic-free regime is provided). (a) $\tau = 1, v_d = 0.5c_{s0}, \delta = \pi/4$ and (b) $\tau = 1, v_d = 1.5c_{s0}, \delta = \pi/2$.

IV.1.2 Intermediate ion magnetization

In our quasineutral treatment, radial density gradients in the infinitesimal Debye sheath are infinite on the presheath length scale. Therefore regardless of the ion magnetization, density contour-surfaces are tangent to the sheath entrance. Those surfaces need however not be straight lines in $\{\mathbf{e}_y, \mathbf{e}_z\}$ cross-sections, and show in fact a fully three-dimensional structure.

Figure (IV-5) shows charge density contour-plots in (a) the $\{0, \mathbf{e}_y, \mathbf{e}_z\}$ and (b)

the $\{0, \mathbf{e}_x, \mathbf{e}_y\}$ -planes for a run with intermediate ion magnetization $\beta_i = 0.5$. Figure (IV-5a) is qualitatively different from, say, Fig. (IV-2c), because the magnetic presheath is thicker hence the upstream density does not seem to sharply drop at the probe surface. More interesting is Fig. (IV-5b), reporting a significant anisotropy of density and fluid streamlines in the major cross-field cross-section $\{0, \mathbf{e}_x, \mathbf{e}_y\}$ arising from two combined finite Larmor radius effects.

The first effect is the so-called magnetic presheath displacement, most noticeable where the probe surface is parallel to the convective electric field. For our sphere the corresponding region is $x \sim 0$, but for an infinite cylinder (regardless of the cross-section shape) whose axis is parallel to \mathbf{E}_{cnv} the entire probe would be affected. The magnetic presheath displacement corresponds to the ion flow being diverted in the direction of the convective electric field by an “ $\mathbf{E} \times \mathbf{B}$ ” drift arising from the radial sheath-edge potential gradient. A schematic view of the phenomenon is proposed in Fig. (7) from Ref. [40], for a semi-infinite cylindrical probe with quadrilateral cross-section¹.

The second effect is strongest where the probe surface is normal to the convective electric field, corresponding for our sphere to $x \sim \pm 1$. At $y \sim 0$ and positive x , the probe induced field adds to \mathbf{E}_{cnv} and increases the “ $\mathbf{E} \times \mathbf{B}$ ” drift in the \mathbf{e}_y direction, while at negative x the fields tend to cancel out, reducing \mathbf{v}_y . This \mathbf{v}_y modulation in turns affects the relative weight of the probe-induced polarization drift, creating an anisotropy in ion collection (Increased collection at $x < 0$ and decreased collection at $x > 0$).

IV.2 Ion saturation current

IV.2.1 Free-flight current

While numerically-computed plasma profiles are an important tool to understand the physics of plasma-object interaction, the most useful quantity to be compared

¹Notice that the axis are oriented differently in Ref. [40]: $\mathbf{E}_{\text{cnv}} \parallel \mathbf{e}_z$ and $\mathbf{B} \parallel \mathbf{e}_x$.

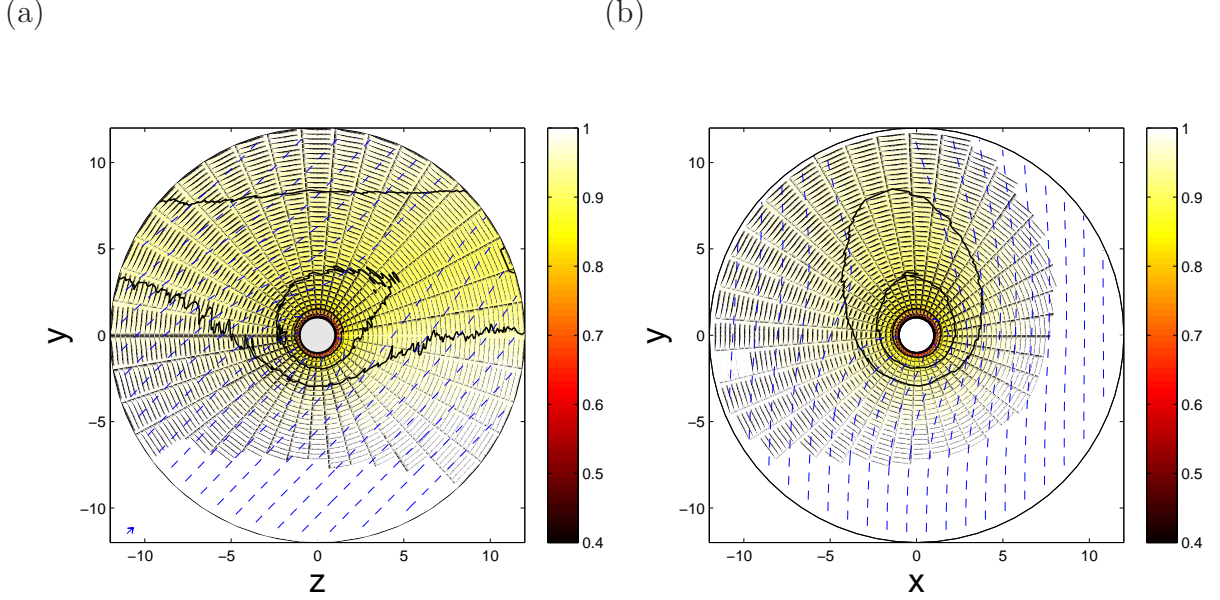


Figure IV-5: Charge density contour-plots in the (a) $\{0, \mathbf{e}_y, \mathbf{e}_z\}$ -plane and (b) $\{0, \mathbf{e}_x, \mathbf{e}_y\}$ -plane, with plasma parameters $\tau = 0.1$, $v_d = 0.2c_{s0}$, $\delta = \pi/4$, $\beta_i = 0.5$. The asymmetry in (b) is due to finite Larmor radius effects. Iso-density contours are full black, while fluid stream lines are dashed blue.

with experimental measurements is the total ion saturation current, and possibly its angular distribution. We start the discussion in the free-flight regime, corresponding to the neglect of probe-induced electric fields on the ions while still accounting for \mathbf{E}_{env} . This treatment is appropriate in the limit $\tau \gg 1$, because the electron pressure is then strongly outweighed by the ion pressure.

When the ions are strongly magnetized, the total saturation current can be obtained by summing the flux density to “slices” in the plane of flow and magnetic field such as shown in Fig. (IV-1a):

$$I_i^{\beta_i=\infty} = R_p^2 \int_{-1}^1 \int_0^{2\pi} \Gamma_{i\parallel}^{\beta_i=\infty}(\eta) (1-x^2)^{1/2} |\sin \eta| d\eta dx = \frac{\pi}{2} R_p^2 \int_0^{2\pi} \Gamma_{i\parallel}^{\beta_i=\infty}(\eta) |\sin \eta| d\eta, \quad (\text{IV.3})$$

where $R_p (1-x^2)^{1/2}$ is the cross-section radius at position x along \mathbf{e}_x . $I_i^{\beta_i=\infty}$ can then be calculated, although not in closed form, with the free-flight strongly magnetized ion flux distribution (Eq. (II.66)):

$$\Gamma_{i\parallel}^{\beta_i=\infty}(\eta) = \Gamma_i^0 \left\{ \exp(-\mu_{ti}^2) + \sqrt{\pi} \mu_{ti} [\pm 1 + \text{erf}(\mu_{ti})] \right\}, \quad (\text{IV.4})$$

where

$$\mu_{ti} = \frac{v_\perp \cot \eta - v_\infty}{v_{ti}}, \quad (\text{IV.5})$$

and “±” stands for “+” downstream, and “−” upstream. To first order in $1/\beta_i$, the effect of finite ion magnetization on the total ion current can be accounted for by changing R_p^2 to $R_p^2(1 + 2/\beta_i)$ in Eq. (IV.3). Such substitution is equivalent to saying that to first order in $1/\beta_i$, the ions see a probe with effective radius $R_p + R_L$; recall that $\beta_i = R_p/R_L$, where R_L is the *average* ion Larmor radius. The ion current is then

$$I_i(\beta_i) = I_i^{|\beta_i=\infty} \left(1 + \frac{2}{\beta_i} \right) + O\left(\frac{1}{\beta_i}\right)^2. \quad (\text{IV.6})$$

In the particular case $\delta = 0$, or $v_\perp = 0$, the problem is rotationally symmetric around the probe magnetic axis, and semi-analytic calculations can be performed (see paragraph V.3.2 for an overview, and Ref. [14] for detailed calculations). To first order in β_i :

$$I_i(\beta_i) = I_i^0 \left\{ \left[\frac{1}{2} \exp(-w_\infty^2) + \frac{\sqrt{\pi}}{2} \left(w_\infty + \frac{1}{2w_\infty} \right) \operatorname{erf}(w_\infty) \right] - \exp(-w_\infty^2) \frac{\beta_i}{3\pi} \right\} + O(\beta_i)^2, \quad (\text{IV.7})$$

with $w_\infty = v_\infty/v_{ti}$.

Figure (IV-6) shows the free-flight current dependence on β_i for different drift angles δ , when (a) $v_d = 0.25v_{ti}$ and (b) $v_d = v_{ti}$. It can be seen that I_i is a decreasing function of β_i regardless of δ , and an increasing function of δ (for $\delta \in [0 : \pi/2]$) regardless of β_i . The solution exactly matches the independent semi-analytic calculation of Refs [41, 14] at $\delta = 0$, as well as the expansion (IV.6) at large β_i , which is a good benchmark of the magnetized particle mover implementation in SCEPTIC3D.

IV.2.2 Self-consistent ion current

When the ion temperature is finite and the self-consistent potential distribution around the probe needs to be accounted for, Eq. (IV.3) should be used with $\Gamma_{i\parallel}^{|\beta_i=\infty}$ from the semi-analytic kinetic solution of chapter II. The high field expansion (IV.6) is then incorrect, but we can argue, at least heuristically by physical continuity, that

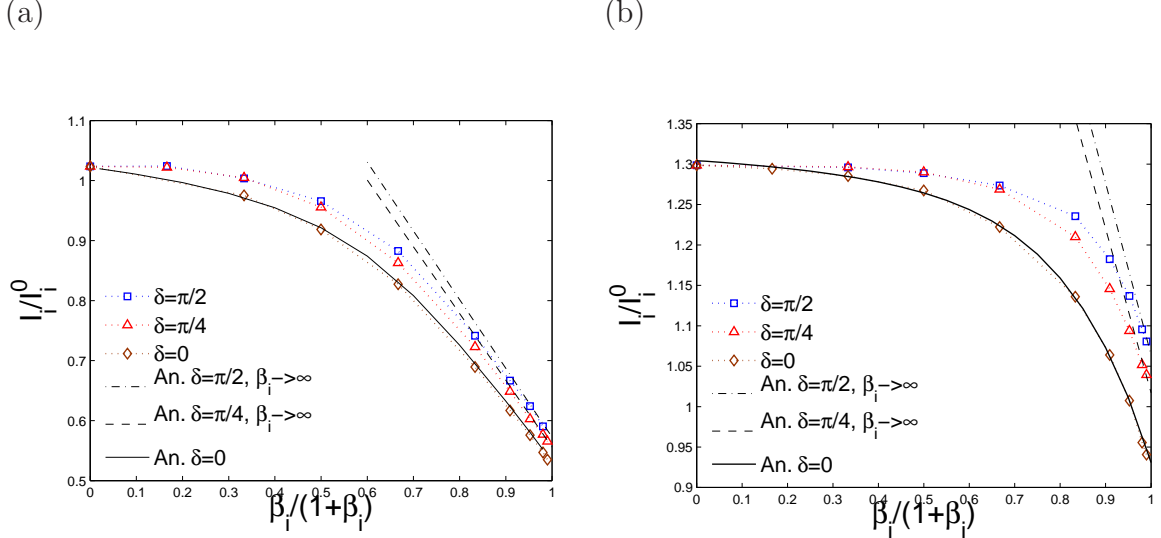


Figure IV-6: Total ion saturation current normalized to $I_i^0 = 4\pi R_p^2 N_\infty v_{ti}/2\sqrt{\pi}$ as a function of ion magnetization β_i in the free-flight regime (i.e. disregarding probe-induced electric field effects on the ions), computed by SCEPTIC3D for different angles of flow and magnetic field δ . “An. $\delta = 0$ ” refers to the semi-analytic treatment of Refs [41, 14] for which the weak field limit is given by Eq. (IV.7). “An. $\beta_i \rightarrow \infty$ ” refers to the high field expansion (IV.6). (a) $v_d = 0.25v_{ti}$ and (b) $v_d = v_{ti}$.

$I_i(\beta_i)$ still has a $1/\beta_i$ term at high β_i . This property is essential because it allows us to connect the current computed by SCEPTIC3D at reasonably high β_i , typically $\beta_i \lesssim 50$, to Eq. (IV.3) at $\beta_i = \infty$.

Figure (IV-7) shows the ion saturation current as a function of β_i for different plasma conditions. (a) $\tau = 0.1$, $v_d = 0.2c_{s0}$, (b) $\tau = 1$, $v_d = 0.5c_{s0}$ and (d) $\tau = 1$, $v_d = 1.5c_{s0}$ are qualitatively similar, although the latter corresponds to a supersonic flow. The current slope at $\beta_i = 0$ seems to be zero, but there is always a linear term (not explicitly shown) that is smaller than what the code can resolve. The dashed portions of curves at high β_i connect the last point from SCEPTIC3D calculations to $I_i^{|\beta_i=\infty}$ (Eq. (IV.3) with $\Gamma_{i\parallel}^{|\beta_i=\infty}$ from chapter II); because there is no slope discontinuity at the connection, we can *a posteriori* confirm that the ion current has indeed a $1/\beta_i$ dependence at high β_i .

When the ion temperature is small and the drift velocity approximately sonic, the ion current has the unexpected property of peaking at intermediate magnetization. An example of such behaviour is shown in Fig. (IV-7c), for the case $\tau = 0.1$ and

$v_d = c_{s0}$. The peak is maximum for $\delta = \pi/2$, and decreases with δ . We have not run self-consistent cases with $\delta = 0$, as a rigorous treatment would involve modeling anomalous cross-field transport in the elongated presheath [23, 27]. However approximate collisionless solutions for $\beta_i \leq 1$ [41] suggest that the current does not peak when the flow is field aligned. Further discussion on this current peak at intermediate magnetization, in the context of finite Debye length plasmas, will be proposed in chapters V,VI.

Figure (IV-8) shows the ion-charge flux-density to the probe major cross-section in the plane of flow and magnetic field $\{0, \mathbf{e}_y, \mathbf{e}_z\}$, as a function of $\cos \theta$; the curves are therefore closed on themselves, the upper portions corresponding to $\sin \theta \leq 0$ and the lower portions to $\sin \theta \geq 0$. As expected, both solutions (a) $\tau = 1, v_d = c_{s0}, \delta = \pi/4$ and (b) $\tau = 0.1, v_d = c_{s0}, \delta = 3\pi/8$ tend to the prediction of chapter II when $\beta_i \rightarrow \infty$. If it were plotted as a function of $\cos(\theta - \delta)$, the curve $\beta_i = 0$ in Fig. (IV-8b) would perfectly match the curves in Fig. (III-5a). Both figures indeed correspond to the same plasma conditions, and $\chi = \theta - \delta$ on the probe major cross-section. The difference is that Fig. (III-5a) has been created with current data from the entire probe surface, while Fig. (IV-8b) with current data from the probe major cross-section only.

Figure (IV-8b) also helps understand the ion saturation current peak at $\beta_i \sim 1$. When $\beta_i = 0$, the probe focusses the ions downstream, creating the “bump” first seen in Fig. (III-5a). As β_i increases, part of the ions that would miss the probe in the absence of magnetic field are collected downstream while the upstream current is unaffected. Eventually when β_i increases further, the dynamics becomes one-dimensional and focussing is suppressed.

IV.3 Transverse Mach probe calibration

Transverse Mach probes seek to measure the external plasma drift velocity by comparing the ion saturation flux-density Γ_i at different angles in a given plane of flow and magnetic field. The two main competing designs are rotating planar probes, and

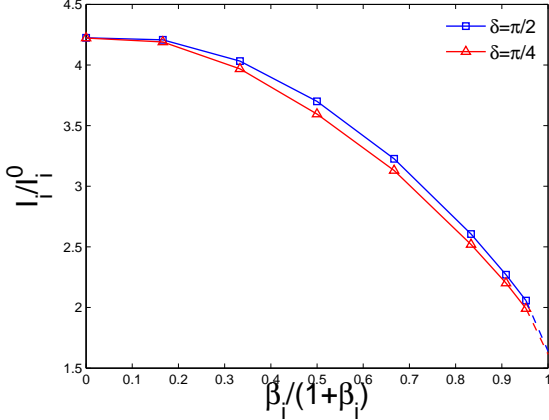
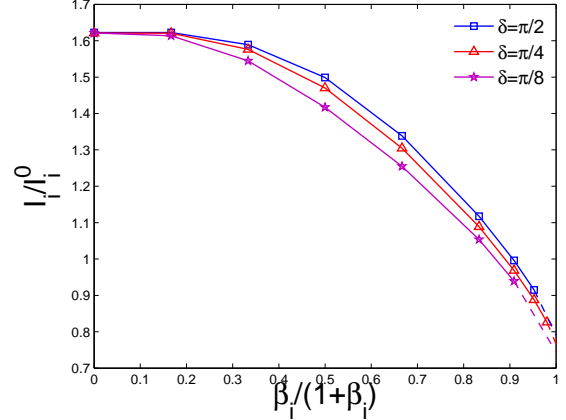
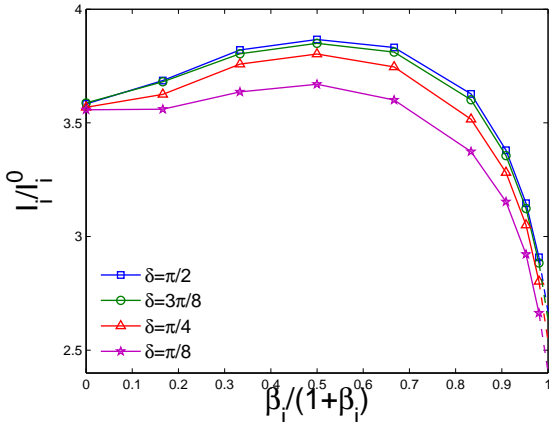
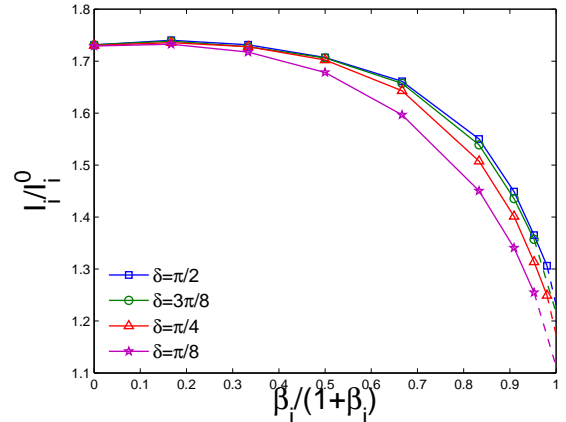
(a) $\tau = 0.1, v_d = 0.2c_{s0}$ (b) $\tau = 1, v_d = 0.5c_{s0}$ (c) $\tau = 0.1, v_d = c_{s0}$ (d) $\tau = 1, v_d = 1.5c_{s0}$ 

Figure IV-7: Total ion saturation current normalized to $I_i^0 = 4\pi R_p^2 N_\infty v_{ti} / 2\sqrt{\pi}$ as a function of ion magnetization β_i , self-consistently calculated with SCEPTIC3D. (a) $\tau = 0.1, v_d = 0.2c_{s0}$. (b) $\tau = 1, v_d = 0.5c_{s0}$. (c) $\tau = 0.1, v_d = c_{s0}$. (d) $\tau = 1, v_d = 1.5c_{s0}$. The dashed portions of curves at high β_i connect our simulations at finite magnetization to $I_i^{|\beta_i=\infty}$ (Eq. (IV.3) with $\Gamma_{i\parallel}^{|\beta_i=\infty}$ from chapter II).

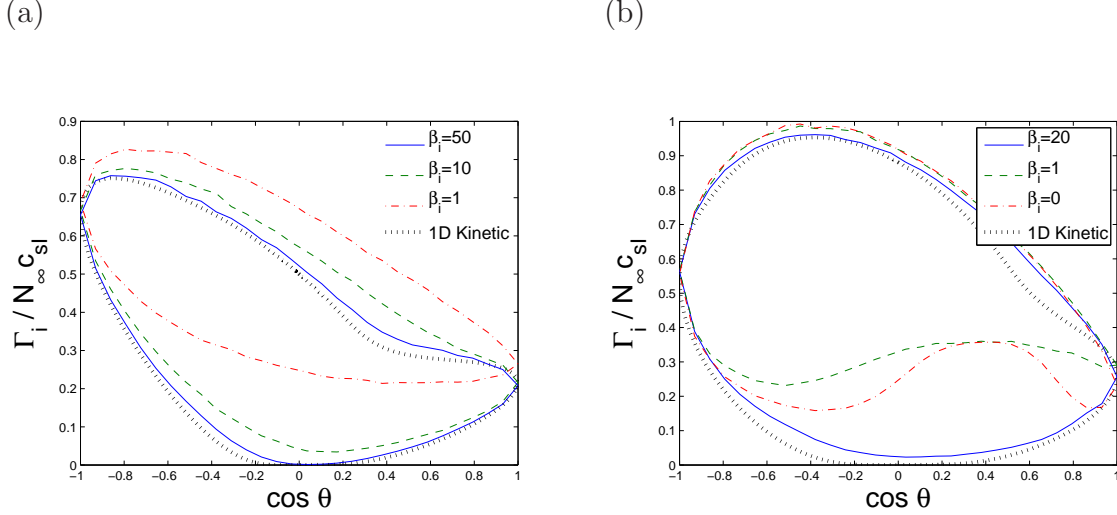


Figure IV-8: Angular ion-charge flux-density distribution to the probe major cross-section in the plane of flow and magnetic field $\{0, \mathbf{e}_y, \mathbf{e}_z\}$ normalized to $N_\infty c_{sI}$, self-consistently calculated with SCEPTIC3D for different ion magnetizations β_i . “1D Kinetic” refers to the semi-analytic solution of chapter II. (a) $\tau = 1$, $v_d = c_{s0}$ and $\delta = \pi/4$. (b) $\tau = 0.1$, $v_d = c_{s0}$ and $\delta = 3\pi/8$.

Gundestrup probes, operating simultaneous measurements at different angles with a set of electrodes spanning a single probe head [26]. It is here convenient to think in terms of M_∞ and M_\perp rather than v_d and δ , where we recall that Mach numbers “ M ” are intended as velocity normalized to the isothermal ion sound speed c_{sI} .

It was argued in chapter II that the only transverse spherical Mach probe calibration method valid at moderate drift for infinite and negligible ion magnetization, yet involving a single calibration factor M_c , consists in measuring the two flux ratios $R_{3\pi/4} = \Gamma_i(\eta = -\pi/4)/\Gamma_i(\eta = 3\pi/4)$ and $R_{\pi/4} = \Gamma_i(\eta = -3\pi/4)/\Gamma_i(\eta = \pi/4)$, and relating them to the external flow by

$$M_\perp = \frac{M_c}{2} (\ln R_{3\pi/4} - \ln R_{\pi/4}) \quad (\text{IV.8})$$

$$M_\infty = \frac{M_c}{2} (\ln R_{3\pi/4} + \ln R_{\pi/4}). \quad (\text{IV.9})$$

Measures can in theory be made in any plane of flow and magnetic field, although it is best to avoid grazing planes located at $x \sim \pm 1$. Figure (IV-9) shows a three-dimensional view of the probe surface, color-plotted according to the local ion flux

density for the example $\tau = 0.3$, $v_d = 0.5c_{s0}$, $\delta = \pi/4$ and $\beta_i = 2$. The most obvious possible plane of measurement is indicated by a dotted circle corresponding to the major cross-section ($x = 0$), best mocking an infinite cylindrical probe. Two more options are a solid and dashed circles, corresponding to quarter cross-sections at $x = \pm 1/\sqrt{3}$, whose particularity is to cut the sphere at points with $x = \pm y = \pm z$ exactly where Mach probe measurements are to be made (i.e. $\tan \eta = \pm 1$). Those configurations therefore best mock the pyramidal probe of Smick and LaBombard [22], where measures are taken on planar electrodes at 45° angle with the three coordinate planes.

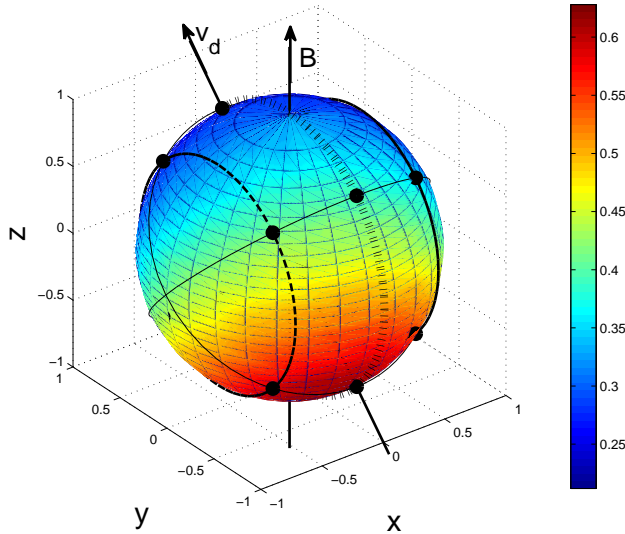


Figure IV-9: Three-dimensional view of the probe surface, color-plotted according to the normalized ion-charge saturation flux $\Gamma_i/(N_\infty c_s I)$ for the plasma parameters $\tau = 0.3$, $v_d = 0.5c_{s0}$, $\delta = \pi/4$ and $\beta_i = 2$. The dotted, solid and dashed circles respectively correspond to cross sections located at $x = 0, 1/\sqrt{3}, -1/\sqrt{3}$, and the thick dots to the points where Mach probe measurements are to be made (i.e. $\tan \eta = \pm 1$).

In the limit $\beta_i = \infty$, M_c does not depend on the measurement cross-section and is given by (see Eq. (II.78))

$$M_c^{\beta_i=\infty} = \frac{1}{2}\kappa + \frac{1}{\sqrt{2\pi}}(1-\kappa), \quad \text{with} \quad \kappa(\tau) \simeq \frac{1}{2}\operatorname{erfc}(0.12 + 0.40 \ln \tau). \quad (\text{IV.10})$$

In the opposite limit $\beta_i = 0$, early simulations with SCEPTIC(2D) [9] have shown

that the ion saturation flux distribution to a spherical probe is approximately given by $\Gamma_i \propto \exp(-K(\cos \chi)v_d/2)$, where again $\cos \chi$ is the position projected on the drift axis, and $K \simeq 1.34/c_{s0}$ for $\tau \lesssim 3$. The flux ratio at angle $\eta + \pi$ over η is therefore $R = \exp(K|\cos(\chi)|v_d)$, yielding for measurements with $\tan \eta = \pm 1$ at azimuthal position ψ :

$$M_c^{|\beta_i=0} = \frac{2}{Kc_{sI}} \frac{|\sin \psi|}{\sqrt{1 + (\sin \psi)^2}}. \quad (\text{IV.11})$$

On the *major* cross-section, $|\sin \psi| = 1$, hence $M_c^{|\beta_i=0} = \sqrt{2}/(Kc_{sI})$. In particular at $\tau = 1$ where $K = 1.34/c_{s0}$: $M_c^{|\beta_i=0} \simeq 0.75$ (and $M_c^{|\beta_i=\infty} \simeq 0.44$). ψ is not constant on the quarter cross-sections since on the sphere surface $x = \sin \theta \cos \psi$. However at the points where $\tan \eta = \pm 1$, $\tan \psi = \pm 1$ as well, therefore at $\tau = 1$ on the *quarter* cross-sections: $M_c^{|\beta_i=0} = 0.91$ (and still $M_c^{|\beta_i=\infty} \simeq 0.44$).

At intermediate magnetization, there is no *a priori* reason to believe that Eqs (IV.8,IV.9) still hold. Perhaps the most important result of this chapter is that they actually do, to well within experimental uncertainty. This can easily be seen on Fig. (IV-10), where $R_{3\pi/4}$ and $1/R_{\pi/4}$ on the major cross section $\{0, \mathbf{e}_y, \mathbf{e}_z\}$ from SCEPTIC3D simulations are plotted in log-space against $M_\perp + M_\infty$ and $M_\perp - M_\infty$, for the particular case $\tau = 1$. The points with $v_d \lesssim c_{sI}$ can be fitted to a line with slope $1/M_c$, identical for $R_{3\pi/4}$ and $R_{-\pi/4}$, and function of β_i only.

The calibration factors M_c in the entire range of ion magnetization and for $\tau \in [0.1 : 10]$, computed by fitting SCEPTIC3D's solutions with $v_d \lesssim c_{sI}$ and $\delta \in [\pi/8 : \pi/2]$, are plotted in Fig. (IV-11) on (a) on the major cross-section and (b) the quarter cross-sections. The fitting error bars, shown in Fig. (IV-11a), are thinner at low and large β_i , where the error mostly arises from numerical noise, and thicker at $\beta_i \simeq 0$ where part of the error is due to Eqs (II.79,II.80) being approximate. Because there never seems to be more than $\sim 10\%$ uncertainty, Eqs (II.79,II.80) can be assumed to be “correct” for experimental purposes.

Error bars have not been plotted on Fig. (IV-11b) to increase readability, but are qualitatively similar to those in Fig. (IV-11a). The noticeable result is here that at intermediate magnetization, Mach probes with electrodes whose normal is not on the

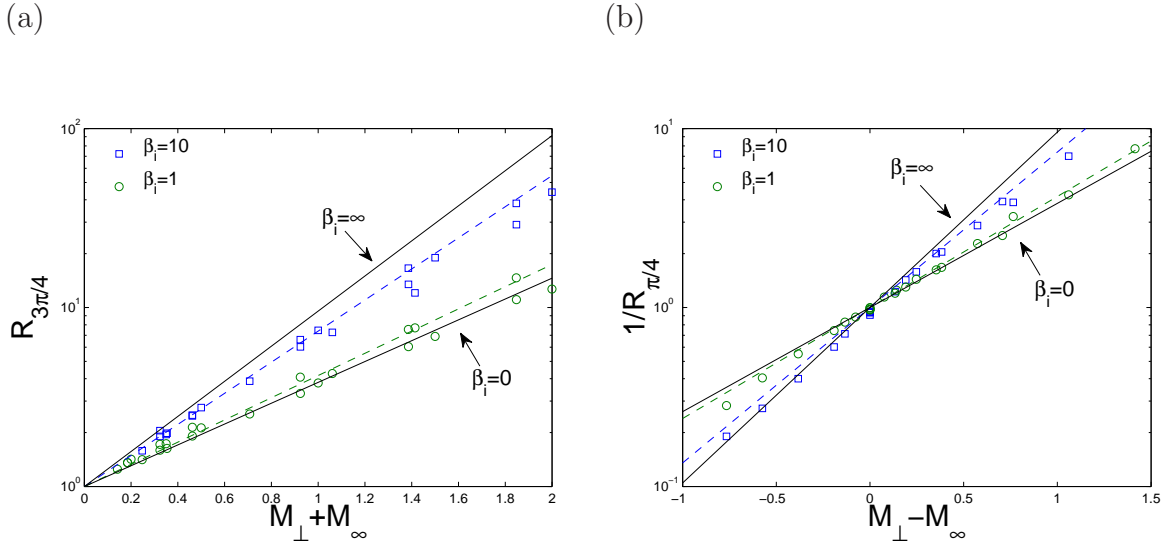


Figure IV-10: Upstream to downstream flux ratio on the probe major cross-section at (a) $\eta = 3\pi/4$ and (b) $\eta = \pi/4$, versus respectively $M_\perp + M_\infty$ and $M_\perp - M_\infty$, from a large set of SCEPTIC3D runs spanning $v_d \in [0 : 2]c_{s0}$ and $\delta \in [\pi/8 : \pi/2]$, for a temperature ratio $\tau = 1$. Also shown are the corresponding fitting lines, whose slopes $1/M_c$ are taken from Fig. (IV-11a).

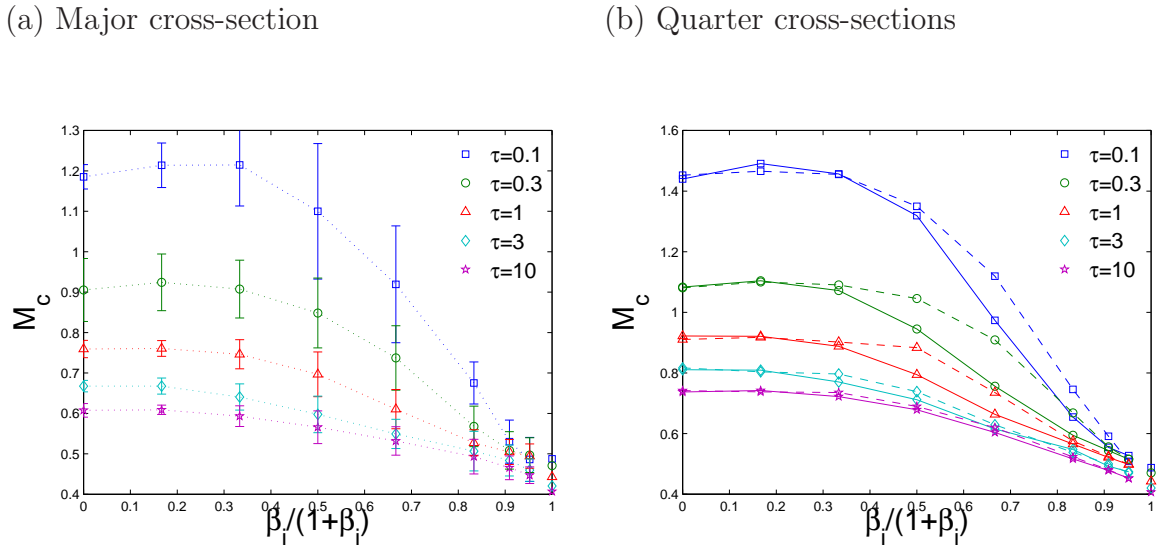


Figure IV-11: Transverse Mach probe calibration factor M_c as a function of magnetization β_i and temperature ratio τ computed with SCEPTIC3D for measurements made (a) on the major cross-section and (b) the quarter cross-sections. (a) also shows the fitting error bars, arising from numerical noise and from Eqs (II.79, II.80) being only approximate. On (b), solid lines refer to measurements at $x = 1/\sqrt{3}$, and dashed lines to measurements at $x = -1/\sqrt{3}$. The points at $\beta_i = \infty$ are given by Eq. (II.78).

plane of flow and magnetic field are sensitive to the magnetic field orientation. This is a consequence of the finite Larmor radius effects observed in Fig. (IV-5); in particular the flow deflection towards the region $x \lesssim 0$ seen in Fig. (IV-5b) causes the flux ratios to be lower at $x = -1/\sqrt{3}$ than $x = 1/\sqrt{3}$.

Chapter V

Spheres in infinite Debye length, arbitrarily magnetized plasmas

The results of chapter IV, obtained with SCEPTIC3D in the quasineutral operation mode, apply when the plasma Debye length is much shorter than the sphere radius. This condition is usually well satisfied when modeling flux-sensing probes in tokamak edge conditions, but accounting for finite shielding is essential to the treatment of smaller collectors such as probes in lower density plasmas [42], or dust particulates.

SCEPTIC3D can treat arbitrary electron Debye length to probe radius ratios, and such capability will be extensively used in chapter VI. This unfortunately requires specification of ϕ_p and λ_{De} , in addition to the four quasineutral parameters v_d , δ , τ and β_i . The total of six parameters is a severe complication in attempting to acquire physical insight into the ion collection physics.

We propose to start with a discussion of the vacuum limit, when the electron Debye length $\Lambda_{De} \propto 1/\sqrt{N_\infty}$ is much larger than the sphere radius R_p and the ion to electron temperature τ will prove to be irrelevant.

After a brief introduction on dusty plasmas and a review of ion collection in large Debye length, unmagnetized conditions (Orbit Motion Limited), we solve the opposite limit of strong ion magnetization, yet large Debye length, using an original 1D-kinetic/2D-drift model. The scaling $R_L \ll R_p \ll \Lambda_{De}$ rarely occurs in experimental settings, but its understanding is helpful to interpret SCEPTIC3D's results in the

more interesting scaling $R_L \sim R_p \lesssim \Lambda_{De}$.

V.1 Foreword on dust charging in the unmagnetized regime

V.1.1 Dusty plasmas

A dusty plasma is an ensemble of dust particles immersed in a plasma containing electrons, ions, and parent neutrals. Those occur quite often in astrophysical contexts, such as in planetary rings, comet tails, interplanetary and interstellar clouds [43], and also in industrial or laboratory plasmas.

Industrial plasma processes usually involve chemically active gases at moderate temperatures, where nano-particles consisting of several hundreds of atoms form through gas-phase nucleation. Those particles can rapidly grow by coagulation up to the 100nm range, and then by vapor deposition to reach micrometer sizes [44]. Because such “dust particles” represent an unacceptable source of contamination in semiconductor processing, active research is ongoing to mitigate their effect.

Dust particles are isolated, hence their steady-state potential floats to balance the net incoming flux of ions and electrons. Depending on the experimental conditions, *solid state* physics reactions resulting in electron emission at the dust surface such as photoemission, secondary emission, and thermionic emission, might be important [45]. In some cases ion-induced secondary emission is present as well; in this thesis however we do only consider bulk current collection. The ion thermal speed being much smaller than the electron’s, the floating potential Φ_f must be negative enough to repel the excess electrons, dimensionally $\Phi_f \sim O(-T_e/e)$, of the same order as the floating potential of Langmuir probes introduced in section II.1. The surface of a micron-sized particle therefore carries several thousands elementary charges, opening the possibility for the formation of ordered dust structures, called plasma crystals [5]. Those formations are today studied in a variety of conditions, typically using spherically-shaped artificial particles such as shown in Fig. (V-1a).

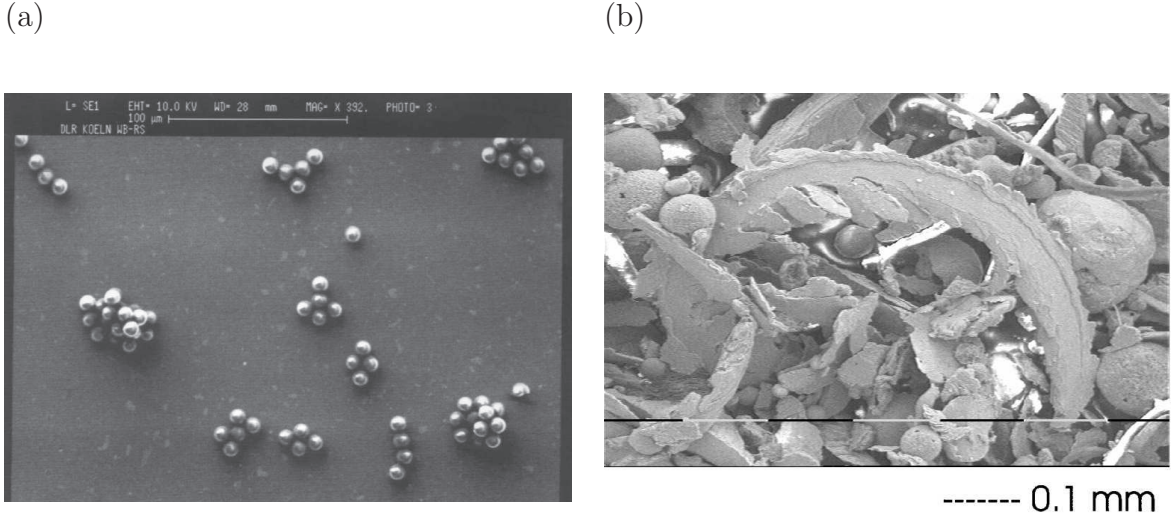


Figure V-1: (a) From http://www.mpe.mpg.de/pke/PKE/images/Emr-08_m.jpg. Micrometer sized melamine-formaldehyde spheres used for dusty plasma crystallization experiments. (b) Dust found in the divertor region of the TEXTOR tokamak [46].

Dust is also commonly found in magnetic confinement fusion devices, where disruptions, ELMs and other violent events can erode micrometer or even millimeter-sized chips from the Plasma Facing Components (PCF). Studies performed on the DIII-D tokamak show that a single disruption can produce up to 10000 dust particles [47]. Those then penetrate in the core plasma, leading to potentially dangerous contamination and degraded performance. Perhaps of major concern to future machines is that dust may be a radiological hazard by retaining tritium; dust inventory in ITER will therefore be strictly regulated. Small quantities of dust are in fact always produced in fusion experiments, in particular on shadowed surfaces such as underneath the wall tiles, although the exact formation mechanisms and rates are not well understood [48]. Figure (V-1b) shows a microscopic view of dust found in the divertor region of the TEXTOR tokamak [46]. Tokamak dust composition includes

- Molybdenum: Used in the divertor, inboard wall and limiters in Alcator C-mod.
- Tungsten: Used in Alcator C-mod's divertor.
- Titanium: Was used in Alcator C-mod's lower-hybrid waveguides for its small thermal expansion properties. Titanium can be tritiated.

- Carbon: Used on most other tokamaks. Carbon can be tritiated as well.
- Boron: Used in Alcator C-mod as a low-Z first-wall coating. Contrary to the previous materials, Boron is a semiconductor, insulating at low temperatures.

Dust radiates in the $1000^{\circ}K$ range before melting, hence can be tracked in visible light. Figure (V-2a) shows metallic dust particles (red dots) spewed in the Alcator C-mod tokamak, after the titanium lower hybrid launcher experienced corrosion by hydrogen/deuterium during the 2005 campaign. Figure (V-2b) shows the thick dust layer deposited on the launcher.

(a)



(b)



Figure V-2: In the 2005 Alcator C-mod tokamak campaign, the lower hybrid launcher experienced corrosion by hydrogen and deuterium, spewing titanium dust across the machine. (a) Dust particles in visible light (red dots), as they radiate before eventually melting. (b) Dust deposited on the launcher after plasma operation.

Most situations of interest, in particular when considering tokamak edge, involve plasmas whose electron Debye length is larger than the dust radius, yet smaller than the ion Larmor radius; relevant sample parameters are summarized in table (V.1).

	T_e (eV)	$T_{i\infty}$ (eV)	B (T)	N_∞ (m $^{-3}$)	R_{Le} (μm)	R_L (μm)	Λ_{De} (μm)
Mid-plane SOL	10	30	5	10^{18}	1.9	200	23
Divertor region	5	5	5	10^{20}	1.3	81	1.7

Table V.1: Sample edge parameters for a typical Alcator C-Mod discharge, for which the average ion Larmor radius r_L compares to the size of dust particles ($r_p \sim 1 - 200\mu\text{m}$), and the electron Debye length Λ_{De} can not be neglected ($\Lambda_{De} \gtrsim 0.01R_p$); when $\Lambda_{De} \ll R_p$ the results of chapter IV apply. The figures are calculated for a DD (Deuterium) discharge.

V.1.2 Orbit Motion Limited shielding

Electrons

In the absence of magnetic field and drift velocity ($\mathbf{B} = 0$ and $\mathbf{v}_d = 0$), the problem is spherically symmetric and the electrostatic potential Φ only depends on the radial coordinate R . Further assuming that Φ varies monotonically between Φ_p and 0, there is a one-to-one relationship between Φ and R and it is possible to calculate the exact electron distribution as follows.

The three-dimensional electron Vlasov equation can be rewritten $d\mathbf{f}_e/dt = 0$, where d/dt is the convective derivative along particle orbits. The stationary Maxwellian being function of the kinetic energy only, and the total electron-orbit energy $W = m_e\mathbf{v}^2/2 - e\Phi$ being conserved, the electron distribution function is

$$f_e(R, \mathbf{v}) = f_e^\infty \left(\mathbf{v}^2 - \frac{2e\Phi(R)}{m_e} \right) \quad (\text{V.1})$$

if the electron orbit (R, \mathbf{v}) can be traced back to infinity, and $f_e(R, \mathbf{v}) = 0$ if it originates from the probe. Because the probe is electron-repelling and the potential variation monotonic, no orbits are bounded or closed on the probe. Conservation of energy (W_0) and angular momentum (J_0) for a given electron reads

$$W_0 = \frac{1}{2}m_e\dot{R}^2 + W_{eff}(R), \quad (\text{V.2})$$

where

$$W_{eff}(R) = \frac{1}{2} \frac{J_0^2}{m_e R^2} - e\Phi(R) \quad (\text{V.3})$$

is the effective potential of the radial motion. An electron orbit characterized by (W_0, J_0) can be traced back to infinity if $\dot{R} < 0$ (directed towards the probe) or $W_0 < W_{eff}(R_p)$ (directed outwards, i.e. reflected by the repulsive effective potential):

$$D_e := \left\{ v_r \leq 0 \text{ or } \mathbf{v}^2 - v_r^{\perp 2} \left(\frac{R}{R_p} \right)^2 < \frac{2e}{m_e} (\Phi - \Phi_p) \right\}, \quad (\text{V.4})$$

where the velocity variable has been decomposed in $\mathbf{v} = v_r \mathbf{e}_r + v_r^\perp \mathbf{e}_r^\perp$. Defining $\mathbf{w} = \mathbf{v}/v_{te}$ and $r = R/R_p$, the electron density distribution is then in dimensionless variables

$$N_e(\phi, r) = N_\infty \exp(\phi) \frac{1}{\pi^{3/2}} \int_{\mathbf{w} \in D_e} \exp(-\mathbf{w}^2) d^3 \mathbf{w}, \quad (\text{V.5})$$

yielding after integration [49]:

$$N_e(\phi, r) = \frac{N_\infty \exp(\phi)}{2} \left\{ 1 + \operatorname{erf} \left(\sqrt{\phi - \phi_p} \right) + \frac{\sqrt{r^2 - 1}}{r} \exp \left(\frac{\phi - \phi_p}{r^2 - 1} \right) \left[1 - \operatorname{erf} \left(r \sqrt{\frac{\phi - \phi_p}{r^2 - 1}} \right) \right] \right\}. \quad (\text{V.6})$$

In the limit $r - 1 \ll 1$, Eq. (V.6) reads

$$N_e(\phi) \simeq \frac{N_\infty \exp(\phi)}{2} \left[1 + \operatorname{erf} \left(\sqrt{\phi - \phi_p} \right) \right]; \quad (\text{V.7})$$

in other words at the probe surface the electron density is 50% of the Boltzmann value, but quickly rises to 85% when $\phi - \phi_p = 1$ and 95% when $\phi - \phi_p = 2$. In the opposite limit $r \gg 1$, Eq. (V.6) reads

$$N_e(\phi) \simeq N_\infty \exp(\phi) \left\{ 1 - \left[1 - \operatorname{erf} \left(\sqrt{\phi - \phi_p} \right) \right] [1 - 2(\phi - \phi_p)] \frac{1}{4r^2} \right\}. \quad (\text{V.8})$$

The “ $1/r^2$ ”-term corresponds to the geometric shadowing of electrons by the probe, and is negligible when $\phi - \phi_p \gtrsim 2$.

This short analysis confirms kinetically, on the particular case $\mathbf{B} = 0$ and $\mathbf{v}_d = 0$, that provided $\Phi_p \lesssim -2T_e/e$ the electron density follows Eq. (A.2) wherever not

negligible.

Ions

In the unmagnetized regime with zero ion drift, we can follow the same argument as for the electrons and write the ion-charge distribution function as

$$f(R, \mathbf{v}) = f^\infty \left(\mathbf{v}^2 + \frac{2Ze\Phi(R)}{m} \right) \quad (\text{V.9})$$

if the ion orbit (R, \mathbf{v}) can be traced back to infinity, and $f(R, \mathbf{v}) = 0$ if it originates from the probe. Conservation of energy (W_0) and angular momentum (J_0) for a given ion reads

$$W_0 = \frac{1}{2}m\dot{R}^2 + W_{eff}(R), \quad (\text{V.10})$$

where

$$W_{eff}(R) = \frac{1}{2}\frac{J_0^2}{mR^2} + Ze\Phi(R) \quad (\text{V.11})$$

is the effective potential of the radial motion. Contrary to the electron case where W_{eff} decreases monotonously between $W_{eff}(R_p)$ and $W_{eff}(\infty)$, there might here be intermediate potential barriers. In the absence of such barriers, the ion orbit characterized by (W_0, J_0) can be traced back to infinity if $W_0 \geq 0$ (non trapped ion), and if either $\dot{R} \leq 0$ (directed towards the probe) and/or $W_0 < W_{eff}(R_p)$ (reflected by the repulsive effective potential):

$$D_i := \left\{ \mathbf{v}^2 + \frac{2Ze\Phi}{m} \geq 0, \text{ and } v_r \leq 0 \text{ or } \mathbf{v}^2 - v_r^{\perp 2} \left(\frac{R}{R_p} \right)^2 < -\frac{2Ze}{m} (\Phi - \Phi_p) \right\}. \quad (\text{V.12})$$

Bernstein and Rabinowitz [50] have shown that the absence of intermediate potential barriers corresponds to the following inequality (when the potential distribution is spherically symmetric):

$$\forall R > R_p, \quad \frac{d}{dR} \left[R^3 \frac{d\Phi}{dR} \right] \geq 0. \quad (\text{V.13})$$

Equation (V.13), referred to as the Orbit Motion Limited (OML) condition, requires the potential to decrease everywhere slower than $1/R^2$. The OML condition is never satisfied at $R \gg \Lambda_{De}$ [51], but approached in the limit $\Lambda_{De} \gg R_p$, where the unperturbed density goes to zero and the potential distribution tends to a Coulomb form ($\Phi \propto 1/R$).

In that case the OML ion-charge density distribution in dimensionless variables is

$$N_i(\phi, r) = N_\infty \exp(\phi) \frac{1}{\pi^{3/2}} \int_{\mathbf{w} \in D_i} \exp(-\mathbf{w}^2) d^3\mathbf{w}, \quad (\text{V.14})$$

where $\mathbf{w} = \mathbf{v}/v_{ti}$, yielding after integration Eq. (23) in Ref. [51]. Recalling the definition of the ion to electron temperature ratio at infinity $\tau = T_{i\infty}/ZT_e$ (Eq. (II.5)), the density far from the probe where $r \gg 1$ and $\phi \simeq 0$ is given by Eq. (31) in Ref. [51]:

$$N_i(\phi, r) = N_\infty \left(1 - \frac{\phi}{\tau} - \frac{1 - 2\phi_p/\tau}{4r^2} \right). \quad (\text{V.15})$$

Contrary to the electron case (Eq. (V.8)), the geometric shadowing term in Eq. (V.15) cannot be neglected for the only reason that $\phi - \phi_p \gtrsim 2$, hence has to be accounted for. Upon linearizing Eq. (V.8) about $\phi = 0$ (and neglecting the electron shadowing term), the electrostatic Poisson equation valid asymptotically in $r = R/R_p \gg 1$ is therefore

$$\frac{1}{r^2} \frac{\partial}{\partial r} \left(r^2 \frac{\partial \phi}{\partial r} \right) = \frac{1}{\lambda_D^2} \left(\phi - \frac{1 - 2\phi_p/\tau}{4(1 + 1/\tau)r^2} \right). \quad (\text{V.16})$$

Equation (V.16) shows that the plasma can schematically be divided in two regions. A presheath where $\Lambda_{De}^2 \nabla^2 \phi \ll (N_i, N_e)/N_\infty$, hence the physics is purely geometrical and the potential distribution obtained by setting the right-hand-side of Eq. (V.16) to zero. This is the quasineutral region ($N_i \sim N_e$):

$$\phi(r) = \frac{1 - 2\phi_p/\tau}{4(1 + 1/\tau)r^2}. \quad (\text{V.17})$$

When $\phi = -O(1)$ still $r \gg 1$, the shadowing term can be neglected and Eq. (V.16)

simplifies to

$$\frac{1}{r^2} \frac{\partial}{\partial r} \left(r^2 \frac{\partial \phi}{\partial r} \right) = \frac{\phi}{\lambda_D^2}. \quad (\text{V.18})$$

This is the sheath, whose solution is a Debye-Hückel potential as anticipated in paragraph III.3.2:

$$\phi(r) = \frac{\phi_p}{r} \exp \left(-\frac{r-1}{\lambda_D} \right), \quad (\text{V.19})$$

but whose shielding length is the linearized Debye length λ_D , defined by

$$\lambda_D = \frac{\lambda_{De}}{(1 + 1/\tau)^{1/2}}. \quad (\text{V.20})$$

As mentioned earlier, the OML approach is valid when $\lambda_D \gg 1$. The *linearization* yielding Eq. (V.18) further requires $\lambda_D \gg -\phi_p/\tau$, in order for the potential distribution close to the probe to be governed by physics occurring where the density is only weakly perturbed.

V.1.3 Orbit Motion Limited charging

Because dust particles are typically smaller than the plasma Debye length, the sharp distinction between Debye sheath and quasineutral presheath operated in the study of electrostatic probes is not appropriate here. As a result the ion current does not saturate to a value of the order $AN_\infty c_{s0}$, and orbital ion effects must be taken into account to study dust charging. This can be done analytically for spherical (or infinite circular cross-section cylindrical) dust particles with radius R_p and potential Φ_p , when $R_p \ll \Lambda_{De}$ and no magnetic field is present.

In the absence of intermediate potential barrier (OML regime), energy and angular momentum conservation imply that each ion with impact parameter p and energy W_0 such that

$$p \leq R_p \left(1 - \frac{Ze\Phi_p}{W_0} \right)^{1/2} \quad (\text{V.21})$$

is collected. If the ion-charge distribution function far from the probe is Maxwellian

with thermal speed $v_{ti} = (2T_{i\infty}/m)^{1/2}$ (Eq. (II.31)) and drift velocity \mathbf{v}_d :

$$f^\infty(\mathbf{v}) = \frac{N_\infty}{(v_{ti}\sqrt{\pi})^3} \exp\left[-\frac{(\mathbf{v} - \mathbf{v}_d)^2}{v_{ti}^2}\right], \quad (\text{V.22})$$

the OML ion current to the probe is simply

$$I_i = \int_{\psi=0}^{2\pi} \int_{v_z=-\infty}^{\infty} \int_{v_\rho=0}^{\infty} f(\mathbf{v}) |\mathbf{v}| \pi R_p^2 \left(1 - \frac{Ze\Phi_p}{W_0}\right) dv_z v_\rho dv_\rho d\psi, \quad (\text{V.23})$$

yielding after integration

$$I_i = 4\pi R_p^2 \Gamma_i^0 \left[\frac{1}{2} \exp(-w_d^2) + \frac{\sqrt{\pi}}{2} \left(w_d + \frac{1}{2w_d} + \frac{\chi_p}{w_d} \right) \operatorname{erf}(w_d) \right], \quad (\text{V.24})$$

where $w_d = v_d/v_{ti}$. This solution, first derived by Whipple [52], depends on the ion drift velocity, the ion thermal speed, and the probe potential normalized to the ion temperature

$$\chi_p = -\frac{Ze\Phi_p}{T_{i\infty}}. \quad (\text{V.25})$$

By setting $w_d = 0$ we recover the well-known Langmuir formula [2]:

$$I_i = I_i^0 (1 + \chi_p). \quad (\text{V.26})$$

Figure (V-3) plots the OML ion current as a function of w_d for different probe potentials. Also shown for comparison is the Langmuir limit (Eq. (V.26)), and the ballistic limit given by $I_i = \pi R_p^2 N_\infty w_d v_{ti}$.

V.2 Ion collection in the drift approximation

While the just-reviewed large- R_L OML collection is well understood, little literature in the scaling $R_L \ll R_p \ll \Lambda_{De}$ is available. In this section, we investigate this regime with a 1D-kinetic/2D-drift model, similar in principle to the quasineutral kinetic approach followed in chapter II.

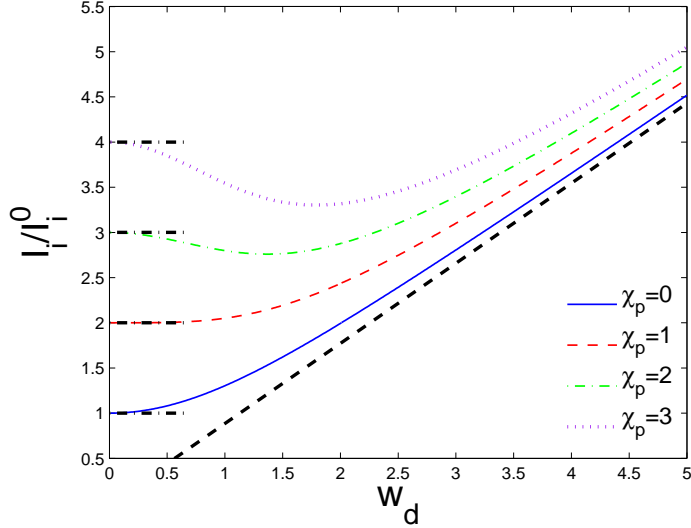


Figure V-3: Attracted ion current to a sphere of radius R_p as function of the drift velocity in OML conditions (Eq. (V.24)), normalized to $I_i^0 = 4\pi R_p^2 N_\infty v_{ti} / 2\sqrt{\pi}$ for different biases $\chi_p = -Ze\Phi_p/T_{i\infty}$. The thick dash-dot lines correspond to Eq. (V.26), and the thick dashed line to the ballistic limit ($I_i = \pi R_p^2 N_\infty w_d v_{ti}$).

V.2.1 1D-kinetic/2D-drift model

Equations and solution method

Let us consider as usual an ion attracting spherical probe, in the conditions $\mathbf{B} \parallel \mathbf{e}_z$ and *external* ion cross-field velocity $\mathbf{v}_\perp \parallel \mathbf{e}_y$. In the limit of infinite magnetization, the motion of a given ion across the magnetic field lines can be treated in the drift approximation, i.e. $(v_x, v_y)^T = \mathbf{E} \times \mathbf{B}/B^2$. Following the approach of chapter II, we can therefore write the parallel ion-charge distribution function f as solution of the 1D kinetic equation

$$v \frac{\partial f}{\partial z} + v_x \frac{\partial f}{\partial x} + v_y \frac{\partial f}{\partial y} - \frac{Ze}{m} \frac{\partial \Phi}{\partial z} \frac{\partial f}{\partial v} = 0, \quad (\text{V.27})$$

showing that f is conserved along (x, y, z, v) orbits that satisfy

$$\frac{d}{dt} \begin{cases} x \\ y \\ z \\ v \end{cases} = \begin{cases} v_x \\ v_y \\ v \\ -\frac{Ze}{m} \frac{\partial \Phi}{\partial z} \end{cases} \quad (\text{V.28})$$

The ion flux-density to a specific elementary portion of the probe surface is then calculated from the local parallel ion distribution function, obtained by tracing back to infinity each orbit having an inward velocity. The orbit integration is performed with the Matlab built-in function “ode45”, using an adaptive fourth or fifth order Runge Kutta scheme.

Contrary to the quasineutral regime, it is incorrect to assume $v_x = 0$ and uniform $v_y = v_\perp$. In the vacuum limit considered here, the probe-induced potential distribution is *exactly* given by Eq. (III.56) with $\lambda_{De} \rightarrow \infty$, i.e. is the sum of a vacuum monopole and dipole:

$$\Phi = \frac{\Phi_p}{r} + [E_{\text{cnv}} R_p] \frac{x}{r^3}, \quad (\text{V.29})$$

where (x, y, z) is the Cartesian position normalized to R_p , and we recall the notation $r = R/R_p$. The potential gradient therefore has the following components:

$$\frac{\partial \Phi}{\partial x} = -\Phi_p \frac{x}{r^3} - 3 [E_{\text{cnv}} R_p] \frac{x^2}{r^5} + [E_{\text{cnv}} R_p] \frac{1}{r^3}, \quad (\text{V.30})$$

$$\frac{\partial \Phi}{\partial y} = -\Phi_p \frac{y}{r^3} - 3 [E_{\text{cnv}} R_p] \frac{xy}{r^5}, \quad (\text{V.31})$$

$$\frac{\partial \Phi}{\partial z} = -\Phi_p \frac{z}{r^3} - 3 [E_{\text{cnv}} R_p] \frac{xz}{r^5}, \quad (\text{V.32})$$

and the *total* drift required to integrate the orbits (V.28), given by $v_y = v_\perp +$

$(\partial\Phi/\partial x)/B$ and $v_x = -(\partial\Phi/\partial y)/B$:

$$v_y = v_{\perp} \left(1 - \frac{1}{r^3} + \frac{\Phi_p}{[E_{\text{cnv}} R_p]} \frac{x}{r^3} + 3 \frac{x^2}{r^5} \right), \quad (\text{V.33})$$

$$v_x = -v_{\perp} \left(\frac{\Phi_p}{[E_{\text{cnv}} R_p]} \frac{y}{r^3} + 3 \frac{xy}{r^5} \right), \quad (\text{V.34})$$

tends to a limit different from $(v_{\perp}, 0)^T$ as B tends to infinity. It is easy to verify from Eqs (V.33,V.34) that the drift vector $(v_x, v_y)^T$ at $R = R_p$ is tangent to the probe surface, which is the physical translation of the probe being equipotential. As a result, if the parallel ion-charge distribution f at the probe surface is known, the parallel ion-charge flux-density (ion-charge collection per unit time per unit surface perpendicular to \mathbf{B}) is given by

$$\Gamma_{i\parallel} = \begin{cases} - \int_{v<0} v f(v) dv & \text{if } z \geq 0, \\ \int_{v>0} v f(v) dv & \text{if } z \leq 0. \end{cases} \quad (\text{V.35})$$

In order to maximize notation consistency within this thesis, the orbit equation (V.28) was written in terms of “ Φ ”. However because in the vacuum limit the electrons do not interact with the ions, the ion to electron temperature ratio τ is physically irrelevant: collected ion flux-densities normalized to $\Gamma_i^0 = N_{\infty} v_{ti} / (2\sqrt{\pi})$ will only depend on the dimensionless parameters w_{\perp} , w_{∞} , $\chi_p = -Ze\Phi_p/T_{i\infty}$ and β_i .

Ion orbits

Figure (V-4) shows a selection of ion orbits integrated backwards from different positions on the sphere surface, using the parameters $\chi_p = 10$, $\beta_i = 50$, and $w_{\perp} = 0.5$. The parallel external drift w_{∞} does not enter the orbit equation, but governs the phase space-density associated to each orbit, hence the collected ion current.

Rewriting the convective electric field in ion thermal units

$$\frac{E_{\text{cnv}}}{T_{i\infty}/Ze} = \frac{\sqrt{\pi} w_{\perp} \beta_i}{R_p} \quad (\text{V.36})$$

shows that part of the sphere becomes ion-repelling when $\sqrt{\pi}w_{\perp}\beta_i \geq \chi_p$, which is the case with our choice of parameters: $\chi(R_p) \in [\chi_p - \sqrt{\pi}w_{\perp}\beta_i : \chi_p + \sqrt{\pi}w_{\perp}\beta_i] \simeq [-34.3 : 54.3] \cdot \chi_p$. Although not a realistic situation (the dust particle's floating potential will adjust to a value negative enough such that electrons are repelled on its entire surface), it helps introduce important concepts.

The orbits on Figs (V-4a,b) “end” at $(x = -1, z = 0^+)$ and $(x = 1, z = 0^+)$, i.e. symmetrically with respect to the $\{0, \mathbf{e}_y, \mathbf{e}_z\}$ -plane, but behave quite differently. Orbit whose end-origin is on the repelling side (a) simply trace back to infinity, while orbits originating on side (b) can either trace back to infinity if their initial velocity $w_0 = v_0/v_{ti}$ is inwards enough, or reintersect the probe otherwise, in which case they do not contribute to the ion current. For this particular example, the orbit starting with $w_0 = -0.52$ is a limiting case since it closely follows the probe surface until it reaches the repelling probe side, and then picks up the cross-field velocity w_{\perp} . Orbits with smaller $|w_0|$ would close on the sphere.

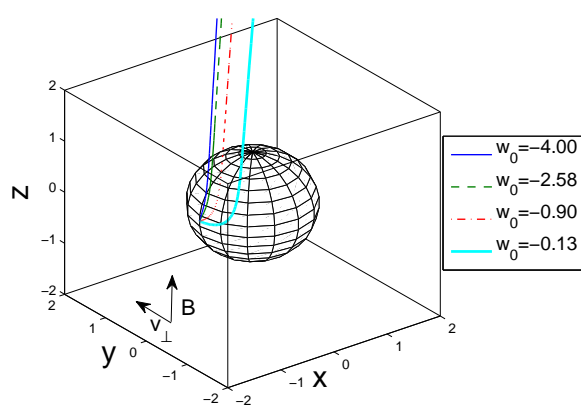
Accounting for finite β_i is necessary when the full potential distribution is considered in order to keep \mathbf{E}_{cnv} finite, not to capture finite Larmor radius effects absent from the drift model.

Investigation of the dipole effect

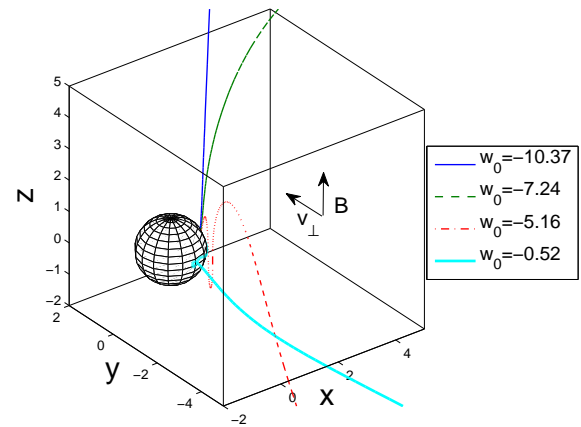
Ion collection in the strongly magnetized vacuum limit differs from its strongly magnetized quasineutral counterpart (chapter II) in two ways:

- The long-range vacuum potential starts deflecting the ion orbits through parallel acceleration $(-c_{s0}^2 \partial\phi/\partial z)$ at $y \ll -1$, while no quasineutral potential perturbation permeates in the region $y \leq -1$.
- In the drift approximation considered here, the ions are collected with purely parallel velocity due to the sphere shielding out the external convective electric field. Furthermore, the sphere's effective potential spanning the range $\chi(R_p) \in [\chi_p - \sqrt{\pi}w_{\perp}\beta_i : \chi_p + \sqrt{\pi}w_{\perp}\beta_i]$, taking the limit $\beta_i = \infty$ does not seem possible in the presence of cross-field drift ($w_{\perp} \neq 0$). Because in the quasineutral limit

(a)



(b)



(c)

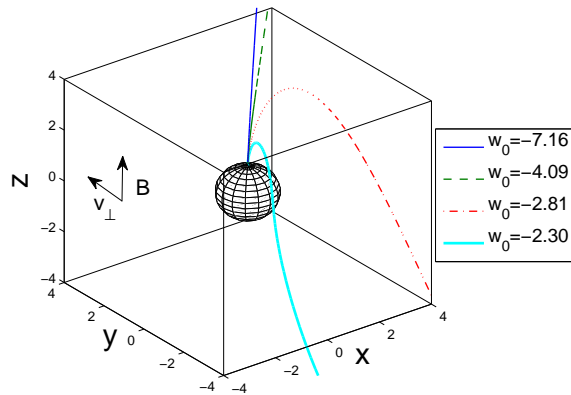


Figure V-4: Selection of 3D ion orbits, solutions of Sys. (V.28), traced backwards from the probe surface at (a) $x = -1$, $z = 0^+$, (b) $x = 1$, $z = 0^+$ and (c) $x = 0$, $y = 0$, $z = 1$. $w_0 = v_0/v_{ti}$ is the “initial” backwards parallel velocity of the considered orbit. The simulation parameters for this example plots are $\chi_p = 10$, $\beta_i = 50$, and $w_\perp = 0.5$.

the probe-induced potential is shielded by a thin layer assumed much smaller than the ion Larmor radius, those effects were not observed.

In order to isolate those two effects, hence increase physical insight, we need to suppress the probe shielding of the convective electric field (effective “dipole”). For this purpose, we need to integrate the orbits in a pure Coulomb field, i.e replace Eq. (V.29) by $\Phi = \Phi_p/r$, Eqs (V.34,V.33) by $v_y = v_\perp$ and $v_x = 0$, and Eq. (V.35) by

$$\Gamma_{i\parallel} = \begin{cases} \int_{v_r < 0} (-v + v_\perp \cot \eta) f(v) dv & \text{if } z \geq 0, \\ \int_{v_r < 0} (v - v_\perp \cot \eta) f(v) dv & \text{if } z \leq 0, \end{cases} \quad (\text{V.37})$$

where as usual η is the angle of probe surface to magnetic field in any $\{\mathbf{e}_y, \mathbf{e}_z\}$ -plane.

The solution without dipole is not really physical, although it could model a thought experiment where the convective electric field is replaced by gravity, or a cumbersome multifaceted spherical probe where each facet is biased to an appropriately chosen different potential such as to approximately support the convective electric field. It is of course independent of β_i , as for the quasineutral limit of chapter II.

V.2.2 Results and physical discussion

Total ion current

The first important physical quantity to compute is the total ion current I_i , obtained after sphere-integration of $\Gamma_{i\parallel}$ (Eq. (V.35) or Eq. (V.37)). For convenience, we recall the formula (IV.3):

$$I_i = \frac{\pi}{2} R_p^2 \int_0^{2\pi} \Gamma_{i\parallel}(\eta) |\sin \eta| d\eta, \quad (\text{V.38})$$

The solution is plotted in Fig. (V-5) as a function of cross-field drift w_\perp for a selection of probe potentials χ_p , in the absence of external parallel drift ($w_\infty = 0$).

Let us start with the analysis of Fig. (V-5b), only accounting for the probe monopole. In the limit $w_\perp \rightarrow 0$, the ion current tends to the geometric value $I_i = I_i^0/2$

regardless of χ_p ; for strongly attractive probes however, the current quickly rises to a local maximum located around $w_\perp = 0(1)$, before progressively reaching the ballistic asymptote given by $I_i = \pi R_p^2 N_\infty w_d v_{ti}$. Figure (V-5a) accounting for the full potential distribution at $\beta_i = 100$ is qualitatively similar, although at equal bias and velocity, the current is lower. This difference is due to the reduction in cross-field velocity experienced by the ions as they approach the conductor. It can be seen, for instance, that in the limit $w_\perp \gg 1$ the ion current falls below the ballistic limit.

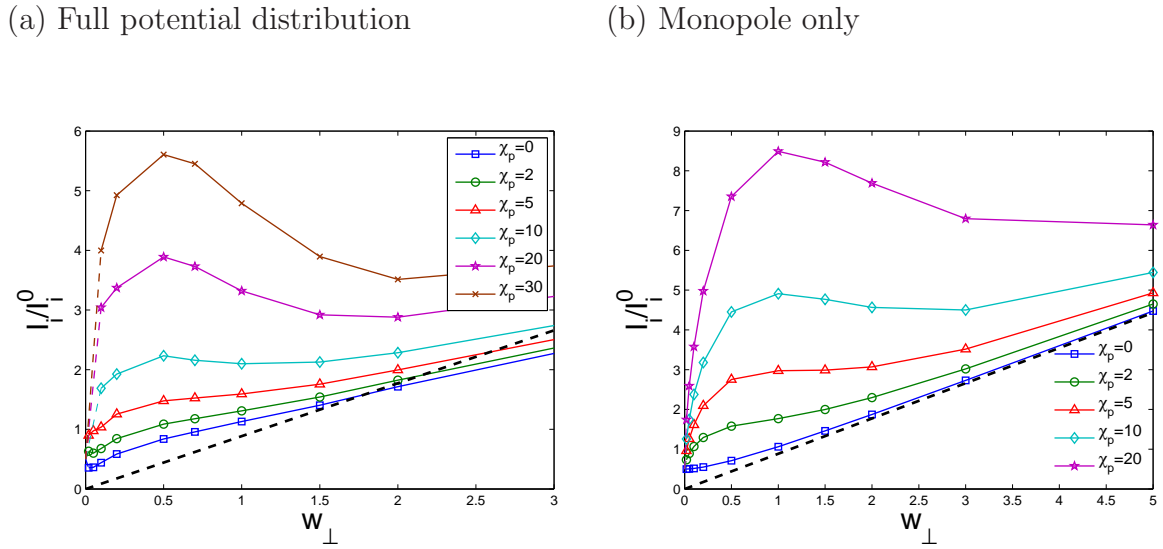


Figure V-5: Total ion current normalized to $I_i^0 = 4\pi R_p^2 N_\infty v_{ti} / 2\sqrt{\pi}$, solution of the 1D-kinetic/2D-drift model in the absence of external parallel drift ($w_\infty = 0$). (a) Accounting for the dipole term, with $\beta_i = 100$. (b) Omitting the dipole term. The thick dashed lines correspond to the ballistic asymptote given by $I_i = \pi R_p^2 N_\infty w_d v_{ti}$.

Figures (V-5a,b) are the counterpart of Fig. (V-3) in the strong magnetization limit. The ion current evolution with increasing drift velocity is a trade-off between a decrease in the number of collected orbits and an increase in the (initial, i.e. at infinity) orbit velocities. The balance of those two effects appears to invert with ion magnetization, since in the absence of magnetic field the (OML) current has a local minimum rather than maximum for high enough χ_p (Fig. (V-3)).

Flux ratios

Flux-sensing probes rarely operate in the simultaneous limit $\Lambda_{De} \gg R_p$ and $\beta_i \gg 1$. It is nevertheless instructive to verify if there is a simple relationship between the plasma drift velocity and the flux ratios $R_{3\pi/4} = \Gamma_i(\eta = -\pi/4)/\Gamma_i(\eta = 3\pi/4)$ and $R_{\pi/4} = \Gamma_i(\eta = -3\pi/4)/\Gamma_i(\eta = \pi/4)$, as in the quasineutral regime (chapters II,IV).

Figures (V-6a,b) show the flux ratio dependence on w_\perp at $w_\infty = 0$, i.e. when $R_{3\pi/4} = R_{\pi/4}$, for a selection of probe biases. When only accounting for the probe monopole, the flux ratios increase monotonically with w_\perp , as intuition would suggest; in the limit $w_\perp = 0$, ion collection becomes purely geometrical: $\Gamma_{i\parallel}(\eta = \pm\pi/4, \pm 3\pi/4) \rightarrow \Gamma_i^0$, hence $R_{\pi/4,3\pi/4} \rightarrow 1$.

Figure (V-6a), showing flux ratios when the full potential distribution is accounted for, is quite different. The ratios still tend to unity at $w_\perp = 0$, but do not increase exponentially with w_\perp . The physical explanation is that regardless of w_\perp , ion collection always occurs with zero transverse velocity and the current is only due to the parallel component of the distribution function. For strong enough cross-field drift, the angular flux distribution is seen to reverse, which is reminiscent of a similar effect observed in the magnetic-free regime by Hutchinson [10]. Because there is no one-to-one relationship between flux ratios and drift velocity, it appears quite difficult to propose a Mach-probe calibration method.

V.2.3 The question of stationary magnetoplasmas

Figure (V-7) is the counterpart of Fig. (V-5) in the collisionless quasineutral limit. Although a direct quantitative comparison is not possible, since the quasineutral and vacuum ion currents depend on different plasma parameters, it clearly appears that the quasineutral current does not tend to the geometric limit $I_i = I_i^0/2$ at zero drift, except in the limit $\tau \gg 1$ (free-flight).

As explained in chapter II, no self-consistent solution to the collisionless magnetized plasma equations exists in the absence of convective drift. My Master thesis [14] was focussed on collisionless ion collection by spherical probes in stationary magne-

(a) Full potential distribution

(b) Monopole only

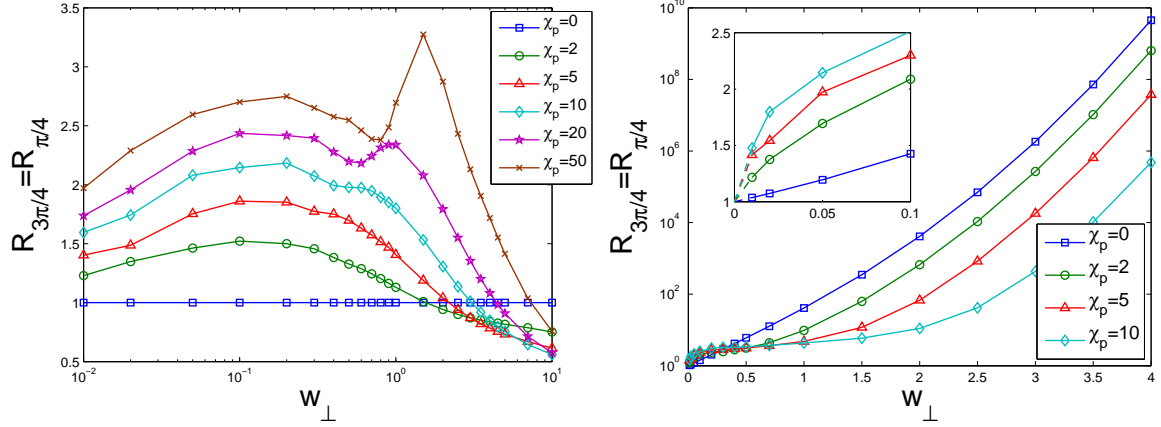


Figure V-6: Flux ratios $R_{3\pi/4} = R_{\pi/4}$ as a function of w_\perp with $w_\infty = 0$, obtained with the 1D-kinetic/2D-drift orbit integration. (a) Accounting for the dipole term, with $\beta_i = 100$. (b) Omitting the dipole term.

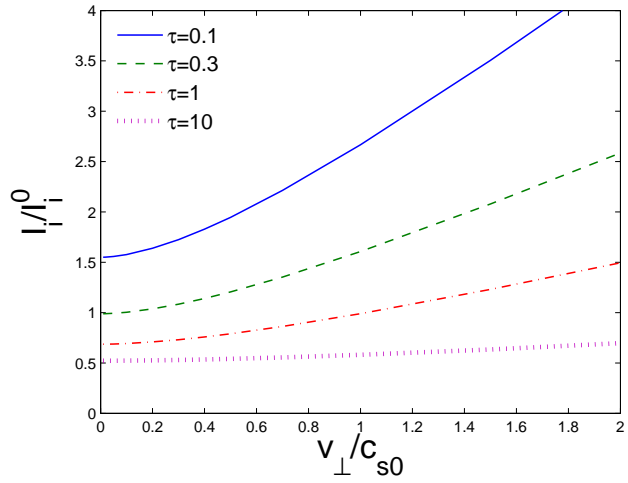


Figure V-7: Total (i.e. sphere-integrated) ion current normalized to $I_i^0 = 4\pi R_p^2 N_\infty v_{ti} / 2\sqrt{\pi}$, solution of the collisionless quasineutral 1D-kinetic model of chapter II (kinetic equation (II.50), valid when $\beta_i \rightarrow \infty$ and $\Lambda_{De} \ll R_L$) with $v_\infty = 0$. Except in the limit $\tau \gg 1$, the ion current at $v_\perp = 0$ is higher than the geometric limit $I_i^0/2$.

toplasmas, and only weak enough magnetic fields $\beta_i \lesssim 1$ could be considered in order to ensure physically meaningful results. Even accounting for cross-field transport in Fig. (V-7) would not drive the zero-drift current towards $I_i^0/2$.

Only the free-flight and the vacuum limits allow a collisionless treatment of the stationary magnetized probe problem, because ions and electrons are decoupled. The problem in the vacuum limit, where the potential naturally adopts a Coulomb form, was first solved by Sonmor and Laframboise [13] by direct orbit integration. The next section briefly reviews concepts pertaining to the stationary (or parallel-drifting) plasma regime, accounting for finite Larmor radius effects.

V.3 Review of collection in stationary, large Debye length magnetoplasmas

V.3.1 Parker-Murphy upper bound current

Let us consider a magnetized plasma in the absence of convective electric field (i.e. the plasma-drift is along the magnetic field lines). Each particle (ion or electron) has then two conserved quantities; for the ions in cylindrical coordinates (z, ρ, ψ) , those are the energy

$$W_0 = \frac{m}{2} (v_\rho^2 + v_z^2 + v_\psi^2) + Ze\Phi, \quad (\text{V.39})$$

and the canonical angular momentum about the magnetic axis

$$J_z = m\rho^2 \frac{d\psi}{dt} + \frac{1}{2} ZeB\rho^2. \quad (\text{V.40})$$

Combination of Eq. (V.39) and Eq. (V.40) gives:

$$W_0 = \frac{m}{2} (\dot{\rho}^2 + \dot{z}^2) + Ze\Phi(z, \rho) + \frac{m}{2} \rho^2 \left(\frac{J_z}{m\rho^2} - \frac{ZeB}{2m} \right)^2. \quad (\text{V.41})$$

Because $\dot{\rho}^2 + \dot{z}^2 \geq 0$, the ion is confined in a “magnetic bottle”, defined by the following implicit equation:

$$\mathfrak{I}(z, \rho) = W_0 - Ze\Phi(z, \rho) - \frac{m}{2}\rho^2 \left(\frac{J_z}{m\rho^2} - \frac{ZeB}{2m} \right)^2 \leq 0. \quad (\text{V.42})$$

One can easily solve Eq. (V.42) for ρ_∞ in the case of a cold plasma with drift velocity $\mathbf{v}_d \parallel \mathbf{B}$. The conserved quantities are $W_0 = mv_d^2/2$ and $J_z = ZeB\rho_\infty^2/2$, therefore:

$$\rho_\infty \leq \rho \left\{ 1 + \frac{2m}{ZeB} \left[\frac{2}{m\rho^2} \left(\frac{1}{2}mv_d^2 - Ze\Phi(\rho, z) \right) \right]^{1/2} \right\}^{1/2}. \quad (\text{V.43})$$

The maximum impact parameter for a particle to be collected is hence given by Eq. (V.43) by setting $\Phi = \Phi_p$ and $\rho = R_p$. This has first been done by Parker and Murphy [53] for a cold stationary plasma:

$$R_{PM} = R_p \left[1 + \frac{2m}{ZeB} \left(\frac{-2Ze\Phi_p}{mR_p^2} \right)^{1/2} \right]^{1/2}. \quad (\text{V.44})$$

They then calculated an upper bound to the collected current by assuming that at infinity the plasma still has a small thermal motion, thus obtaining:

$$I_i \leq I_i^{PM} = 2N_\infty \left[\frac{v_{ti}}{2\sqrt{\pi}} (\pi R_{PM}^2) \right] = I_i^0 \left[\frac{1}{2} + \frac{2}{\sqrt{\pi}} \frac{\sqrt{\chi_p}}{\beta_i} \right] \quad (\text{V.45})$$

Figure (V-8) shows the critical magnetic bottles for the case $W_0 = 0$ (stationary cold ion at infinity), and a Coulomb potential distribution $\Phi(\rho, z) = \Phi_p/\sqrt{\rho^2 + z^2}$ with $8m\Phi_p/ZeB^2R_p^2 = -5$. Those are obtained from Eq. (V.42) with $\rho_\infty = R_{PM}$ using the Matlab implicit plotting capabilities.

Later, Rubinstein and Laframboise [54] extended Parker’s result to a stationary Maxwellian plasma with arbitrary temperature. Their expression, given by Eqs (30,33,35) from the previous reference, is quite complicated and not reported here. We will refer to it as the canonical upper bound I_i^{Can} .

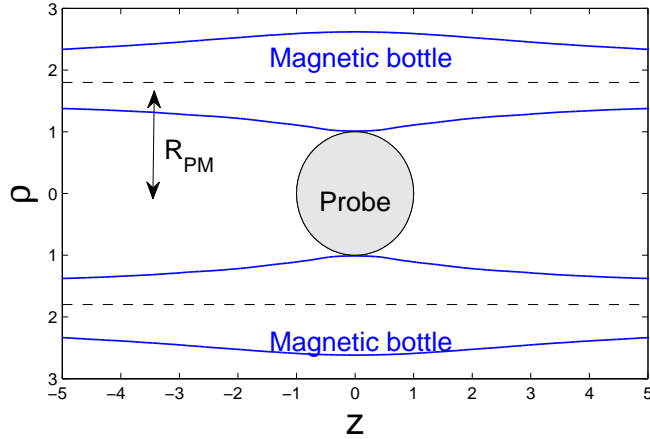


Figure V-8: Magnetic bottles for an ion starting at $\rho = R_{PM}$ (Eq. (V.44)) with zero velocity, using example plasma parameters such that $8m\Phi_p/ZeB^2R_p^2 = -5$ and an assumed Coulomb potential distribution. The Parker-Murphy upper bound current is calculated by assuming that each ion starting at $\rho \leq R_{PM}$ is collected.

V.3.2 Free-flight magnetized current

Zero drift

In the intermediate magnetic field regime ($0 < \beta_i < \infty$), the current to a spherical electrode of radius unity at space potential can be evaluated by summing the contribution of helices of radius s , wave length $2\pi t$, guiding center distance to the magnetic axis of the probe u , and phase $\varphi \in [0 : 2\pi]$ distributed according to a drifting Maxwellian (only four variables are necessary to describe the helices because we have azimuthal symmetry about the magnetic axis). Figure (V-9) is a schematic of the problem.

The calculation was first done in the stationary case ($v_d = 0$) by Whipple [55], whose expression can be recovered by setting $D = 0$ in Eq. (9) from Ref. [54].

$$\frac{I_i}{I_i^0} = \frac{1}{4}\pi^2\beta_i^4 \int_{s=0}^{\infty} \int_{t=0}^{\infty} \tilde{f}(\beta_i, s, t) \left[\frac{1}{2}\theta(1-s)(1-s)^2 + \int_{u=|s-1|}^{s+1} \frac{1}{2\pi} \int_{\varphi=0}^{2\pi} H(u, s, t, \varphi) u du \right] s t ds dt \quad (\text{V.46})$$

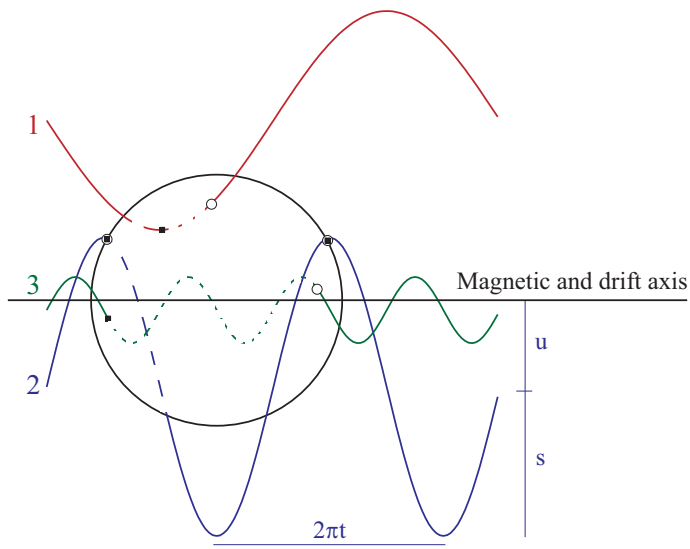


Figure V-9: Schematic of three different kind of orbits. Solid portions of orbits are visible, dashed portions are behind the sphere, and dotted portions are inside the probe. Orbit n^o1 has $s_1 + u_1 > 1$ and $|s_1 - u_1| < 1$. The phase φ_1 is such that the orbit crosses the sphere, but because the wavelength is “long” ($t_1 > t_1^*(s_1, t_1, u_1)$, see Appendix A in Ref. [14]), there are phases $\tilde{\varphi}$ such that $H(u_1, s_1, t_1, \tilde{\varphi}) = 0$. Orbit n^o2 , for which the geometrical meaning of s , t and u is shown, has $s_2 + u_1 > 1$ and $|s_2 - u_2| < 1$. It is a critical orbit because $H(u_2, s_2, t_2, \varphi_2) = 1$ regardless of φ_2 ($t_2 = t_2^*(s_2, t_2, u_2)$). Orbit n^o3 has $u_3 + s_3 < 1$, hence $H(u_3, s_3, t_3, \varphi_3) = 1$ regardless of φ_3 .

with:

$$\tilde{f}(\beta_i, s, t) = \exp\left[-\frac{\pi}{4}\beta_i^2(s^2 + t^2)\right]. \quad (\text{V.47})$$

I_i/I_i^0 (Eqs (V.46,V.47)) can be seen as the current reduction factor from the value in an unmagnetized plasma. \tilde{f} is a form of the Boltzmann exponential appearing in the Maxwellian distribution function. The term $\frac{1}{2}\theta(1-s)(1-s)^2$ counts the orbits with $s+u < 1$, that we know for sure are collection orbits (θ is the Heaviside step function). The term $\int_{u=|s-1|}^{s+1} \frac{1}{2\pi} \int_{\varphi=0}^{2\pi} H(u, s, t, \varphi) u du$ counts the current collected from the orbits with $s+u \geq 1$ and $|u-s| \leq 1$. That is to say helixes part in the magnetic shadow and part outside. The impact factor $H(u, s, t, \varphi)$ (equal to 1 if the orbit characterized by (u, s, t, φ) intersects the sphere at least once and 0 otherwise) has been calculated by Rubinstein and Laframboise in Ref. [54]. Orbits characterized by $u > s+1$ do not intersect the sphere.

This integral is expensive to evaluate as $\beta_i \rightarrow 0$ and was performed in Ref. [14] using a second order trapezoidal rule with adaptive step-size down to $\beta_i = 0.002$. The result is shown in Fig. (I-4) of Ref. [14].

It was shown (see Appendix A, Ref. [14]) by expansion starting from the integral expression of Eq. (V.46) that the slope of the current reduction at $\beta_i = 0$ is $C = 1/3\pi$:

$$\frac{I_i}{I_i^0}(\beta_i) = 1 - \frac{1}{3\pi}\beta_i + O(\beta_i^2). \quad (\text{V.48})$$

Equation (V.48) is in contradiction to the statement of Rubinstein and Laframboise (“Results and discussions” [54]) that the dependence on β_i is quadratic. The physical origin of this linear dependence can be understood as follows. We can choose a given point on the sphere surface, and consider the orbits there. Under the hypothesis of small β_i , the majority of those orbits can be traced back to infinity, while a small fraction re-intersect the probe at least once. Orbits that reintersect the sphere are unpopulated. It is this effect that entirely accounts for flux reduction. In order of magnitude, the reintersecting orbits require $|v_z| \lesssim R_p\omega_c/\pi$, which delimits a solid angle proportional to $|v_z|$ (not v_z^2 as erroneously argued by Rubinstein and Laframboise). Since at small velocity the Maxwellian distribution is independent of \mathbf{v} , doubling β_i

will simply double the fraction of such orbits, therefore doubling the depletion due to the magnetic field.

Extension to parallel drifts

Extension of Eq. (V.48) to plasmas drifting parallel to the magnetic field is discussed in Ref. [14]. Because the problem is still axisymmetric with respect to the magnetic axis, Eq. (V.46) still applies provided \tilde{f} is replaced by the average of the Boltzmann exponential appearing in the drifting Maxwellian with drift velocities $w_d = v_d/v_{ti}$ and $-w_d$:

$$\tilde{f}(\beta_i, s, t, w_d) = \frac{1}{2} \exp \left\{ -\frac{\pi}{4} \beta_i^2 \left[s^2 + \left(t - w_d \frac{2}{\beta_i \sqrt{\pi}} \right)^2 \right] \right\} - \frac{1}{2} \exp \left\{ -\frac{\pi}{4} \beta_i^2 \left[s^2 + \left(t + w_d \frac{2}{\beta_i \sqrt{\pi}} \right)^2 \right] \right\}. \quad (\text{V.49})$$

The corresponding current solution expanded at low β_i was given by Eq. (IV.7).

V.3.3 Helical upper bound current

The ion current to a stationary spherical probe in a collisionless, stationary magnetoplasma is framed by its value at $\beta_i = 0$ and $\beta_i = \infty$. The first bound is simply Eq. (V.26), while the second is independent of the probe potential by virtue of flux conservation, and is given by

$$I_i^{|\beta_i=\infty} = \frac{1}{2} I_i^0. \quad (\text{V.50})$$

In order to improve this framing, the idea developed by Rubinstein and Laframboise [54] is to assume that the effects of orbit depletion due to multiple intersections with the probe occur in a neighborhood of the probe where the ions have already been accelerated by χ_p . An upper bound, called “Helical” in order to avoid a confusion with the “Canonical” bound, is obtained taking this portion of distribution function to be given by f^{3D} :

$$f^{3D}(\mathbf{v}) = \begin{cases} \frac{N_\infty}{(v_{ti}\sqrt{\pi})^3} \exp \left(-\frac{v^2}{v_{ti}^2} + \chi_p \right) & \text{if } v^2/v_{ti}^2 - \chi_p \geq 0, \\ 0 & \text{if } v^2/v_{ti}^2 - \chi_p < 0. \end{cases} \quad (\text{V.51})$$

The normalized current can therefore be written as:

$$\frac{I_i}{I_i^0} = \frac{\exp(\chi_p)}{4} \pi^2 \beta_i^4 \int_{s=0}^{\infty} \int_{t=0}^{\infty} \tilde{\theta}(\beta_i, \chi, s, t) \tilde{f}(\beta_i, s, t) \\ \left[\frac{1}{2} \theta(1-s)(1-s)^2 + \int_{u=|s-1|}^{s+1} \frac{1}{2\pi} \int_{\varphi=0}^{2\pi} H(u, s, t, \varphi) u du \right] stdsdt \quad (\text{V.52})$$

with \tilde{f} given by Eq. (V.47), $\tilde{\theta}(\beta_i, \chi, s, t) = \theta(s^2 + t^2 - D^2)$, and D defined by :

$$D = \frac{2}{\beta_i} \sqrt{\frac{\chi_p}{\pi}}. \quad (\text{V.53})$$

It is demonstrated in Appendix A from Ref. [14] that:

$$\frac{I_i^{\text{Hel}}}{I_i^0} = (1 + \chi_p) - \left[\frac{1}{3\pi} \text{erfc}(\sqrt{\chi_p}) \exp(\chi_p) + \frac{2}{3} \frac{\sqrt{\chi_p}}{\pi^{3/2}} \right] \beta_i + O(\beta_i^2) \quad (\text{V.54})$$

In the limit $\chi_p \rightarrow 0$, the upper bound becomes exact as it tends towards the free-flight current (V.48). For high enough potentials, I_i^{Hel} is higher than I_i^{Can} . The optimum upper bound is therefore

$$I_i^{\text{UP}} = \min(I_i^{\text{Hel}}, I_i^{\text{Can}}). \quad (\text{V.55})$$

V.3.4 Ion current calculations

SCEPTIC(2D) has built in a sophisticated ion reinjection scheme based on energy and angular momentum conservation [10], whose operation in the absence of magnetic field is *equivalent* to injecting ions at the outer boundary accounting for the potential drop existing between the reinjection point and infinity. This feature is particularly convenient in large Debye length plasmas, as it mitigates the need for a large computational domain. Of course individual ions' angular momentum with respect to the probe center is not conserved in magnetized plasmas, and we have in this thesis no choice but taking a computational domain large enough for the electrostatic potential to be negligible at the outer boundary (or at least at the upstream outer boundary in flowing cases), and reinject a Maxwellian there.

The question is, what does “negligible potential” mean ? The problem of ion current collection by a Coulomb sphere in a stationary magnetoplasma ($\Phi(R) = \Phi_p R_p / R$) has been solved by Sonmor and Laframboise [13] by direct orbit integration. Numerical experimentation shows that in general SCEPTIC calculations in an exact Coulomb potential approach Sonmor and Laframboise’s results to $\sim 10\%$ when using the domain size $R_b = 100R_p$. A highly unreasonable domain size of the order $R_b \sim 1000R_p$ would presumably be required to reduce the discrepancy to less than 1%.

We therefore abandon the hope of simulating *infinite* Debye length magnetized plasmas, and consider instead a plasma with large but finite Debye length. Here we bypass SCEPTIC3D’s Poisson solver and impose the potential distribution

$$\Phi(R) = \Phi_p \frac{R_p}{R} \left[\frac{\exp\left(-\frac{R-R_p}{\Lambda_s}\right)}{1 - \exp\left(-2\frac{R_b-R_p}{\Lambda_s}\right)} + \frac{\exp\left(\frac{R-R_p}{\Lambda_s}\right)}{1 - \exp\left(2\frac{R_b-R_p}{\Lambda_s}\right)} \right]. \quad (\text{V.56})$$

Equation (V.56) is the solution of the spherically symmetric Debye-Hückel equation (V.18) with shielding length Λ_s , vanishing at the domain boundary R_b rather than infinity. By choosing $\Lambda_s = R_b = 70R_p$, we hope to be close enough to the Coulomb form, yet have a zero outer potential and a manageable domain size.

Figure (V-10) shows the ion current dependence on magnetization β_i in the absence of plasma drift, computed with SCEPTIC(2D) by direct orbit integration in the “quasi” Coulomb potential (V.56) for two probe biases ($\chi_p = 5$ and $\chi_p = 15$). It can be seen that the current tends to the OML value predicted by Eq. (V.26) at $\beta_i = 0$, and to $I_i^0/2$ at $\beta_i = \infty$ (geometric collection). The curves labeled “Sonmor” refer to table I from Ref. [13], hence valid in an exact Coulomb potential. We conclude that our *ad hoc* potential (V.56) with $\Lambda_s = R_b = 70R_p$ successfully mocks the Coulomb potential for $\beta_i \gtrsim 1$ (perfect match between SCEPTIC and Sonmor’s calculations), as well as for $\beta_i \sim 0$ (perfect match with the OML solution). A discrepancy of order 10% exists at $\beta_i \sim 0.3$, that would presumably disappear by increasing R_b and Λ_s .

The ion current to a stationary sphere is a monotonically decreasing function of β_i ; this current reduction is exclusively due to the geometric effects reducing the

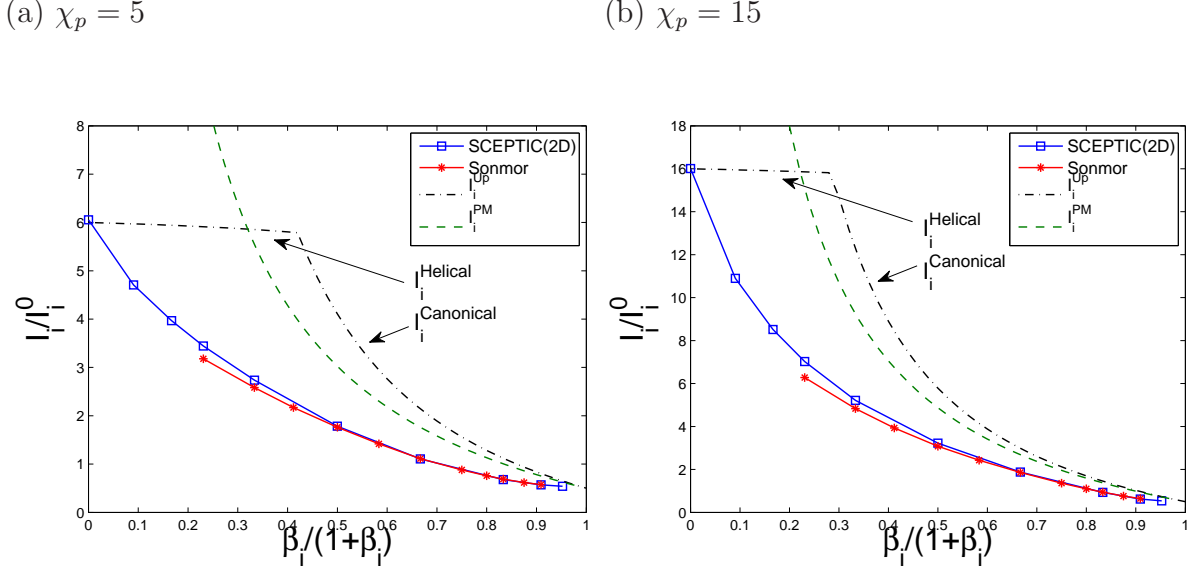


Figure V-10: Total ion current normalized to $I_i^0 = 4\pi R_p^2 N_\infty v_{ti}/2\sqrt{\pi}$ as a function of ion magnetization β_i , calculated by direct orbit integration with SCEPTIC3D using the potential distribution (V.56). The external plasma is stationary ($\mathbf{v}_d = 0$). Curves labeled “Sonmor” refer to table I from Ref. [13], I_i^{UP} to the upper bound, and I_i^{PM} to the Parker-Murphy upper bound (Eq. (V.45)). (a) Probe potential $\chi_p = -\phi_p/\tau = 5$; (b) $\chi_p = 15$.

“apparent” cross-sectional area of the collector as shown in Fig. (V-8). The figure also shows the upper bound I_i^{UP} (Eq. (V.55)), and the Parker-Murphy’s upper bound (Eq. (V.45)). The high-field portion of I_i^{UP} , corresponding to I_i^{Can} , slightly exceeds I_i^{PM} because the latter does not take into account thermal effects. We refer to Ref. [13] for more discussion on how the exact current approaches the bounds.

V.4 Ion collection in arbitrarily magnetized flowing plasmas

V.4.1 Total ion current

The natural extension of sections V.2, V.3 is to consider a flowing plasma at finite ion magnetization, still in the vacuum limit. SCEPTIC3D can easily model this problem, using an imposed potential distribution given by the monopole term (V.56) plus the appropriate additional vacuum dipole term.

Figure (V-11) shows the total ion current as a function of β_i for two probe biases (a) $\chi_p = 1$ and (b) $\chi_p = 50$, in the drift conditions $w_\perp = 0.5$, $w_\infty = 0$. At moderate magnetization, the qualitative behaviour of the ion current is similar to what was observed in the quasineutral regime in the presence of strong cross-field flow (e.g. Fig. (IV-7c)). The ion current first increases starting from the unmagnetized limit (here given by the OML solution (V.24)), before peaking and decreasing.

The vertical dotted lines in Fig. (V-11) separate the physically relevant parameter regime where the entire probe surface is ion-attracting ($|E_{\text{cnv}}R_p| < |\Phi_p|$, left) from the regime where part of the probe is ion-repelling. Indefinitely increasing β_i at fixed w_\perp causes the attracting part of the sphere to be more and more attracting, while the repulsive part can't compensate more than collecting no ions. This effect can be seen in Fig. (V-11a), where the total ion current increases when $\beta_i \gtrsim 20$.

(a) $\chi_p = 1$

(b) $\chi_p = 50$

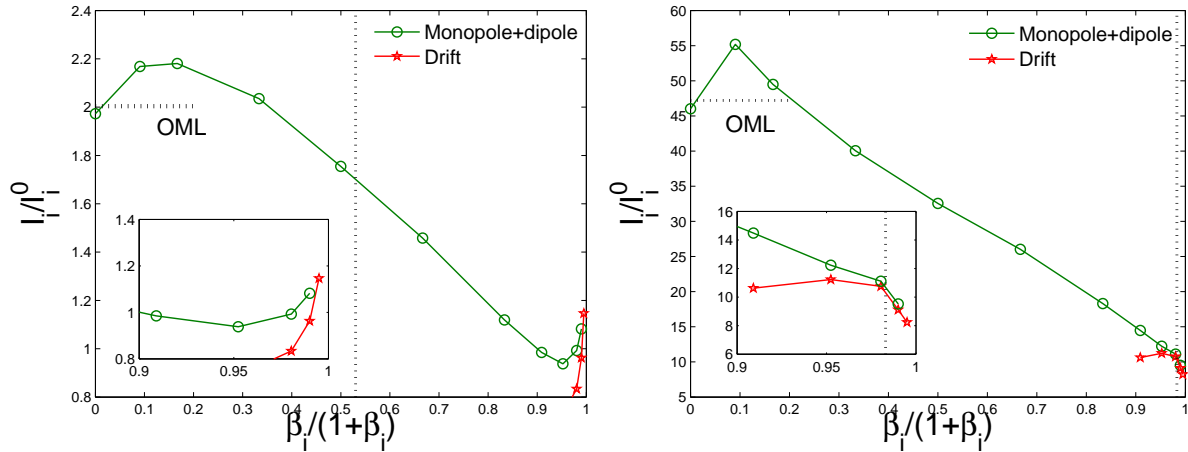


Figure V-11: Total ion current normalized to $I_i^0 = 4\pi R_p^2 N_\infty v_{ti} / 2\sqrt{\pi}$ as a function of ion magnetization β_i , calculated by direct orbit integration with SCEPTIC3D, for probe biases (a) $\chi_p = 1$ and (b) $\chi_p = 50$, in a pure cross-field drift $w_\perp = 0.5$. In (a) and (b), SCEPTIC3D calculations accounting for the full potential distribution (“Monopole+dipole”) are compared with the solutions of the 1D-kinetic/2D-drift model of paragraph V.2 (“Drift”).

Also shown in Fig. (V-11) is a successful comparison with the 1D-kinetic/2D-drift calculations at strong magnetization, validating both methods. It must be recalled that the 1D-kinetic/2D-drift solution dependence on β_i is solely due to the effec-

tive probe dipole affecting the transverse ion drifts and the parallel dynamics; finite Larmor radius effects are *not* taken into account, explaining why agreement with SCEPTIC3D is only reached at extremely strong magnetic field ($\beta_i \gtrsim 100$).

V.4.2 Angular ion flux-density distribution

Figure (V-12) shows the ion flux-density to the probe major cross-section in the plane of flow and magnetic field $\{0, \mathbf{e}_y, \mathbf{e}_z\}$ as a function of $\cos \theta$ (recall that θ is the angle of position to magnetic field in spherical coordinates, as defined for instance in Fig. (III-2a)); the curves are therefore closed on themselves, the upper portions corresponding to $\sin \theta \leq 0$ and the lower portions to $\sin \theta \geq 0$. The conditions are $w_\perp = 0.5$, $w_\infty = 0$, and $\chi_p = 50$.

The dotted curve, referring to the 1D-kinetic/2D-drift solution, vanishes on the probe leading edge ($\theta = -\pi/2$) in addition to vanishing on the wake edge ($\theta = \pi/2$), which is different from what was observed in the quasineutral regime. Of course finite ion magnetization tends to smooth discontinuities, causing SCEPTIC3D's computed current never to vanish.

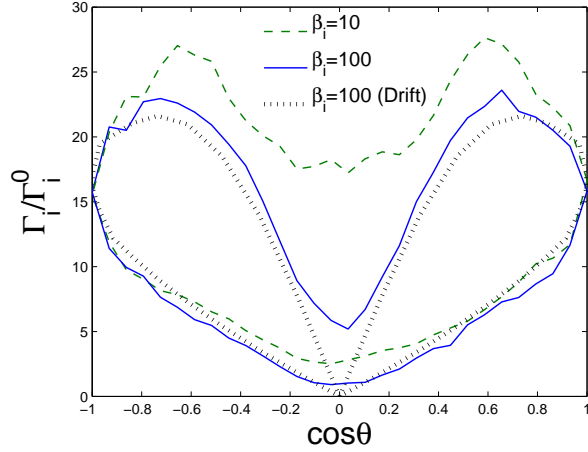


Figure V-12: Angular ion flux-density distribution to the probe major cross-section in the plane of flow and magnetic field $\{0, \mathbf{e}_y, \mathbf{e}_z\}$ normalized to $\Gamma_i^0 = N_\infty v_{ti} / (2\sqrt{\pi})$. Calculations have been performed in with SCEPTIC3D in a prespecified vacuum potential for $\beta_i = 10$ and $\beta_i = 100$. “drift” refers to the 1D-kinetic/2D-drift solution. The probe bias is $\chi_p = 50$.

The observation that in the limit of vanishing Larmor radius no current is collected on the $\{0, \mathbf{e}_x, \mathbf{e}_y\}$ -plane was already made in Ref. [56] in the context of electron collection by positively charged spacecraft.

V.4.3 Plasma profiles

Figure (V-13) shows two density contour-plots computed by SCEPTIC3D in the $\{0, \mathbf{e}_y, \mathbf{e}_z\}$ -plane for $\beta_i = 5$ (transition between intermediate and strong magnetization), $w_\perp = 0.5$ and $w_\infty = 0$, with (a) $\chi_p = 15$ and (b) $\chi_p = 50$.

A quick comparison with Fig. (IV-2) shows that the plasma responds quite differently to the probe depending on the Debye length. In the quasineutral limit, no information could propagate against the cross-field drift and the fluid stream-lines started to curve at $y \sim -1$. Here, we see that the stronger the probe bias, the wider the collection flux-tube (critical streamlines, in red). In the presence of non negligible cross-field drift then, the current increase with increasing probe bias can be explained by the parallel ion dynamics only. The situation was different in the stationary case (Fig. (V.3)), where current increase with increasing probe bias was due to ion demagnetization (polarization drift), hence directly dependent on the Larmor radius.

The initial current increase with β_i at weak magnetization observed in Fig. (V-11) has the same physical origin as in the quasineutral regime. When $\beta_i = 0$, the probe focusses the ions downstream; as β_i increases, part of the ions that would miss the probe in the absence of magnetic field are collected downstream while the upstream current is unaffected. Perhaps an easier way to understand this phenomenon is to look at the critical streamlines in the $\{0, \mathbf{e}_y, \mathbf{e}_z\}$ -plane at $\beta_i = 0$ and $\beta_i = 0.1$, shown in Fig. (V-14) for $\chi_p = 15$, $w_\perp = 0.5$ and $w_\infty = 0$. The collection flux-tube is broader for weak but non-zero magnetic field. In the absence of drift (or if the drift is parallel to the probe), this phenomenon cannot happen, and the current *must* decrease with increasing β_i as observed in Fig. (V-10).

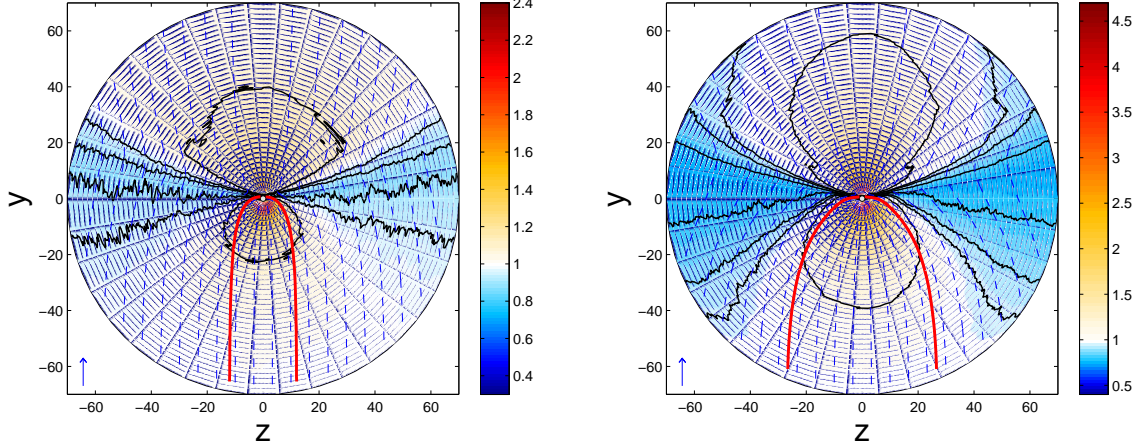
(a) $\chi_p = 15$ 

Figure V-13: Normalized ion charge-density contour-plots in the $\{0, \mathbf{e}_y, \mathbf{e}_z\}$ -plane with ion magnetization $\beta_i = 5$. (a) Probe bias $\chi_p = 15$, and (b) $\chi_p = 50$. Also shown as dashed blue lines are a selection of fluid streamlines, and as thick red lines the critical streamlines delimiting the collection flux-tube. The external drift velocity is $w_\perp = 0.5$ and $w_\infty = 0$.

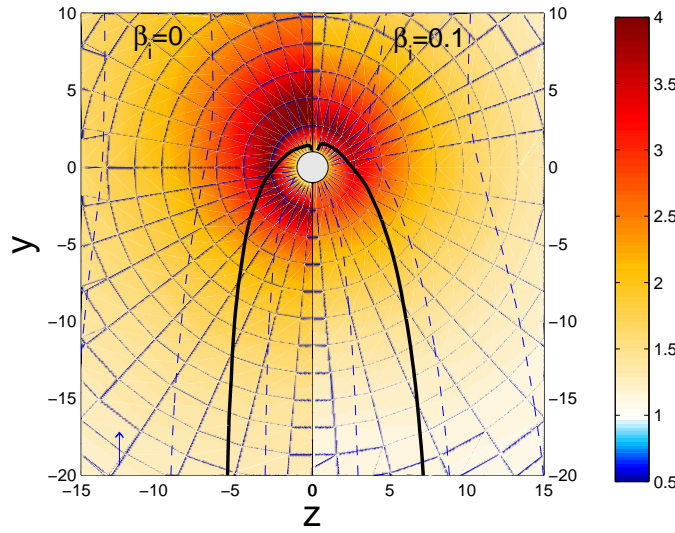


Figure V-14: Normalized ion charge-density contour-plots in the $\{0, \mathbf{e}_y, \mathbf{e}_z\}$ -plane with (left) zero and (right) weak magnetization $\beta_i = 0.1$. The probe bias is $\chi_p = 15$, and the external drift velocity is $w_\perp = 0.5$ and $w_\infty = 0$. The thick black lines are the critical stream-lines delimiting the collection flux-tube.

Chapter VI

Spheres in finite Debye length, arbitrarily magnetized plasmas

In chapter V, the problem of collisionless ion collection by a spherical object under magnetized conditions was solved in the limiting regime of electron Debye length much greater than the sphere radius ($\Lambda_{De} \gg R_p$). Because space-charge effects were neglected, the potential distribution around the sphere approached a vacuum form and the task was reduced to integrating particle orbits in a prespecified potential. In chapter IV, the Particle in Cell code SCEPTIC3D was used to investigate the problem in the opposite limit of negligible shielding length, where quasineutrality holds down to an infinitesimally thin sheath layer at the sphere surface.

We here propose to perform the calculation in the general situation where the shielding length can neither be approximated by zero or infinity, requiring us to resolve the ion motion self-consistently with the electrostatic Poisson's equation. The problem has therefore two additional degrees of freedom with respect to the quasineutral limit (the electron Debye length $\Lambda_{De} = \sqrt{\epsilon_0 T_e / e^2 N_\infty}$ and the probe potential Φ_p), and two with respect to the vacuum limit (Λ_{De} and the ion to electron thermal energy ratio $\tau = T_{i\infty} / ZT_e$).

VI.1 Foreword on electron-collecting space tethers

The purpose of this thesis being to investigate probes in the ion collection regime, it would be beside the point to give a comprehensive review of electron collection by positively charged electrodes. It is nevertheless instructive to briefly review some results of positively charged space tether experiments, as the corresponding physics of attracted electrons is similar to the physics of attracted ions discussed so far.

VI.1.1 Electrodynamic tethers

The idea of using electrodynamic tethers (EDT) as power generator or thruster for satellites in Low Earth Orbit (LEO) has been proposed since the early days of space exploration. An EDT is, to simplify, a long shielded electric wire drawn from the satellite across the earth magnetic field lines. It is connected to an electron gun on the satellite side, and to an electron collector on its opposite end (see Fig. (VI-1) for an artist view of the concept). We also mention the existence of an alternative design where the wire is naked and the end collector absent, but will not discuss it further. The operating principle of an EDT is to circulate a current I , closed in the ambient plasma via the electron collector and gun. If the tether has a length L , a Lorentz force $F = ILB$ normal to both the tether and the magnetic field will then thrust or slow down the satellite, depending on the relative orientation of the current, satellite orbital velocity \mathbf{v}_d and Earth magnetic field \mathbf{B} .

The tether being built in conducting material, it is (almost) an equipotential in its own frame. It however sees an effective gradient in the external space potential $\nabla\Phi_0 = \mathbf{v}_d \times \mathbf{B}$, due to the convective electric field generated by the satellite motion $-\mathbf{v}_d$ across the Earth magnetic field \mathbf{B} . Omitting resistive dissipation, the total circuit load (Collector-gun potential) is therefore $\Delta\Phi = \pm L|\mathbf{v}_d \times \mathbf{B}| + \Phi_c - \Phi_g$, where Φ_c is the (positive) collector bias with respect to its neighboring plasma, and Φ_g the (negative) gun bias with respect to its neighboring plasma. When a current I circulates in the tether, part of the electric power is lost in plasma heating ($eI(\Phi_c - \Phi_g)$), and part goes into the satellite thrust or slow-down through the Lorentz force ($\pm ILBv_d$).

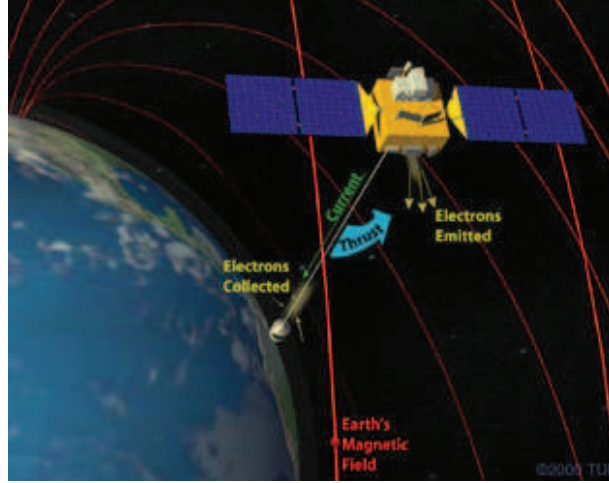


Figure VI-1: Artist view of the Electro Dynamic Tether concept (From <http://www.tethers.com/EDTethers.html>).

VI.1.2 Electron collection by the TSS subsatellite

Experimental observations

One of the most important question regarding space tethers is the relationship between the subsatellite (or electron collector) bias with respect to the local plasma, and the collected electron current. One of the major goals of the first Tethered Satellite System flight (TSS-1, 1992) and reflight (TSS-1R, 1996) was to study this question [7].

The experiment used a spherical electron collector of radius $R_p = 80\text{cm}$, and operated in plasma conditions approximately given by $N_\infty \simeq 10^{11}\text{m}^{-3}$, $T_{e\infty} \simeq T_{i\infty} \simeq 0.1\text{eV}$, $B \simeq 3 \cdot 10^{-5}\text{T}$ and $v_\perp \simeq 8\text{km} \cdot \text{s}^{-1}$. From those conditions we infer an average electron Larmor radius $R_{Le} \simeq 3\text{cm}$ and an electron Debye length $\Lambda_{De} \simeq 0.75\text{cm}$. The electron-ion momentum exchange collision mean free path, easily calculated from Eq. (II.34), is $l_{ei} \simeq 1\text{km}$, while the magnetic presheath extent is of the order $\sim 2R_p v_{te} / v_\perp \simeq 40\text{m}$. The electron dynamics around the positively biased spherical subsatellite is therefore collisionless, and verifies the scaling $\Lambda_{De} \ll R_{Le} \ll R_p$: one could therefore think that it should follow the same ion collection equations discussed in chapter II.

Figure (VI-2) shows a compilation of current-voltage characteristics from the TSS-

1R mission, for positive subsatellite voltages up to about 1kV. It can be seen that the electron current does not saturate, despite the extremely strong bias compared to the plasma temperature. The situation is therefore clearly different from what observed in Matthew's experiment (Fig. (II-1)) where the electron current reached approximate saturation at $\Phi_p \gtrsim 4T_e/e$.

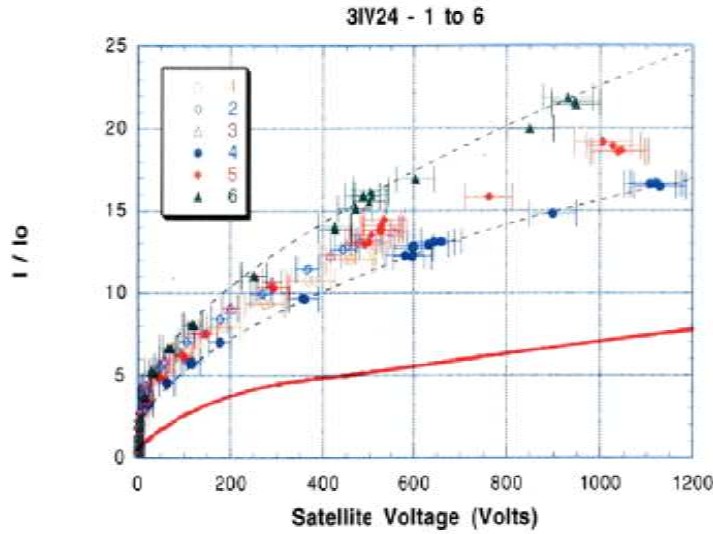


Figure VI-2: Compilation of Current-Voltage characteristics from the TSS-1R experiment (colour version of Fig. (2) in Ref. [57]). The points correspond to different voltage sweeps, and the thick red line to the Parker-Murphy upper bound (Eq. (V.44)).

For completeness, we mention that the physics of laboratory probes at electron saturation is very different. The electron-ion Coulomb collision frequency for the sample SOL parameters considered in section II.2 is $\bar{\nu}_{ei} = 2.6 \cdot 10^6 s^{-1}$ (Eq. (II.34)), while Ω_c and Ω_a for the electrons are as for the ions (Table II.1) since cross-field diffusion is assumed to be ambipolar. In other words $\bar{\nu}_{ei} \gg \Omega$, and the parallel electron dynamics is diffusive rather than collisionless when the electrons are attracted. Several authors have treated this regime, with either a kinetic [34] or a fluid [35, 36] approach, but we will not discuss this problem further.

Usual physical interpretation

In magnetic-free plasmas, the straightforward interpretation of non saturating characteristics is that the sheath cannot be assumed infinitesimal, and thickens as the probe bias increases (see for instance Eq. (II.17)). In the presence of a magnetic field, to this effect must be added the demagnetization of gyrating particles induced by the probe bias. This effectively increases the attracted particles' Larmor radius in the probe neighborhood (here the electrons, but generally the ions in this thesis), hence the probe apparent transverse cross-sectional area.

Let us assume that an estimate of the apparent probe radius for an hypothetic collisionless stationary plasma (recall that this situation is physically impossible in the presence of a magnetic field, unless the Debye length is infinite) is given by the canonical Parker-Murphy upper bound R_{PM} , discussed in paragraph V.3.1 for the case of attracted ions. An upper bound to the collected current is then obtained by considering that the probe magnetic shadow, of radius R_{PM} , extends to infinity where the plasma thermal flux-density in the parallel (to the magnetic field) direction is Γ_e^0 :

$$I_e^{PM} = 2\Gamma_e^0 (\pi R_{PM}^2) = I_e^0 \left(\frac{1}{2} + \frac{2}{\sqrt{\pi}} \frac{\sqrt{\Phi_p/T_{e\infty}}}{\beta_e} \right). \quad (\text{VI.1})$$

The C-V characteristics of Fig. (VI-2) are about 3 to 4 times larger than the Parker and Murphy upper bound, which *must* be a consequence of the transverse plasma flow past the satellite. Singh and Chaganti [58] proposed the following very simple picture. They assume the presheath to be a cylinder of radius R_{PM} and length L , repopulated not from its ends but from its leading edge where transverse plasma inflow occurs; the probe electron current is therefore $I_e \sim 4LR_{PM}N_\infty v_\perp$. A straightforward estimate for the convective presheath length is $L \sim 2R_{PM}v_{te}/v_\perp$, yielding $I_e \sim 8R_{PM}^2 N_\infty v_{te}$. This is of course an over-estimate since it assumes that each electron entering the presheath is collected, while in fact part of them are only deflected. We will see in paragraph VI.3.2 to what extent SCEPTIC3D computations help asses the validity of this picture.

VI.2 Plasma profiles

In the finite Debye length regime, the three important scale lengths are the probe radius R_p , the external electron Debye length Λ_{De} and the external average ion Larmor radius R_L . We here propose to start by analyzing the plasma profiles, first in the limit of strong ion magnetization still intended as $\beta_i = R_p/R_L \gg 1$.

VI.2.1 Strong ion magnetization

Because running SCEPTIC3D with $\lambda_{De} \lesssim 0.03$ is hardly practical due to the excessive number of radial cells required, yet we would like to explore the regime $0 \neq \Lambda_{De} \ll R_L$, we select $\beta_i = 5$ (i.e. an average external ion Larmor radius equal to a fifth of probe radius), recognizing that we are just entering the strong magnetization zone and using $\beta_i \geq 20$ would be better.

Ion density

Figure (VI-3) shows a selection of density contour-plots computed by SCEPTIC3D in the $\{0, \mathbf{e}_y, \mathbf{e}_z\}$ -plane for $\beta_i = 5$; the electron Debye length is increased from $\lambda_{De} = 0.03$ to $\lambda_{De} = 1$ while the other parameters are kept fixed ($\tau = 1$, $v_d = c_{s0}$, $\delta = \pi/4$ and $\phi_p = -8$).

Figures (VI-3a,b), computed with $\lambda_{De} = 0.03$ and $\lambda_{De} = 0.1$, are qualitatively similar to each other and to the quasineutral contour-plots discussed in chapter IV (see Fig. (IV-2)). The property demonstrated in the quasineutral, strongly magnetized regime stating that density contour-lines in the probe magnetic shadow are straight and tangent to the probe surface still approximately holds, although the leading edge perturbation front extends further with finite Debye length.

Profiles in Fig. (VI-3c,d), computed with $\lambda_{De} = 0.3$ and $\lambda_{De} = 1$, are significantly different. In particular the contour-lines do not appear tangent to the collector, and an ion accumulation point forms at the probe leading edge. The transition occurs between $\lambda_{De} = 0.1$ and $\lambda_{De} = 0.3$, i.e. when the electron Debye length approximately equals the external average ion Larmor radius. The reason for the accumulation point

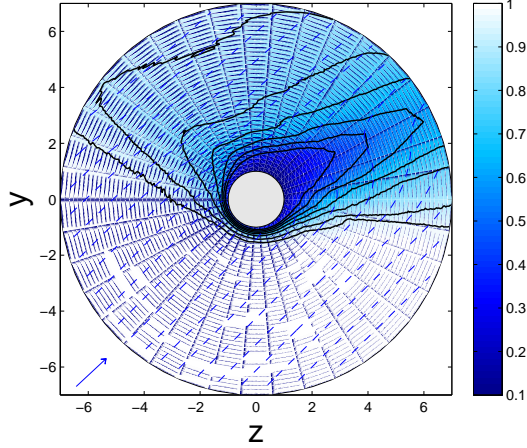
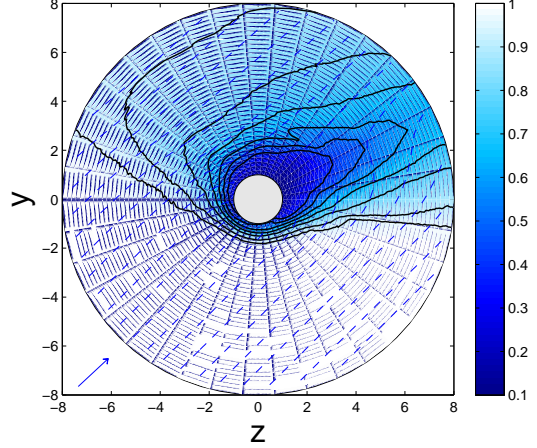
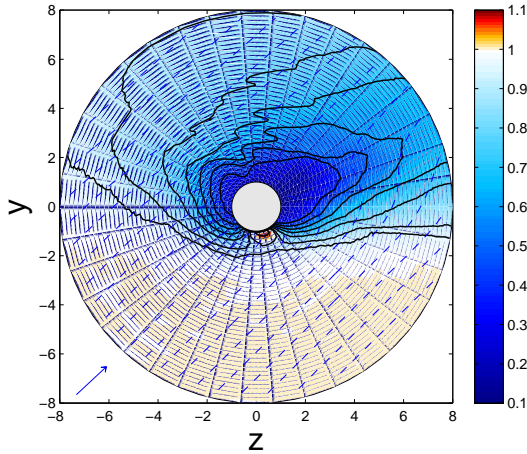
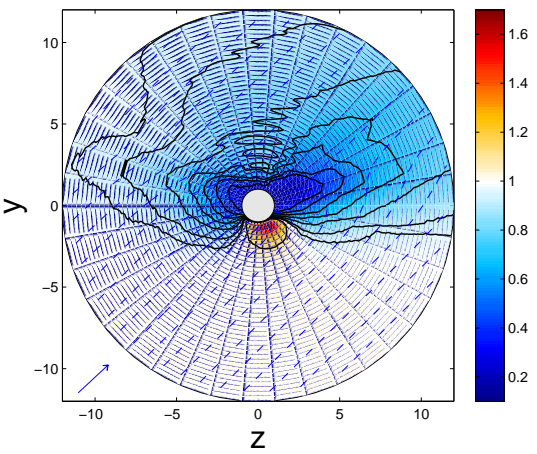
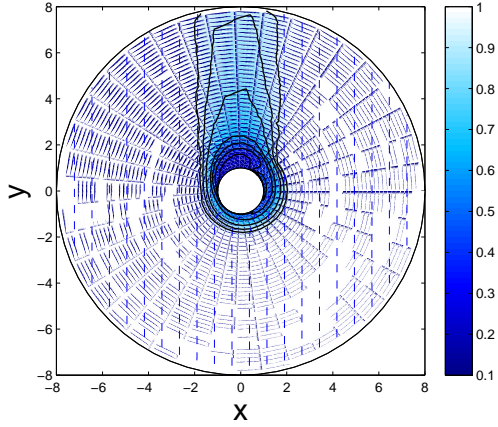
(a) $\lambda_{De} = 0.03$ (b) $\lambda_{De} = 0.1$ (c) $\lambda_{De} = 0.3$ (d) $\lambda_{De} = 1$ 

Figure VI-3: Selection of ion charge-density contour-plots in the $\{0, \mathbf{e}_y, \mathbf{e}_z\}$ -plane, with magnetization $\beta_i = 5$ for $\tau = 1$, $v_d = c_{s0}$, $\delta = \pi/4$, $\phi_p = -8$, and different electron Debye lengths. Iso-density contours for $n = 0.4, 0.5, 0.6, 0.7, 0.8, 0.9, 0.95, 1.1$ are full black, while fluid stream lines are dashed blue. The external velocity is indicated by a blue arrow on the figures' lower left corners.

is that as the ion Larmor radius becomes smaller than the Debye length, the ions can approach the probe surface close enough to feel the convective electric field shielding, hence their cross-field velocity v_{\perp} is reduced.

The regime transition at $\Lambda_{De} \simeq R_L$ is perhaps even clearer in Fig. (VI-4), where ion charge-density contour-plots for the same parameters ($\beta_i = 5$, $\tau = 1$, $v_d = c_{s0}$, $\delta = \pi/4$, $\phi_p = -8$) are plotted in the $\{0, \mathbf{e}_x, \mathbf{e}_y\}$ -plane for (a) $\lambda_{De} = 0.1$ and (b) $\lambda_{De} = 0.3$. While $R_L \lesssim \Lambda_{De}$ (and of course $R_L \ll R_p$), the ion cross-field velocity is approximately constant and given by \mathbf{v}_{\perp} ; the physical picture given in Fig. (IV-1) according to which each slice in the plane of flow and magnetic field is independent of each other still (approximately) holds. When $R_L \gtrsim \Lambda_{De}$ on the contrary, the probe negative bias permeates far enough in the plasma region for an effect similar to the magnetic presheath displacement to occur.

(a) $\lambda_{De} = 0.1$



(b) $\lambda_{De} = 0.3$

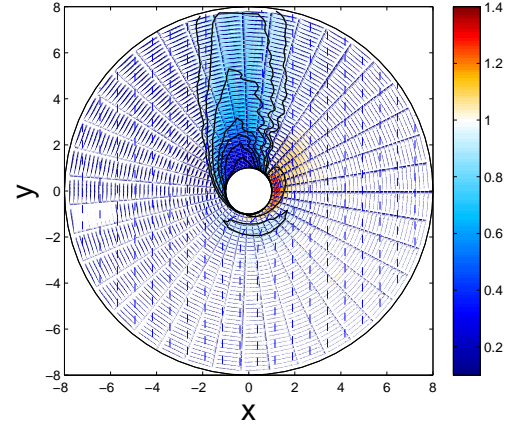


Figure VI-4: Selection of ion charge-density contour-plots in the $\{0, \mathbf{e}_x, \mathbf{e}_y\}$ -plane, with magnetization $\beta_i = 5$ for $\tau = 1$, $v_d = c_{s0}$, $\delta = \pi/4$, $\phi_p = -8$ and (a) $\lambda_{De} = 0.1$, (b) $\lambda_{De} = 0.3$. Iso-density contours for $n = 0.4, 0.5, 0.6, 0.7, 0.8, 0.9, 0.95, 1.1$ are full black, while fluid stream lines are dashed blue.

Electrostatic potential

Figure (VI-5) shows electrostatic potential (ϕ) contour-lines at $\lambda_{De} = 0.1$ and $\lambda_{De} = 3$, using the same parameters as in Figs (VI-3, VI-4).

It can be seen that when $\Lambda_{De} \ll R_p$, the potential contours are well coupled to the ion density distribution (compare Figs (VI-5a,b) with Figs (VI-3b,VI-4a)). Because Poisson equation smooths out density gradients over a scale length Λ_{De} , the potential contours when $\Lambda_{De} \gtrsim R_p$ tend to a more circular form in the $\{0, \mathbf{e}_y, \mathbf{e}_z\}$ -plane. In the $\{0, \mathbf{e}_x, \mathbf{e}_y\}$ -plane (Fig. (VI-5d)), the potential contours in the probe vicinity are shifted in the positive x direction, due to the effective probe dipole permeating in the plasma region.

Ion temperature

Figure (VI-6) shows contour-lines of $T_{i,zz}$ normalized to $T_{i\infty}$ for $\lambda_{De} = 0.1$ and $\lambda_{De} = 3$, and other parameters set as in Fig. (VI-3). The transition between $\Lambda_{De} < R_L$ and $\Lambda_{De} > R_L$ materializes in two ways. First as an increase in parallel temperature around the leading edge of the probe, simultaneously with the density increase. Second as a much stronger symmetrization of the profiles than observed with density.

Also of interest are the transverse temperature contours $T_{i,xx}$ and $T_{i,yy}$, shown in Fig. (VI-7) for the same runs. Because in the strong magnetization limit the ion magnetic moment is an adiabatic invariant, the transverse ion temperature should be uniform, at least out of the magnetic presheath where the Larmor rotation is broken. In the considered cases $\beta_i = 5$, and a mild transverse heating in the wake can be observed. Nevertheless because of the fast ion gyration, at fixed Debye length the $T_{i,xx}$ and $T_{i,yy}$ profiles are almost identical. It can also be observed that contrary to $T_{i,zz}$, increasing the Debye length does not symmetrize the transverse temperature.

VI.2.2 Intermediate ion magnetization

Close density contours

Figure (VI-8) shows ion charge-density contour-plots computed by SCEPTIC3D in the $\{0, \mathbf{e}_y, \mathbf{e}_z\}$ -plane for $\beta_i = 1$, $\tau = 0.1$, $v_d = 0.35c_{s0}$, $\delta = \pi/2$, $\phi_p = -8$ and (a) $\lambda_{De} = 0.3$, (b) $\lambda_{De} = 3$.

Although the contour-lines in Fig. (VI-8a) are not tangent to the probe surface

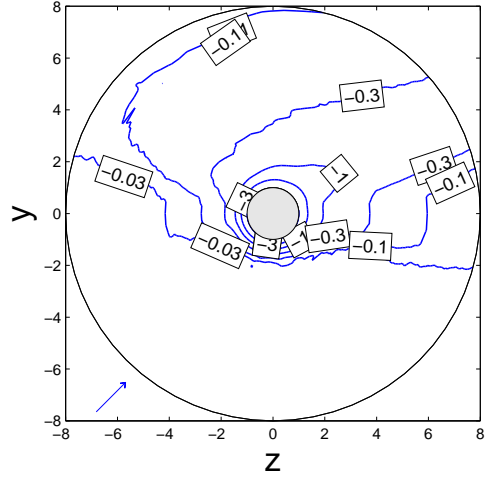
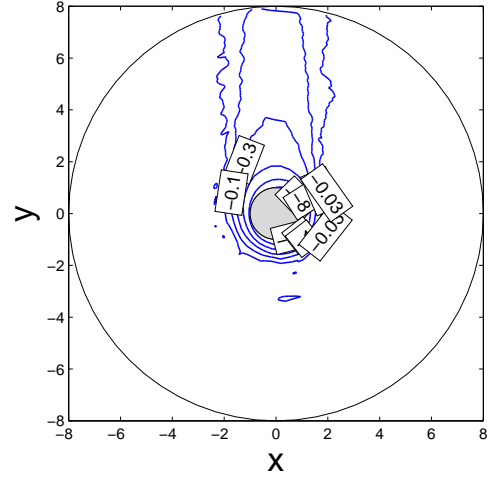
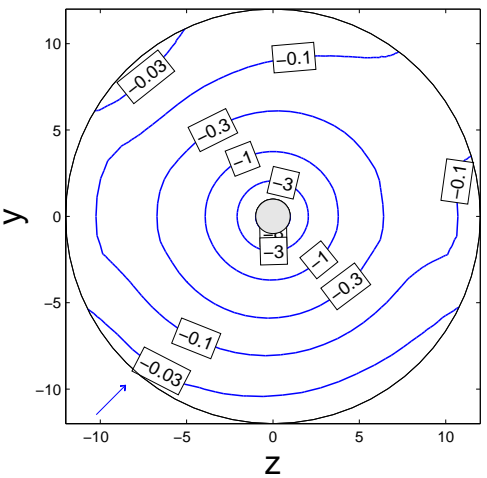
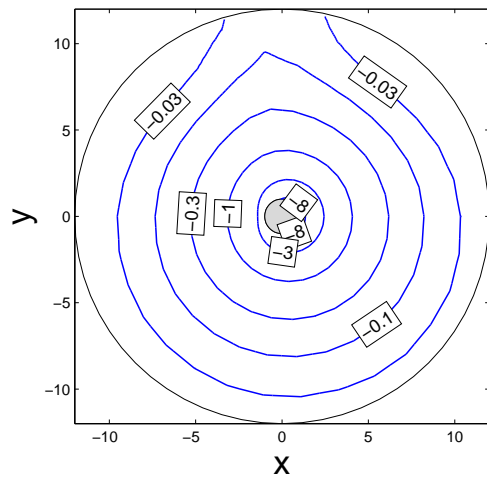
(a) $\{0, \mathbf{e}_y, \mathbf{e}_z\}$, $\lambda_{De} = 0.1$ (b) $\{0, \mathbf{e}_x, \mathbf{e}_y\}$, $\lambda_{De} = 0.1$ (c) $\{0, \mathbf{e}_y, \mathbf{e}_z\}$, $\lambda_{De} = 3$ (d) $\{0, \mathbf{e}_x, \mathbf{e}_y\}$, $\lambda_{De} = 3$ 

Figure VI-5: Potential (ϕ) contour-lines with magnetization $\beta_i = 5$ for $\tau = 1$, $v_d = c_{s0}$, $\delta = \pi/4$, $\phi_p = -8$ and (a) $\{0, \mathbf{e}_y, \mathbf{e}_z\}$ -plane and $\lambda_{De} = 0.1$, (b) $\{0, \mathbf{e}_x, \mathbf{e}_y\}$ -plane and $\lambda_{De} = 0.1$, (c) $\{0, \mathbf{e}_y, \mathbf{e}_z\}$ -plane and $\lambda_{De} = 3$ and (d) $\{0, \mathbf{e}_x, \mathbf{e}_y\}$ -plane and $\lambda_{De} = 3$. The external velocity is indicated by a blue arrow on the figures' lower left corners.

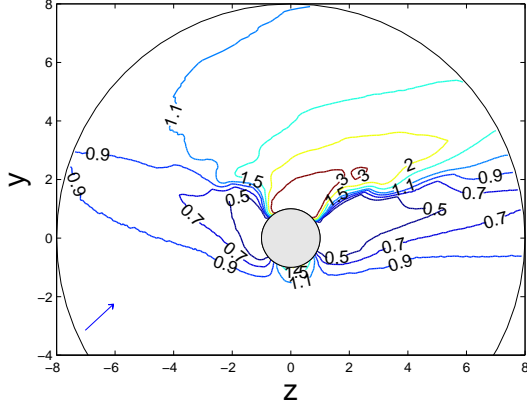
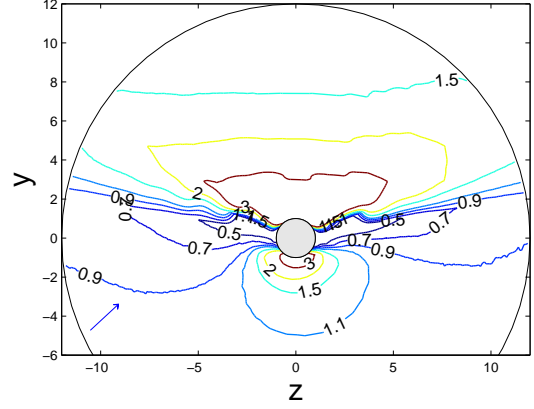
(a) $\lambda_{De} = 0.1$ (b) $\lambda_{De} = 3$ 

Figure VI-6: Contour-lines of $T_{i,zz}/T_{i\infty}$ in the $\{0, \mathbf{e}_y, \mathbf{e}_z\}$ -plane, with magnetization $\beta_i = 5$, for $\tau = 1$, $v_d = c_{s0}$, $\delta = \pi/4$, $\phi_p = -8$ and (a) $\lambda_{De} = 0.1$, (b) $\lambda_{De} = 3$. The external velocity is indicated by a blue arrow on the figures' lower left corners.

due to the non negligible electron Debye length, they are qualitatively similar to what observed in Figs (VI-3a,b), taking into account the fact that the drift velocity is different. Figure (VI-8b) on the contrary reminds us of Figs (VI-3c,d), with the leading-edge accumulation point. The transition occurs between $\lambda_{De} = 0.3$ and $\lambda_{De} = 3$, i.e. when $\Lambda_{De} \simeq R_L$ as already noticed at stronger magnetization.

Figure (VI-8b) also shows an accumulation point in the trailing edge, absent in Figs (VI-3c,d) because the drift velocity was too high. Both the leading and trailing edge accumulation points correspond to regions where the convective electric field is shielded enough from the ions to have negligible cross-field velocity, hence the ions perform a mirror like oscillation along the field lines in the probe-induced potential well. An interesting investigation that is deferred to future work is to look for trapped ions there.

Figure (VI-9) shows ion density-contours in the $\{0, \mathbf{e}_x, \mathbf{e}_y\}$ -plane, computed using the same parameters as in Fig. (VI-8). As first observed in Fig. (VI-4), the fluid streamlines belonging to the cross-field plane start to encircle the probe when $\Lambda_{De} \gtrsim R_L$. Figure (VI-9b) is qualitatively comparable to Fig. (11) in Ref. [56], showing magnetized electron orbits encircling a positively charged probe in the vacuum

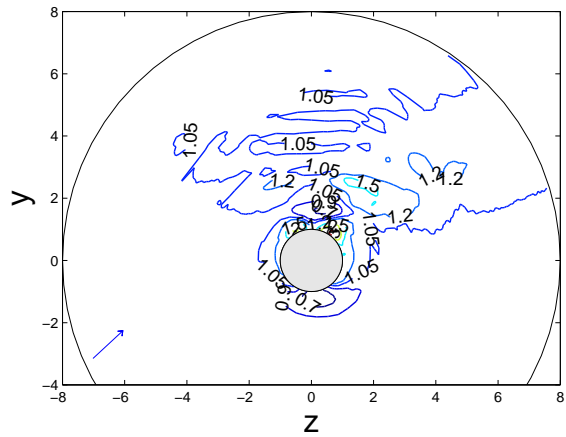
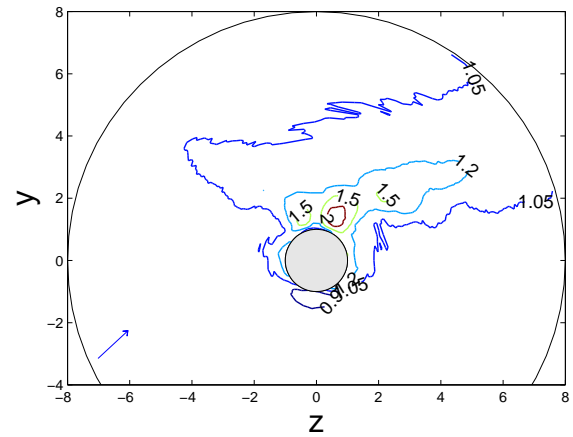
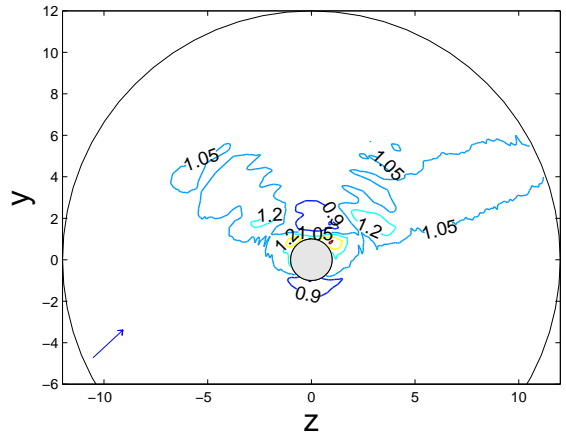
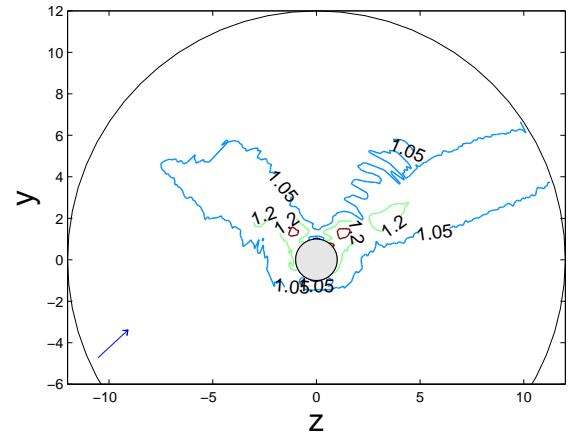
(a) $T_{i,xx}$, $\lambda_{De} = 0.1$ (b) $T_{i,yy}$, $\lambda_{De} = 0.1$ (c) $T_{i,xx}$, $\lambda_{De} = 3$ (d) $T_{i,yy}$, $\lambda_{De} = 3$ 

Figure VI-7: Contour-lines of $T_{i,xx}/T_{i\infty}$ and $T_{i,yy}/T_{i\infty}$ in the $\{0, \mathbf{e}_y, \mathbf{e}_z\}$ -plane, with magnetization $\beta_i = 5$, for $\tau = 1$, $v_d = c_{s0}$, $\delta = \pi/4$, $\phi_p = -8$ and (a,b) $\lambda_{De} = 0.1$, (c,d) $\lambda_{De} = 3$. The external velocity is indicated by a blue arrow on the figures' lower left corners.

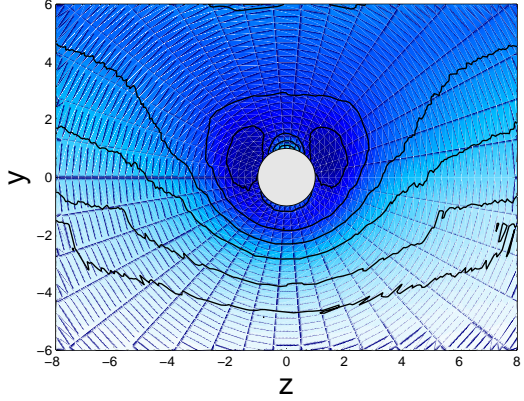
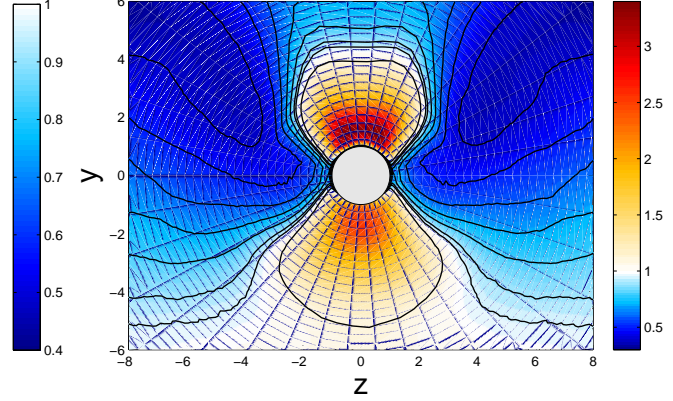
(a) $\lambda_{De} = 0.3$ (b) $\lambda_{De} = 3$ 

Figure VI-8: Ion charge-density contour-plots in the $\{e_y, e_z\}$ -plane, for $\tau = 0.1$, $\beta_i = 1$, $\phi_p = -8$, $v_d = 0.35c_{s0}$ and $\delta = \pi/2$. (a) $\lambda_{De} = 0.3$ and (b) $\lambda_{De} = 3$. The computational domain sizes are respectively $r_b = 10$ and $r_b = 12$, but for clarity we only show the region of interest.

limit.

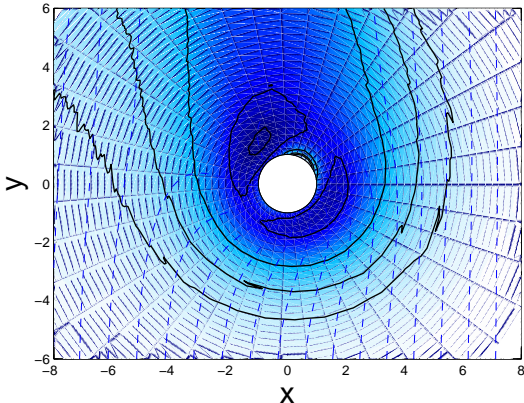
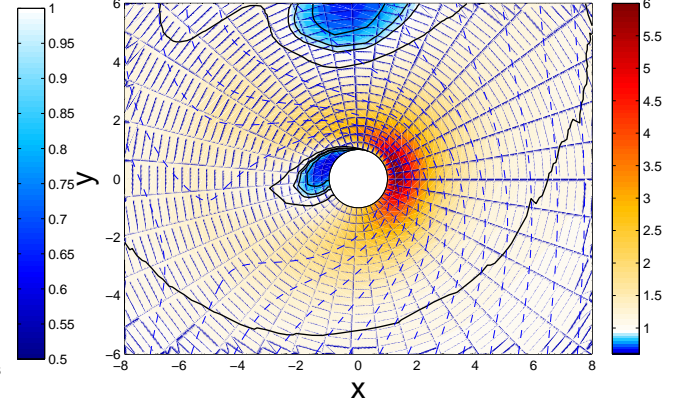
(a) $\lambda_{De} = 0.3$ (b) $\lambda_{De} = 3$ 

Figure VI-9: Ion charge-density contour-plots in the $\{e_x, e_y\}$ -plane, in the same conditions as in Fig. (VI-8).

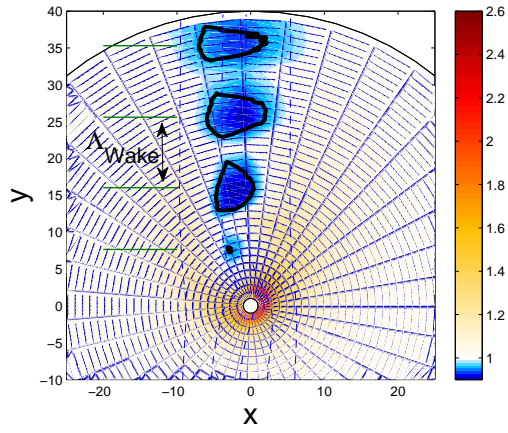
Wakefields

Looking further away from the probe, where the potential is weak and the plasma dynamics can be modeled linearly, we should in theory observe ion cyclotron wakes whose wave-length is given by

$$\Lambda_{Wake} = 2\pi \frac{v_\perp}{\omega_c} = 4\sqrt{\pi} R_p \frac{w_\perp}{\beta_i}. \quad (\text{VI.2})$$

Figure (VI-10a) shows the ion-density contour plot in the $\{0, \mathbf{e}_x, \mathbf{e}_y\}$ -plane for $\tau = 1$, $\phi_p = 8$, $v_d = c_{s0}$, $\delta = \pi/2$ and $\beta_i = 0.5$. The cyclotron wake is clearly visible, and has a wavelength matching the theoretical formula (VI.2) within less than 2% for the first two nodes, and 1% afterwards. The wakefield is parallel to \mathbf{v}_\perp , but slightly out of axis at about $x \simeq -R_p$. The Debye length has little influence on the wake provided it is large enough, approximately $\lambda_{De} \gtrsim 3$, limit below which cyclotron damping (proportional to the plasma frequency square, hence Λ_{De}^{-2}) appears to be too strong. For example in Fig. (VI-9b) the first node of the wakefield is visible at $y \simeq 5.55R_p$ ($\lambda_{De} = 3$), but not in Fig. (VI-9a) where $\lambda_{De} = 0.3$.

(a) $\tau = 1$, $\lambda_{De} = 10$



(b) $\tau = 0.1$, $\lambda_{De} = 20$

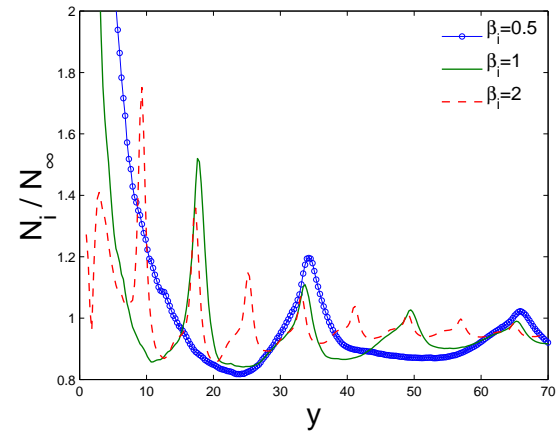


Figure VI-10: (a) Ion-density contour-plot in the $\{0, \mathbf{e}_x, \mathbf{e}_y\}$ -plane, for $\tau = 1$, $\phi_p = 8$, $v_d = c_{s0}$, $\delta = \pi/2$, $\lambda_{De} = 10$ and $\beta_i = 0.5$. The depletion nodes of the wakefield are indicated by thick black contour-lines at $N_i/N_\infty = 0.95$. (b) Ion charge-density contour-plots at $z = 0$ and $x = -R_p$ as a function of y , for $\tau = 0.1$, $\phi_p = -8$, $v_d = c_{s0}$, $\delta = \pi/2$, $\lambda_{De} = 20$, and different ion magnetization levels.

Reducing the ion temperature increases the intensity of the wakefield, since the probe potential in ion thermal units χ_p , responsible for the “kick” launching the wake, increases. Figure (VI-10b) is a plot of wake ion charge-density versus cross-field position at $x = -R_p$ and $z = 0$ for $\tau = 0.1$, $\phi_p = -8$, $v_d = c_{s0}$, $\delta = \pi/2$, $\lambda_{De} = 20$ and three levels of magnetization multiple of each other ($\beta_i = 0.5, 1, 2$). In the considered conditions, Eq. (VI.2) predicts $\Lambda_{Wake} = 31.7, 15.6, 7.9R_p$ ($w_\perp \simeq 2.23$), value matching SCEPTIC3D computations to within 1%, i.e. about the uncertainty in plot reading.

VI.3 Self-consistent ion current

VI.3.1 Current dependence on ion magnetization

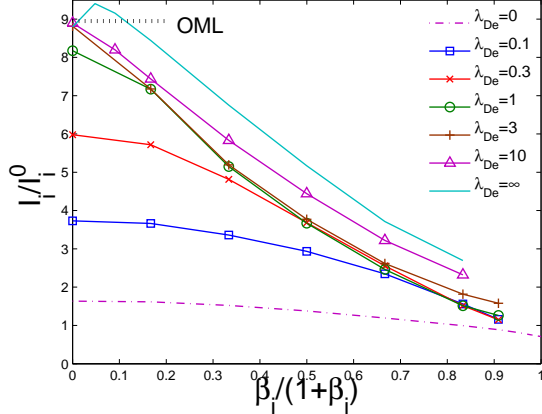
We start our analysis of ion collection with Fig. (VI-11), showing the total ion current dependence on ion magnetization β_i for a selection of transverse drift velocities and electron Debye lengths, with probe potential $\phi_p = -8$ and temperature ratio $\tau = 1$.

We first see that curves of current versus magnetization at $\lambda_{De} = 0$ and $\lambda_{De} = \infty$ are envelopes for the curves at intermediate shielding. Although this observation is intuitive in unmagnetized conditions, because the current increases from the quasineutral saturation value to the OML upper bound (Eq. (V.24)), no *a priori* argument can be used to generalize the rule to magnetized conditions. In fact it was shown in Ref. [59] that in weakly magnetized stationary plasmas, the current would peak at $\lambda_{De} \sim 1$.

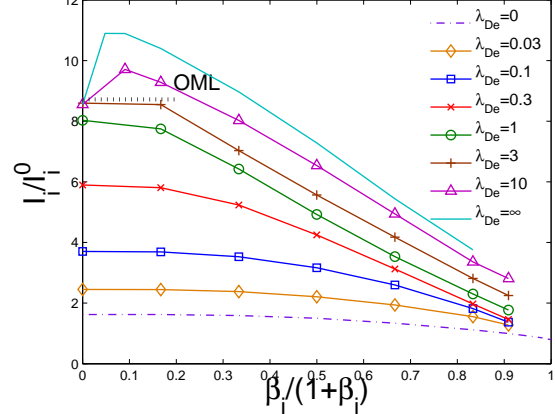
It was shown in chapters IV, V that in the presence of cross-field flow, the total ion current could exceed the unmagnetized value at low but non-zero magnetic field. We can see here that the faster the cross-field flow, the lower the Debye length threshold at which this peak appears. A further observation is that when the peak is present, its maximum is located at a magnetization level increasing with decreasing Debye length. Although it is hard to propose a ready-to-use formula predicting the location and height of those maxima, the location qualitatively scales as $R_p/v_\perp \sim 1/\omega_c$ ($\beta_i \sim w_\perp$),

i.e. when the transverse ion transit time compares to its Larmor period.

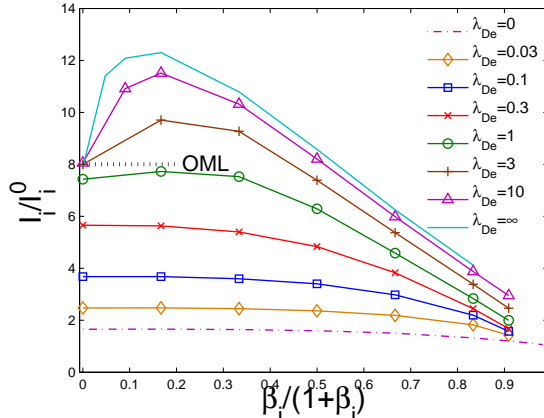
(a) $v_d = 0.2c_{s0}$



(b) $v_d = 0.5c_{s0}$



(c) $v_d = c_{s0}$



(d) $v_d = 1.5c_{s0}$

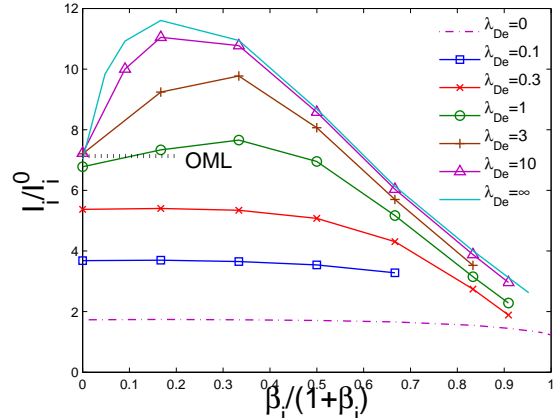


Figure VI-11: Total ion current normalized to $I_i^0 = 4\pi N_\infty R_p^2 v_{ti}/2\sqrt{\pi}$ as a function of ion magnetization β_i , self-consistently calculated with SCEPTIC3D with $\tau = 1$, $\phi_p = -8$ and $\delta = \pi/2$. Curves labeled “ $\lambda_{De} = 0$ ” refer to quasineutral computations (chapter IV), and curves labeled “ $\lambda_{De} = \infty$ ” to direct orbit integration (chapter V). (a) $v_d = 0.2c_{s0}$. (b) $v_d = 0.5c_{s0}$. (c) $v_d = c_{s0}$. (d) $v_d = 1.5c_{s0}$.

The ion current in Fig. (VI-11) seems to have a $1/\beta_i$ dependence at high β_i , which is consistent with observations made in the quasineutral regime (chapter IV). Of course this is because we limit our simulations to values of β_i such that no part of the probe is ion-repelling (to be rigorous, points at $\beta_i = 10$ in Figs (VI-11c,d) should be excluded), otherwise the current would start to increase at very high β_i as observed

for example in Fig. (V-5a).

VI.3.2 Current-Voltage characteristics at low Debye length SCEPTIC3D computations

We now have all the tools in place to discuss the TSS C-V characteristics shown in Fig. (VI-2), upon mentally inverting ions and electrons. We have to bear in mind that the comparison is not perfect, because ionospheric flows are mesosonic (i.e. faster than the ion thermal speed and slower than the electron thermal speed), hence cannot be reproduced in the SCEPTIC3D simulation.

Figure (VI-12) shows a selection of C-V characteristics computed by SCEPTIC3D, for different magnetization levels and flows. If we except the low bias region (say $\chi_p = -\phi_p/\tau \lesssim 5$), the curves look very similar to the experimental data in Fig. (VI-2)

Personal interpretation of the mixed model

Sing and Chaganti's picture to explain the C-V characteristics in Fig. (VI-2), briefly reviewed in paragraph VI.1.2, can be adapted to the process of ion collection discussed in this thesis in a quantitative way to yield what we can call a "mixed model". The idea is to consider that the collected ion current is equal to the strongly magnetized, quasineutral solution of the kinetic model presented in chapter II, multiplied by $(R_{PM}/R_p)^2$. For convenience we here rewrite the Parker-Murphy radius (Eq. (V.44)) as

$$R_{PM} = R_p \left(1 + \frac{R_L^*}{R_p} \right)^{1/2}, \quad (\text{VI.3})$$

where

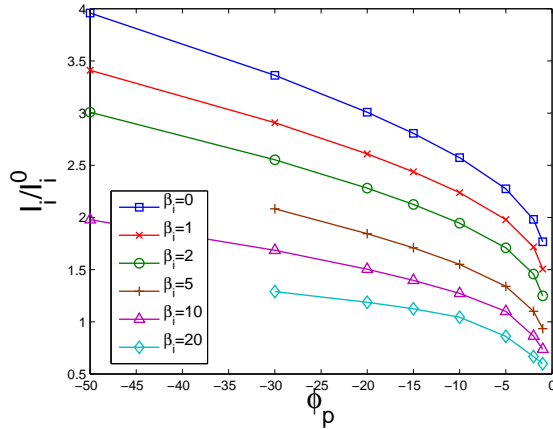
$$R_L^* = \left(\frac{-8m\Phi_p}{ZeB^2} \right)^{1/2} = R_p \frac{4}{\sqrt{\pi}} \frac{\sqrt{\chi_p}}{\beta_i} \quad (\text{VI.4})$$

is a measure of the demagnetized ion Larmor radius; hence the Parker-Murphy current rewrites

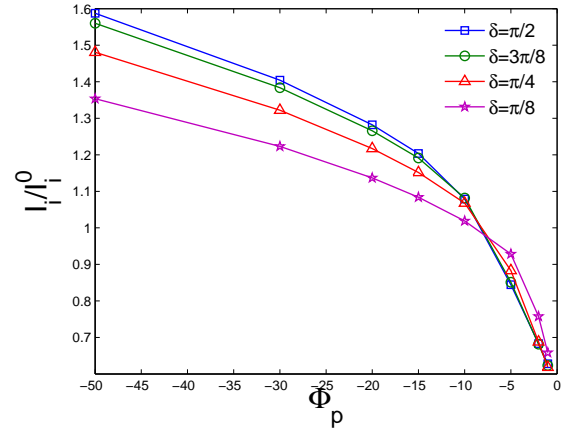
$$I_i^{PM} = \frac{I_i^0}{2} \left(1 + \frac{R_L^*}{R_p} \right) \quad (\text{VI.5})$$

Figure (VI-13) shows the same data as Fig. (VI-12), but the ion current is plotted

(a) $\tau = 1$, $\lambda_{De} = 0.03$, $v_d = 0.35c_{s0}$, $\delta = \pi/2$ (b) $\tau = 1$, $\lambda_{De} = 0.03$, $v_d = 0.5c_{s0}$, $\beta_i = 20$



(c) $\tau = 0.1$, $\lambda_{De} = 0.1$, $v_d = 0.35c_{s0}$, $\delta = \pi/2$



(d) $\tau = 0.1$, $\lambda_{De} = 0.03$, $v_d = 0.2c_{s0}$, $\delta = \pi/2$

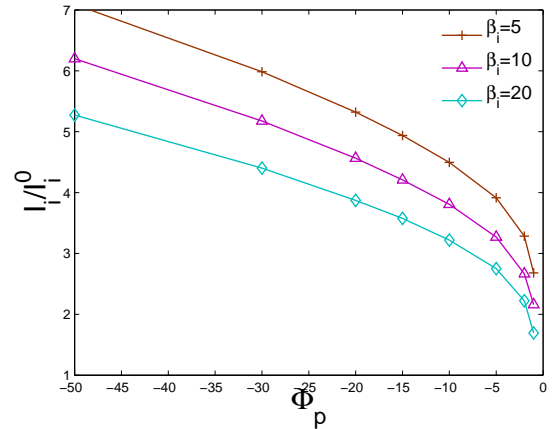
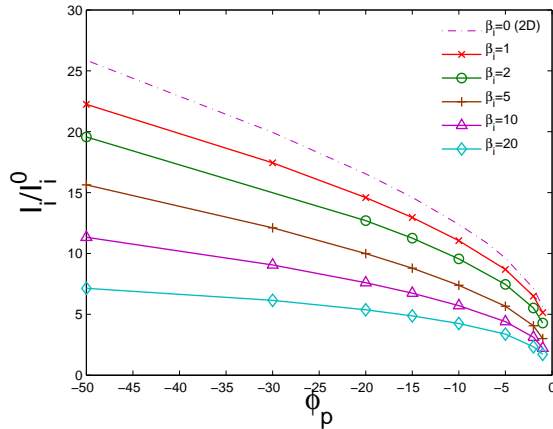


Figure VI-12: Ion C-V characteristics self-consistently computed by SCEPTIC3D as a function (a,c,d) of ion magnetization β_i and (b) flow to magnetic field angle δ .

against the Parker-Murphy upper bound. It can be seen that past the low bias region, the curves (at fixed β_i) are linear, confirming the current dependence $I_i \propto \sqrt{\chi_p}$ predicted by Eq. (VI.5). The curves at different β_i however are not aligned, which is an indication that the current dependence on β_i is not $\sim 1/\beta_i$ as predicted by Eq. (VI.5). In fact the $\sim 1/\beta_i$ dependence only holds at moderate probe potential (and large magnetic field), as seen in Fig. (VI-11). On the same figure are plotted the predictions of the mixed model, which of course cannot be aligned with non aligned lines.

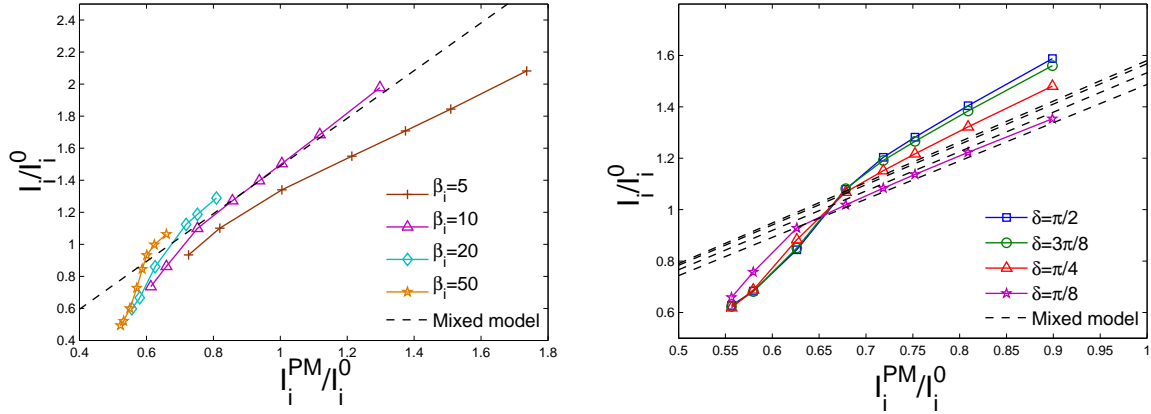
In summary, although several authors tried to express the C-V voltage characteristics from ionospheric missions (hence in strongly magnetized (for the electrons), short Debye length, cross-field drifting plasmas) in terms of the Parker-Murphy upper bound, the approach is fallacious because only the $\sim \sqrt{\chi_p}$ dependence is correct. Their approach seemed successful only because the magnetic field in the earth ionosphere is fixed.

The inappropriateness of the Parker-Murphy upper bound at low Debye length

It is now instructive to understand why the Parker-Murphy upper bound does not work in short Debye length plasmas. I_i^{PM} was derived with the assumption that each ion whose energy and canonical angular momentum at infinity is compatible with collection is collected. Figure (V-8) showed an example of critical magnetic bottle calculated for a Coulomb potential in a stationary magnetoplasma, in the interior of which an ion starting at infinity with cylindrical radius $\rho = R_{PM}$ (Eq. (V.44)) is confined by conservation of energy and canonical angular momentum. The ion will presumably have a complex helical motion in the bottle, and because it might or might not be collected, I_i^{PM} (Eq. (V.45)) is only an upper bound.

A second reason for which I_i^{PM} is only an upper bound, disregarded in several publications, is that if the Debye length is too small, the critical magnetic bottle does not connect the probe surface to infinity. Figure (VI-14) shows the critical magnetic bottles computed for $R_L^{*2} = 5R_p^2$ as in Fig. (V-8), but the Coulomb potential is

- (a) $\tau = 1$, $\lambda_{De} = 0.03$, $v_d = 0.35c_{s0}$, $\delta = \pi/2$ (b) $\tau = 1$, $\lambda_{De} = 0.03$, $v_d = 0.5c_{s0}$, $\beta_i = 20$



- (c) $\tau = 0.1$, $\lambda_{De} = 0.1$, $v_d = 0.35c_{s0}$, $\delta = \pi/2$ (d) $\tau = 0.1$, $\lambda_{De} = 0.03$, $v_d = 0.2c_{s0}$, $\delta = \pi/2$

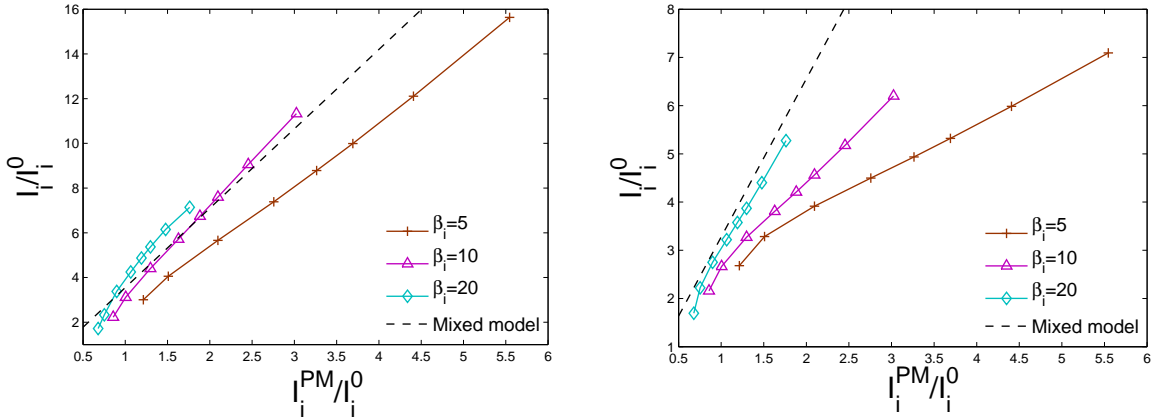


Figure VI-13: Ion current from the runs of Fig. (VI-12), plotted against the Parker-Murphy upper bound I_i^{PM} . The curves labeled “Mixed model” correspond to the multiplication of I_i^{PM} by the quasineutral, strongly magnetized limit current for the same parameters computed with the kinetic method of chapter II.

replaced by a Debye-Hückel distribution with shielding length Λ_s . It can be seen that as the shielding length is reduced, the critical magnetic bottle shrinks, until the plasma part detaches from the probe and a virtual bubble forms inside it.

The critical magnetic bottle's implicit equation is given by Eq. (V.42) with $W_0 = 0$ (cold plasma assumption of Parker and Murphy) and $J_z = ZeB\rho_\infty/2 = ZeBR_{PM}/2$ (critical bottle):

$$\mathfrak{I}(z, \rho) = -Ze\Phi(z, \rho) - \frac{(ZeB)^2}{8m}\rho^2 \left(\frac{R_{PM}^2}{\rho^2} - 1 \right)^2 \leq 0, \quad (\text{VI.6})$$

with $\mathfrak{I}(0, R_p) = 0$. For this bottle to be connected to infinity, the inequality

$$\frac{\partial \mathfrak{I}}{\partial \rho}_{|z=0, \rho=R_p} \leq 0 \quad (\text{VI.7})$$

must be satisfied, corresponding for a Debye-Hückel potential with shielding length Λ_s to

$$\lambda_s \geq \frac{R_L^*/R_p}{4 + R_L^*/R_p}, \quad (\text{VI.8})$$

where R_L^* is defined in Eq. (VI.4). For the example of Fig. (VI-14) we have $R_L^{*2} = 5R_p^2$, hence the transition occurs at $\lambda_s \simeq 0.36$. In the limit of strong demagnetization, i.e. $R_L^* \gg R_p$, the condition (VI.8) requires $\lambda_s \geq R_L^*/R_p$, while in the opposite limit $R_L^* \ll R_p$ the condition is $\lambda_s \geq R_L^*/4R_p$.

The physical explanation for this phenomenon is that if the shielding length is too short, an ion starting at the Parker-Murphy cylindrical radius at infinity will “not know about the probe potential early enough”. This is quite similar to the formation of intermediate potential barriers in unmagnetized plasmas explaining why the OML limit is only reached when $\lambda_s \gg 1$.

VI.3.3 Transverse Mach probe calibration

It was shown in section IV.3 that in the quasineutral regime, transverse Mach probes measuring flux-ratios at angles $\eta = \pi/4$ and $\eta = 3\pi/4$ to the magnetic field in a plane of flow and magnetic field could be calibrated with a single factor M_c using

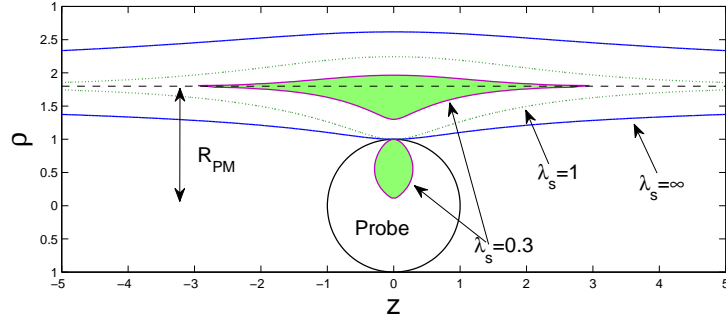


Figure VI-14: Critical magnetic bottles for an ion starting at $\rho = R_{PM}$ (Eq. (VI.3)) with zero velocity, using example plasma parameters such that $R_L^{*2} = 5R_p^2$, and an assumed Debye-Hückel potential distribution with shielding length Λ_s .

Eqs (IV.8,IV.9). In the opposite limit of infinite Debye length on the contrary, flux-ratios have been shown to be hardly relatable to the external flow because of the conducting probe shielding the convective electric field.

The question therefore arises as to applicability of the form (IV.8,IV.9) to finite Debye length conditions. Intuitively, we require $R_L \geq \Lambda_{De}$ in order for the ions not to see the probe shielding of the convective electric field, and $\Lambda_{De} \ll R_p$ in order for orbital effects not to ‘shuffle’ information about the external velocity; for example the particular choice $\lambda_{De} = 0.1$ with $\beta_i \leq 10$ should satisfy those conditions. This can be seen in Fig. (VI-15), where scatter plots of $R_{3\pi/4}$ and $1/R_{\pi/4}$ on the probe major cross-section, computed by SCEPTIC3D for $\tau = 1$, $\phi_p = -8$, $\lambda_{De} = 0.1$ and variable v_d and δ , are reasonably well aligned in log-space against $M_\perp + M_\infty$ and $M_\perp - M_\infty$.

The calibration factors M_c in the ion magnetization range $\beta_i \in [0 : 10]$ for $\tau = 1$ and $\phi_p = -8$, computed by fitting SCEPTIC3D’s solutions with $v_d \lesssim c_{sI}$ and $\delta \in [\pi/8 : \pi/2]$, are plotted in Fig. (VI-16) on (a) on the major cross-section and (b) the quarter cross-sections. The fitting error bars, shown in Fig. (VI-16a), get thicker as the Debye length increases, indicating that the fitting (IV.8,IV.9) becomes less and less appropriate. Error bars for $\lambda_{De} \gtrsim 0.3$ being excessively large, we can qualitatively say that efficient calibration is limited to $\lambda_{De} \lesssim 0.1$. At strong magnetization, the calibration factor is not very sensitive to the Debye length, and using the quasineutral

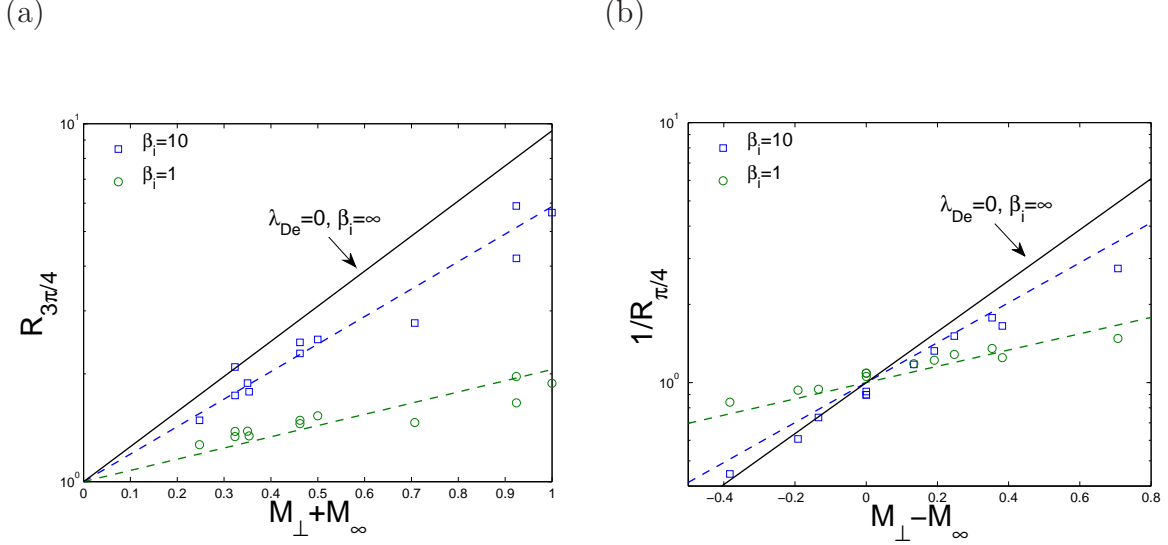
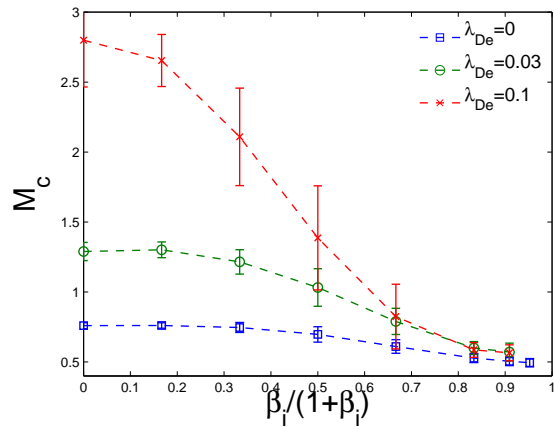


Figure VI-15: Upstream to downstream flux ratios on the probe major cross-section at (a) $\eta = 3\pi/4$ and (b) $\eta = \pi/4$, versus respectively $M_\perp + M_\infty$ and $M_\perp - M_\infty$, from a large set of SCEPTIC3D runs spanning $v_d \in [0 : 1]c_{s0}$ and $\delta \in [\pi/8 : \pi/2]$, for $\tau = 1$, $\lambda_{De} = 0.1$, and $\phi_p = -8$. Also shown are the corresponding fitting lines, whose slopes $1/M_c$ are taken from Fig. (VI-16a).

strongly magnetized value plotted in Fig. (II-10) should yield an error well below typical experimental uncertainties.

(a) Major cross-section



(b) Quarter cross-sections

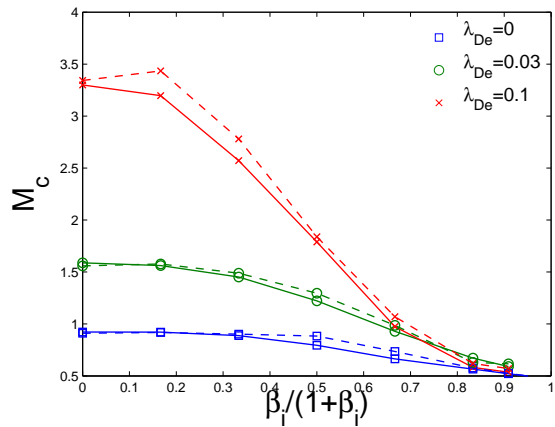


Figure VI-16: Transverse Mach probe calibration factor M_c as a function of ion magnetization β_i and electron Debye length λ_{De} for $\tau = 1$ and $\phi_p = -8$, computed with SCEPTIC3D for measurements made (a) on the major cross-section and (b) the quarter cross-sections. (a) also shows the fitting error bars, arising from numerical noise and from Eqs (II.79,II.80) being only approximate. On (b), solid lines refer to measurements at $x = 1/\sqrt{3}$, and dashed lines to measurements at $x = -1/\sqrt{3}$. Curves labeled “ $\lambda_{De} = 0$ ” are taken from Fig. (IV-11).

Chapter VII

Dust grain dynamics

VII.1 Foreword on unmagnetized dust dynamics

A single dust grain embedded in a flowing plasma can experience different forces depending on the ambient conditions, amongst which the following arise from physics captured by SCEPTIC3D:

- The external electromagnetic force, caused by the action of *external* \mathbf{E} and \mathbf{B} fields on the dust charge Q . In this thesis we place ourselves in the dust rest frame and only consider situations where the electric field is purely convective, hence

$$\mathbf{F}_Q = Q\mathbf{E}_{\text{env}} \quad (\text{VII.1})$$

as first discussed in paragraph III.3.2;

- The internal Lorentz force, caused by currents circulating in the dust particle to balance possible anisotropies in ion and electron collection. Upon defining \mathbf{j} as the net current-density in the dust and Ω as the dust volume:

$$\mathbf{F}_j = \left(\int_{\text{Dust}} \mathbf{j} d\Omega \right) \times \mathbf{B}. \quad (\text{VII.2})$$

As shown in paragraph III.3.3, this force corresponds to the magnetostatic Maxwell stress integrated over the dust surface.

- The ion-drag force \mathbf{F}_i , caused by the direct action of the ion flow (and possible electron pressure) on the dust particle.

Of course in experimental configurations other forces such as neutral drag, electron drag, thermophoretic force, rocket ablation force, radiation pressure ... might be significant. Because uncorrelated with SCEPTIC3D calculations however, we shall not discuss them further.

SCEPTIC3D being an ion code, we cannot solve the plasma-probe interaction with a self-consistent dust floating potential balancing ion and electron collection. The sphere potential Φ_p is rather treated as an input, *a posteriori* related to the charge Q via the self-consistent sphere capacitance $Q = C\Phi_p$ (Eq. (III.52)).

In this introductory section, we review analytic calculations of the ion-drag force \mathbf{F}_i in the unmagnetized, large Debye length regime.

VII.1.1 Dielectric response approach to the ion-drag force

The ion-drag force itself is usually divided in three parts:

- The ion-impact force \mathbf{F}_{im}^p , equal to the rate of momentum transfer from collected ions;
- The electrostatic force \mathbf{F}_E^p , caused by the action of the ion-flow-induced potential distribution anisotropy on the dust charge;
- The electron pressure force \mathbf{F}_e^p , which must be negligible within our repelling-electron assumption (see Appendix A).

where the superscripts “ p ” remind us that the quantities are to be evaluated at the particle surface: $\mathbf{F}_i = \mathbf{F}_i^p = \mathbf{F}_{im}^p + \mathbf{F}_E^p$.

The simplest unmagnetized analytic calculations are performed in the so-called point-like dust approximation, when the linearized plasma shielding length $\Lambda_D = (\Lambda_{Di}^{-2} + \Lambda_{De}^{-2})^{-1/2}$ is much larger than the Coulomb radius $R_C = R_p\chi_p$. In this regime \mathbf{F}_{im}^p is negligible compared to \mathbf{F}_E^p , and the latter can be calculated using the dielectric response formalism as follows.

The linearized potential around a test particle with charge Q embedded in a plasma flowing at normalized velocity $\mathbf{w}_d = \mathbf{v}_d/v_{ti}$ is [60]

$$\Phi(\mathbf{R}) = \frac{Q}{\epsilon_0} \int \frac{\exp(i\mathbf{k} \cdot \mathbf{R})}{k^2 \epsilon(-\mathbf{k} \cdot \mathbf{v}_d, k)} \frac{d\mathbf{k}}{(2\pi)^3}, \quad (\text{VII.3})$$

where \mathbf{R} is the coordinate with respect to the particle center and $\epsilon = 1 + \chi_e + \chi_i$ is the plasma permittivity. ϵ should be evaluated with the Boltzmann electron susceptibility $\chi_e = (k\Lambda_{De})^{-2}$, and the collisionless ion susceptibility $\chi_i(\omega, k) = [1 + \xi \mathfrak{Z}(\xi)] (k\Lambda_{Di})^{-2}$, where $\xi = \omega/(kv_{ti})$ and \mathfrak{Z} is the Fried-Conte dispersion function. Once the (anisotropic part of the) potential distribution is computed from Eq. (VII.3), the electrostatic drag straightforwardly arises as $\mathbf{F}_E^p = -Q\nabla\Phi|_{R=0}$. Ivlev gives (Eq. (8) in Ref. [60] upon setting the collisional parameter \mathfrak{K} to 0 and changing the units), to first order in w_d :

$$\mathbf{F}_E^p = \frac{8\sqrt{\pi}}{3} F_i^0 \chi_p^2 \mathbf{w}_d \ln \Lambda, \quad (\text{VII.4})$$

where

$$F_i^0 = N_\infty R_p^2 T_{i\infty} / Z \quad (\text{VII.5})$$

is the unperturbed ion pressure force over a sample surface R_p^2 (recall that the ion density at infinity is N_∞/Z), and $\ln \Lambda = \ln(k_{\max}/k_{\min})$ is the Coulomb logarithm.

The challenge in evaluating the integral (VII.3) is to choose the appropriate bounds in $|\mathbf{k}|$, k_{\min} and k_{\max} . Typically one adopts $k_{\min} \sim 1/\Lambda_D$ (no significant interaction outside the Debye sphere) and $k_{\max} \sim 1/R_C$ (the interaction is non-linear within the Coulomb radius). In our point-like particle scaling this yields $k_{\max}/k_{\min} \gg 1$; because of the logarithmic dependence of $\ln \Lambda$ on k_{\max}/k_{\min} , the exact value of the integration bounds is not required and we are left with

$$\ln \Lambda \simeq \ln \left(\frac{\Lambda_D}{p_{90}} \right), \quad (\text{VII.6})$$

where $p_{90} = R_C$ is the 90° scattering impact parameter for a “typical ion” with velocity $v = \sqrt{T_{i\infty}/m}$.

VII.1.2 Binary collision approach to the ion-drag force

The dielectric response approach suffers from only being valid when $\Lambda_D \gg p_{90} \gg R_p$. In steady-state however, momentum conservation implies that the *total* ion-drag force \mathbf{F}_i be also equal to the rate of momentum flux through any control surface surrounding the dust. By taking this surface at infinity, the ion-drag : $\mathbf{F}_i = \mathbf{F}_i^\infty = \mathbf{F}_{im}^\infty + \mathbf{F}_E^\infty$ can formally be evaluated for arbitrary plasma parameters when the OML conditions (Large Debye length) are satisfied.

Impact force

In OML conditions, \mathbf{F}_{im}^∞ is given by Eq. (V.23) with an additional term $m\mathbf{v}$ in the integral. After tedious but straightforward algebra [11]:

$$\mathbf{F}_{im}^\infty = F_i^0 \left\{ \frac{\pi}{2} \left[4w_d^2 + 4 - \frac{1}{w_d^2} - \frac{2}{w_d^2} (1 - 2w_d^2) \chi_p \right] \text{erf}(w_d) + \frac{\sqrt{\pi}}{w_d} (2w_d^2 + 1 + 2\chi_p) \exp(-w_d^2) \right\} \mathbf{e}_d, \quad (\text{VII.7})$$

where \mathbf{e}_d is the unit vector in the drift direction ($\mathbf{v}_d = v_d \mathbf{e}_d$); also recall the notation $w_d = v_d/v_{ti}$.

Electrostatic force

\mathbf{F}_E^∞ is usually referred to as “orbital force”, as its calculation can be reduced to the usual Coulomb collision problem. The momentum transfer collision frequency for an electron with velocity v_e on (infinitely massive) stationary ions with charge Z and charge-density N_∞ is

$$\nu_{ei} = \frac{N_\infty}{Z} \frac{4\pi}{m_e^2 v_e^3} \left(\frac{Ze^2}{4\pi\epsilon_0} \right)^2 \ln \Lambda, \quad (\text{VII.8})$$

where $\ln \Lambda$ is the Coulomb logarithm given by Eq. (VII.6) with $p_{90} = -e^2 Z / (4\pi\epsilon_0 m_e v_e^2)$ and still $\Lambda_D = (\Lambda_{Di}^{-2} + \Lambda_{De}^{-2})^{-2}$. By virtue of momentum conservation, the ion-electron

momentum transfer collision frequency is $\nu_{ie} = \nu_{ei}m_e/m$, and the force felt by a stationary ion is the average over the electron distribution function of $m_e\nu_{ei}\mathbf{v}_e = m\nu_{ie}\mathbf{v}_e$.

Upon mentally replacing the colliding electrons by ions, and the stationary target ion by the dust particle, we can therefore write

$$\mathbf{F}_{\mathbf{E}}^{\infty} = \frac{4\pi}{m} \left(\frac{QZe}{4\pi\epsilon_0} \right)^2 \ln \Lambda \int \frac{\mathbf{v}}{v^3} \frac{f(\mathbf{v})}{Z} d^3\mathbf{v}, \quad (\text{VII.9})$$

where Q is here the dust charge and f the ion-charge distribution function. Transforming the velocity variable in spherical coordinates such that $v = |\mathbf{v}|$ and $v_z = |\mathbf{v}|c$ (“ $c = \cos \theta$ ”), hence $d^3v = 2\pi v^2 dc$, Eq. (VII.9) rewrites

$$\mathbf{F}_{\mathbf{E}}^{\infty} = \frac{N_{\infty}}{Z} \frac{8\pi}{mv_{ti}^2 \sqrt{\pi}} \left(\frac{QZe}{4\pi\epsilon_0} \right)^2 \ln \Lambda \int \exp(-w^2) \exp(1-c^2) \exp[-(wc - w_d)^2] cdcdw \mathbf{e}_d, \quad (\text{VII.10})$$

which upon integration yields the well known form [11]

$$\mathbf{F}_{\mathbf{E}}^{\infty} = 8\pi \left(\frac{QZe}{4\pi\epsilon_0} \right)^2 \frac{N_{\infty}/Z}{mv_{ti}^2} G(w) \ln \Lambda \mathbf{e}_d, \quad (\text{VII.11})$$

where

$$G(w) = \frac{\operatorname{erf}(w) - 2w \exp(-w^2)/\sqrt{\pi}}{2w^2} \quad (\text{VII.12})$$

is the Chandrasekhar function. Sometimes only the low argument limit $G(w) \sim 2w/(3\sqrt{\pi})$ is considered.

In the large Debye length limit where the sphere capacitance is $C = 4\pi\epsilon_0 R_p$, Eq. (VII.11) can be rewritten in terms of sphere potential $\chi_p = -Ze\Phi_p/T_{i\infty}$:

$$\mathbf{F}_{\mathbf{E}}^{\infty} = 4\pi F_i^0 \chi_p^2 G(w) \ln \Lambda \mathbf{e}_d. \quad (\text{VII.13})$$

The Coulomb logarithm

When integrating over the ion distribution function to obtain Eq. (VII.9), the Coulomb logarithm has implicitly been taken as independent of velocity, which is incorrect. $\ln \Lambda$ in Eq. (VII.13) must therefore be evaluated for a “characteristic” ion in the distribu-

tion function at infinity.

The “exact” Coulomb logarithm is given by the integral over impact parameter $p \in [p_{\min}, p_{\max}]$

$$\ln \Lambda = \int_{p_{\min}}^{p_{\max}} \frac{pd p}{p_{90}^2 + p^2} = \frac{1}{2} \ln \left[\frac{p_{90}^2 + p_{\max}^2}{p_{90}^2 + p_{\min}^2} \right]; \quad (\text{VII.14})$$

Khrapak [61] proposed to set p_{\min} to the minimal impact parameter below which the particle is collected (hence its contribution to the ion-drag already accounted for in Eq. (VII.7)), and p_{\max} to the impact parameter such that the point of closest approach is located at a distance Λ_s from the dust center, where Λ_s is an appropriate plasma shielding length. In OML conditions where no intermediate potential barriers occur and the potential is spherically symmetric, conservation of angular momentum (see Eq. (V.21)) yields

$$p_{\min} = R_p \left(1 + 2 \frac{p_{90}}{R_p} \right)^{1/2}, \quad (\text{VII.15})$$

$$p_{\max} = \Lambda_s \left(1 + 2 \frac{p_{90}}{\Lambda_s} \right)^{1/2}, \quad (\text{VII.16})$$

hence the rather simple and compact formula [61]

$$\ln \Lambda \simeq \ln \left(\frac{p_{90} + \Lambda_s}{p_{90} + R_p} \right). \quad (\text{VII.17})$$

Equation (VII.17) can be considered as “exact” in the OML regime, although uncertainty remains as to how to evaluate the characteristic parameters p_{90} and Λ_s . In Ref. [12], Hutchinson suggests as a first approximation

$$p_{90} = \frac{R_p}{2} \frac{\chi_p}{1 + w_d^2}, \quad (\text{VII.18})$$

$$\Lambda_s = \Lambda_{De} \left\{ 1 + [\tau (1 + 2w_d^2)]^{-1} \right\}^{-1/2}, \quad (\text{VII.19})$$

yielding $p_{90} = R_C/2$ and $\Lambda_s = \Lambda_D$ in the limit $w_d \ll 1$, and $p_{90} = -Ze\Phi_p R_p/mv_d^2$ and $\Lambda_s = \Lambda_{De}$ in the limit $w_d \gg 1$.

VII.1.3 Force Evaluation with SCEPTIC

In the absence of magnetic field, the ion-drag force can be computed with SCEPTIC(2D) at the sphere surface as the sum of

- Integral of the electrostatic Maxwell stress tensor at the dust surface (\mathbf{F}_E^P);
- Ion momentum collection averaged over the last 25% of the PIC simulation time-steps (\mathbf{F}_{im}^P);
- Electron pressure at the sphere surface, which is negligible within the strongly electron-repelling sphere assumption, and exactly zero for an equipotential collector in the absence of external field.

Figure (VII-1) shows a sample of ion-drag calculations for the case $\tau = 0.1$, $\phi_p = -4$, $\lambda_{De} = 20$, and increasing drift velocity v_d . For this particular set of runs we used domain size $r_b = 70$ and $\phi(r_b) = 0$ as outer boundary condition for the potential. The solution is plotted in units of $R_p^2 N_\infty T_e$ rather than $F_i^0 = R_p^2 N_\infty T_{i\infty}/Z$, which is more convenient when running SCEPTIC in self-consistent mode (i.e. not in the free-flight regime).

Figure (VII-1) also shows a comparison with the low-velocity expansion ($w_d \ll 1$)

$$\mathbf{F}_i^\infty = \mathbf{F}_{im}^\infty + \mathbf{F}_E^\infty = \frac{8\sqrt{\pi}}{3} F_i^0 (2 + \chi_p + \chi_p^2 \ln \Lambda) \mathbf{w}_d + O(w_d)^2, \quad (\text{VII.20})$$

often used in cold dusty plasmas experiments where typical drift velocities are deeply subthermal. The agreement between the analytic drag estimates and the “exact” solution computed by SCEPTIC is good except when the flow is slightly subsonic, as discussed in detail by Hutchinson [12]. The physical picture of the analytic model is nevertheless correct, and we shall take advantage of it in our study of magnetized plasmas. Also an important point to keep in mind is that while indeed $\mathbf{F}_i^P = \mathbf{F}_{im}^P + \mathbf{F}_E^P = \mathbf{F}_i^\infty = \mathbf{F}_{im}^\infty + \mathbf{F}_E^\infty$, the terms do not individually match, i.e. $\mathbf{F}_{im}^P \neq \mathbf{F}_{im}^\infty$ and $\mathbf{F}_E^P \neq \mathbf{F}_E^\infty$.

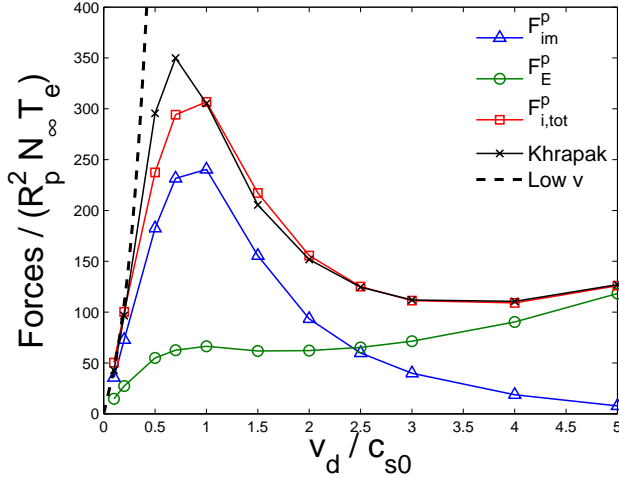


Figure VII-1: Comparison of ion-drag force computed by SCEPTIC(2D) (\mathbf{F}_i^p , decomposed in \mathbf{F}_{im}^p and \mathbf{F}_E^p) with Khrapak’s analytic solution (sum of \mathbf{F}_{im}^∞ (Eq. (VII.7)) and \mathbf{F}_E^∞ (Eq. (VII.13)) with $\ln \Lambda$ given by Eq. (VII.17), and the low velocity limit (VII.20)). The parameters are $\tau = 0.1$, $\phi_p = -4$, and $\lambda_{De} = 20$.

VII.2 2D calculations in parallel-drifting magnetoplasmas

VII.2.1 Free-flight calculations

To the best of our knowledge, no analytic theory or model describing the ion-drag in magnetized plasmas has been published. We start the exploration of magnetic field effects in the free-flight regime, where no electric field but the convective field driving the cross-field flow is considered, hence at the dust surface only the ion collection force \mathbf{F}_{im}^p is non-zero. The free-flight model was already discussed in chapters II, IV, arguing that it could be seen as the “correct” solution in the limit $\tau \gg 1$; this property only holds in zero-Debye length plasmas where the effective probe dipole does not permeate into the plasma region. In the finite Debye length regime, free-flight calculations can be related to the physical situation $\tau \gg 1$ only in the presence of purely parallel drifts, where ion collection force calculations can be performed analytically. Indeed at fixed β_i and $w_\perp \neq 0$, the convective electric field in ion thermal units is independent of τ (given by Eq. (V.36)).

In magnetic-free plasmas the force is straightforwardly given by Eq. (VII.7) with $\chi_p = 0$:

$$\mathbf{F}_{\text{im}}^{\beta_i=0} = F_i^0 \left\{ \frac{\pi}{2} \left[4w_d^2 + 4 - \frac{1}{w_d^2} \right] \operatorname{erf}(w_d) + \frac{\sqrt{\pi}}{w_d} (2w_d^2 + 1) \exp(-w_d^2) \right\} \mathbf{e}_d. \quad (\text{VII.21})$$

In the opposite limit $\beta_i = \infty$, the ions can be seen as flowing one-dimensionally along the magnetic field lines, hence the parallel collection force to the sphere is equal to that to a disc with cross-section πR_p^2 collecting ions from both sides:

$$\mathbf{F}_{\text{im}}^{\beta_i=\infty} = \frac{N_\infty/Z}{v_{ti}\sqrt{\pi}} \left\{ \int_0^\infty \exp \left[-\frac{(v-v_d)^2}{v_{ti}^2} \right] v^2 dv - \int_{-\infty}^0 \exp \left[-\frac{(v-v_d)^2}{v_{ti}^2} \right] v^2 dv \right\} m\pi R_p^2 \mathbf{e}_d, \quad (\text{VII.22})$$

yielding after integration

$$\mathbf{F}_{\text{im}}^{\beta_i=\infty} = 2\pi F_i^0 \left[\frac{w_d \exp(-w_d^2)}{\sqrt{\pi}} + \left(w_d^2 + \frac{1}{2} \right) \operatorname{erf}(w_d) \right] \mathbf{e}_d. \quad (\text{VII.23})$$

At intermediate magnetization, the collection force is given by the triple integral

$$\mathbf{F}_{\text{im}} = F_i^0 \left\{ \frac{1}{2} \pi^3 \beta^2 \int_{s=0}^\infty \int_{t=0}^\infty \tilde{f}(\beta, s, t) \left[\frac{1}{2} \theta(1-s)(1-s)^2 + \int_{u=|s-1|}^{s+1} \frac{1}{2\pi} \int_{\psi=0}^{2\pi} H(u, s, t, \psi) u du \right] st^2 ds dt \right\} \mathbf{e}_d, \quad (\text{VII.24})$$

where \tilde{f} is still given by Eq. (V.49). Equation (VII.24) corresponds to Eq. (V.46) with an additional term $2\pi t \beta_i \mathbf{e}_d = 4\sqrt{\pi} \mathbf{w}$ to raise the moment one order. Numeric integration of Eq. (VII.24) confirms that F_{im} tends to Eq. (VII.21) when $\beta_i \rightarrow 0$, and to Eq. (VII.23) when $\beta_i \rightarrow \infty$.

Figure (VII-2) compares the ion collection force F_{im}^p computed by direct orbit integration with SCEPTIC in free-flight conditions, with the semi-analytic formula (VII.24). The agreement is excellent, with a fractional error less or equal to 0.3% that could be improved by refining the orbit integrator time-step. While the free-flight current to a sphere in parallel-flowing magnetoplasmas was found to decrease linearly with β_i at low β_i (see Eq. (IV.7)), the force dependence is quadratic

in β_i , and almost no magnetic-field effect is felt unless $\beta_i \gtrsim 1$.

(a) $w_d = 0.5$

(b) $w_d = 1.5$

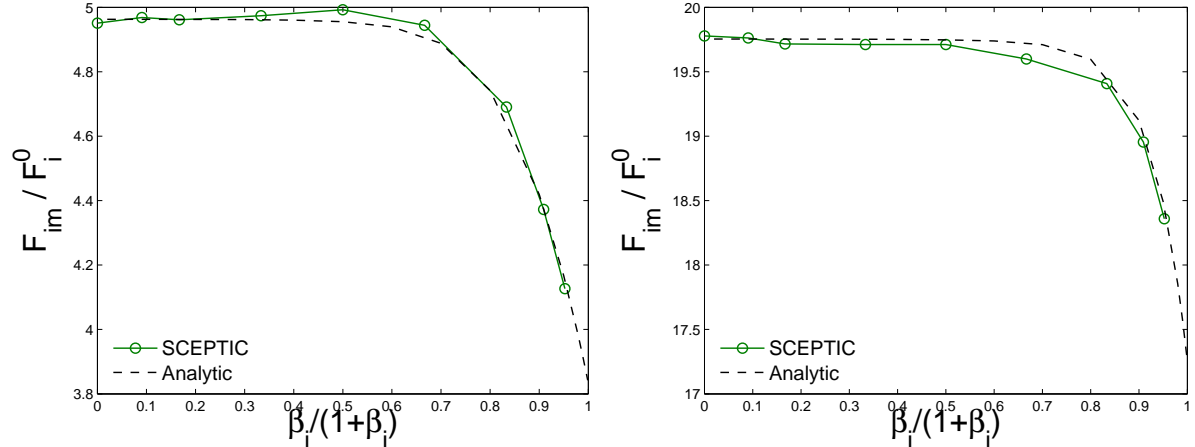


Figure VII-2: Ion-drag normalized to $F_i^0 = N_\infty R_p^2 T_{i\infty} / Z$ as a function of ion magnetization β_i in the free-flight regime (i.e. disregarding probe-induced electric field effects on the ions), computed by SCEPTIC3D (SCEPTIC2D would give the same solution) for a purely parallel drift (a) $w_d = 0.5$ and (b) $w_d = 1.5$. “Analytic” refers to the semi-analytic solution given by the integral (VII.24).

VII.2.2 Self-consistent calculations

The formal absence of solution in parallel-drifting plasmas

As shown in paragraph VII.1.1, the electrostatic part of the ion-drag is due to the dust-flow-interaction-induced plasma polarization effect on the dust charge, which mathematically arises from the Landau damping term in the ion susceptibility. It might be tempting to perform similar calculations in magnetized plasmas, although there is little hope of obtaining a closed-form expression for the integral (VII.3) if the full hot magnetoplasma susceptibility tensor is used. The endeavour would however be pointless. Indeed tractable calculations have been performed with the cold plasma equations [62] in the presence of parallel ion flow, and show that the potential distribution around the test charge tends to zero at infinity only when the external Mach number is higher than unity.

This observation is a confirmation that no self-consistent solution to the plasma-probe interaction problem in parallel-flowing magnetoplasmas exists unless $\Lambda_{De} = \infty$ *exactly*, as discussed in paragraph V.2.3, or if the magnetized Bohm condition is pre-satisfied in the unperturbed plasma. While current calculations were possible by artificially imposing a Coulomb potential in the SCEPTIC simulation, this cannot be done for force-calculations because the integrated Maxwell-stress at the dust surface would be zero. We therefore have to select a finite electron Debye length, run the code in self-consistent mode, and impose a zero outer potential to force decay at infinity. This is *not* a rigorous treatment, but we briefly discuss it in order to gain insight in the effect of ion magnetization on the parallel ion-drag.

Adaptation of Fermi's model

Disregarding all of the above subtleties about the self-consistent problem being ill-defined, the electrostatic part of the ion-drag can be estimated by the binary collision method in a Coulomb field accounting for the ion magnetization. This might be considered as the classical magnetized Rutherford scattering problem, which has no analytic solution except in the limit of weak deflection ($p \gg p_{90}$) and zero original pitch angle ($v_{\parallel} \gg v_{\perp}$). The corresponding calculation is due to Fermi, and the resulting drag can be expressed by Eq. (VII.4) upon replacing $\ln \Lambda$ by

$$\ln \Lambda = \int_{p_{\min}}^{p_{\max}} \left[\frac{\omega_c p}{v_{\parallel}} K_1 \left(\frac{\omega_c p}{v_{\parallel}} \right) \right]^2 \frac{dp}{p} = F \left(\frac{p_{\min}}{R_L^{\parallel}} \right) - F \left(\frac{p_{\max}}{R_L^{\parallel}} \right), \quad (\text{VII.25})$$

where $R_L^{\parallel} = v_{\parallel}/\omega_c$ is an ion Larmor radius calculated with the parallel ion velocity v_{\parallel} [63], and the function F can be expressed in terms of modified Bessel functions:

$$F(x) = \frac{x^2}{2} [K_1(x)^2 - K_0(x)^2] - x K_0(x) K_1(x). \quad (\text{VII.26})$$

Setting $p_{\min} = p_{90}$ and $p_{\max} = \Lambda_s$, we see that Eq. (VII.25) yields:

- At zero magnetization:

$$\ln \Lambda = \int_{p_{\min}}^{p_{\max}} \frac{dp}{p} = \ln \left(\frac{\Lambda_s}{p_{90}} \right), \quad (\text{VII.27})$$

i.e. as expected the weak deflection limit of Eq. (VII.14).

- At strong magnetization: $\ln \Lambda = 0$. The ions are so tied to the field lines that they are not deflected by the dust, hence do not loose momentum to it.
- At intermediate magnetization, when $p_{90} \lesssim R_L^{\parallel} \lesssim \Lambda_s$: $\ln \Lambda \simeq \ln \left(R_L^{\parallel} / p_{90} \right)$. In other words only ions whose impact parameter is below the Larmor radius are deflected.

To apply Fermi's Coulomb logarithm to plasmas with finite ion temperature, we will use the *ad hoc* expression $R_L^{\parallel} = \sqrt{v_d^2 + v_{ti}^2} / \omega_c$, and in order to tend towards the more general formula (VII.17) at zero magnetization we set:

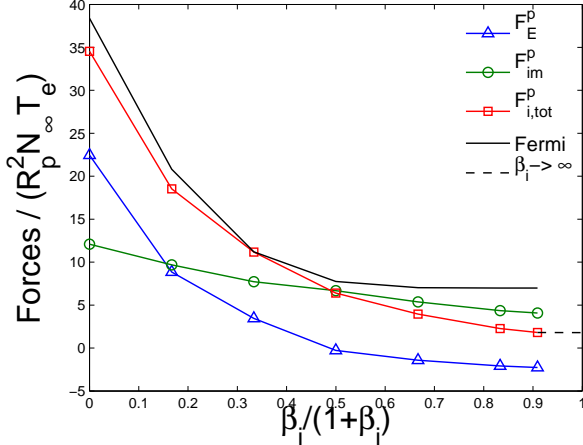
$$\ln \Lambda \simeq \ln \left(\frac{p_{90} + \Lambda_s}{p_{90} + R_p} \right) \frac{F \left(\frac{p_{90}}{R_L^{\parallel}} \right) - F \left(\frac{\Lambda_s}{R_L^{\parallel}} \right)}{\ln \left(\Lambda_s / p_{90} \right)}. \quad (\text{VII.28})$$

Sample SCEPTIC solutions

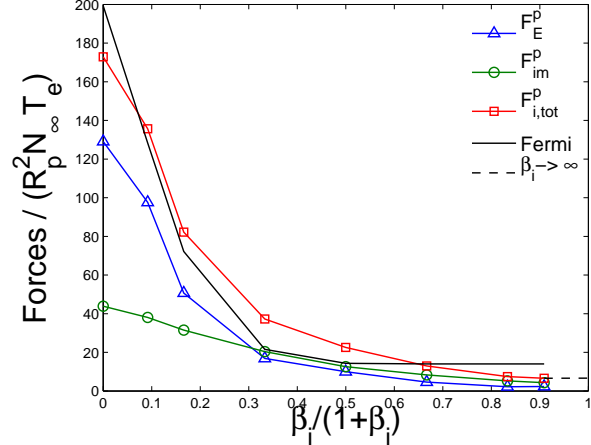
Figure (VII-3) shows the ion-drag force computed by SCEPTIC in parallel-flowing and large Debye-length conditions. It can be seen, as anticipated in paragraph VII.2.1, that the ion impact force decreases with increasing magnetic field, although with a rather weak slope. We can therefore obtain an analytic estimate of the total ion-drag by summing the zero-magnetic field OML expression for the impact force at infinity (VII.7), with the electrostatic force at infinity (VII.13) computed using the *ad hoc* Fermi Coulomb logarithm (VII.28).

The agreement between the resulting expression (labeled "Fermi") and the total ion drag computed by SCEPTIC is very reasonable in view of the several approximations made, and confirms that the picture of an electrostatic interaction radius equal to the minimum of the plasma shielding length and the ion Larmor radius is appropriate.

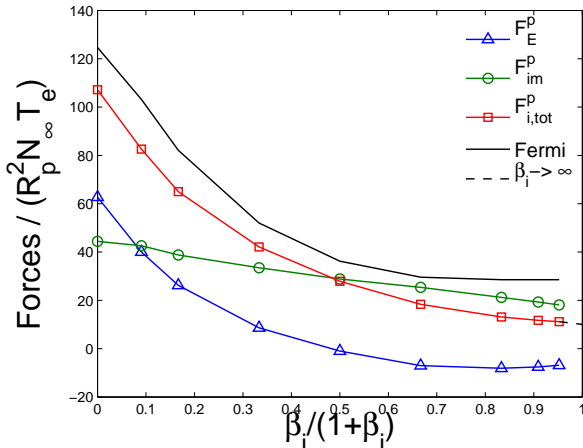
(a) $\tau = 1$, $v_d = 0.35c_{s0}$, $\lambda_{De} = 20$



(b) $\tau = 0.1$, $v_d = 0.35c_{s0}$, $\lambda_{De} = 20$



(c) $\tau = 1$, $v_d = 1.5c_{s0}$, $\lambda_{De} = 20$



(d) $\tau = 0.1$, $v_d = c_{s0}$, $\lambda_{De} = 30$

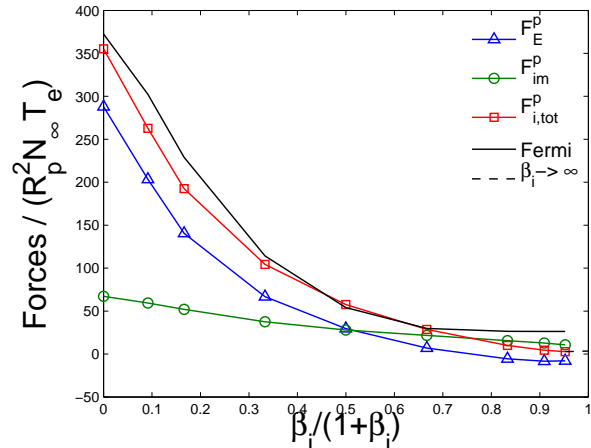


Figure VII-3: Ion-drag normalized to $R_p^2 N_\infty T_e$ as a function of ion magnetization β_i self-consistently computed with SCEPTIC(2D) for a purely parallel drift with $\phi_p = -4$ and different plasma parameters. Curves labeled “Fermi” correspond to the sum of the zero-magnetic field OML expression for the impact force at infinity (VII.7), and the electrostatic force at infinity (VII.13) computed using the *ad hoc* Fermi Coulomb logarithm (VII.28). Curves labeled “ $\beta_i \rightarrow \infty$ ” connect the last SCEPTIC point to the analytic limit (VII.23).

In the strong magnetization limit, when the ions move one-dimensionally along the field lines, the *total* ion-drag is still given by the free-flight equation (VII.23), as shown by the curves labeled “ $\beta_i \rightarrow \infty$ ”. The impact force calculated by SCEPTIC at the dust surface is higher because the ions have been accelerated by its negative charge before being collected, but the action and reaction rule implies that the electrostatic stress at the dust surface be negative.

VII.3 Capacitance calculations in $\mathbf{E} \times \mathbf{B}$ fields

The ion dynamics around the dust particle is governed by the dust-induced electrostatic potential perturbation Φ , solution of Poisson’s equation with inner boundary condition the effective dust potential $\Phi_p + \mathbf{E}_{\text{cnv}} \cdot \mathbf{x}$. The dust particle dynamics is more complicated to model, because it depends on the action of the potential perturbation Φ on its charge Q , the two quantities being related by an *a priori* unknown capacitance C (Eq. (III.52)). The purpose here is to investigate the effect of ion magnetization on the capacitance, before moving on to the force calculations in $\mathbf{E} \times \mathbf{B}$ fields in the next section.

In the limit of large Debye length, the capacitance is given by the well-known vacuum expression $C = 4\pi\epsilon_0 R_p$, which we used to derive the analytic formula (VII.13) for the electrostatic ion-drag. The capacitance at short Debye length is larger because plasma shielding causes the potential gradient at the dust surface to be steeper. The linearized theory without ion response gave $C = 4\pi\epsilon_0 R_p (1 + R_p/\Lambda_{De})$ (Eq. (III.59)), which was shown by Hutchinson to be inappropriate whenever $\Lambda_{De} \lesssim 2R_p$ [11]. An improved empirical expression valid in weakly magnetized conditions was given in Ref. [64] as

$$C = 4\pi\epsilon_0 R_p \left(1 + \frac{R_p}{\Lambda_s} \right), \quad (\text{VII.29})$$

where

$$\Lambda_s \simeq \frac{\Lambda_{De}}{\left\{ 1 + [\tau(1 + 2w_d^2)]^{-1} \right\}^{1/2}} + \Lambda_{De} \ln \left(1 + \frac{R_p}{\Lambda_{De}} \right) \quad (\text{VII.30})$$

is an appropriate shielding length averaged over the sphere surface. Equation (VII.30)

tends to Eq. (VII.19) when $\Lambda_{De} \gg R_p$, but is more satisfactory in the short Debye length regime.

Figure (VII-4) shows a selection of plots of effective shielding length Λ_s versus ion magnetization, where Λ_s is defined such that Eq. (VII.29) matches the self-consistent capacitance computed by SCEPTIC3D. The general trend is a slight increase in shielding length at intermediate magnetization, i.e. a slight decrease in capacitance. An important point is that solid and dashed lines, corresponding to runs with respectively $\delta = \pi/2$ and $\delta = \pi/4$, are almost identical, indicating that the relative orientation of flow and magnetic field has only little influence on the capacitance. The dotted horizontal lines at $\beta_i = 0$ correspond to the empirical, unmagnetized formula (VII.30).

VII.4 Force calculations in $\mathbf{E} \times \mathbf{B}$ fields

VII.4.1 Free-flight calculations at infinite magnetization

In the presence of cross-field flow, analytic free-flight force calculations do not seem feasible except at $\beta_i = 0$ (in which case Eq. (VII.7) still holds) and $\beta_i = \infty$.

The force at infinite magnetization on an elementary dust surface located at cylindrical coordinates η (as usual the angle between sphere surface and magnetic field in a plane of flow and magnetic field) and x along \mathbf{e}_x is, in Cartesian coordinates:

$$dF_{im,z}^p = mN_i \langle v_y v \rangle \cos \eta - mN_i \langle v^2 \rangle \sin \eta, \quad (\text{VII.31})$$

$$dF_{im,y}^p = mN_i \langle v_y^2 \rangle \cos \eta - mN_i \langle vv_y \rangle \sin \eta, \quad (\text{VII.32})$$

$$dF_{im,x}^p = mN_i \langle v_y v_x \rangle \cos \eta - mN_i \langle vv_x \rangle \sin \eta. \quad (\text{VII.33})$$

From the kinetic calculations of chapter II, we know that at the entrance of the magnetic presheath $v_x = 0$, $v_y = v_\perp$, and $T_{ix} = T_{iy} = T_{i\infty}$; we also have analytic expressions for N_i , $\langle v \rangle$, and T_{iz} (Eqs (II.65,II.66,II.67)). Unfortunately, while current is conserved in the magnetic presheath, momentum is not because of asymmetries in the Lorentz force acting on orbits intersecting the sphere. Unless accurate

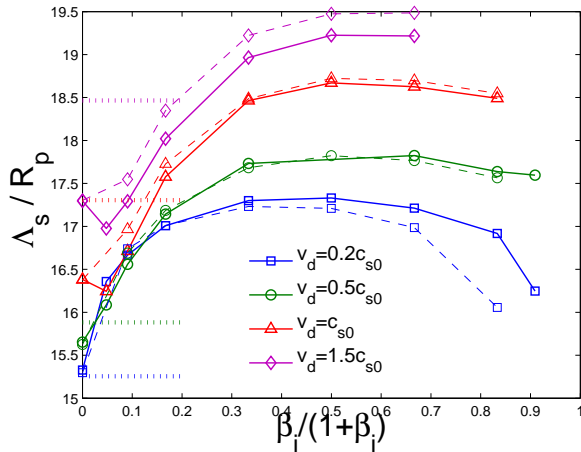
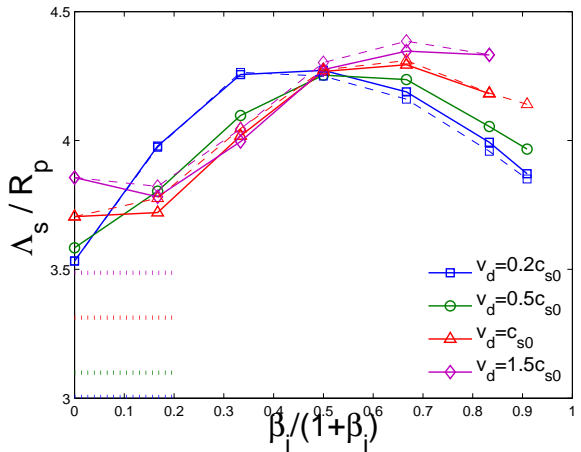
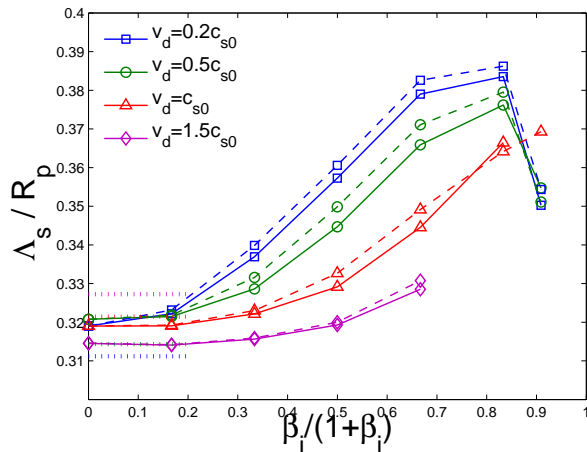
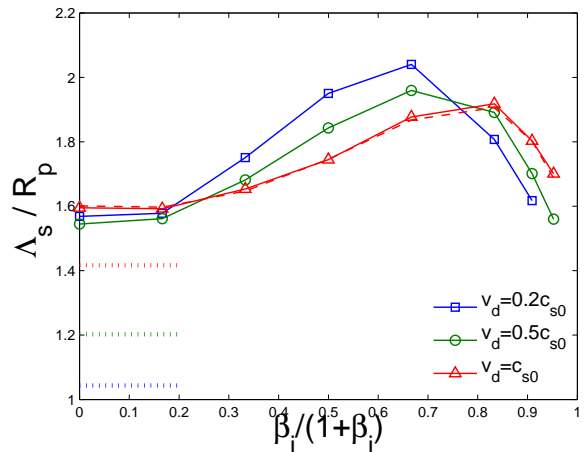
(a) $\tau = 1, \lambda_{De} = 20$ (b) $\tau = 1, \lambda_{De} = 3$ (c) $\tau = 1, \lambda_{De} = 0.1$ (d) $\tau = 0.1, \lambda_{De} = 1$ 

Figure VII-4: Effective shielding length Λ_s such that the self-consistent dust capacitance computed by SCEPTIC3D is expressed as (VII.29). Solid lines correspond to pure cross-field flows ($\delta = \pi/2$), and dashed lines to $\delta = \pi/4$. The dotted limits at $\beta_i = 0$ are given by Eq. (VII.30).

analytic orbit-sphere intersection calculations are performed, which is out of the scope of this thesis (of course SCEPTIC3D does it numerically), only $dF_{im,z}^p$ can be evaluated:

$$dF_{im,z}^p = \frac{N}{N_\infty} \sin \eta \left[2\langle w \rangle (w_\perp \cot \eta - \langle w \rangle) - \frac{T_{iz}}{T_{i\infty}} \right] (N_\infty T_{i\infty}). \quad (\text{VII.34})$$

The total parallel force is then given by integration over η and x :

$$F_z = \frac{\pi}{2} R_p^2 \left[\int_0^\pi dF_{im,z|\text{Do}}^p |\sin \eta| d\eta + \int_0^\pi dF_{im,z|\text{Up}}^p |\sin \eta| d\eta \right], \quad (\text{VII.35})$$

where upfield ($z \leq 0$) and downfield ($z \geq 0$) calculations must be performed separately.

Figure (VII-5) shows the ion collection force F_{im}^p computed by direct orbit integration with SCEPTIC3D in free-flight conditions, in the presence of cross-field flow (velocity $w_d = 0.5$ and different drift to magnetic field angles δ). Figure (VII-5a) shows the force along the magnetic axis, and excellent agreement is found with the analytic limits at $\beta_i = 0$ (Eq. (VII.23)) and $\beta_i = \infty$ (Eq. (VII.35)); at $\delta = \pi/2$ the force is zero by symmetry. Figure (VII-5b) shows the force in the cross-field direction, and Fig. (VII-5c) in the flow direction. We notice that the force in the drift direction is almost not sensitive to δ , and as for pure parallel flows almost no magnetic field effect is felt at $\beta_i \lesssim 1$.

Also of interest is Fig. (VII-5d), showing the impact force in (minus) the convective field direction, which for obvious symmetry reasons is zero at $\beta_i = 0$. As magnetization increases, the ions, whose macroscopic motion is in the \mathbf{e}_y direction, strike the dust preferentially at $y < 0$ with a phase such that the velocity in the \mathbf{e}_x direction is positive. The force seems to peak at $\beta_i \sim 0.8$, but does not tend to zero when $\beta_i \rightarrow \infty$. Indeed the Lorentz force experienced by the ions during their last Larmor gyration before collection is proportional to the magnetic field, while the period of a Larmor gyration is inversely proportional to that field. It is this effect that prevented easy evaluation of Eqs (VII.32, VII.33).

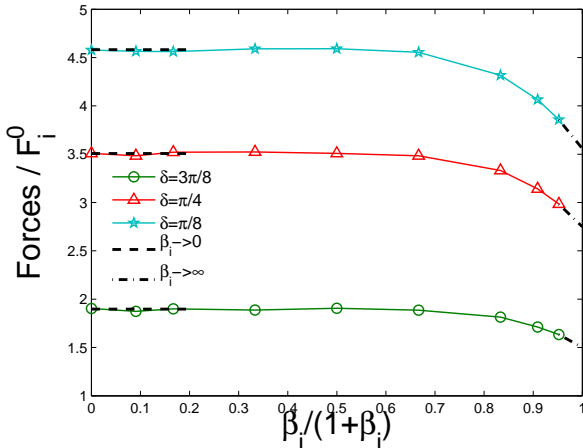
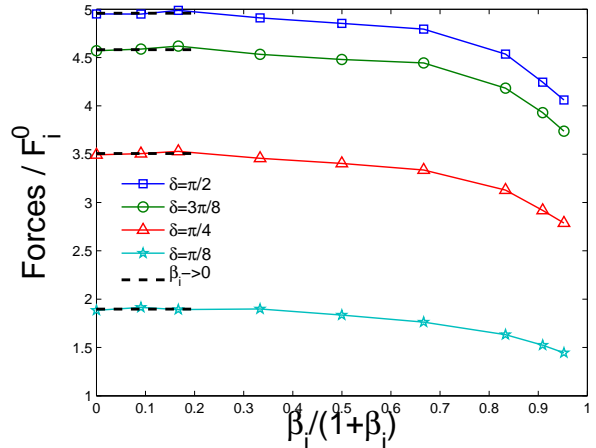
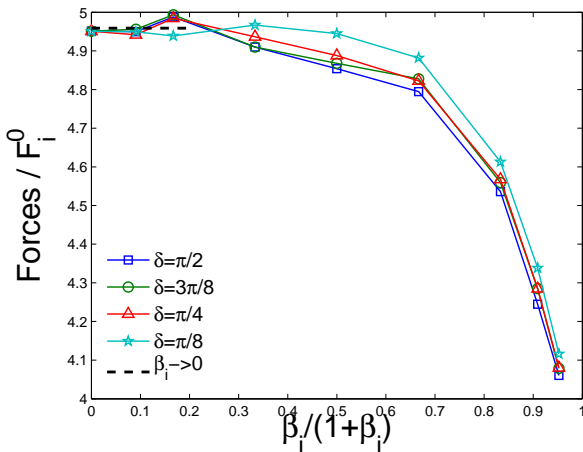
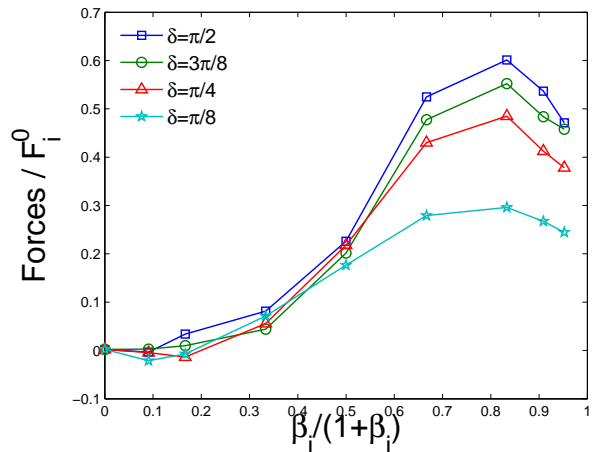
(a) Along \mathbf{e}_z (i.e. \parallel to \mathbf{B})(b) Along \mathbf{e}_y (i.e. \perp to \mathbf{B} and \mathbf{E}_{cnv})(c) Along \mathbf{w}_d (d) Along \mathbf{e}_x (i.e. \parallel to $-\mathbf{E}_{\text{cnv}}$)

Figure VII-5: Ion-drag normalized to $F_i^0 = N_\infty R_p^2 T_{i\infty} / Z$ as a function of ion magnetization β_i in the free-flight regime (i.e. disregarding probe-induced electric field effects on the ions), computed by SCEPTIC3D for $w_d = 0.5$ and different drift to magnetic field angles δ along different axis. (a) Along the magnetic axis, (b) along the cross-field axis, (c) along the drift axis (i.e. weighted sum of (a) and (b)), and (d) along the convective electric field axis. The thick dashed lines indicate the analytic unmagnetized limit (Eq. (VII.23)), and the thick dash-dotted lines in (a) connect the last SCEPTIC3D point to the strongly magnetized limit given by Eq. (VII.35).

VII.4.2 Calculation of the non ion-drag forces

Before discussing in detail the *self-consistent* ion-drag force physics in $\mathbf{E} \times \mathbf{B}$ fields, it is necessary to estimate the magnitude of the non ion-drag forces on the dust, namely the external electrostatic and internal Lorentz forces (Eqs (VII.1,VII.2)).

Electrostatic term

The external electrostatic force \mathbf{F}_Q is easily computed by SCEPTIC3D, upon multiplication of the self-consistently calculated dust capacitance (Eq. (III.52)) with the dust potential Φ_p and the convective electric field \mathbf{E}_{cnv} .

Magnetostatic term

The internal Lorentz force on the dust grain is given by Eq. (VII.2), which involves the net current density \mathbf{j} in the dust particle, solution of the conservation equation $\nabla \cdot \mathbf{j} = 0$ with boundary conditions set by the ion and electron flux-densities to the surface $\Gamma_{i,e}$.

Fortunately we do not need to compute the precise internal current-density pattern. Instead we write

$$\mathbf{F}_j \cdot \mathbf{e}_x = e \left(\int_{-R_p}^{R_p} \bar{I}_{iy} dy - \int_{-R_p}^{R_p} \bar{I}_{ey} dy \right) B, \quad (\text{VII.36})$$

$$\mathbf{F}_j \cdot \mathbf{e}_y = -e \left(\int_{-R_p}^{R_p} \bar{I}_{ix} dx - \int_{-R_p}^{R_p} \bar{I}_{ex} dx \right) B, \quad (\text{VII.37})$$

where \bar{I} refers to the *total* ion or electron current that would flow in the dust particle through a given cross-section normal to \mathbf{e}_x or \mathbf{e}_y if the dust volume were “empty”, and as usual $\mathbf{e}_x \parallel -\mathbf{E}_{\text{cnv}}$ and $\mathbf{e}_z \parallel \mathbf{B}$. The “overbar” notation is used to avoid confusion with the *total* ion and electron current to the dust surface: $I_{i,e} = \int_{\text{Dust}} \Gamma_{i,e} dS$.

\bar{I} is only function of the ion and electron flux-densities to the dust surface:

$$\bar{I}_{i,ex}(x) = \int_{a=-R_p}^x \int_{\alpha=0}^{2\pi} \Gamma_{i,e} d\alpha da, \quad (\text{VII.38})$$

$$\bar{I}_{i,ey}(y) = \int_{a=-R_p}^y \int_{\alpha=0}^{2\pi} \Gamma_{i,e} d\alpha da, \quad (\text{VII.39})$$

where α is the azimuthal angle around the \mathbf{e}_x or \mathbf{e}_y -axis. The ion terms \bar{I}_{ix} and \bar{I}_{iy} can easily be computed by a postprocessing routine from SCEPTIC3D's ion flux-density solutions. On the contrary, estimating the electron terms requires some hypothesis.

First, we assume steady-state, hence the *total* ion and electron currents to the dust are equal: $I_i = I_e = \bar{I}_{ix}(R_p) = \bar{I}_{ex}(R_p) = \bar{I}_{iy}(R_p) = \bar{I}_{ey}(R_p)$.

Second, we assume for the electron flux-density to the surface the general form $\Gamma_e(x, y, z) = f(x)g(z)$, where f and g are arbitrary functions. The motivation for this choice is that the repelled electron flux-density should depend on the local dust potential (function of x), and the angle of magnetic field to dust normal (function of z). Of course the dust is a two-dimensional surface, hence Γ_e is also a function of $y = \sqrt{R_p^2 - x^2 - z^2}$.

\bar{I}_{ey} can be rewritten

$$\bar{I}_{ey}(y) = \int_{-R_p}^y h(a) da, \quad (\text{VII.40})$$

where $h(a) = \int_{\alpha=0}^{2\pi} f(\sqrt{R_p^2 - a^2} \cos \alpha) g(\sqrt{R_p^2 - a^2} \sin \alpha) d\alpha$ is the integral of Γ_e over an elementary crown normal to \mathbf{e}_y located on the sphere surface at $y = a$. We can proceed further by taking advantage of the current balance hypothesis $I_e = \int_{-R_p}^{R_p} h(a) da = I_i$:

$$\bar{I}_{ey}(y) = \frac{1}{2} \left[\int_{-R_p}^{R_p} h(a) da + \int_{-y}^y h(a) da \right] = \frac{I_i}{2} + \frac{1}{2} \int_{-y}^y h(a) da, \quad (\text{VII.41})$$

and h being symmetric in a to write $\int_{y=-R_p}^{R_p} \int_{a=-y}^y h(a) da dy = 0$. This shows that the internal Lorentz force along the \mathbf{e}_x -axis is independent of the precise electron collection pattern:

$$\mathbf{F}_j \cdot \mathbf{e}_x = e \left[\int_{-R_p}^{R_p} \bar{I}_{iy}(y) dy - I_i R_p \right] B. \quad (\text{VII.42})$$

Unfortunately, no such general calculation can be performed to calculate \bar{I}_{ex} , that we rewrite as follows

$$\bar{I}_{ex}(x) = \int_{a=-R_p}^x \int_{\alpha=0}^{2\pi} f(a)g\left(\sqrt{R_p^2 - a^2}\sin\alpha\right) d\alpha da. \quad (\text{VII.43})$$

The obvious choice for f is $f(x) \propto \exp[e(\Phi_p + E_{\text{cnv}}x)/T_e]$, while g is an *a priori* unknown function of β_i . In the limit of strongly magnetized electrons, $g(z) \propto |z|$ as the electrons only see the projection of the sphere along the magnetic field lines:

$$\bar{I}_{ex}(x) \propto \int_{a=-R_p}^x \int_{\alpha=0}^{2\pi} \exp\left(e \frac{E_{\text{cnv}}a}{T_e}\right) \sqrt{R_p^2 - a^2} |\sin\alpha| d\alpha da. \quad (\text{VII.44})$$

Integration over α is easy to perform, but the integral over a has a closed form expression only when $x = R_p$:

$$\bar{I}_{ex}(R_p) = I_e \propto \frac{T_e}{e [E_{\text{cnv}}R_p]} \text{I}_1\left(\frac{e [E_{\text{cnv}}R_p]}{T_e}\right), \quad (\text{VII.45})$$

where I_1 is the modified Bessel function defined by Eq. (A.7). Equation (VII.45) is proportional to the strongly magnetized electron current derived in Appendix A (Eq. (A.6)), which is no surprise as the same hypothesis has been used for both derivations. Because SCEPTIC3D is not run in floating potential mode however, the proportionality coefficient must here be selected such as to balance the ion current I_i .

The Lorentz force along the \mathbf{e}_y -axis is then given by

$$\begin{aligned} \mathbf{F}_j \cdot \mathbf{e}_y &= -e \left\{ \int_{-R_p}^{R_p} \bar{I}_{ix}(x) dx \right. \\ &\quad \left. - I_i \frac{e [E_{\text{cnv}}R_p] / T_e}{\text{I}_1(e [E_{\text{cnv}}R_p] / T_e)} \int_{x=-R_p}^{R_p} \int_{a=-R_p}^x \exp\left(e \frac{E_{\text{cnv}}a}{T_e}\right) \sqrt{R_p^2 - a^2} da dx \right\} B. \end{aligned} \quad (\text{VII.46})$$

Of course when the electrons are unmagnetized, the choice $g(z) \propto |z|$ is not appropriate and we must take g constant instead. However in the absence of magnetic field f is uniform over the sphere, in which case \bar{I}_{ex} is independent of g (for the same

argument that \bar{I}_{ey} was found independent of g). Equation (VII.46), although derived with $g(z) \propto |z|$, must therefore still hold; it is a very robust expression.

VII.4.3 Momentum conservation in SCEPTIC3D

In self-consistent steady-state operation, the total flux of momentum to the inner sphere (the dust particle) must be equal to the net flux of momentum to the outer sphere (computational domain boundary), which can be broken down into

- Integral of the electrostatic Maxwell stress at the outer surface (\mathbf{F}_E^o), only computed from the dust-induced potential perturbation Φ ;
- Ion momentum collection averaged over the last 25% of the PIC simulation time-steps (\mathbf{F}_{im}^o);
- Electron pressure \mathbf{F}_e^o , non negligible at the outer boundary where the potential is non-uniform and the normalized electron density close to unity.
- Integral of the magnetostatic Maxwell stress at the outer surface minus the inner surface (not accounted for in the ion-drag, but considered as the additional force \mathbf{F}_j discussed in paragraph VII.4.2), which according to Eq. (III.63) is the integral over the entire computational domain of the Lorentz force acting on the ions. From this must be subtracted the volumetric momentum flux due to the convective field action on the ions, resulting in a total contribution

$$\mathbf{F}_M^o = e \int_{\text{Comp. D.}} (\langle \mathbf{v} \rangle - \mathbf{v}_d) d\Omega \times \mathbf{B}, \quad (\text{VII.47})$$

where $\langle \mathbf{v} \rangle$ is the ion fluid velocity averaged over the last 25% of the PIC simulation time-steps. As shown in appendix A, the cross-field electron velocity in the domain is everywhere equal to the *background* “ $\mathbf{E} \times \mathbf{B}$ ” velocity (Eq. (A.3)), hence $(\langle \mathbf{v}_e \rangle - \mathbf{v}_d) \times \mathbf{B} = 0$ in the entire simulation volume.

Figure (VII-6) shows the ion-drag force evolution with increasing magnetic field self-consistently calculated with SCEPTIC3D in the presence of parallel and cross-

field flow ($\delta = \pi/4$), along the three coordinate axes using the parameters $\lambda_{De} = 1$, $\tau = 0.1$, $v_d = 0.35c_{s0}$, $\delta = \pi/4$ and $\phi_p = -8$. The contributions to the ion-drag force at the collecting sphere (solid lines) and outer boundary (dashed lines) are different, but very convincingly add up to the same total.

VII.4.4 Ion-drag solutions at low Debye length

It is convenient to analyze SCEPTIC3D’s solutions from low to large Debye lengths, starting in this paragraph with $\lambda_{De} = 0.03$. Figure (VII-7) shows the ion-drag force computed at the dust surface in the presence of an equithermal ($\tau = 1$), purely perpendicular flow ($\delta = \pi/2$), for drift velocities $v_d = 0.35c_{s0}$ and $v_d = c_{s0}$. The dust potential is arbitrarily set to $\phi_p = -8$, and the ion magnetization allowed to vary from 0 to the maximum value such that no part of the dust particle is positively charged.

The ion impact force along the \mathbf{e}_y -axis behaves similarly to what computed from free-flight calculations (see Fig. (VII-5)), i.e. is only weakly dependent on the magnetic field. The electrostatic part of the ion-drag along the same axis is found to be negative. The explanation is, as first observed for the case of parallel flows at strong magnetization (see Fig. (VII-3)), that the dust “pulls” on the ions as they are attracted, and by reaction feels a negative electrostatic drag. At $\beta_i = 0$, momentum conservation implies that the *total* ion-drag be positive, which we observe here. No such requirement exists in the presence of magnetic field since the external electric field is allowed to work on the ions, but it appears that regardless of β_i the ion-drag in the flow direction remains positive.

The ion impact force along the \mathbf{e}_x -axis also behaves similarly to what is computed from free-flight calculations, i.e. is positive and does not tend to zero at infinite magnetization. The highest magnetizations considered are $\beta_i = 10$ for $v_d = 0.35c_{s0}$, and $\beta_i = 5$ for $v_d = c_{s0}$, corresponding to $[E_{cnv}R_p] \simeq -4.4T_e/e$ and $-6.26T_e/e$, respectively. The dust potential being set to $\phi_p = -8$, we can hardly go further without jeopardizing the validity of the repelled-electron assumption.

The electrostatic part of the ion-drag along the \mathbf{e}_x -axis is positive and increases

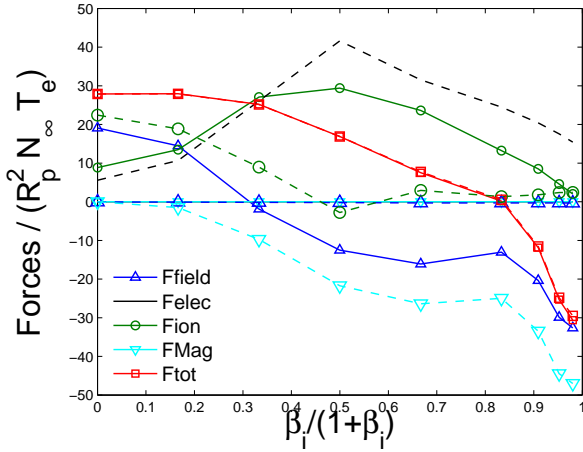
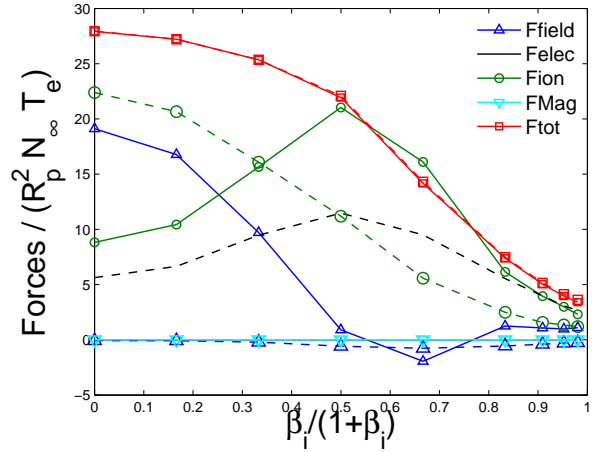
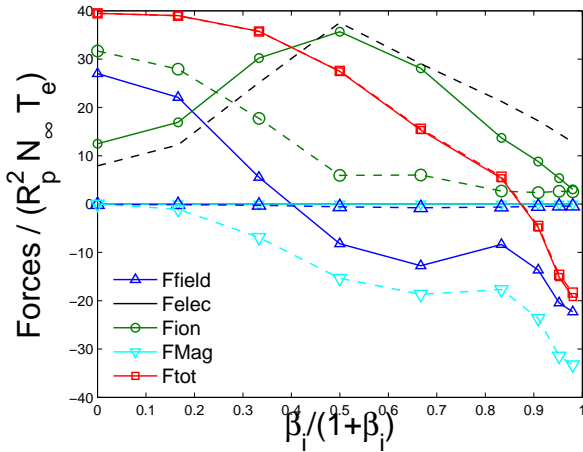
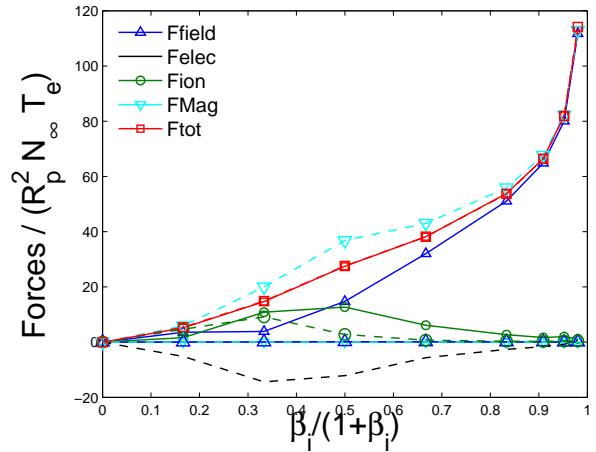
(a) e_y -axis(b) e_z -axis(c) e_d -axis(d) e_x -axis

Figure VII-6: Example of SCEPTIC3D magnetized calculations for $\lambda_{De} = 1$, $\tau = 0.1$, $v_d = 0.35c_{s0}$, $\delta = \pi/4$, $\phi_p = -8$, and increasing ion magnetization β_i on a computational domain of radius $r_b = 8$. The contributions to the ion-drag force at the collecting sphere (solid lines) and outer boundary (dashed lines) are different, but add up to the same total. “Ffield” refers to the electrostatic Maxwell stress F_E , “Felec” to the electron pressure force F_e , “Fion” to the ion collection force F_{im} , “FMag” to the integral over the computational domain volume of the Lorentz force minus the convective force F_M , and “Ftot” to the total ion-drag force F_i .

with ion magnetization. This force arises from the plasma polarization induced by the dust effective dipole feeding back on the dust monopole. A crude estimate of its magnitude is given by the linearized solution (III.58) upon replacing Λ_{De} by the “capacitance shielding length” Λ_s (Eq. (VII.30)). In ion thermal units:

$$\mathbf{F}_{\mathbf{E}_x}^{\mathbf{p}} \sim \frac{4}{3}\pi\sqrt{\pi}F_i^o \frac{\Lambda_{De}^2}{\Lambda_s^2} \tau \chi_p w_{\perp} \beta_i \mathbf{e}_x. \quad (\text{VII.48})$$

Equation (VII.48) states that $\mathbf{F}_{\mathbf{E}_x}^{\mathbf{p}}$ should be approximately proportional to β_i and w_{\perp} , which can easily be verified in Figs (VII-7c,d) although quantitative agreement is quite poor.

We now need to compare the just-computed ion-drag with the additional forces felt by the dust particle. Figure (VII-8) shows that regardless of the drift velocity, the \mathbf{e}_y component of the internal Lorentz force becomes stronger than the ion-drag when $\beta_i \sim 2$. The positive sign of \mathbf{F}_{j_x} is due to the electrons being predominantly collected at $x < 0$ (weakly electron-repelling zone), while the ion collection pattern is more isotropic or shifted towards $x > 0$ (strongly ion-attracting zone). This results in the internal dust current flowing predominantly in the $-\mathbf{e}_x$ direction. For the same reason $|\mathbf{F}_{j_y}| > |\mathbf{F}_{j_x}|$.

Perhaps the most surprising result of Fig. (VII-8) is that the magnitude of \mathbf{F}_{j_x} , \mathbf{F}_{i_x} and \mathbf{F}_Q are comparable. In our treatment where the dust is stationary and the plasma flowing, \mathbf{F}_Q arises from the convective field action on the dust charge. In most situations however, the dust is moving in a stationary plasma, and a straightforward Lorentz transform shows that in that case \mathbf{F}_Q corresponds to the “ $\mathbf{v} \times \mathbf{B}$ ” force responsible for the dust Larmor rotation. In small Debye length plasmas, a dust particle’s Larmor angular frequency is therefore significantly faster than what is predicted by the simple-minded formula QB/m_{Dust} .

Figure (VII-9) shows the ion-drag force computed at the dust surface with the same parameters as Fig. (VII-7), except the angle of flow and magnetic field is now $\delta = \pi/4$. The ion-drag dependence on β_i along the convective field axis \mathbf{e}_x follows the same physics as in Fig. (VII-7), although its magnitude is lower by a factor

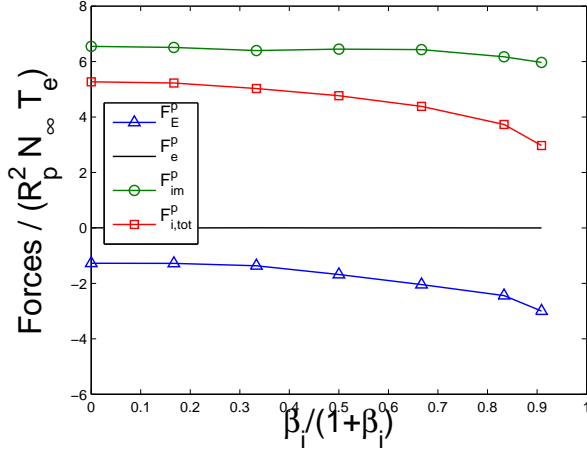
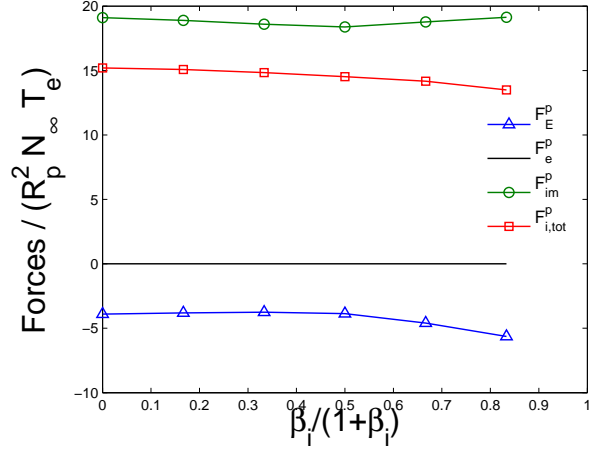
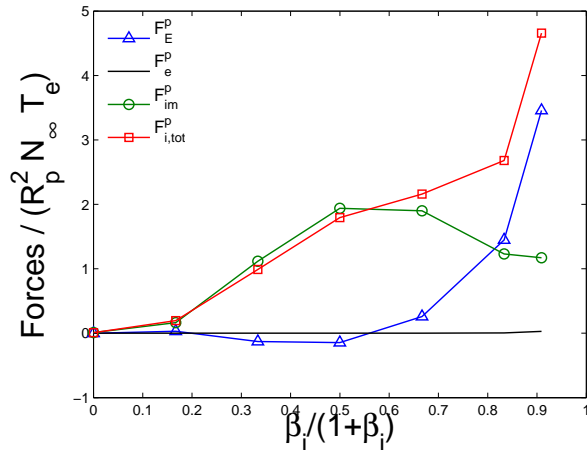
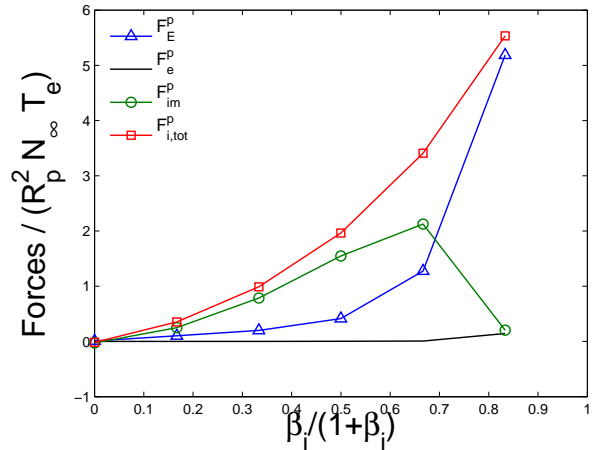
(a) $v_d = 0.35c_{s0}$, \mathbf{e}_y -axis(b) $v_d = c_{s0}$, \mathbf{e}_y -axis(c) $v_d = 0.35c_{s0}$, \mathbf{e}_x -axis(d) $v_d = c_{s0}$, \mathbf{e}_x -axis

Figure VII-7: Self-consistent ion-drag computed at the inner boundary (collecting sphere surface) by SCEPTIC3D for increasing ion magnetization β_i using the parameters $\tau = 1$, $\lambda_{De} = 0.03$, $\phi_p = -8$, and (a,c) $v_d = 0.35c_{s0}$, (b,d) $v_d = c_{s0}$. The flow is purely transverse ($\delta = \pi/2$), hence forces along the magnetic axis \mathbf{e}_z are zero by symmetry.

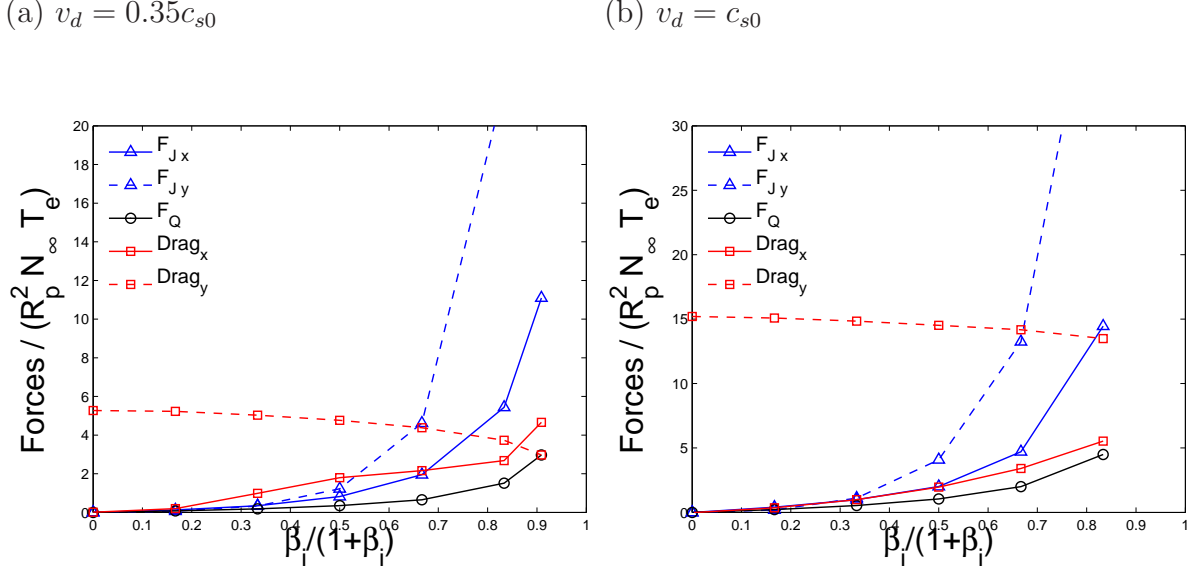


Figure VII-8: Comparison of the total ion-drag force computed by SCEPTIC3D with the parameters of Fig. (VII-7), with the non ion-drag forces \mathbf{F}_j and \mathbf{F}_Q . For easy reading, lines referring to forces acting along \mathbf{e}_x are solid, and dashed for \mathbf{e}_y .

$$\sim \sin \delta = 1/\sqrt{2}.$$

Contrary to the case of Fig. (VII-7) however, the parallel force is non-zero. Because at $\delta = \pi/4$ the drift vector bisects the magnetic and cross-field axis, at $\beta_i = 0$ we see that the forces along \mathbf{e}_y and \mathbf{e}_z are equal. As the magnetic field increases, the ion-drag force along \mathbf{e}_y behaves as in Fig. (VII-7), i.e. the impact part \mathbf{F}_{im}^p is approximately constant, and the electrostatic part becomes more negative. Also the force along \mathbf{e}_y and \mathbf{e}_z -axis are very similar, hence the ion-drag in the $\{\mathbf{e}_y, \mathbf{e}_z\}$ -plane is approximately flow-aligned.

VII.4.5 Ion-drag solutions at intermediate and large Debye length

Figures (VII-10,VII-11) show a gallery of ion-drag force computations at the dust surface for $\lambda_{De} \in [0.3 : 20]$ and $v_d \in [0.2 : 1.5]c_{s0}$, the other parameters being set as in Fig. (VII-7).

Let us start the analysis with the forces along \mathbf{e}_y (drift direction, since $\delta = \pi/2$), in Fig (VII-10). It can first be seen that in intermediate and large Debye length

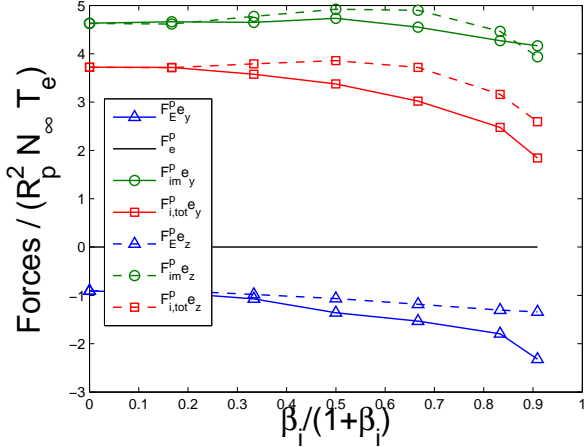
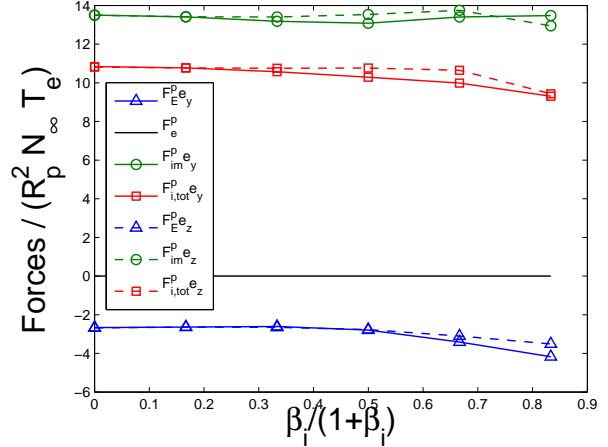
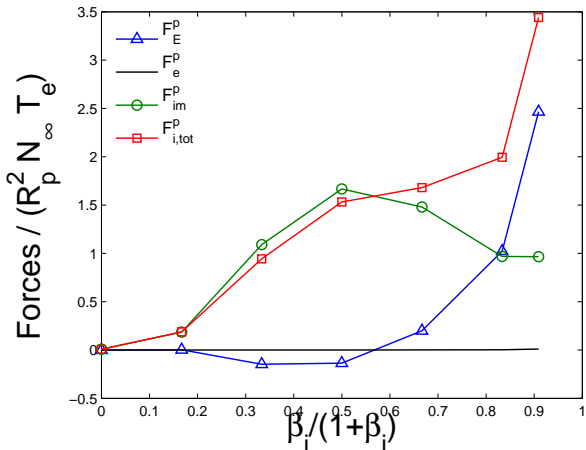
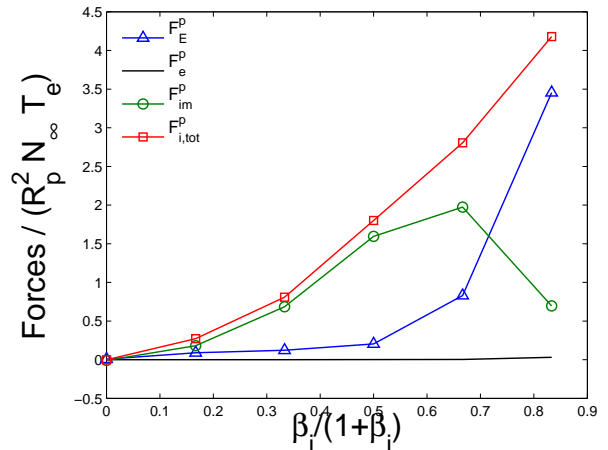
(a) $v_d = 0.35c_{s0}$, $\mathbf{e}_y, \mathbf{e}_z$ -axis(b) $v_d = c_{s0}$, $\mathbf{e}_y, \mathbf{e}_z$ -axis(c) $v_d = 0.35c_{s0}$, \mathbf{e}_x -axis(d) $v_d = c_{s0}$, \mathbf{e}_x -axis

Figure VII-9: Self-consistent ion-drag computed at the inner boundary (collecting sphere surface) by SCEPTIC3D for increasing ion magnetization β_i using the parameters of Fig. (VII-7) except the angle of flow and magnetic field is set to $\delta = \pi/4$. (a,b) simultaneously show the forces along the cross-field (solid lines) and magnetic (dashed lines) axes.

conditions, the ion impact force behaves as in the short Debye length regime, i.e. it slowly decreases with β_i but almost no magnetic field effect is felt when $\beta_i \lesssim 1$. A crude estimate of $\mathbf{F}_{\text{im}}^{\text{p}}$ at low field can be obtained by multiplying the ion mass current to the dust by the characteristic velocity at which the ions are collected, yielding $F_{\text{im}}^p \sim mI_i\sqrt{v_d^2 + v_{ti}^2\chi_p}$. Therefore as the Debye length increases past $\lambda_{De} \sim 1$, when the ion current approaches the large Debye length limit (OML at $\beta_i = 0$ for instance), the ion impact force is not affected by a further increase in λ_{De} . A second effect of interest is that $\mathbf{F}_{\text{im}}^{\text{p}}$ tends to zero at infinite magnetization, because as extensively discussed in chapter V the conducting dust shields the convective field out, hence in the drift limit the ions can only be collected with parallel velocity.

The physics of the electrostatic force $\mathbf{F}_{\text{E}}^{\text{p}}$ is more complicated. At $\beta_i = 0$, it increases continuously with λ_{De} , from the negative values observed in Fig. (VII-7) at low Debye length to highly positive values proportional to $\ln \Lambda$ at large Debye length. Therefore the relative weight of $\mathbf{F}_{\text{im}}^{\text{p}}$ and $\mathbf{F}_{\text{E}}^{\text{p}}$ inverts at intermediate Debye length. The most surprising result here is that at intermediate Debye length and low enough drift velocity, the *total* ion-drag can reverse. The physical mechanism is that the dust pulls on the upstream ion flow, which contrary to the short Debye length regime discussed in Fig. (VII-7) is deflected by the dust and only collected with parallel momentum.

Figure (VII-11) shows the ion-drag for the same runs as in Fig. (VII-10), but along the \mathbf{e}_x -axis. An interesting point is that the electrostatic drag $\mathbf{F}_{\text{E}}^{\text{p}}$ reverses between $\lambda_{De} \simeq 3$ and $\lambda_{De} \simeq 10$, phenomenon for which we have no concrete explanation.

We now need to compare the just-computed ion-drag with the additional forces felt by the dust particle. Figure (VII-12) shows that, similarly to what observed at $\lambda_{De} = 0.03$ in Fig. (VII-8), the magnitude of the \mathbf{e}_y -component of the internal Lorentz force becomes stronger than the ion-drag when $\beta_i \sim 2$. It therefore seems that although the cross-field ion-drag can reverse, the *total* force felt by the dust particle is less likely to do so. In view of our approximate treatment of electron collection used to calculate \mathbf{F}_{jy} however, no definitive answer on the question can be given.

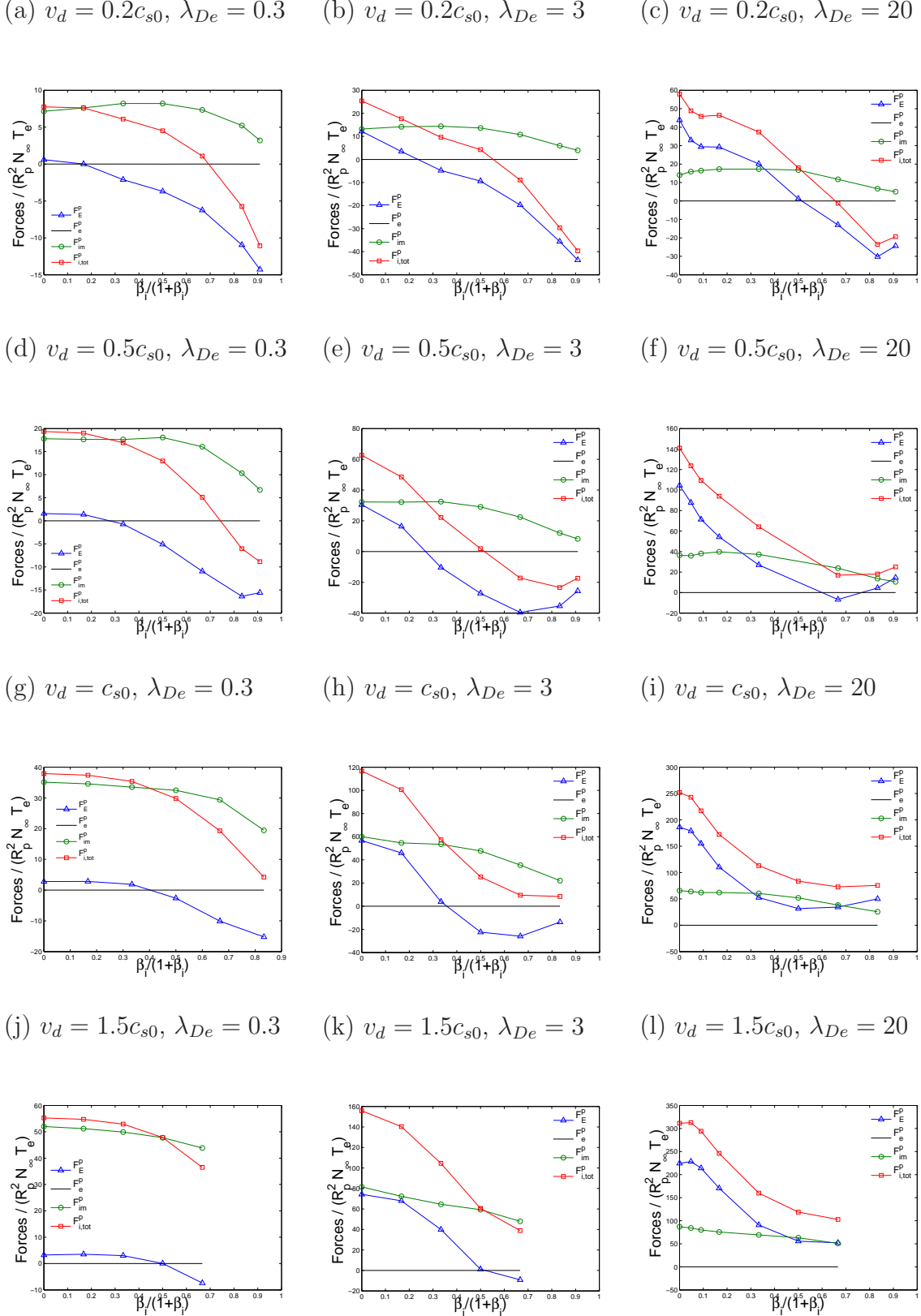


Figure VII-10: Self-consistent ion-drag computed at the dust surface by SCEPTIC3D along \mathbf{e}_y as a function of β_i with $\tau = 1$, $\phi_p = -8$, $\delta = \pi/2$, and variable λ_{De} and v_d .

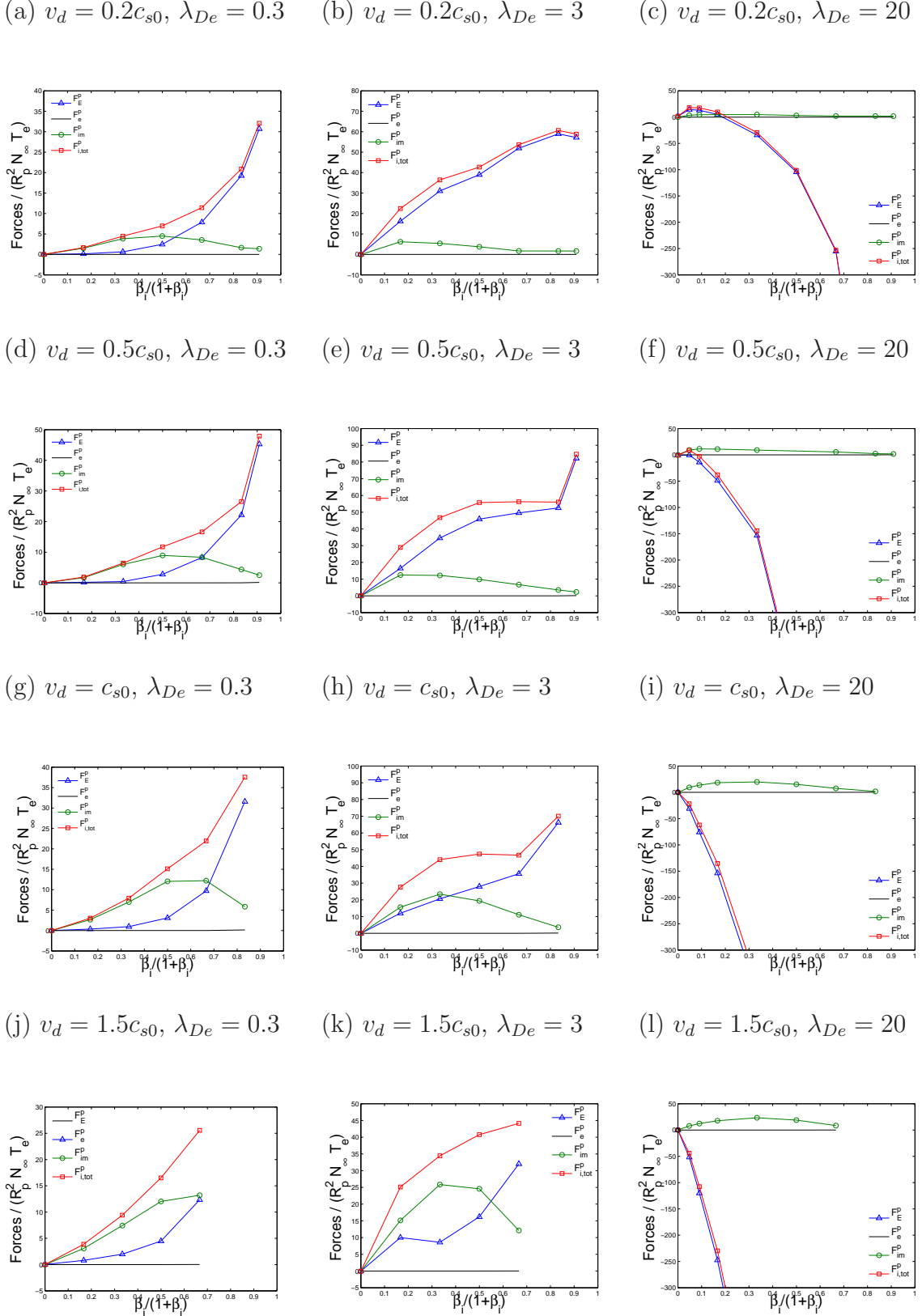


Figure VII-11: Self-consistent ion-drag along the convective field axis \mathbf{e}_x computed at the inner boundary using the parameters of Fig. (VII-10).

Analysis in the \mathbf{e}_x direction is much easier, because as the Debye length increases the external electrostatic force \mathbf{F}_Q becomes strongly dominant. Indeed $\mathbf{F}_Q = Q\mathbf{E}_{\text{cnv}}$, and the dust charge Q is almost independent on the plasma Debye length when it is large enough (the capacitance tends to $C = 4\pi\epsilon_0 R_p$); in ion thermal units:

$$\mathbf{F}_Q^p \sim 4\pi\sqrt{\pi}F_i^0 \frac{\Lambda_{De}^2}{R_p^2} \tau \left(1 + \frac{R_p}{\Lambda_s}\right) \chi_p w_\perp \beta_i \mathbf{e}_x. \quad (\text{VII.49})$$

All the other forces on the contrary are directly dependent on the ion current or the feedback of plasma polarization on the dust charge, both linearly depending on the plasma density N_∞ , hence $\propto 1/\Lambda_{De}^2$ in absolute value, or independent of Λ_{De} when expressed in units of F_i^0 or $R_p^2 N_\infty T_e$.

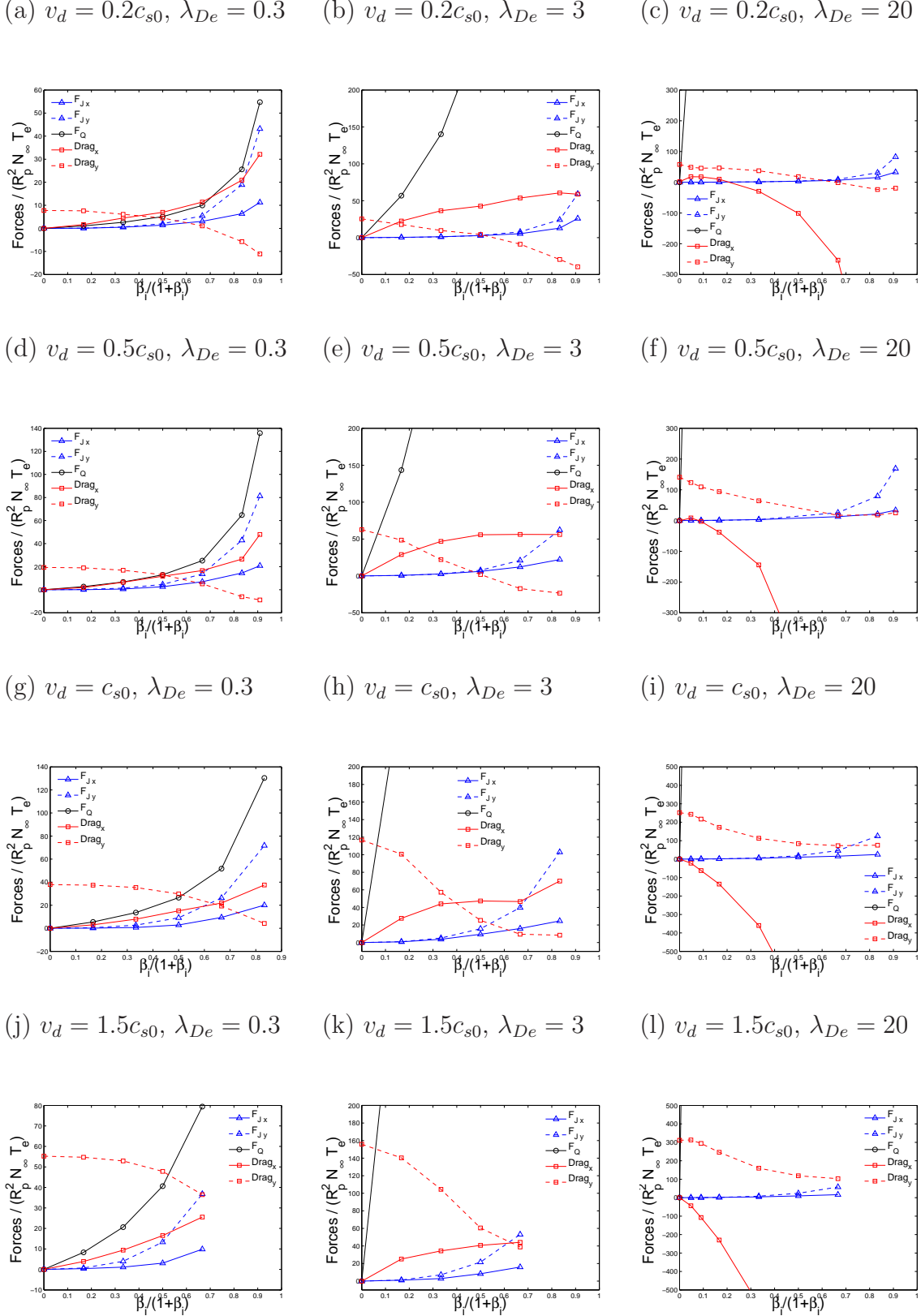


Figure VII-12: Comparison of the total ion-drag force computed by SCEPTIC3D with the parameters of Fig. (VII-10), with the non ion-drag forces \mathbf{F}_j and \mathbf{F}_Q . For easy reading, lines referring to forces acting along \mathbf{e}_x are solid, and dashed for \mathbf{e}_y .

Chapter VIII

Conclusions

VIII.1 Position of the problem and computational approach

This thesis presented a comprehensive solution to the equations governing a collisionless plasma flow past an ion-collecting conducting sphere, in the presence of crossed electric and magnetic fields. It should be seen as is in line with the never-ending endeavour of plasma physicists to understand the details of plasma-surface interaction, undergridding the behaviour of systems as diverse as electrostatic probes, dust particles, and ionospheric spacecraft. The rationale behind our admittedly oversimplified model is to limit the number of free parameters to a minimum, in order to only capture the fundamental physics and gain valuable insight that can possibly be applied to more complex and realistic situations.

The core tool developed for this investigation is the Particle In Cell code SCEPTIC3D, derived from the 2D code SCEPTIC originally written by Hutchinson [9]. The two key characteristics of the SCEPTIC approach are a Boltzmann treatment of the repelled electrons, relaxing the necessity to resolve electron-transit time-scales, and the use of a spherical grid isomorphic to the ion collector, in order to accurately capture the plasma-surface interface. SCEPTIC3D is fully parallelized (particle advance + Poisson solver), and includes arbitrary uniform magnetic field, external velocity

magnitude and direction, ion temperature and electron Debye length.

A significant number of successful SCEPTIC3D benchmarks have been carried out, including comparisons with prior SCEPTIC(2D) calculations, comparisons with analytic or semi-analytic solutions in a selection of limiting regimes (zero ion response, zero Debye length and infinite magnetic field, infinite Debye length and infinite magnetic field), and verification that momentum (mechanical + electromagnetic) is conserved in the simulation.

VIII.2 Summary of physical results

Strong magnetization and zero Debye length

The results derived in this thesis apply when coherent cross-field flow dominates anomalous transport, hence the physics is purely convective. In the limit of small ion Larmor radius and negligible Debye length, the problem is therefore two-dimensional and each plane of flow and magnetic field can be treated independently. We showed that provided we do not need to analyze the downstream shock, the presheath solution (ion distribution function) only depends on the angle of probe tangent to magnetic field. This enabled us to solve the ion kinetic equation self-consistently with the quasineutrality condition by the method of characteristics, without using SCEPTIC3D.

The key result is that to second and almost third order in the external flow Mach number, the ion flux-ratio to electrodes whose tangents are oriented at angle $\eta + \pi$ and η with respect to the magnetic field in the plane of flow and magnetic field is given by $R = \exp [(M_\infty - M_\perp \cot \eta) / M_c]$ (Eq. (II.75)). Although the model is not isothermal, Mach numbers are normalized to the isothermal ion sound speed. M_c is the Mach probe “calibration factor”, function of ion to electron temperature ratio τ only, found to vary between $M_{c|\tau=0} = 1/2$ and $M_{c|\tau=\infty} = 1/\sqrt{2\pi} \simeq 0.4$ (Eq. (II.76)). As can be seen in Fig. (II-11), the exponential form (II.75) can be used for supersonic external flows as well, albeit introducing a small error, of the order $\sim 10\%$ at $M_\infty - M_\perp \cot \eta = 2$ for instance. Measuring the flux ratios at angles $3\pi/4$

and $\pi/4$ then readily gives the external Mach numbers (Eqs (II.79,II.80)). Recalling the isothermal fluid solution [15] yields $M_c = 0.5$ regardless of τ , we conclude that the isothermal approximation induces an error less than $\sim 20\%$ on M_c , which might not be detectable in today's Mach probe measurements. Although not a proof, it is reasonable to expect the more sophisticated isothermal calculations accounting for diamagnetic and self-consistent convective drifts of Ref. [40] to be valid within experimental accuracy as well.

Arbitrary magnetization and zero Debye length

At intermediate magnetization yet negligible Debye length, when the ion Larmor radius compares to the probe radius, the plasma profiles show a complex three-dimensional structure that SCEPTIC3D can fully resolve. In particular we observe the effect of magnetic presheath displacement described in Ref. [40], as well as polarization drift modulation where the probe surface is grazing the magnetic field. An unexpected finding in this regime is that for cold ions and close to sonic flows, the total saturation current peaks here (see Fig. (IV-7c)).

Although the full ion charge-flux distribution to the probe depends on the plasma parameters in a non-straightforward way, the major result of this study is that flux ratios at $\pm 45^\circ$ to the magnetic field in planes of flow and magnetic field can very easily be related to the external Mach numbers. To within $\sim 10\%$ accuracy (at least for $\tau \geq 0.1$), there exists a single factor M_c , function of magnetization β_i and temperature ratio τ only, such that M_\perp and M_∞ satisfy Eqs (II.79,II.80). Except at infinite magnetization, M_c is probe-shape dependent, and sphere solutions on the major and quarter cross-sections are given in Fig. (IV-11). This provides the theoretical calibration for transverse Mach probes with appropriately placed electrodes. Of course probes are rarely spherical in practice, nevertheless we believe that the provided solutions should reasonably well apply to infinite cylindrical probes with circular cross-section, and pyramidal probes such as the Alcator C-mod WASP [22], respectively.

Arbitrary magnetization and finite Debye length

The physics at finite Debye length is more complex, because information on the sphere potential permeates into the plasma region. In particular, when the electron Debye length goes over the average ion Larmor radius ($\Lambda_{De} \gtrsim R_L$), the concept of magnetic presheath breaks down and the ions experience the probe shielding of the external convective electric field. The ion “ $\mathbf{E} \times \mathbf{B}$ ” velocity in the probe neighborhood is then tangent to the surface, as shown in Fig. (VI-9), and information about the external transverse velocity is lost. In the idealized regime of infinite Debye length for example, it was shown that flux ratios are not even a monotonic function of the external cross field drift (see Fig. (V-6a)). The Mach probe calibration method proposed in the context of quasineutral plasmas (Eqs (II.79,II.80)) is shown to hold up to Debye lengths equal to about 10% of the probe radius ($\lambda_{De} \lesssim 0.1$), the corresponding calibration factors at $\tau = 1$ being plotted against ion magnetization in Fig. (VI-16).

Studies of ion collection show that exceeding of the unmagnetized current limit, first observed in Fig. (IV-7c), strengthens as the Debye length increases. As can be seen in Fig. (VI-11), for large enough Debye length and cross-field velocity, the current is found to significantly exceed the Orbit Motion Limited (OML) limit. This effect, non present in the absence of cross-field drift, is due to the magnetic field focussing towards the probe of ions which, in unmagnetized conditions, would just have been deflected.

Force calculations

SCEPTIC3D has also been used to study the question of forces experienced by the sphere, that we separate into ion-drag calculated at the surface (ion impact force, electrostatic Maxwell stress accounting only for the sphere-induced potential distribution, and the typically negligible electron pressure on electron-repelling objects), external electrostatic force (action of \mathbf{E}_{env} on the sphere charge), and internal Lorentz force (caused by currents circulating in the sphere, whose role is to balance asymmetries in ion and electron collection).

It is found that in tokamak-edge conditions the *total* ion-drag in the direction of cross-field flow can reverse, mostly at intermediate Debye lengths ($\Lambda_{De} = O(R_p)$), although (approximate) calculations of the net current circulating in the sphere indicate that the internal Laplace force is in the positive direction and larger in magnitude than the ion-drag. Also of interest to the study of dust dynamics is the observation that for short electron Debye lengths ($\Lambda_{De} \lesssim R_p$), the ion-drag and internal Lorentz force in the direction antiparallel to the convective electric field are in the same direction and have the same magnitude as QE_{cav} . We therefore predict that in such conditions, dust particles should have a significantly faster gyromotion than what predicted by the Larmor formula QB/m_{Dust} .

VIII.3 Directions for future work

Several paths could be followed to build on the core capabilities of SCEPTIC3D and obtain new high impact results.

One route would be to complexify the ion physics. SCEPTIC2D has built in a Monte Carlo routine treating constant collision-frequency charge exchange events [65, 66], that could easily be ported in SCEPTIC3D in order to investigate the coupled effect of ion magnetization and collisionality. This is particularly relevant to the understanding of low temperature dusty plasma experiments where the background neutral density is significant. There is however much more to be done with collisionless ions. First, it would be relatively easy, at least computationally speaking, to treat multiple ion species or multiple charge states; this would allow investigation of basic plasma physics questions such as the multi-species sheath formation mechanism [67], as well as obtain more practical results applicable for instance to probe operation in DT tokamak discharges. Second, it would be interesting to allow reinjection of ions from a distribution function with transverse temperature or density gradients. Indeed in this thesis cross-field flow has been taken as purely convective, while transverse pressure gradients in tokamak edges might drive non-negligible diamagnetic drifts. Important analytic progress in the understanding of strongly magnetized Mach probes

in such conditions has recently been made in the isothermal fluid approximation [40]. A valuable contribution would be to validate the isothermal approximation as well as the extent to which the strongly magnetized limit is valid, by comparison with PIC simulations as done in this thesis for the convective drift case.

A second, more ambitious direction involves the abandon of the Boltzmann electron treatment. This would first allow to run the code in the floating potential regime, and to consider insulating collectors. In Ref. [64] an empirical formula relating the electron flux to a negatively biased sphere was given, but it requires validation in cross-field flows, and does not work for supersonic drifts relevant for instance to ionospheric satellites. Adding PIC electrons would also allow to model situations where surface emission (such as thermionic, secondary, or photo-emission) is significant [45]. In those conditions dust particles can charge up positively [68], and most available treatments of such regime are in the linearized approximation hence need benchmarking.

In addition to probes, dust and spacecraft, a fourth category of physical objects can be modeled as a sphere embedded in a cross-field plasma flow, namely celestial objects such as planetary moons [69, 70]. Unfortunately while typical magnetospheric thermal speeds are well below the speed of light, length scales involved are of the order of the thousand kilometers, hence the uniform magnetic field approximation breaks down. Once PIC electrons are added in the code, a third challenging undertaking would be to implement an Ampere solver, in order to self-consistently treat global MHD dynamics with finite Larmor radius effects. A key ingredient not to forget for this studies is Coulomb collisionality between ions and electrons, responsible for resistivity.

The last direction that I would like to suggest, in parallel or in addition to the previous, is a change in geometry. Because the philosophy of SCEPTIC is to treat simplified models, but well, in particular the plasma surface boundary, only shapes that can easily be mapped to a structured grid seem appropriate. Presumably the present code structure could be modified to treat ellipsoids, upon appropriate rescaling of the ions' equations of movement, Poisson solver, and reinjection scheme. A

second geometry of interest, in particular for the modeling of electric probes, would be cylindrical.

Appendix A

Boltzmann electron response

A.1 Electron density distribution

Omitting collisional terms, the steady-state perpendicular and parallel electron momentum equations are

$$\begin{cases} m_e N_e [(\langle \mathbf{v}_e \rangle \cdot \nabla) \langle \mathbf{v}_e \rangle]_{\perp} = -e N_e (\mathbf{E}_{\text{cnv}} - \nabla_{\perp} \Phi + \langle \mathbf{v}_e \rangle \times \mathbf{B}) - \nabla_{\perp} P_e, \\ m_e N_e [(\langle \mathbf{v}_e \rangle \cdot \nabla) \langle \mathbf{v}_e \rangle]_{\parallel} = -e N_e (-\nabla_{\parallel} \Phi) - \nabla_{\parallel} P_e, \end{cases} \quad (\text{A.1})$$

where $\langle \mathbf{v}_e \rangle$ refers to the electron fluid velocity, N_e to the electron density, $P_e = N_e T_e$ to the electron pressure that we immediately assume to be scalar, $-e$ to the electron charge and Φ to the *a priori* unknown self-consistent potential distribution around the probe.

We assume the probe to be strongly electron repellent, implying $|\nabla T_e|/T_e \ll |\nabla N_e|/N_e$: this is the ion-collecting probe approximation. Furthermore, typical flow velocities in the bulk plasma being of the order $c_{s0} \ll v_{te}$ (Eq. (II.13)), we can write $m_e N_e |(\langle \mathbf{v}_e \rangle \cdot \nabla) \langle \mathbf{v}_e \rangle| \ll T_e |\nabla N_e|$: this is the massless electron approximation coupled to the hypothesis of sub-electron-thermal flow conditions.

The electron temperature T_e is therefore constant in the bulk plasma and equal to its value at infinity, justifying the notation T_e rather than $T_{e\infty}$ for its unperturbed value. Furthermore the inertial term $m_e (\langle \mathbf{v}_e \rangle \cdot \nabla) \langle \mathbf{v}_e \rangle$ is negligible, hence integra-

tion of the parallel momentum equation shows that the electrons are Boltzmann distributed:

$$N_e = N_\infty \exp\left(\frac{e\Phi}{T_e}\right) = N_\infty \exp\phi, \quad (\text{A.2})$$

while integration of the perpendicular momentum equation shows that the electron cross-field velocity is given by

$$\langle \mathbf{v}_e \rangle_\perp = \mathbf{E}_{\text{cnv}} \times \frac{\mathbf{B}}{\mathbf{B}^2} \quad (\text{A.3})$$

regardless of the self-consistent potential gradient.

The above fluid argument is not valid in the immediate probe vicinity, where half the electron orbits are directed outwards hence unpopulated by probe shadowing. In particular the electron distribution function there being one-sided, the electron fluid velocity compares to v_{te} rather than c_{s0} , and m_e cancels in the inertial term $m_e |(\langle \mathbf{v}_e \rangle \cdot \nabla) \langle \mathbf{v}_e \rangle|$. Because the probe is strongly electron-repellent however, the electron density at the surface is negligible compared to N_∞ and calculating its exact value is not important.

All calculations in this thesis are therefore performed assuming Boltzmann electrons (A.2) in the entire domain, regardless of the plasma parameters.

A.2 Electron current

Using the constancy of the electron distribution function along electron orbits already invoked to derive Eq. (V.1), the unmagnetized electron flux density to the probe is equal to the free-space one-dimensional flux density scaled down by the same factor as N_e :

$$\Gamma_e^{\beta_e=0} = N_\infty \exp\left(\frac{e\Phi_p}{T_e}\right) \frac{v_{te}}{2\sqrt{\pi}}, \quad (\text{A.4})$$

where $\Phi(R_p, \theta, \psi) = \Phi_p$ is uniform in the unmagnetized regime.

The derivation of Eq. (A.4) assumes that (a) the electron drift velocity is much smaller than v_{te} , which is always true in our massless electron treatment, and (b)

that all the orbits striking the probe are connected to infinity, which is again true if $\mathbf{B} = 0$ (i.e. $\beta_e = 0$). When a background magnetic field is present however (b) is no longer a good approximation. The flux is reduced because some helical orbits intersect the probe several times. Orbit arcs that intersect the sphere at both ends are unpopulated, as shown in Fig. (A-1).

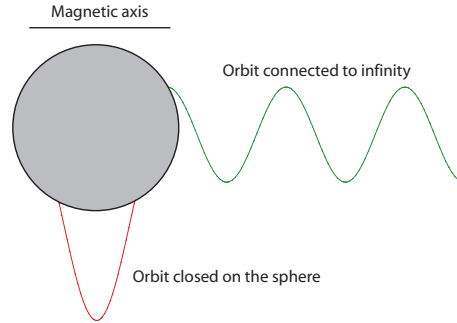


Figure A-1: Schematic representation of the two kind of orbits intersecting the probe in the presence of a background magnetic field. In a collisionless plasma orbits that close on the sphere are empty.

When the electron Larmor radius is much larger than the sphere radius R_p , that is in the limit $\beta_e = 0$, then no such empty orbits exist and one can use Eq. (A.4), giving for the total current to an equipotential repelling sphere of radius R_p :

$$I_e^{\beta_e=0} = 4\pi R_p^2 N_\infty \frac{v_{te}}{2\sqrt{\pi}} \exp\left(\frac{e\Phi_p}{T_e}\right). \quad (\text{A.5})$$

In the opposite limit of infinitesimal Larmor radius, the electrons move one-dimensionally along the field, and encounter only the projection of the probe area ($2\pi R_p^2$, where the 2 is due to the electrons coming from both sides of the probe) in the field direction. Even if $|\mathbf{v}_d| \ll v_{te}$, a cross-field drift originating from a convective electric field \mathbf{E}_{cnv} strongly affects the electron flux because the probe potential in that case is not uniform, rather given by Eq. (III.12). Therefore the current instead

becomes, for $\beta_e = \infty$:

$$\begin{aligned} I_e^{\beta_e=\infty} &= 2R_p^2 N_\infty \frac{v_{te}}{2\sqrt{\pi}} \int_{\rho=0}^1 \int_{\psi=0}^{2\pi} \exp\left(\frac{e(\Phi_p + [E_{\text{cnv}} R_p] \rho \cos \psi)}{T_e}\right) \rho d\rho d\psi \\ &= 4\pi R_p^2 N_\infty \frac{v_{te}}{2\sqrt{\pi}} \exp\left(\frac{e\Phi_p}{T_e}\right) \frac{T_e}{e [E_{\text{cnv}} R_p]} \mathbb{I}_1\left(\frac{e [E_{\text{cnv}} R_p]}{T_e}\right). \end{aligned} \quad (\text{A.6})$$

where \mathbb{I}_n is the modified Bessel function defined by

$$\mathbb{I}_n(x) = \frac{1}{\pi} \int_0^\pi \exp(x \cos \alpha) \cos(n\alpha) d\alpha. \quad (\text{A.7})$$

If $[E_{\text{cnv}} R_p] \ll T_e/e$, the strongly magnetized electron current given by Eq. (A.6) is half the unmagnetized one. In this thesis we will not need the exact value of the electron current. For a discussion of how to bridge the gap between the limits $\beta_e = 0$ and $\beta_e = \infty$ the reader is referred to Ref. [64].

Bibliography

- [1] I. Langmuir and H.M. Mott-Smith. The pressure effect and other phenomena in gaseous discharges. *G.E. Rev.*, 27:449, 538, 616, 762, 1924.
- [2] H.M. Mott-Smith and I. Langmuir. The Theory of Collectors in Gaseous Discharges. *Phys. Rev.*, 28:727–763, 1926.
- [3] P.M. Chung, L. Talbot, and K.J. Touryan. *Electric Probes in Stationary and Flowing Plasmas: Theory and Application*. Springer, New York, 1975.
- [4] I.H. Hutchinson. *Principles of Plasma Diagnostics*, 2nd ed. Cambridge University Press, Cambridge, UK, 2002.
- [5] V.E. Fortov, A.C. Ivlev, S.A. Khrapak, A.G. Khrapak, and G.E. Morfill. Complex (dusty) plasmas: Current status, open issues, perspectives. *Phys. Reports*, 421:1–103, 2005.
- [6] M.J. Goeckner, J.A. Goree, and T.E. Sheridan Jr. Monte Carlo Simulations of Ions in a Magnetron Plasma. *IEEE Trans. plasma science*, 19(2), 1991.
- [7] J.G. Laframboise. Current collection by a positively charged spacecraft: Effects of its magnetic presheath. *J. Geophysical Research*, 102(A2):2417–2432, 1997.
- [8] C.K. Birdsall and A.B. Langdon. *Plasma Physics Via Computer Simulation*. Taylor & Francis, Institute of Physics, Series in Plasma Physics, NY, 1985.
- [9] I.H. Hutchinson. Ion collection by a sphere in a flowing plasma: 1. Quasineutral. *Plasma Phys. Control. Fusion*, 44:1953–1977, 2002.
- [10] I.H. Hutchinson. Ion collection by a sphere in a flowing plasma: 2. Non-zero Debye length. *Plasma Phys. Control. Fusion*, 45:1477–1500, 2003.
- [11] I.H. Hutchinson. Ion collection by a sphere in a flowing plasma: 3. Floating potential and drag force. *Plasma Phys. Control. Fusion*, 47:71–87, 2005.
- [12] I.H. Hutchinson. Collisionless ion drag force on a spherical grain. *Plasma Phys. Control. Fusion*, 48:185–202, 2006.
- [13] L.J. Sonmor and J.G. Laframboise. Exact current to a spherical electrode in a collisionless, large Debye-length magnetoplasma. *Phys. Fluids*, 3:2472–2490, 1991.

- [14] L. Patacchini. Collisionless Ion Collection by a Sphere in a Weakly Magnetized Plasma. Master's thesis, Massachusetts Institute of Technology, Nuclear Science and Engineering Department, May 2007.
- [15] I.H. Hutchinson. Ion Collection by Oblique Surfaces of an Object in a Transversely Flowing Strongly Magnetized Plasma. *Phys. Rev. Letters*, 101:035004, 2008.
- [16] G.F. Matthews, S.J. Fielding, G.M. McCracken, C.S. Pitcher, P.C. Stangeby, and M. Ulrickson. Investigation of the fluxes to a surface at grazing angles of incidence in the tokamak boundary. *Plasma Phys. Control. Fusion*, 32(14):1301–1320, 1990.
- [17] A.J.H. Donné. Diagnostics for current density and radial electric field measurements: overview and recent trends. *Plasma Phys. Control. Fusion*, 44:B137, 2002.
- [18] B. LaBombard, J.W. Hughes, and N. Smick. Critical gradients and plasma flows in the edge plasma of Alcator C-mod. *Phys. Plasmas*, 15(5):056106, 2008.
- [19] F. Wagner, G. Becker, and K. Behringer *et al.* Regime of Improved Confinement and High Beta in Neutral-Beam-Heated Divertor Discharges of the ASDEX Tokamak. *Phys. Rev. Letters*, 49:1408, 1982.
- [20] K.H. Burrel, E.J. Doyle, and P. Gohil *et al.* Role of the radial electric field in the transition from L (low) mode to H (high) mode to VH (very high) mode in the DIII-D tokamak. *Phys. Plasmas*, 1(5):1536, 1994.
- [21] C.S. MacLatchy, C. Boucher, D.A. Poirier, and J. Gunn. Gundestrup: A Langmuir/Mach probe array for measuring flows in the scrape-off layer of TdEV. *Rev. Sci. Instr.*, 63(8):3923, 1992.
- [22] N. Smick and B. Labombard. Wall scanning probe for high-field side plasma measurements on Alcator C-mod. *Rev. Sci. Instr.*, 80:023502, 2009.
- [23] I.H. Hutchinson. A fluid theory of ion collection by probes in strong magnetic fields with plasma flow. *Phys. Fluids*, 30(12), 1987.
- [24] I.H. Hutchinson. Ion collection by probes in strong magnetic fields with plasma flow. *Phys. Rev. A*, 37(11):4358, 1988.
- [25] I.H. Hutchinson. Reply to the comments of Stangeby. *Phys. Fluids*, 31(9):2728, 1988.
- [26] J.P. Gunn, C. Boucher, P. Devynck, I. Ďuran, K. Dyabilin, J. Horaček, M. Hron, J. Stöckel, G. Van Oost, H. Van Goubergen, and F. Žáček. Edge flow measurements with Gundestrup probes. *Phys. Plasmas*, 8(5):1995–2001, 2001.

- [27] K.S. Chung and I.H. Hutchinson. Kinetic theory of ion collection by probing objects in flowing strongly magnetized plasmas. *Phys. Rev. A*, 38(9):4721, 1988.
- [28] K-S. Chung, H-J. Woo, and M-J. Lee. Effect of Recombination and Ionization on the Deduction of Mach Numbers in Flowing Magnetized Plasmas. In *35th EPS Conference on Plasma Phys. Hersonissos*, number 32D in Proceedings, June 2008.
- [29] J-L. Delcroix and A. Bers. *Physique des plasmas tomes 1 et 2 (In French)*. CNRS Editions, EDP sciences, Paris, 1994.
- [30] S. Gangadhara and B. LaBombard. Impurity plume experiments in the edge plasma of the Alcator C-Mod tokamak. *Plasma Phys. Control. Fusion*, 46:1617–1646, 2004.
- [31] H. Van Goubergen, R.R Weynants, S. Jachmich, M. Van Schoor, G. Van Oost, and E. Desoppere. A 1D fluid model for the measurement of perpendicular flow in strongly magnetized plasmas. *Plasma Phys. Control. Fusion*, 41(6), 1999.
- [32] I.H. Hutchinson. The magnetic presheath boundary condition with $\mathbf{E} \wedge \mathbf{B}$ drifts. *Phys. Plasmas*, 3(6), 1996.
- [33] A.V. Gurevich and L.P. Pitaevskii. Non-linear dynamics of a rarefied ionized gas. *Prog. Aerospace Sci.*, 16(3), 1975.
- [34] J.R. Sanmartin. Theory of a Probe in a Strong Magnetic Field. *Phys. Fluids*, 13(1):103–116, 1970.
- [35] P.C. Stangeby. Effect of bias on trapping probes and bolometers for tokamak edge diagnosis. *J. Phys. D: Appl. Phys.*, 15(15):1007, 1982.
- [36] R.A. Pitts and P.C. Stangeby. Experimental tests of Langmuir probe theory for strong magnetic fields. *Plasma Phys. Control. Fusion*, 32(13):1237–1248, 1990.
- [37] L. Patacchini and I.H. Hutchinson. Explicit time-reversible orbit integration in Particle In Cell codes with static homogeneous magnetic field. *J. Comp. Phys.*, 228(7):2604–2615, 2009.
- [38] W.H. Press, S.A. Teukolsky, W.T. Vetterling, and B.P. Flannery. *Numerical Recipes (3^d edition)*. Cambridge University Press, NY, 2007.
- [39] J.E. Daugherty, R.K. Porteous, and D.B. Graves. Electrostatic forces on small particles in low-pressure discharges. *J. Appl. Phys*, 73(4):1617–1620, 1993.
- [40] I.H. Hutchinson. Oblique ion collection in the drift approximation: How magnetized Mach probes really work. *Phys. Plasmas*, 15:123503, 2008.
- [41] L. Patacchini and I.H. Hutchinson. Angular distribution of current to a sphere in a flowing, weakly magnetized plasma with negligible Debye length. *Plasma Phys. Control. Fusion*, 49:1193–1208, 2007.

- [42] E. Ko and N. Hershkowitz. Asymmetry reversal of ion collection by Mach probes in flowing unmagnetized plasmas. *Plasma Phys. Control. Fusion*, 48(5):621–634, 2006.
- [43] C.K. Goertz. Dusty plasmas in the solar system. *Rev. Geophysics*, 27(2):271–292, 1989.
- [44] L. Ravi and S.L. Girshick. Coagulation of nanoparticles in a plasma. *Phys. Rev. E*, 79:026408, 2009.
- [45] G.L. Delzanno, A. Bruno, G. Sorasio, and G. Lapenta. Exact orbital motion theory of the shielding potential around an emitting spherical body. *Phys. Plasmas*, 12:062102, 2005.
- [46] J. Winter. Dust in fusion devices-experimental evidence, possible sources and consequences. *Plasma Phys. Control. Fusion*, 40:1201–1210, 1998.
- [47] D.L. Rudakov, W.P. West, M. Groth, J.H. Yu, and J.A. Boedo. Dust Studies in DIII-D Tokamak. *Multifacets of dusty plasmas: Conference proceedings*, 1041:55–58, 2008.
- [48] A.Yu. Pigarov, S.I. Krasheninnikov, T.K. Soboleva, and T.D. Rognlien. Dust-particle transport in tokamak edge plasmas. *Phys. Plasmas*, 12:122508, 2005.
- [49] Y.L. Alpert, A.V. Gurevich, and L.P. Pitaevskii. *Space Physics with Artificial Satellites*. Consultants Bureau, New York, 1965.
- [50] I.B. Bernstein and I.N. Rabinowitz. Theory of electrostatic probes in a low-density plasma. *Phys. Fluids*, 2:112–121, 1959.
- [51] J.E. Allen, B.M. Annaratone, and U. de Angelis. On the orbital motion limited theory for a small body at floating potential in a Maxwellian plasma. *J. Plasma Phys.*, 63:299–309, 2000.
- [52] E.C. Whipple. Potential of surfaces in space. *Rep. Prog. Physics*, 44:1197–1250, 1981.
- [53] L.W. Parker and B.L. Murphy. Potential buildup on an electron-emitting ionospheric satellite. *J. Geophys. Res.*, 72:1631–1636, 1967.
- [54] J. Rubinstein and J.G. Laframboise. Theory of a spherical probe in a collisionless magnetoplasma. *Phys. Fluids*, 25:1174–1182, 1982.
- [55] E.C. Whipple. *The Equilibrium Electric Potential of a Body in the Upper Atmosphere and in Interplanetary Space*. PhD Thesis, George Washington University, 1965.
- [56] N. Singh, W.C. Leung, and G.M. Singh. Enhanced current collection by a positively charged spacecraft. *J. Geophysical Research*, 105(A9):20935–20947, 2000.

- [57] N.H. Stone, W.J. Raitt, and Jr. K.H. Wright. The TSS-1R electrodynamic tether experiment: Scientific and technological results. *Advances in Space Research*, 24(8):1037–1045, 1999.
- [58] N. Singh and V.S. Chaganti. Electron collection by a highly positive satellite in the ionosphere: Test particle simulation. *J. Geophysical Research*, 99(A1):469–478, 1994.
- [59] L. Patacchini and I.H. Hutchinson. Ion-collecting sphere in a stationary, weakly magnetized plasma with finite shielding length. *Plasma Phys. Control. Fusion*, 49:1719–1733, 2007.
- [60] A.V. Ivlev, S.A. Khrapak, S.K. Zhdanov, G.E. Morfill, and G. Joyce. Force on a Charged Test Particle in a Collisional Flowing Plasma. *Phys. Rev. Letters*, 92:205007, 2004.
- [61] S.A. Khrapak, A.V. Ivlev, G.E. Morfill, and H.M. Thomas. Ion drag force in complex plasmas. *Phys. Rev. E*, 66:046414, 2002.
- [62] H.N. Nitta, N. Nambu, N. Salimullah, and P.K. Shukla. Dynamical potential in a magnetized plasma. *Phys. Letters A*, 308:451–454, 2003.
- [63] D.K. Geller and J.C. Weisheit. Classical electron-ion scattering in strongly magnetized plasmas I. A generalized Coulomb logarithm. *Phys. Plasmas*, 12(4):4258, 1997.
- [64] L. Patacchini, I.H. Hutchinson, and G. Lapenta. Electron collection by a negatively charged sphere in a collisionless magnetoplasma. *Phys. Plasmas*, 14:062111, 2007.
- [65] I.H. Hutchinson and L. Patacchini. Computation of the effect of neutral collisions on ion current to a floating sphere in a stationary plasma. *Phys. Plasmas*, 14:013505, 2007.
- [66] L. Patacchini and I.H. Hutchinson. Fully Self-Consistent Ion-Drag-Force Calculations for Dust in Collisional Plasmas with an External Electric Field. *Phys. Rev. Letters*, 101:025001, 2008.
- [67] D. Lee, L. Oksuz, and N. Hershkowitz. Exact Solution for the Generalized Bohm Criterion in a Two-Ion-Species Plasma. *Phys. Rev. Letters*, 99:155004, 2007.
- [68] S.A. Khrapak, G.E. Morfill, V.E. Fortov, L.G. D'yachkov, A.G. Khrapak, and O.F. Petrov. Attraction of Positively Charged Particles in Highly Collisional Plasmas. *Phys. Rev. Letters*, 99:055003, 2007.
- [69] C.T. Russel. Interaction of the Galilean Moons with their plasma environments. *Planetary Space Science*, 53:473–485, 2005.

- [70] S.H. Brecht, J.G. Luhmann, and D.J. Larson. Simulation of the Saturnian magnetospheric interaction with Titan. *J. Geophys. Res.*, 105(A6):13119–13130, 2000.